SUPRAMOLECULAR CHEMISTRY OF SMALL MOLECULAR FUNDAMENTALS TO DRUG – RECEPTOR APPLICATIONS

by

DHANUSHI THATHSARA WELIDENIYA

B.S., University of Colombo, 2007

AN ABSTRACT OF A DISSERTATION

submitted in partial fulfillment of the requirements for the degree

DOCTOR OF PHILOSOPHY

Department of Chemistry
College of Arts and Sciences

KANSAS STATE UNIVERSITY
Manhattan, Kansas

2015

Abstract

A family of *bis*-pyridine based pharmaceutical active ingredients were synthesized and co-crystallized with four iodoperfluoroalkanes. Thirteen new crystal structures that are driven by I···N(py) halogen bonds, are presented and compared with that of their hydrogen-bonded analogues. Halogen bonded co-crystals exhibit two different structural arrangements, as opposed to layered architectures observed in hydrogen bonded co-crystals.

In order to explore the effect of aromatic stacking interactions on hydrogen and halogen bond driven co-crystallization process, we utilized a series of aromatic hydrogen and halogen bond donors in combination with *bis*-pyridine based pharmaceutical active ingredients. Aromatic stacking between the donor and the acceptor were limited, due to the lack of complementarity between the donor and the acceptor in terms of size, shape and geometry. In that case, homomeric interactions between the single components were translated into the structure of the binary co-crystals.

According to our charge calculations, similarly activated hydrogen and iodine atoms possess similar electrostatics. Therefore, we wanted to investigate the interchangeability of hydrogen bonds and halogen bonds by utilizing 2-aminopyrimidine as the backbone for C(*sp*)-H and C(*sp*)-I functionalities which makes self-complementary ribbons via NH···N synthons. Our results show that the ethynyl proton is capable of acting as a synthon mimic of ethynyl iodine by interchangeable C(*sp*)-H···N hydrogen bonds and C(*sp*)-I···N halogen bonds.

We exploited the halogen bonding donor capability of iodo, bromo and chloro ethynyl functionalities towards a series of halide ions. Based on the grinding experiments these donors showed 90%, 70% and 50% success rates towards halides. Among the halides, chlorides exhibited the highest red shift compared to bromides and iodides.

We synthesized a series of cavitands functionalized with hydrogen bond donor and acceptor groups and studied their binding preferences towards a series of active ingredients. We have shown that suitably functionalized cavitands can act as carriers of active ingredients and especially, selective binding of aspirin is demonstrated using a two-point binding mode.

SUPRAMOLECULAR CHEMISTRY OF SMALL MOLECULAR FUNDAMENTALS TO DRUG – RECEPTOR APPLICATIONS

by

DHANUSHI THATHSARA WELIDENIYA

B.Sc., University of Colombo, 2007

A DISSERTATION

submitted in partial fulfillment of the requirements for the degree

DOCTOR OF PHILOSOPHY

Department of Chemistry
College of Arts and Sciences

KANSAS STATE UNIVERSITY
Manhattan, Kansas

2015

Approved by:

Major Professor
Christer B. Aakeröy

Copyright

Abstract

A family of *bis*-pyridine based pharmaceutical active ingredients were synthesized and co-crystallized with four iodoperfluoroalkanes. Thirteen new crystal structures that are driven by I···N(py) halogen bonds, are presented and compared with that of their hydrogen-bonded analogues. Halogen bonded co-crystals exhibit two different structural arrangements, as opposed to layered architectures observed in hydrogen bonded co-crystals.

In order to explore the effect of aromatic stacking interactions on hydrogen and halogen bond driven co-crystallization process, we utilized a series of aromatic hydrogen and halogen bond donors in combination with *bis*-pyridine based pharmaceutical active ingredients. Aromatic stacking between the donor and the acceptor were limited, due to the lack of complementarity between the donor and the acceptor in terms of size, shape and geometry. In that case, homomeric interactions between the single components were translated into the structure of the binary co-crystals.

According to our charge calculations, similarly activated hydrogen and iodine atoms possess similar electrostatics. Therefore, we wanted to investigate the interchangeability of hydrogen bonds and halogen bonds by utilizing 2-aminopyrimidine as the backbone for C(*sp*)-H and C(*sp*)-I functionalities which makes self-complementary ribbons via NH···N synthons. Our results show that the ethynyl proton is capable of acting as a synthon mimic of ethynyl iodine by interchangeable C(*sp*)-H···N hydrogen bonds and C(*sp*)-I···N halogen bonds.

We exploited the halogen bonding donor capability of iodo, bromo and chloro ethynyl functionalities towards a series of halide ions. Based on the grinding experiments these donors showed 90%, 70% and 50% success rates towards halides. Among the halides, chlorides exhibited the highest red shift compared to bromides and iodides.

We synthesized a series of cavitands functionalized with hydrogen bond donor and acceptor groups and studied their binding preferences towards a series of active ingredients. We have shown that suitably functionalized cavitands can act as carriers of active ingredients and especially, selective binding of aspirin is demonstrated using a two-point binding mode.

Table of Contents

List of Figures

List of Tables

Acknowledgements

First and foremost, I would like to express my sincere gratitude to my advisor, Professor Christer B. Aakeröy for his continual guidance, encouragement, and motivation throughout these four years. I learned so much from your unique perspectives on writing and presenting research, personal integrity and expectations of excellence. I never got lost because you always steered me in the right direction in the road towards completion of this dissertation. I feel myself very lucky and I truly believe that it's been amazingly wonderful and been a great privilege to work with you.

I would also like to thank my Ph.D. advisory committee, Professor Eric A. Maatta, Professor Paul E. Smith, Professor James E. Edgar and Professor Ramaswamy Krishnamoorthi for their valuable time and inputs on this dissertation.

I'm grateful to Dr. John Desper for solving all the nice crystal structures and without them most of the chapters in this dissertation would not have been possible.

Big thanks to all the Aakeroy group members, past and present, for all the support and for all the fun times we had together. It was always a great group of people to work with. The lab was a very pleasant environment to work with because of all of you. Aakeroy group rocks!

I owe special thanks to Dr. Prashant Chopade for mentoring me with cavitand work. Thank you for all the support, suggestions and motivation on this big project.

Thanks to Dr. Leila Maurmann for helping me out with NMR studies. Thanks to Dr. Yasmin Patel, Mr. Jim Hodgson, Mr. Ron Jackson, Mr. Tobe Eggers, Ms. Mary Dooley, and Ms. Kimberly Ross as they made my research and life at K-state easier.

Special thanks goes to Dr. Dinusha Udukala and Dr. Manindu Weerasinghe for your great support in my admission to K-state.

I'm very fortunate to have met all my friends here in K-state. It's been an amazingly enjoyable four years of experience and I never felt I was away from home, because I had all of you with me. Thanks for being there for me and taking care of me during hard times. Special thanks to Tharanga for taking care of my teaching duties during the whole three months that I was sick. Last but not least, I want to thank my parents for their unconditional love, for all the blessings and for giving me strength to reach for the stars.

Dedication

To my dearest amma and appachchi

For their endless love

Chapter 1 - Introduction

1.1 From molecular chemistry towards supramolecular chemistry

Molecular chemistry, the chemistry of the covalent bond, is a powerful discipline for creating sophisticated molecules and materials as well as for establishing a connection between molecular structure and reactivity. The evolution of synthetic molecular chemistry began with Friedrich Wöhler's synthesis of urea in 1828; "I can make urea with no need of a kidney, or let alone an animal, be it a man or a dog".[1] Since then, the toolbox of covalent synthesis has grown rapidly with so called "name reactions"[2] that involve making or breaking of the covalent bonds allowing the "control over covalent bond".[3] Multiple steps, specific catalysts and reagents, solvents, isolation of intermediates, purification conditions are crucial in every aspect of strategic covalent synthesis. Systematic studies of these elaborative synthesis processes over the years have developed molecular chemistry to a higher level of sophistication beyond that realized in the early stage.[4]

"Just as there is a field of molecular chemistry based on the covalent bond, there is a field of supramolecular chemistry, the chemistry of molecular assemblies and of the intermolecular bond."[5] Supramolecular chemistry was defined by Jean-Marie Lehn, who won the Nobel Prize in 1987[6], as "chemistry beyond molecule" which introduce so called "supermolecules" as complex species that are synthesized by combining two or more molecules via non-covalent interactions. In supramolecular chemistry, molecules communicate with each other via reversible intermolecular interactions (e.g. hydrogen bonds, halogen bonds, van der Waals interactions and coordination bonds) as opposed to covalent bonds in molecular chemistry (Figure 1.1). Moreover supramolecular synthesis is carried out as one pot single step or one pot multiple step reactions[7] to isolate the final product without any intermediates and without further purification.

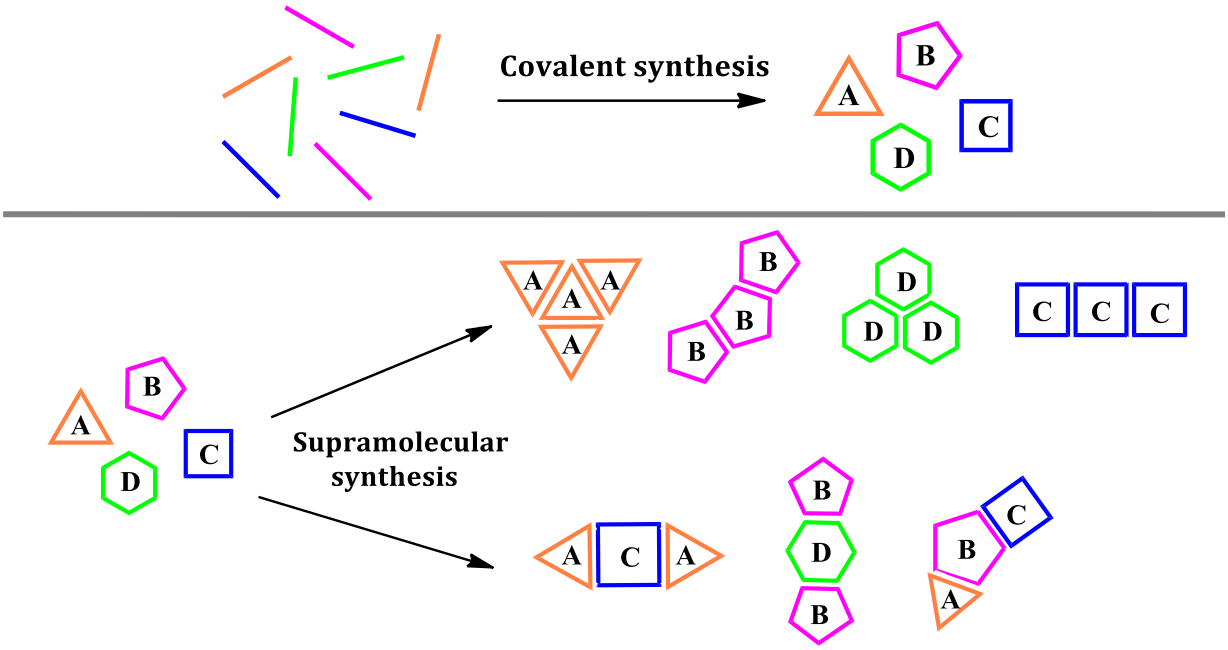

Figure 1.1 Schematic representation of covalent synthesis vs. supramolecular synthesis

Molecular recognition is a key aspect of supramolecular chemistry with a focus on size, shape, and complementarity match between the two components (host and the guest) of a molecular association event (Figure 1.2). Selectivity as the basic concept of molecular recognition was enunciated by H. E. Fischer[8] by his "lock-and-key" model related to enzyme-substrate interactions, and presented a crucial part of specificity and complementarity between the host and the guest. Advances of this concept has become the central topic in rational drug design with the aid of intelligent molecular docking.[9] Thus, molecular recognition involves structurally well-defined pattern of intermolecular interactions organized to accomplish a specific function.

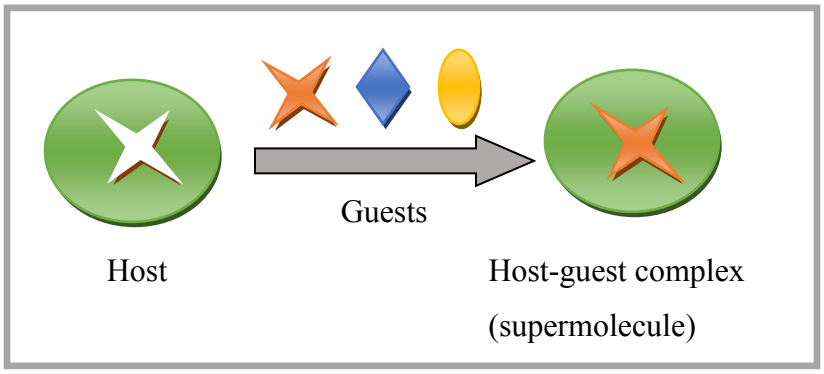

Figure 1.2 Example of selective molecular recognition event

1.2 Crystal engineering

Crystal engineering, a subset of supramolecular chemistry involves molecular recognition in the solid state. G. M. Schmidt coined the term "crystal engineering" as designing packing motifs of crystals in solid-state reactions using organic solid-state photochemistry.[10] The concept is to exert rational design of organic crystals by engineering intermolecular interactions to generate desired supramolecular architectures in solid state. Indeed Dunitz has referred to organic crystals as "supermolecule(s) *par excellence"*[11] as the association of supermolecules can be controlled to design new functional solids with desired physical and chemical properties.

Recent advances in engineered structural motifs enable a specific function via carefully tailored multi components in a crystal lattice. Development of crystal-engineering strategies towards exploitation of technologically important materials has become a captivating field to date. Such interesting outcome is demonstrated by enantioselective [2+2] photodimerization reaction with favorable molecular spacing of the two components and predetermined hydrogen-bonded dimers in the crystal lattice (Figure 1.3).

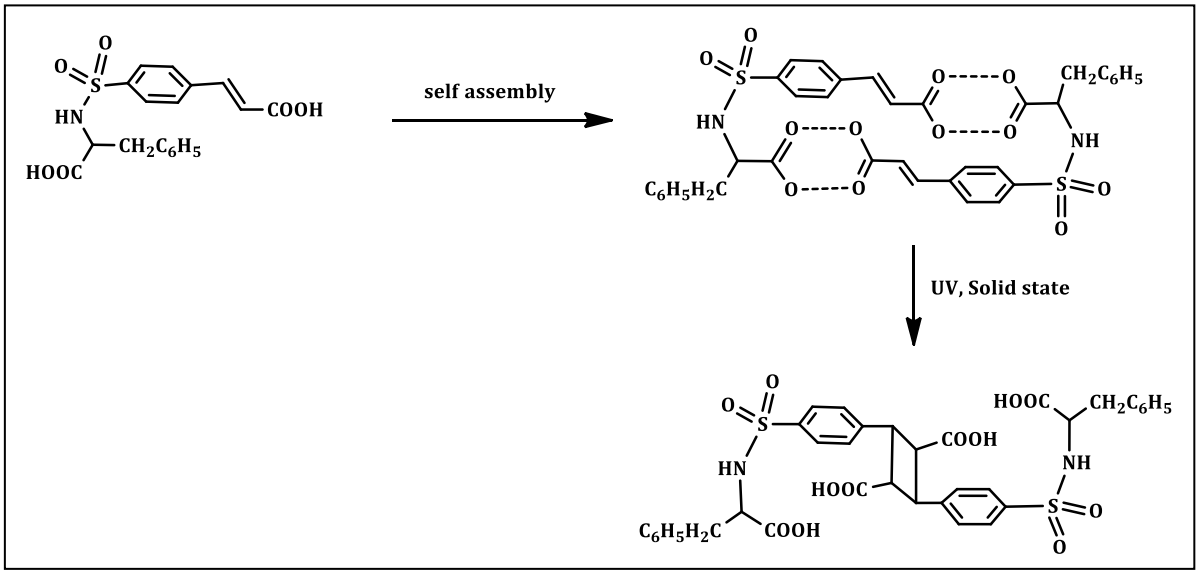

Figure 1.3 Design strategy for the construction of photo-reactive homo dimers and solid state photodimerization upon UV irradiation[12]

Noveron and coworkers[13] elucidated modulated magnetic properties of a series of crystalline solids containing N-(4-pyridyl)benzamide (NPBA) and metal ions where NPBA is engaged in three modes of intermolecular interactions, (hydrogen bonding, metal coordination

and π stacking). The resulting solid state supramolecular scaffolds, that are in periodic 1-D, 2-D and 3-D networks, display paramagnetic properties.

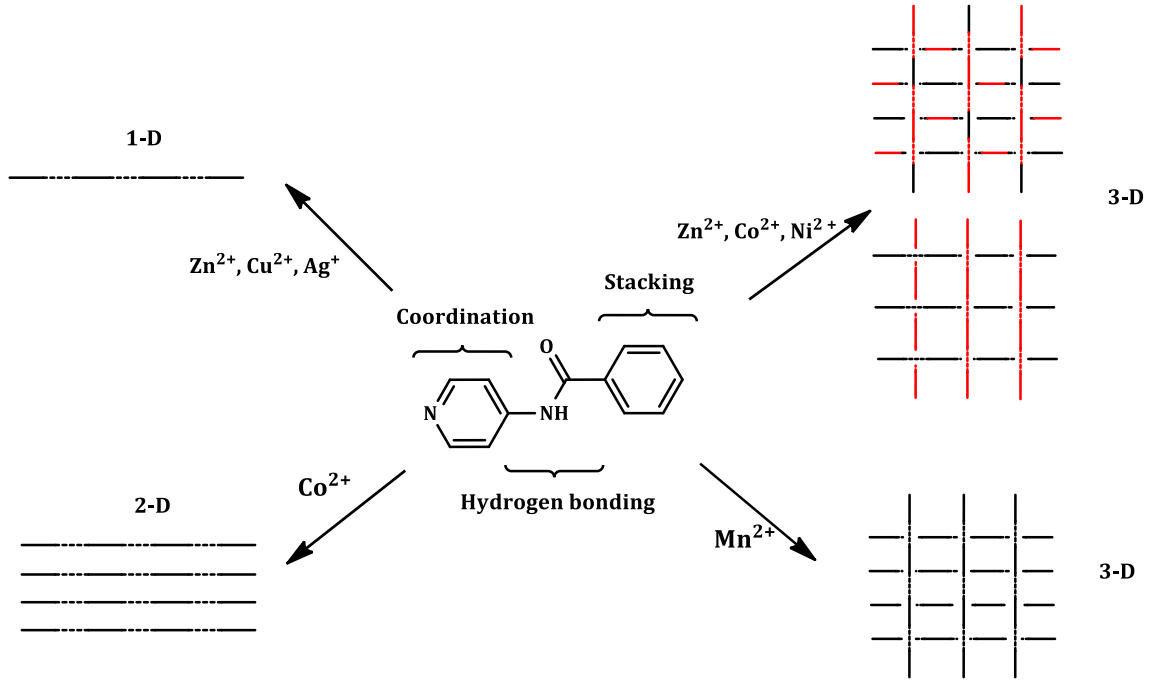

Figure 1.4 NPBA forming 1-D, 2-D and 3-D supramolecular architectures with metal ions[13]

Moreover, Desiraju and co-workers[14] developed novel NLO materials in which the two dipoles of the chromophores are oriented in non-centrosymmetric fashion (Figure 1.5) in the same crystal lattice (Figure 1.6a). In another example, nonlinear-optical-active centrosymmetric solids (Figure 1.5) are synthesized by combining bent linking groups and metal centers with well-defined coordination geometries (Figure 1.6b). These 2D coordination networks are carefully engineered to achieve NLO materials with high degree of predictability.[15]

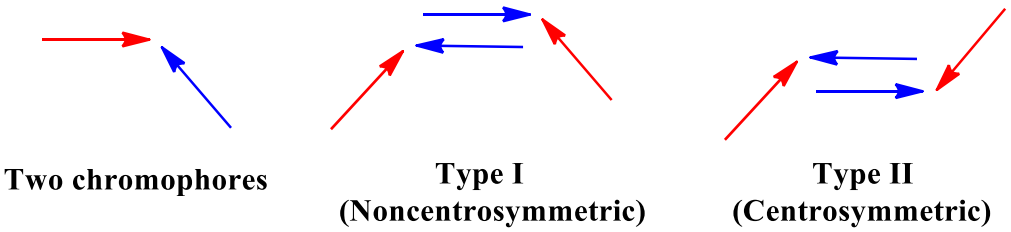

Figure 1.5 Primary arrangement of the two chromophores and the two possible orientations of the pair of chromaphors[14]

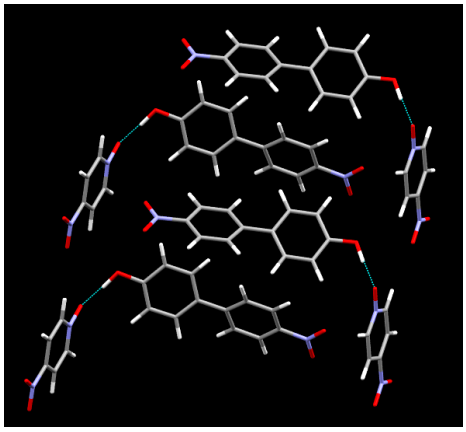

(a)

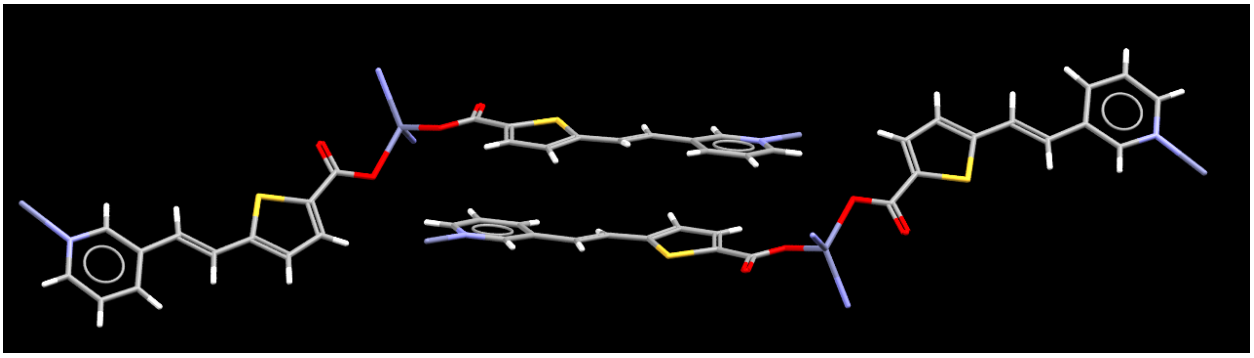

(b)

Figure 1.6 Arrangement of the chromophores in (a) non-centrosymmetric fashion (b) centrosymmetric fashion

These examples show that, crystal engineering can be employed to design materials with specific function as far as the molecular arrangement and connectivity is achieved. The connectivity between the molecules in a crystal lattice is governed by numerous intermolecular interactions such as van der Waals forces, (i.e.dispersion forces),[16] dipole-dipole interactions,[17] π stacking interactions,[18] hydrogen bonding and halogen bonding. Thus in a crystal structure, a combination of these intermolecular interactions that co-exist between molecules are responsible for different angles and directionalities that wind up as a balance in overall crystal packing. Thus it is important to understand these non-covalent interactions in order to create reliable synthetic routes to generate predictable supramolecular assemblies. Hydrogen bonding and halogen bonding are the two most common intermolecular forces widely applied in supramolecular synthesis.

1.2.1 Importance of hydrogen bonds in crystal engineering

Hydrogen bond is the most utilized intermolecular interaction in molecular recognition of macromolecules and supramolecular synthesis of molecular solids due to its strength and directionality.[19] According to the latest IUPAC project, the hydrogen bond is "an attractive interaction between a hydrogen atom from a molecule or a molecular fragment, X−H···A in which X is more electronegative than H, and an atom or a group of atoms in the same or different molecule, in which there is evidence of bond formation".[20] Hydrogen bonding is ubiquitous in nature, best examples being the DNA double helix composed of complementary base pairs and protein secondary structure of α-helix and β sheet assembled via hydrogen bonding (Figure 1.7).[21] An example where hydrogen bonding finds its application is synthetic material science, i.e. hydrogen bond mediated supramolecular semi conducting devices. The hydrogen bonding reinforce intermolecular π stacking to support mobilities up to 1.5 cm^2/Vs with T80 lifetimes comparable with the most stable organic semiconducting materials (Figure 1.8).[22]

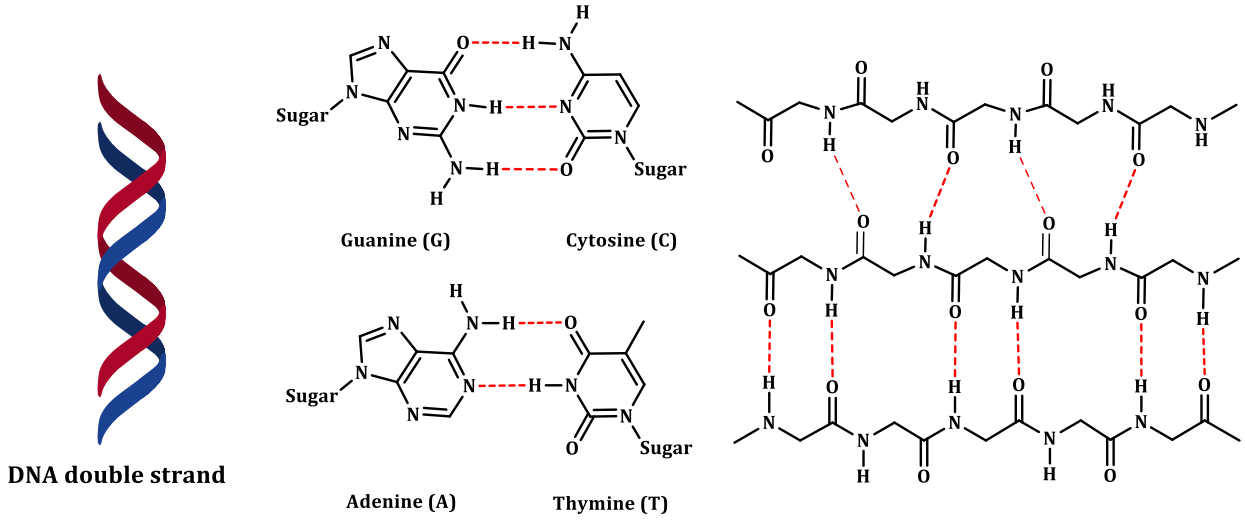

(a) (b)

Figure 1.7 Hydrogen bonding between (a) DNA base pairs (b) polypeptide chains of β sheets

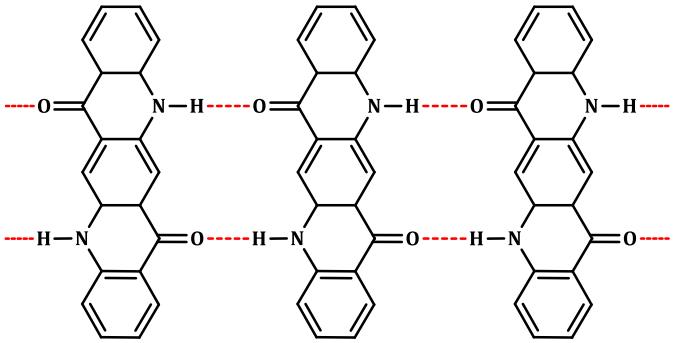

Figure 1.8 Hydrogen bonding between quinacridine molecules templating intermolecular π stacking

1.2.2 Halogen bonds- "A world parallel to hydrogen bonding"[23]

Halogen bonds (XB),[23-24] a recently added item to the supramolecular tool box, has gained widespread attraction as a counterpart to hydrogen bonding (HB). It is an intermolecular interaction between an electron deficient halogen atom and an electron-rich partner (Figure 1.9).[25] The anisotropic distribution of the electrostatic potential leaves an amphiphilic character to the halogen atom, where there is a region of positive potential along the C-X bond, the "σ hole"[26] and a region of negative potential perpendicular to the C-X bond (Figure 1.10). Therefore, a covalently bound halogen can interact with both electronegative and electropositive entities depending on the approaching direction.

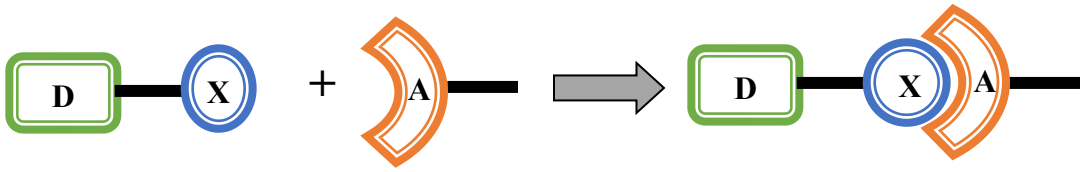

D-C, N, halogen, etc.

X-Cl, Br, I

A-N, O, S, Cl, Br, I, Cl^-, Br^-, I^-

Figure 1.9 Schematic diagram showing the formation of halogen bonds

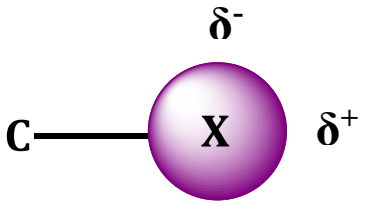

Figure 1.10 Anisotropic distribution of positive and negative electrostatic potential on halogen atom[27]

The understanding of halogen bonds in protein-ligand complexes consisting of X···π, X···N, X···O, X···S interactions is quite useful in synthesizing halogenated ligands as inhibitors in drug discovery and biomolecular design.[28] Distribution of these interactions in biological systems is displayed in Figure 1.11.

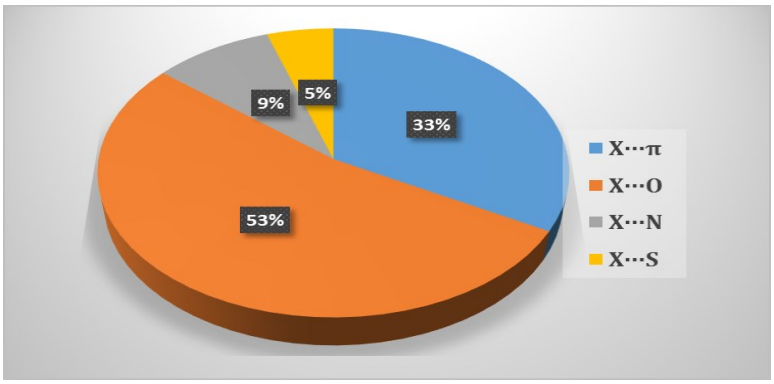

Figure 1.11 Distribution of different XB interactions present in biological systems

Halogen bond based recognition processes have been widely used to drive molecular assembly in the solid state, and rapid development in this area has moved towards functional materials. For example, XB has proven to be involved in effective catalytic systems, by activation of an electrophile towards a nucleophilic attack owing to the selectivity and directionality possessed by halogen bonds.[29] In one of those examples, iodine trichloride act as a strong XB donor which catalyze a ring-opening reaction by activation of the carbonyl group (Figure 1.12).[30]

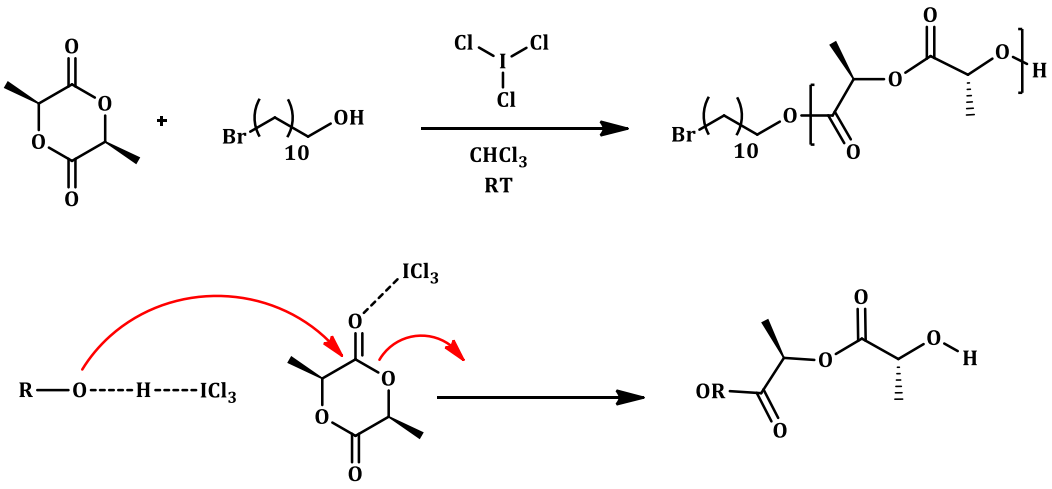

Figure 1.12 Halogen bond catalyzed ring opening

Halogen bonding has been advantageous with recycling and resolution processes which is an important segment in synthetic chemistry in terms of economic and environmental point of view. Resolution of a mixture of racemic perfluorocarbons is mediated by XB based adduct formation using Br^- and I^- anions.[31]

Hydrogen and halogen bond strengths can range from 5-200 kJ/mol depending on the system based on both experimental as well as theretical calculations.[32]

1.2.3 Supramolecular synthons

Supramolecular synthons are defined by Desiraju as "structural units within supermolecules which can be formed and/or assembled by known or conceivable synthon operations involving intermolecular interactions".[33] Supramolecular synthons are thus, the simplest robust units of a supramolecular architecture that carry key information encoded in the molecular recognition event.[34] By dissecting the complex supramolecular structures into simpler units or supramolecular synthons, defined by "supramolecular retrosynthesis",[35] it simplifies the understanding of the assembly process (Figure 1.13). Moreover, it helps to recognize the interchangeability of the synthons which is a crucial component in crystal engineering and this can be observed by molecules that contain different functionalities with similar crystal structures.[36] Also, it is possible to get control over supramolecular synthesis, if the synthons can be designed with predictability. Examples of robust supramolecular synthons that are commonly used in hydrogen bonding and halogen bonding are shown in Figure 1.14, which are further classified as homosynthons (occur between same complementary functional groups) and heterosynthons (occur between different complementary functional groups).

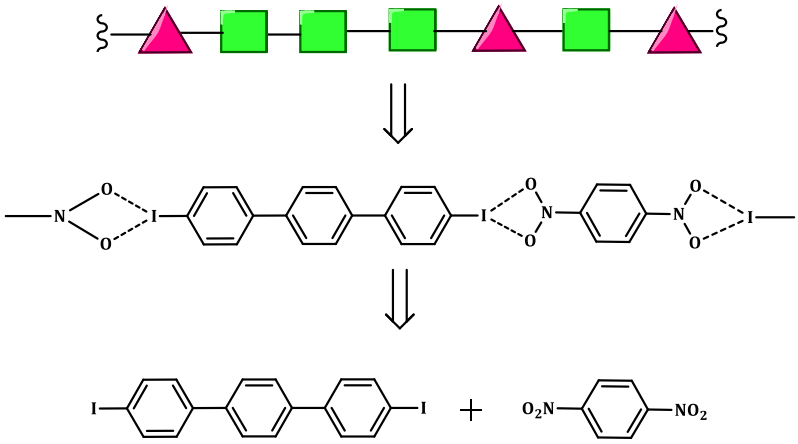

Figure 1.13 Retrosynthetic analysis from molecular synthons to supramolecular synthons[35]

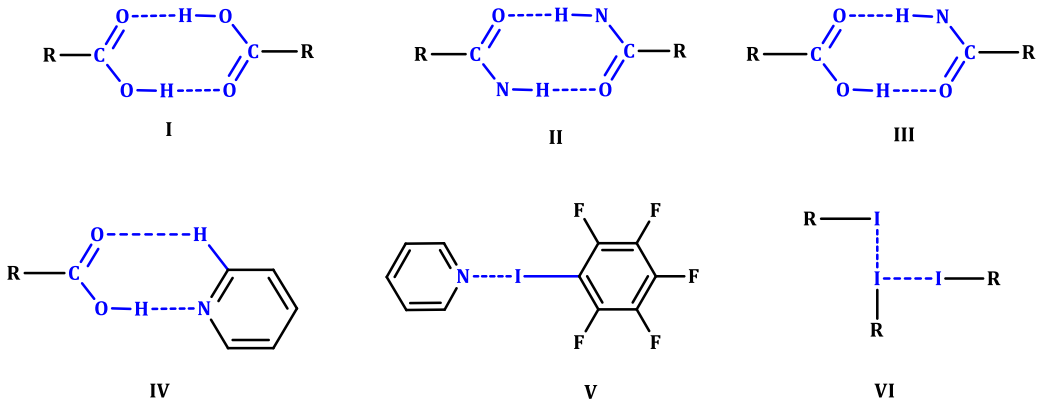

Figure 1.14 (I) acid-acid,[37] (II) amide-amide homosynthons and (III) acid-amide,[38] (IV) acid-pyridine,[39] (V) iodo-pyridine,[40] (VI) iodo-iodo[41] heterosynthons

1.2.4 Co-crystallizations as means of exploring intermolecular interactions

In the process of co-crystallization, two molecular components are brought together in the same crystal lattice with the use of supramolecular synthons without making or breaking covalent bonds.[42] The two possible outcomes of this process are either undesired homomeric interactions (recrystallization) or desired heteromeric interactions (co-crystallization) where the former is favorable over the latter (Figure 1.15). Co-crystal formation is being explored in pharmaceutical industry, agrochemicals, explosives etc. due to the possibility of modulating physical properties without changing the integrity of the parent component.

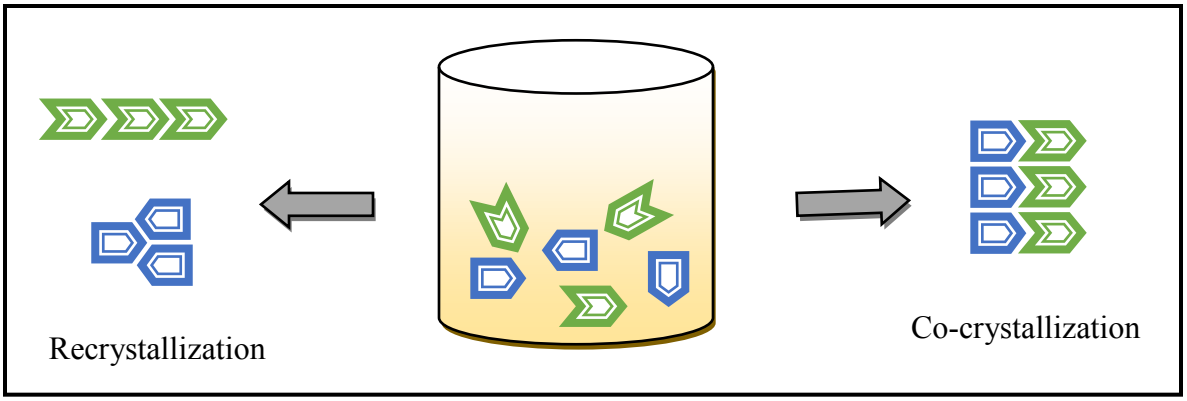

Figure 1.15 Schematic representation of co-crystallization and recrystallization

In one of those examples, Ethenzamide, a poorly soluble non-steroidal anti-inflammatory drug, showed improved solubility and dissolution rate by co-crystallization with a suitable co-former (Figure 1.16).[43] Similarly, alternative solid forms of agrochemical actives which display improved physical properties, such as improved melting points, decreased solubility, improved storage and formulation stability, modified crystal morphology can be achieved by co-crystallization.[44,45] The ability of fine-tuning the solubility of an agrochemical active, cyprodinil, via co-crystallization is shown in Figure 1.17.[46]

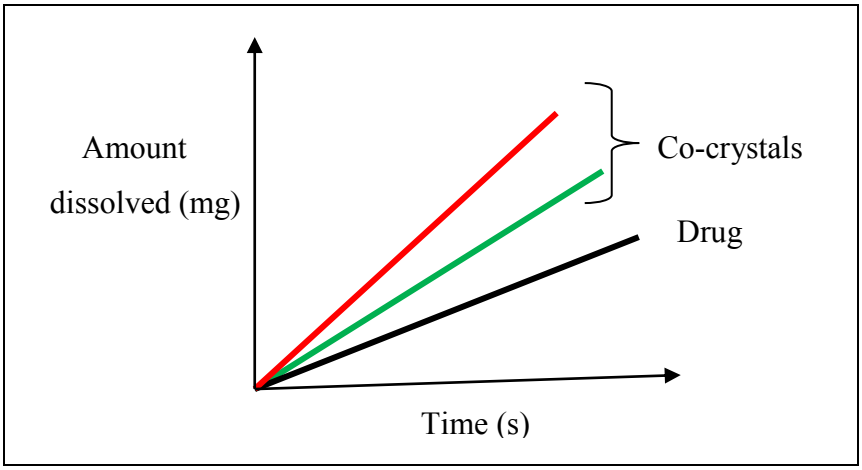

Figure 1.16 Dissolution rate profiles of Ethenzamide co-crystals[43]

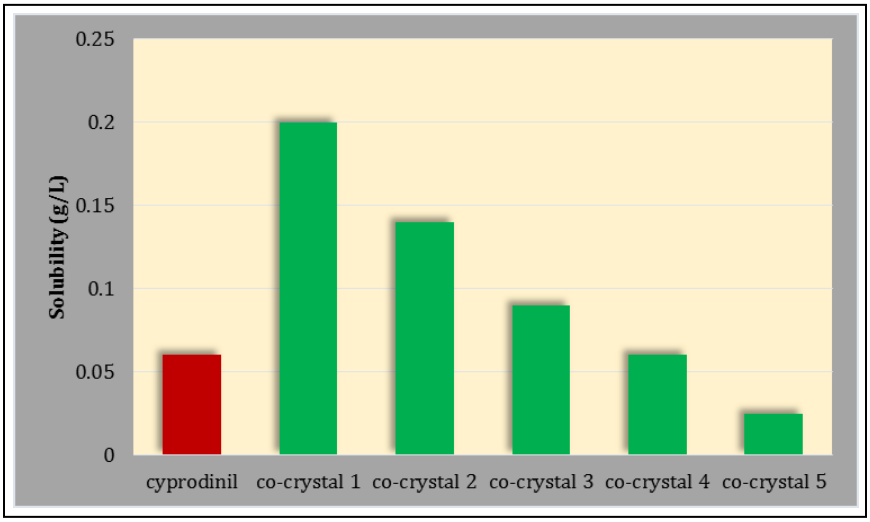

Figure 1.17 Solubility profile of cyprodinil co-crystals[46]

1.3 The importance of molecular receptors

Development of nano scale synthetic receptors as molecular recognition host molecules has been explored with numerous receptors such as, crown ethers, cryptands, spherands, cavitands, calixarenes, cyclophanes, cryptophanes, cyclodextrins, cucurbiturils and so on. For several decades now, these receptors have proven high affinity and high selectivity in binding to complementary guest molecules.[47] With the pre-organized binding pockets, they are good candidates for studying and understanding the unique nano scale structure-function relationship which is fundamentally different from the macroscopic level. The confined space provided by these molecular receptors grant a specific and controlled function in both biological processes and synthetic systems.

One of the most popular applications is catalysis inside a molecular host, in order to emulate nature's most efficient catalysts, enzymes. Captivity of the specific substrates inside enzymatic pockets is a powerful strategy in order to control catalytic activity in cells.[48] Inspired by nature, artificial molecular pockets have been designed to mimic catalysis in a restricted space to date. A reversible capsule composed of two resorcinarene units accelerate the 1,3-dipolar cycloaddition between phenylacetylene and phenyl azide where the product act as a template to displace the reagents out of the compartment (Figure 1.18). The highly selective molecular recognition properties of the capsule make a regioselective product in few days, without the capsule, it takes a year for the reaction completion.[49]

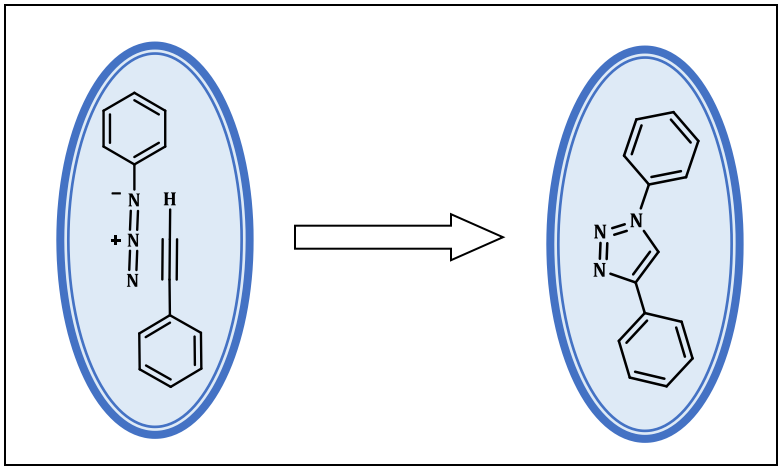

Figure 1.18 1,3-dipolar cycloaddition reaction taking place inside capsule[49]

Macrocyclic receptors are more suitable as drug delivery vehicles compared to dendrimers, nanoparticles or carbon nanotubes, since they have the ability to isolate the drugs within the structure, preventing drug degradation and deactivation. One of the receptors that are extensively studied and are already been included in tablets for oral delivery are cucurbit[n]urils (CB[n]) due to the increased chemical and physical stabilityof the drug, improved drug solubility and controlled drug release by formation of drug–CB[n] complexes (Figure 1.19).[50] Some of the drugs that are studied include cis-platin,[51] paracetamol,[52] glibenclamide,[52] memantine,[52] coumarin,[53] and prelocaine.[54]

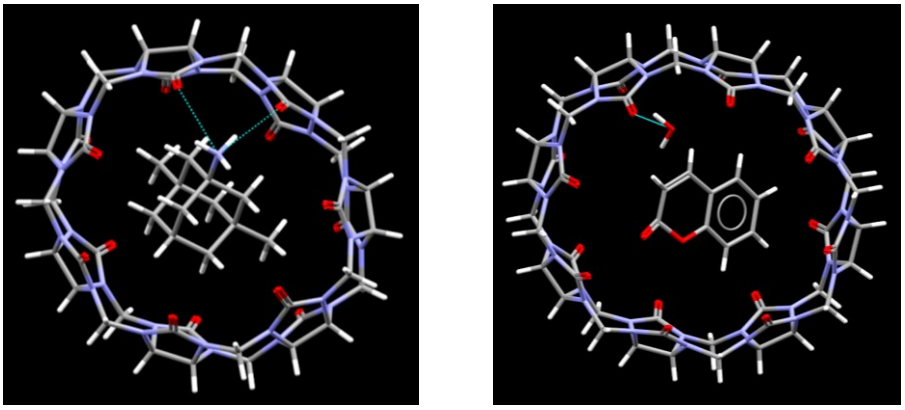

(a) (b)

Figure 1.19 Drug inclusion complexes of (a) memantine-CB[7][52] and (b) coumarin-CB[8][53]

The versatility of the macrocyclic receptors have gained attention in the design of supramolecular chemosensors. Kumai and co-workers have designed a supramolecular fluorescence sensor base on a boronic acid fluorophore and boronic acid-modified γ-cyclodextrin (CD) complex for selective recognition of sugar in water (Figure 1.20). These sensors displayed high selectivity for glucose over fructose and galactose. The multi-point interaction capability of CD hosts via hydrogen bonds resulted high sensitivity towards glucose recognition.

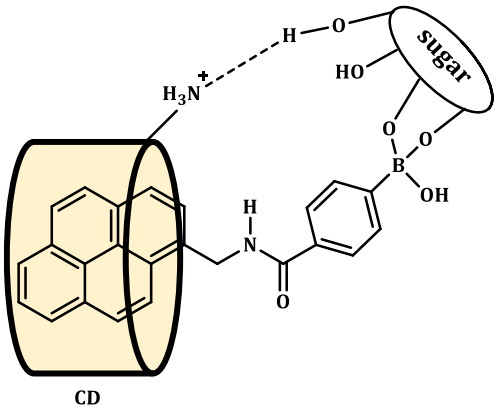

Figure 1.20 Multipoint recognition of sugars by suitably functionalized cyclodextrins

1.4 Goals of the thesis

A deeper understanding of the intermolecular interactions is necessary if we are to design new solid forms with pre-determined connectivity. The molecular building blocks should be designed in such a way that they can convey directional and selective interactions to construct supramolecular networks with high predictability, as opposed to random and coincidental assembly. Since there is a function behind every binding event, controlled supramolecular assemblies lead to understand the correlation between structure-property relationship. After all, hydrogen bonding and halogen bonding are two parallel synthetic tools, it is advantageous to look for distinctive features and resemblance features of the two interactions as far as the molecular recognition events are subjected to occur in the same environment.

Understanding of supramolecular synthetic strategies will be first exerted with small molecules in order to establish robust and reliable supramolecular architectures using hydrogen bonding and halogen bonding. Structural outcomes are always analyzed with respect to hydrogen and halogen bonding by comparison. Then, same hydrogen bonding and halogen bonding functionalities will be employed into large molecular receptors in order to understand the molecular recognition events in solid state and in solution.

The goals of this thesis are as follows;

I. Mapping out the structural landscape of a series of halogen bonded co-crystals comparative to the analogous hydrogen bonded co-crystals (Chapter 2).

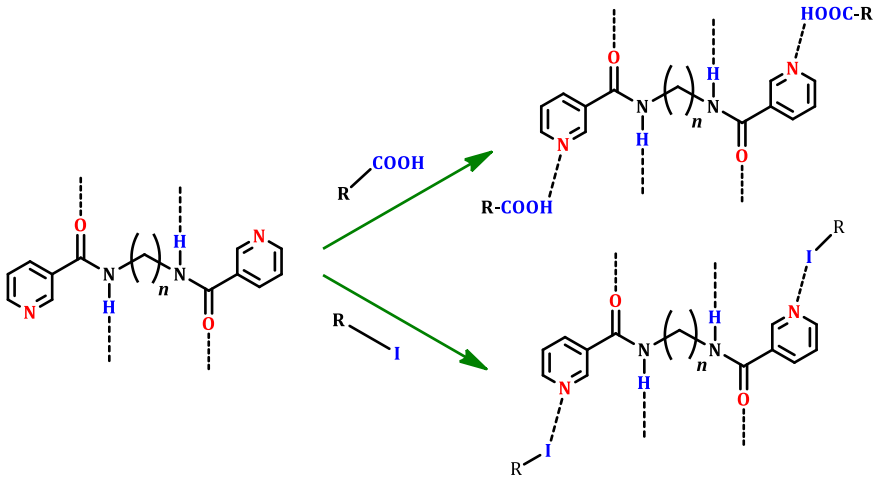

II. Explore the effect of secondary π stacking interactions on supramolecular architectures in the presence of hydrogen and halogen bonding. This study will focus on co-crystallization of the same acceptors (A) used in Chapter 2 with a series of aromatic hydrogen and halogen bond donors (D) that are analogous to each other (Chapter 3).

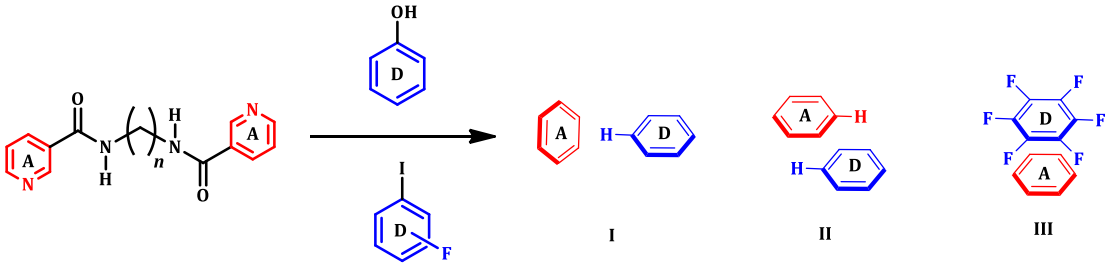

III. Investigate the interchangeability of hydrogen bonds and halogen bonds in the solid state, when incorporated into the same molecular backbone. This will be studied by co-crystallizing the hydrogen and halogen bond donors with symmetric ditopic acceptor molecules (Chapter 4).

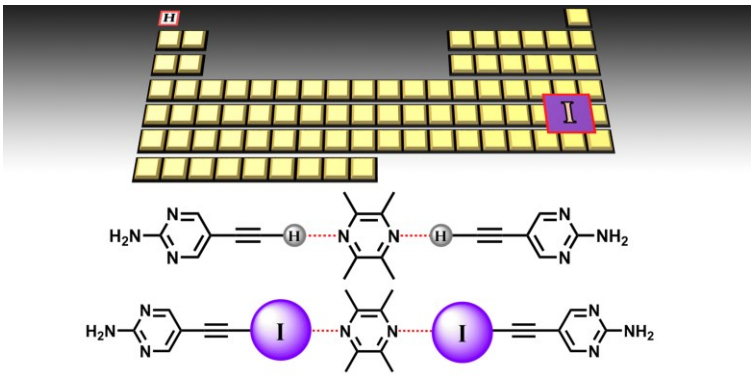

IV. Establish selectivity in halogen bond based anion recognition using three halogen bond donors equipped with iodo, bromo and choro bisethynyl functionalities. These are co-crystalized with a series of chlorides, bromides and iodides to test the halogen-halide donor-acceptor ability (Chapter 5).

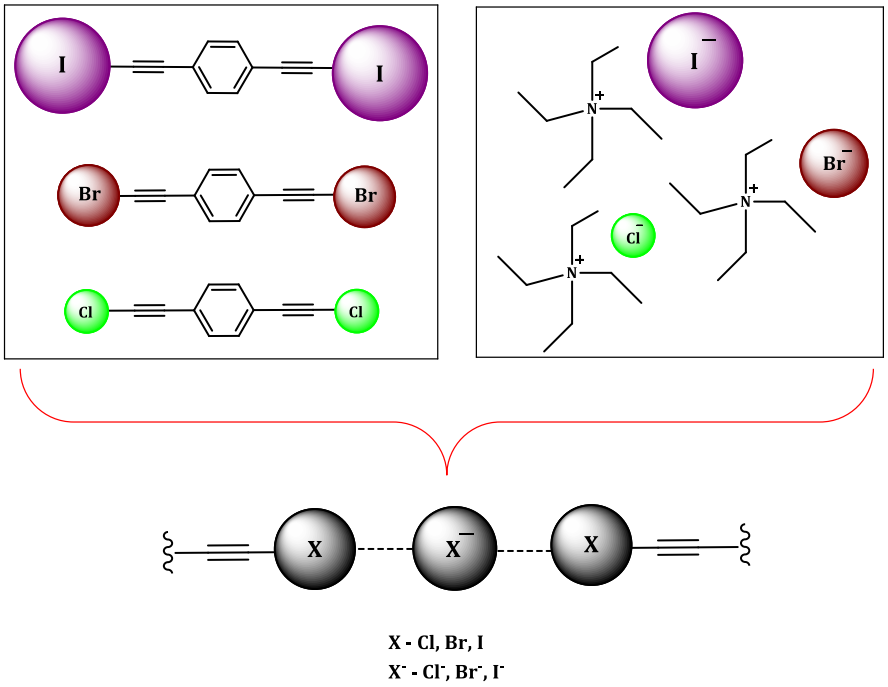

V. Design and synthesis of cavitands functionalized with hydrogen and halogen bond donor and acceptor groups. The cavitands bearing pyridy, pyridyl-N-oxide, carboxylic acid and iodoethynyl functionalities will be synthesized. The binding ability of these cavitands towards a series active ingredients (guests) will be examined in solid state as well as in solution (Chapter 6).

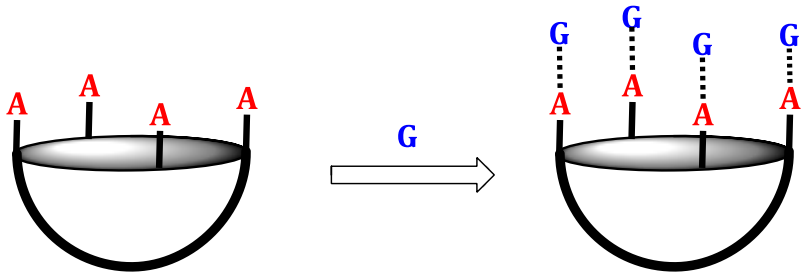

1.5 References

1. Wöhler, F. *Ann. Phys.* **1828,** *88* (2), 253-256.

2. Waldvogel, S. R. *Angew. Chem. Int. Ed.* **2005,** *44* (32), 5005-5006.

3. Lehn, J.-M. *Angew. Chem. Int. Ed. Engl.* **1988,** *27* (1), 89-112.

4. (a) Corey, E. J. *Chem. Soc. Rev.* **1988,** *17* (0), 111-133; (b) Young, D. G. J. *J. Chem. Educ.* **2008,** *85* (12), 1626.

5. Phlip, D. *Adv. Mater.* **1996,** *8* (10), 866-868.

6. Jean-Marie Lehn - Nobel Lecture: Supramolecular Chemistry - Scope and Perspectives: Molecules - Supermolecules - Molecular Devices". Nobelprize.org. Nobel Media AB 2014. Web. 23 Feb 2015

7. (a) Friščić, T.; Meštrović, E.; Škalec Šamec, D.; Kaitner, B.; Fábián, L. *Chem. Eur. J.* **2009,** *15* (46), 12644-12652; (b) Cincic, D.; Friscic, T. *CrystEngComm* **2014,** *16* (44), 10169-10172.

8. Fischer, E. *Ber. Dtsch. Chem. Ges.* **1894,** *27* (3), 2985-2993.

9. Babine, R. E.; Bender, S. L. *Chem. Rev.* **1997,** *97* (5), 1359-1472.

10. Schmidt, G. M. J. Photodimerization in the solid state. In *Pure Appl. Chem.*, 1971; Vol. 27, p 647.

11. (a) Desiraju, G. R.; Sharma, C. V. K. *Crystal Enginering and Molecular Recognition-Twin Facets of Supramolecular Chemistry. In Perspectives in Supramolecular Chemistry*. John Wiley & Sons: 2007; (b) Dunitz, J. D. Thoughts on Crystals as Supermolecules. In Perspectives in Supramolecular Chemistry. John Wiley & Sons: 2007; pp 1-30.

12. Wheeler, K. A.; Wiseman, J. D.; Grove, R. C. *CrystEngComm* **2011,** *13* (9), 3134-3137.

13. Noveron, J. C.; Lah, M. S.; Del Sesto, R. E.; Arif, A. M.; Miller, J. S.; Stang, P. J. *J. Am. Chem. Soc.* **2002,** *124* (23), 6613-6625.

14. Muthuraman, M.; Masse, R.; Nicoud, J.-F.; Desiraju, G. R. *Chem. Mater.* **2001,** *13* (5), 1473-1479.

15. Evans, O. R.; Lin, W. *Chem. Mater.* **2001,** *13* (9), 3009-3017.

16. Zhou, K.-G.; Withers, F.; Cao, Y.; Hu, S.; Yu, G.; Casiraghi, C. *ACS Nano* **2014,** *8* (10), 9914-9924.

17. Madura, I. D.; Czerwińska, K.; Jakubczyk, M.; Pawełko, A.; Adamczyk-Woźniak, A.; Sporzyński, A. *Cryst. Growth Des.* **2013,** *13* (12), 5344-5352.

18. Chang, Y.-C.; Chen, Y.-D.; Chen, C.-H.; Wen, Y.-S.; Lin, J. T.; Chen, H.-Y.; Kuo, M.-Y.; Chao, I. *J. Org. Chem.* **2008,** *73* (12), 4608-4614.

19. (a) Legon, A. C.; Millen, D. J. *Acc. Chem. Res.* **1987,** *20* (1), 39-46; (b) Wood, P. A.; Allen, F. H.; Pidcock, E. *CrystEngComm* **2009,** *11* (8), 1563-1571.

20. Arunan, E.; Desiraju, G. R.; Klein, R. A.; Sadlej, J.; Scheiner, S.; Alkorta, I.; Clary, D. C.; Crabtree, R. H.; Dannenberg, J. J.; Hobza, P.; Kjaergaard, H. G.; Legon, A. C.; Mennucci, B.; J., N. D. *Pure Appl. Chem.* **2011,** *83* (8), 1619-1636.

21. Nelson, D. L.; Lehninger, A. L.; Cox, M. M. In *Lehninger principles of biochemistry*, W.H. Freeman: New York, 2008.

22. Głowacki, E. D.; Irimia-Vladu, M.; Kaltenbrunner, M.; Gsiorowski, J.; White, M. S.; Monkowius, U.; Romanazzi, G.; Suranna, G. P.; Mastrorilli, P.; Sekitani, T.; Bauer, S.; Someya, T.; Torsi, L.; Sariciftci, N. S. *Adv. Mater.* **2013,** *25* (11), 1563-1569.

23. Metrangolo, P.; Neukirch, H.; Pilati, T.; Resnati, G. *Acc. Chem. Res.* **2005,** *38* (5), 386-395.

24. Metrangolo, P.; Resnati, G. *Chem. Eur. J.* **2001,** *7* (12), 2511-2519.

25. Metrangolo, P.; Meyer, F.; Pilati, T.; Resnati, G.; Terraneo, G. *Angew. Chem. Int. Ed.* **2008,** *47* (33), 6114-6127.

26. Clark, T.; Hennemann, M.; Murray, J.; Politzer, P. *J. Mol. Model.* **2007,** *13* (2), 291-296.

27. Desiraju, G. R.; Vittal, J. J.; Ramanan, A. *Crystal Engineering: A textbook*. World Scientific: Singapore, 2011.

28. (a) Lu, Y.; Liu, Y.; Xu, Z.; Li, H.; Liu, H.; Zhu, W. *Expert Opin. Drug Discovery* **2012,** *7* (5), 375-383; (b) Lu, Y.; Shi, T.; Wang, Y.; Yang, H.; Yan, X.; Luo, X.; Jiang, H.; Zhu, W. *J. Med. Chem.* **2009,** *52* (9), 2854-2862; (c) Lu, Y.; Wang, Y.; Zhu, W. *PCCP* **2010,** *12* (18), 4543-4551.

29. (a) Walter, S. M.; Kniep, F.; Herdtweck, E.; Huber, S. M. *Angew. Chem. Int. Ed.* **2011,** *50* (31), 7187-7191; (b) Bruckmann, A.; Pena, M. A.; Bolm, C. *Synlett* **2008,** *2008* (06), 900-902; (c) Dordonne, S.; Crousse, B.; Bonnet-Delpon, D.; Legros, J. *Chem. Commun.* **2011,** *47* (20), 5855-5857.

30. Coulembier, O.; Meyer, F.; Dubois, P. *Polym. Chem.* **2010,** *1* (4), 434-437.

31. (a) Metrangolo, P.; Carcenac, Y.; Lahtinen, M.; Pilati, T.; Rissanen, K.; Vij, A.; Resnati, G. *Science* **2009,** *323* (5920), 1461-1464; (b) Farina, A.; Meille, S. V.; Messina, M. T.; Metrangolo, P.; Resnati, G.; Vecchio, G. *Angew. Chem. Int. Ed.* **1999,** *38* (16), 2433-2436.

32. (a) Wolters, L. P.; Bickelhaupt, F. M. *ChemistryOpen* **2012,** *1* (2), 96-105; (b) Brammer, L.; Bruton, E. A.; Sherwood, P. *Cryst. Growth Des.* **2001,** *1* (4), 277-290; (c) Hao, M.-H. *J. Chem. Theory Comput.* **2006,** *2* (3), 863-872.

33. Desiraju, G. R. *J. Am. Chem. Soc.* **2013,** *135* (27), 9952-9967.

34. Reddy, D. S.; Craig, D. C.; Desiraju, G. R. *J. Am. Chem. Soc.* **1996,** *118* (17), 4090-4093.

35. Thalladi, V. R.; Goud, B. S.; Hoy, V. J.; Allen, F. H.; Howard, J. A. K.; Desiraju, G. R. *Chem. Commun.* **1996,** (3), 401-402.

36. Desiraju, G. R. *Crystal Engineering: The Design of Organic Solids*. Elsevier: Amsterdam, 1989.

37. Sanphui, P.; Bolla, G.; Das, U.; Mukherjee, A. K.; Nangia, A. *CrystEngComm* **2013,** *15* (1), 34-38.

38. Tothadi, S.; Joseph, S.; Desiraju, G. R. *Cryst. Growth Des.* **2013,** *13* (7), 3242-3254.

39. Dubey, R.; Desiraju, G. R. *Chem. Commun.* **2014,** *50* (10), 1181-1184.

40. Han, N.; Zeng, Y.; Sun, C.; Li, X.; Sun, Z.; Meng, L. *J. Phys. Chem. A* **2014,** *118* (34), 7058-7065.

41. (a) Pedireddi, V. R.; Reddy, D. S.; Goud, B. S.; Craig, D. C.; Rae, A. D.; Desiraju, G. R. *J. Chem. Soc., Perk. Trans. 2* **1994,** (11), 2353-2360; (b) Yamada, M.; Kanazawa, R.; Hamada, F. *CrystEngComm* **2014,** *16* (13), 2605-2614.

42. Aakeroy, C. B.; Salmon, D. J. *CrystEngComm* **2005,** *7* (72), 439-448.

43. Aitipamula, S.; Wong, A. B. H.; Chow, P. S.; Tan, R. B. H. *CrystEngComm* **2012,** *14* (24), 8515-8524.

44. (a) Nauha, E.; Nissinen, M. *J. Mol. Struct.* **2011,** *1006* (1–3), 566-569; (b) Nauha, E.; Kolehmainen, E.; Nissinen, M. *CrystEngComm* **2011,** *13* (21), 6531-6537; (c) Mereiter, K. *Acta Crystallographica Section E: Structure Reports Online* **2011,** *67* (Pt 9), o2321-o2322.

45. (a) George, N.; Forrest, J. O.; Burton, R. C.; Aakeroy, C. B. (Syngenta Limited, USA). Co-crystals of pyrimethanil or cyprodinil. US Patent WO2011128618 A1 (b) Weiss, M.; Storch, D.; Wirth, W.; Olenik, B.; Weiss, H.; Schwiedop, U. (Bayer Itechnology Services Gmbh). Co-crystal of 4-furan-2(5h)-one with salicylic acid and use thereof as pesticide. US Patent US20120252766 A1

46. Panikkattu, S. designing molecular solids with structural control and tunable physical properties using co-crystallization techniques. Kansas State University, August 2008.

47. Lehn, J. M. *Supramolecular Chemistry*. VCH: Weinheim, 1995.

48. Wörsdörfer, B.; Woycechowsky, K. J.; Hilvert, D. *Science* **2011,** *331* (6017), 589-592.

49. (a) Chen, J.; Körner, S.; Craig, S. L.; Lin, S.; Rudkevich, D. M.; Rebek, J. *Proc. Natl. Acad. Sci. U. S. A.* **2002,** *99* (5), 2593-2596; (b) Chen, J.; Rebek, J. *Org. Lett.* **2002,** *4* (3), 327-329.

50. Walker, S.; Oun, R.; McInnes, F. J.; Wheate, N. J. *Isr. J. Chem.* **2011,** *51* (5-6), 616-624.

51. Wheate, N. J.; Buck, D. P.; Day, A. I.; Collins, J. G. *Dalton Trans.* **2006,** (3), 451-458.

52. McInnes, F. J.; Anthony, N. G.; Kennedy, A. R.; Wheate, N. J. *Org. Biomol. Chem.* **2010,** *8* (4), 765-773.

53. Wang, R.; Bardelang, D.; Waite, M.; Udachin, K. A.; Leek, D. M.; Yu, K.; Ratcliffe, C. I.; Ripmeester, J. A. *Org. Biomol. Chem.* **2009,** *7* (11), 2435-2439.

54. Wyman, I. W.; Macartney, D. H. *Org. Biomol. Chem.* **2010,** *8* (1), 247-252.

Chapter 2 - Halogen-bond driven co-crystallization of potential anti-cancer compounds

2.1 Introduction

The process of co-crystallization, which involves incorporation of two different molecular species in the same crystalline lattice held together by intermolecular forces, represents a foundation for potentially very diverse technologies for fine-tuning physicochemical properties of active ingredients and specialty chemicals covering areas such as pharmaceuticals,[1] agrochemicals[2] and explosives,[3] *etc*. In particular, pharmaceutical co-crystals, a co-former and the API (Active Pharmaceutical Ingredient) associated in specific stoichiometry in a crystalline lattice, have opened the opportunity to engineer new solid forms without tampering with the integrity of the API. These new solid forms enables adjustment of many biopharmaceutical properties of a drug such as solubility, bioavailability, dissolution and melting point.[4]

Hydrogen bonds are the most widely used tools for co-crystal synthesis due to their strength and directionality.[5] However, halogen bonds have emerged as an analogous non-covalent interaction, sharing fundamental characteristics with hydrogen bonds,[6] such as strength,[7] and electrostatic and geometric requirements.[8] Therefore, halogen-bond based synthons have recently been employed in the synthesis of co-crystals with predetermined stoichiometry and topology.[9] Halogen bonding can offer opportunities for engineering precise physical properties, such as liquid-crystalline behaviors,[10] in organic molecular solids.[11] Furthermore, halogen bonds are intrinsically more lipophilic and hydrophobic than their hydrogen-bonding counterparts, thus they may be well suited to biological applications, especially in drug delivery and transport.[12]

It is important to compare the structural outcomes when halogen- and hydrogen bonds are confronted with similar chemical environments,[13] since by carefully mapping out the structural landscape of molecular solids it may be possible to forge supramolecular synthetic strategies that are versatile, robust and reliable in the assembly of solid-state architectures with desirable connectivities and composition.[14] In this context, it is also necessary to identify supramolecular synthons that can operate side-by-side with limited 'synthon-crossover'[15] to ensure that a desired motif or architecture can be realized.

Hydrogen bonded pharmaceutical co-crystals have been extensively exploited with improved physico-chemical properties compared to that of the pure API. A recent study[16] demonstrated, O-H···N hydrogen-bond based co-crystals between aliphatic dicarboxylic acids and a family of *bis*-acetamides (**A8**-**A0**) (Figure 2.1) that exhibit improved solubility and thermal stability with respect to the API itself. The co-crystals are synthesized using well-known acid···pyridine and amide···amide synthons (Figure 2.2). The one-dimensional chains constructed via COOH···N(py) hydrogen bonds are cross-linked into well-defined two-dimensional layers by self-complementary N-H···O=C interactions (Figure 2.3). All the co-crystals displayed two dimensional arrangements with structural consistency and the representation of one of the resulted co-crystals of **A4** with succinic acid is shown in Figure 2.4. As a result of the structural consistency in their binary co-crystals it was possible to alter some physical properties of the resulting solids in a predictable manner.

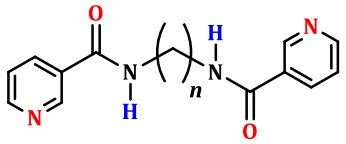

n = 8, 6, 4, 2, 0

Figure 2.1 3-Pyridyl *bis*-acetamides n = 8 (A_8), 6 (A_6), 4 (A_4), 2 (A_2), 0 (A_0).

Since the most frequently studied halogen-bond interactions involve 'fluorine-activated' iodine atoms and a nitrogen heterocycle as the halogen-bond acceptor,[17] it is of interest to determine if the O-H···N hydrogen bond (HB) can be replaced with an I···N halogen bond (XB) within the same structural context as shown in Figure 2.3.

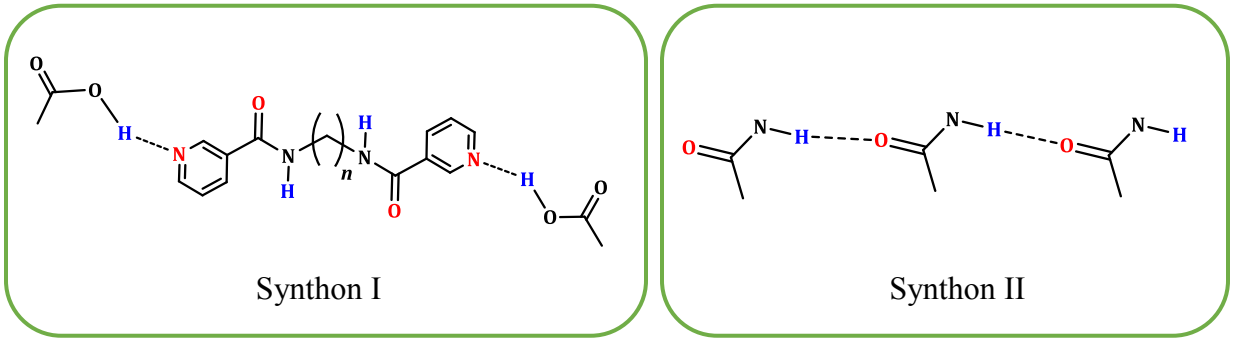

Figure 2.2 Co-crystals synthesized via primary acid···pyridine synthon (synthon I) and amide···amide synthon (synthon II)

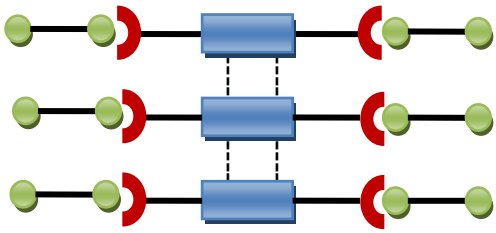

Figure 2.3 Infinite 1-D horizontal chains (from O-H···N hydrogen bonds) connected vertically by N-H···O=C hydrogen bonds into 2-D layers in co-crystals of 3-pyridyl *bis*-acetamides and aliphatic dicarboxylic acids[16]

The chosen counterparts to the *bis*-acetamides are a family of haloperfluoroalkanes, Figure 2.5, known to form robust I···N(py) halogen bonds,[18] and they are intended to mimic the role played by the aliphatic dicarboxylic acids in the previous study.[16]

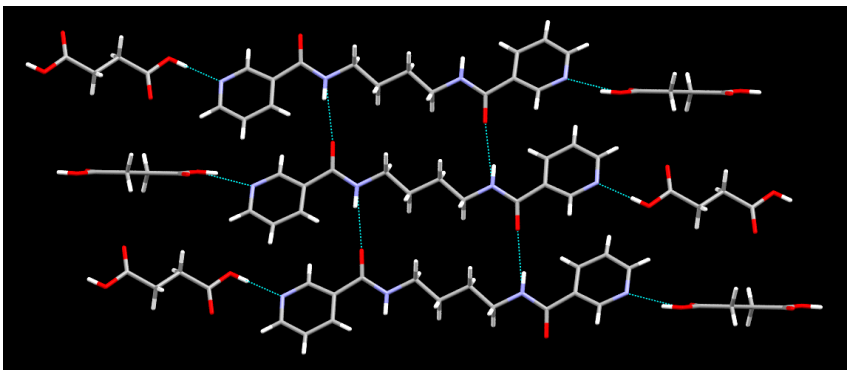

Figure 2.4 Primary interactions in the structure of **A4** and succinic acid[16]

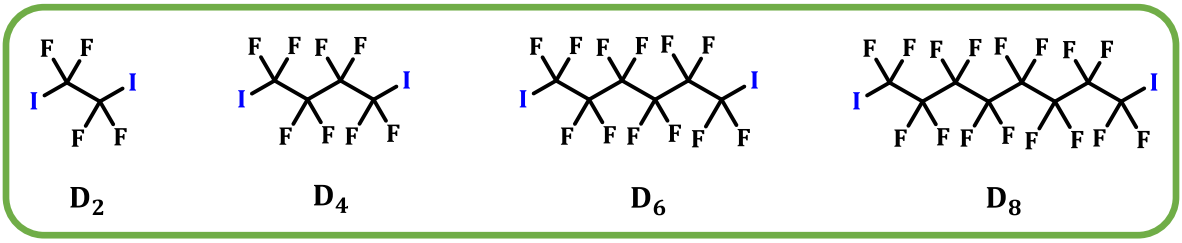

Figure 2.5 Family of halogen-bond donors, **D2-D8** with fluorine- activated iodine atoms

In this chapter we will examine/answer two different questions:

(i) How well can a set of halogen-bond donors mimic the structural behavior of a series of hydrogen-bond donors in the assembly of binary co-crystals?

(ii) Can appropriate hydrogen-bond and halogen-bond moieties operate in an independent manner in terms of directionality and selectivity?

2.2 Experimental

2.2.1 Synthesis

All chemicals were purchased from Sigma Aldrich unless otherwise noted. Column chromatography was carried out on silica gel (150 Å pore size) from Analtech, Inc. Melting point/decomposition point determinations were done using Fisher-Johns melting point apparatus and are uncorrected. ^{1}H, ^{19}F and ^{13}C NMR spectra were recorded on a Varian Unity plus 400 MHz or 200 MHz spectrometer in $CDCl_3$ or DMSO-d_6. Infrared spectroscopy analysis was carried out using Nicolet 380 FT-IR with a digital resolution of 0.9 cm^{-1} and data processed using software, Omnic 8.0 © 1992-2008 Thermo Fisher Scientific Inc.

2.2.1.1 Synthesis of N,N'-bis(nicotinic acid)hydrazide, A_0[19]

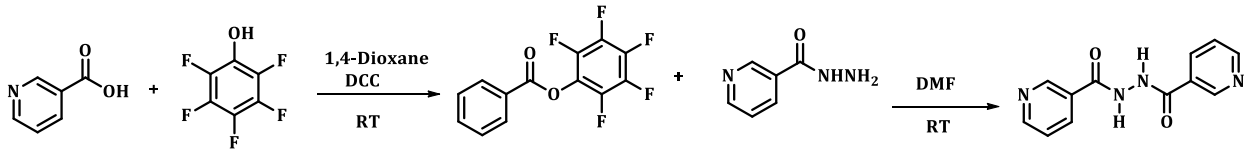

Nicotinic acid (1.52 g, 0.012 mol), pentafluorophenol (2.49 g, 0.013 mol) and dicyclohexylcarbodimide (DCC) (2.54 g, 0.012 mol) were dissolved in dry 1,4-dioxane (50 mL) and allowed to stir at room temperature for 24 hrs. The white precipitate obtained was filtered off and discarded. The filtrate was concentrated on a rotary evaporator to give a yellow oil. To this yellow oil, dimethylformamide (DMF) (40 mL) and nicotinic hydrazide (1.85 g, 0.013 mol) were added and left to stir at room temperature for 36 hrs. The solvent was removed on a rotary evaporator to yield a pale yellow solid which upon recrystallization from ethyl acetate gave pure **A_0** as light yellow crystalline solid (1.57 g, 65%). M. p. 230-232 ºC (Reported M. p. 229-232 ºC)[19] ^{1}H NMR (δH; 200 MHz, DMSO-d_6): 10.82 (s, 2H), 9.08 (s, 2H) 8.79 (d, 2H, J = 4.8 Hz), 8.27 (d, 2H, J =6.2 Hz), 7.59 (m, 2H); IR: υ 3155, 3003, 2850, 1632, 1537, 1298, 1201, 1119, 1023, 876, 700 cm^{-1}.

2.2.1.2 Synthesis of N,N'-1,2-ethanediylbis-3-pyridinecarboxamide, A_2[20]

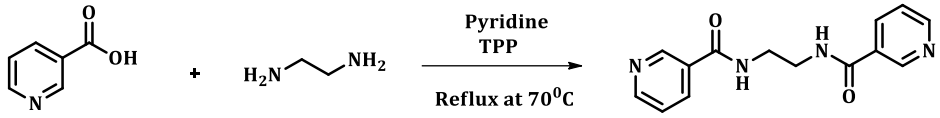

1,2-Diaminoethane (1.56 g, 0.024 mol) was slowly added to a solution of nicotinic acid (5.90 g, 0.048 mol) in pyridine (60 mL). The mixture was stirred for 15 minutes and triphenyl phosphite (TPP) (12.6 mL, 0.48 mol) was slowly added with a dropping funnel over a period of 15 minutes. The mixture was heated under reflux at 70 ºC for 6 hrs and the volume reduced to 10 mL under vacuum. The solution was then left to stand at room temperature upon which a white solid resulted. The solid was filtered off, washed with cold water to yield pure **A2** (4.47 g, 72%) . M. p. 221-222 ºC (Reported M. p. 216-220 ºC);[20] ^{1}H NMR (δH; 200 MHz, DMSO-d_6): 9.00 (s, 2H), 8.80 (s, 2H) 8.69 (d, 2H, J = 3.5 Hz), 8.16 (d, 2H, J =8.2 Hz), 7.51 (m, 2H), 3.47 (m, 4H); IR: υ 3360, 3036, 2936, 1638, 1537, 1418, 1297, 1240, 1158, 1026, 880, 698 cm^{-1}.

2.2.1.3 Synthesis of N,N'-1,4-butanediylbis-3-pyridinecarboxamide, A_4[20]

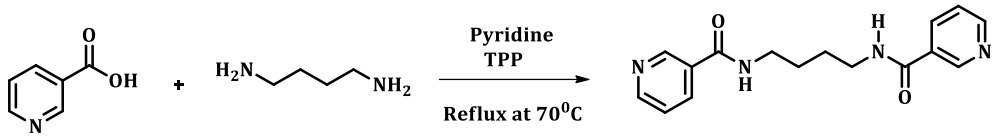

1,4-Diaminobutane (2.05 g, 0.023 mol) was slowly added to a solution of nicotinic acid (5.72 g, 0.46 mol) in pyridine (100 mL). The mixture was stirred for 15 minutes and triphenyl phosphite (TPP) (12.0 mL, 0.046 mol) was slowly added with a dropping funnel over a period of 15 minutes. The mixture was heated under reflux at 70 ºC for 6 hrs and volume reduced to 10 mL under vacuum. The solution then left to stand at room temperature upon which a white solid resulted. The solid was filtered off, washed with water and recrystallized from ethanol to produce **A4** (5.48 g, 80%). M. p. 202-204 ºC (Reported M. p. 199-204 ºC);[20] ^{1}H NMR (δH; 200 MHz, DMSO-d_6): 8.98 (s, 2H), 8.67 (m, 4H) 8.17 (d, 2H, J = 4.8 Hz), 7.50 (d, 2H, J =6.2 Hz), 3.31 (m, 3H), 1.51 (m, 4H); IR: υ 3294, 3073, 2932, 1628, 1591, 1544, 1475, 1421, 1311, 1164, 1020, 836, 704 cm^{-1}.

2.2.1.4 Synthesis of N,N'-1,6-hexanediylbis-3-pyridinecarboxamide, A_6[21]

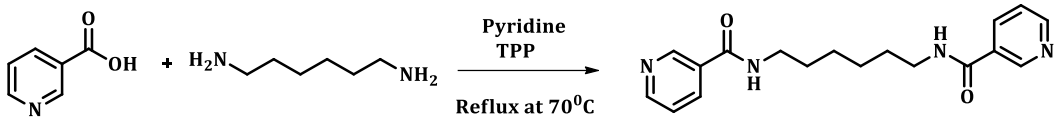

1,6-Diaminohexane (1.58 g, 0.013 mol) was slowly added to a solution of nicotinic acid (3.20 g, 0.026 mol) in pyridine (40 mL). The mixture was stirred for 15 minutes and triphenyl phosphite (TPP) (6.8 mL, 0.026 mol) was slowly added with a dropping funnel over a period of 15 minutes. The mixture was heated under reflux at 70 ºC for 6 hrs and the volume reduced to 10 mL under vacuum. The solution was then left to stand at room temperature upon which a pale yellow solid resulted. The solid was filtered off, washed with water and recrystallized from ethanol to produce colorless crystals of **A_6** (2.54 g, 61%). M. p. 166-167 ºC (Reported M. p. 168-170 ºC);[21] ^{1}H NMR (δH; 200 MHz, DMSO-d_6): 8.98 (s, 2H), 8.67 (d, 2H, J =4.6 Hz), 8.61 (m, 2H) 8.17 (d, 2H, J = 6.4 Hz), 7.50 (m, 2H), 3.26 (m, 6H), 1.54 (m, 6H); IR: υ 3310, 3046, 2934, 2869, 1629, 1587, 1528, 1476, 1419, 1341, 1291, 1158, 1024, 863, 707 cm^{-1}.

2.2.1.5 Synthesis of N,N'-1,8-octanediylbis-3-pyridinecarboxamide, A_8[20-21]

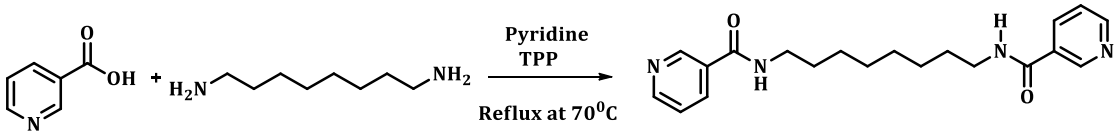

1,8-Diaminooctane (1.49 g, 0.010 mol) was slowly added to a solution of nicotinic acid (2.54 g, 0.020 mol) in pyridine (30 mL). The mixture was stirred for 15 minutes and triphenyl phosphite (TPP) (5.2 mL, 0.020 mol) was slowly added with a dropping funnel over a period of 15 minutes. The mixture was heated under reflux at 70 ºC for 6 hrs and the volume reduced to 10 mL under vacuum. The solution was then left to stand at room temperature upon which a white solid resulted. The solid was filtered off, washed with water and recrystallized from ethanol to produce colorless crystals of **A_8** (1.91 g, 54%). M. p. 150-152 ºC (Reported M. p. 150-154 & 154-158 ˚C);[20-21] ^{1}H NMR (δH; 200 MHz, DMSO-d_6): 8.98 (s, 2H), 8.68 (d, 2H, J =4.9 Hz), 8.61 (m, 2H) 8.17 (d, 2H, J = 7.9 Hz), 7.50 (m, 2H), 3.26 (m, 9H), 1.51 (m, 6H); IR: υ 3320, 3039, 2932, 2862, 1622, 1530, 1474, 1419, 1319, 1275, 1164, 1020, 865, 706 cm^{-1}.

2.2.2 Synthesis of co-crystals

Bis-acetamide based ditopic acceptor ligands, **A_0-A_8** were subjected to co-crystallization experiments with four aliphatic halogen bond donors: 1,2-diiodotetrafluoroethane **D_2**, 1,4-diiodooctafluorobutane **D_4**, 1,6-diiodoperfluorohexane **D_6**, 1,8-diiodoperfluorooctane **D_8**. Donor and acceptor were combined in 1:1 stoichiometric amounts and ground together with a drop of methanol until a solid paste is resulted, which was then analyzed using IR spectroscopy for product formation. This procedure was performed on all 20 (5x4) combinations and single crystals suitable for X-ray diffraction were obtained by dissolving the ground mixture in suitable solvents in borosilicate vials and carrying out slow evaporation (thirteen single crystals were obtained by using this method).

2.2.2.1 Synthesis of N,N-1,2-ethanediylbis-3-pyridinecarboxamide 1,4-diiodooctafluorobutane, $A_2 \cdot D_4$

N,N-1,2-Ethanediylbis-3-pyridinecarboxamide (0.010 g, 0.037 mmol) was dissolved in 1 mL of methanol. To this solution was added 1,4-diiodooctafluorobutane (0.017 g, 0.037 mmol, 8 μL) in 1 mL of methanol. The resulting solution was allowed for slow evaporation in a 2 dram borosilicate vial at room temperature. Colorless prism-shaped crystals were obtained after three days. Dec. 89 ºC.

2.2.2.2 Synthesis of N,N-1,2-ethanediylbis-3-pyridinecarboxamide 1,6-diiodoperfluorohexane, $A_2 \cdot D_6$

N,N-1,2-Ethanediylbis-3-pyridinecarboxamide (0.010 g, 0.037 mmol) was dissolved in 1 mL of methanol. To this solution was added 1,6-diiodoperfluorohexane (0.020 g, 0.037 mmol) in 1 mL of methanol. The resulting solution was allowed for slow evaporation in a 2 dram borosilicate vial at room temperature. Colorless plate-shaped crystals were obtained after five days. Dec. 86 ºC.

2.2.2.3 Synthesis of N,N-1,2-ethanediylbis-3-pyridinecarboxamide 1,8-diiodoperfluorooctane, $A_2 \cdot D_8$

N,N-1,2-Ethanediylbis-3-pyridinecarboxamide (0.010 g, 0.037 mmol) was dissolved in 1 mL of methanol. To this solution was added 1,8-diiodoperfluorooctane (0.024 g, 0.037 mmol) in 1 mL of methanol. The resulting solution was allowed for slow evaporation in a 2 dram

borosilicate vial at room temperature. Colorless prism-shaped crystals were obtained after seven days. Dec. 99 ºC.

2.2.2.4 Synthesis of N,N-1,4-butanediylbis-3-pyridinecarboxamide 1,2-diiodotetrafluoroethane, $A_4 \cdot D_2$

N,N-1,4-Butanediylbis-3-pyridinecarboxamide (0.010 g, 0.032 mmol) was dissolved in 1 mL of methanol. To this solution was added 1,2-diiodotetrafluoroethane (0.012 g, 0.032 mmol, 7 µL) in 1 mL of methanol. The resulting solution was allowed for slow evaporation in a 2 dram borosilicate vial at room temperature. Colorless crystals were obtained after five days. Dec.95 ˚C.

2.2.2.5 Synthesis of N,N-1,4-butanediylbis-3-pyridinecarboxamide 1,4-diiodooctafluorobutane, $A_4 \cdot D_4$

N,N-1,4-Butanediylbis-3-pyridinecarboxamide (0.010 g, 0.032 mmol) was dissolved in 1 mL of methanol. To this solution was added 1,4-diiodooctafluorobutane (0.014 g, 0.032 mmol, 7 µL) in 1 mL of methanol. The resulting solution was allowed for slow evaporation in a 2 dram borosilicate vial at room temperature. Colorless crystals were obtained after seven days. Dec. 101 ˚C.

2.2.2.6 Synthesis of N,N-1,4-butanediylbis-3-pyridinecarboxamide 1,6-diiodoperfluorohexane, $A_4 \cdot D_6$

N,N-1,4-Butanediylbis-3-pyridinecarboxamide (0.010 g, 0.032 mmol) was dissolved in 1 mL of methanol. To this solution was added 1,6-diiodoperfluorohexane (0.017 g, 0.032 mmol) in 1 mL of methanol. The resulting solution was allowed for slow evaporation in a 2 dram borosilicate vial at room temperature. Colorless prism-shaped crystals were obtained after three days. Dec. 76 ˚C.

2.2.2.7 Synthesis of N,N-1,4-butanediylbis-3-pyridinecarboxamide 1,8-diiodoperfluorooctane, $A_4 \cdot D_8$

N,N-1,4-Butanediylbis-3-pyridinecarboxamide (0.010 g, 0.032 mmol) was dissolved in 1 mL of methanol. To this solution was added 1,8-diiodoperfluorooctane (0.02 g, 0.032 mmol) in 1 mL of methanol. The resulting solution was allowed for slow evaporation in a 2 dram

borosilicate vial at room temperature. Colorless rod-shaped crystals were obtained after five days. Dec. 125 ˚C.

2.2.2.8 Synthesis of N,N-1,6-hexanediylbis-3-pyridinecarboxamide 1,2-diiodotetrafluoroethane, $A_6 \cdot D_2$

N,N-1,6-Hexanediylbis-3-pyridinecarboxamide (0.010 g, 0.030 mmol) was dissolved in 1 mL of ethanol. To this solution was added 1,2-diiodotetrafluoroethane (0.012 g, 0.030 mmol, 7 μL) in 1 mL of ethanol. Chloroform (1 mL) was added to get everything dissolved. The resulting solution was allowed for slow evaporation in a 2 dram borosilicate vial at room temperature. Yellow color plate-shaped crystals were obtained after two days. Dec. 78 ˚C.

2.2.2.9 Synthesis of N,N-1,6-hexanediylbis-3-pyridinecarboxamide 1,6-diiodoperfluorohexane, $A_6 \cdot D_6$

N,N-1,6-Hexanediylbis-3-pyridinecarboxamide (0.010 g, 0.030 mmol) was dissolved in 1 mL of ethanol. To this solution was added 1,6-diiodoperfluorohexane (0.017 g, 0.030 mmol) in 1 mL of ethanol. Chloroform (1 mL) was added to get everything dissolved. The resulting solution was allowed for slow evaporation in a 2 dram borosilicate vial at room temperature. Colorless plate-shaped crystals were obtained after five days. Dec. 81 ˚C.

2.2.2.10 Synthesis of N,N-1,6-hexanediylbis-3-pyridinecarboxamide 1,8-diiodoperfluorooctane, $A_6 \cdot D_8$

N,N-1,6-Hexanediylbis-3-pyridinecarboxamide (0.010 g, 0.030 mmol) was dissolved in 1 mL of ethanol. To this solution was added 1,8-diiodoperfluorooctane (0.017 g, 0.030 mmol) in 1 mL of ethanol. Chloroform (1 mL) was added to get everything dissolved. The resulting solution was allowed for slow evaporation in a 2 dram borosilicate vial at room temperature. Colorless plate-shaped crystals were obtained after seven days. Dec. 86 ˚C.

2.2.2.11 Synthesis of N,N-1,8-octanediylbis-3-pyridinecarboxamide 1,2-diiodotetrafluoroethane, $A_8 \cdot D_2$

N,N-1,8-Octanediylbis-3-pyridinecarboxamide (0.010 g, 0.030 mmol) was dissolved in 1 mL of ethanol. To this solution was added 1,2-diiodotetrafluoroethane (0.009 g, 0.030 mmol, 8 μL) in 1 mL of ethanol. The resulting solution was allowed for slow evaporation in a 2 dram

borosilicate vial at room temperature. Colorless plate-shaped crystals were obtained after five days. Dec. 72 ˚C.

2.2.2.12 Synthesis of N,N-1,8-octanediylbis-3-pyridinecarboxamide 1,4-diiodooctafluorobutane, $A_8 \cdot D_4$

N,N-1,8-Octanediylbis-3-pyridinecarboxamide (0.010 g, 0.030 mmol) was dissolved in 1 mL of ethanol. To this solution was added 1,4-diiodooctafluorobutane (0.012 g, 0.030 mmol, 8 μL) in 1 mL of ethanol. The resulting solution was allowed for slow evaporation in a 2 dram borosilicate vial at room temperature. Colorless prism-shaped crystals were obtained after seven days. Dec. 79 ˚C.

2.2.2.13 Synthesis of N,N-1,8-octanediylbis-3-pyridinecarboxamide 1,6-diiodoperfluorohexane, $A_8 \cdot D_6$

N,N-1,8-Octanediylbis-3-pyridinecarboxamide (0.010 g, 0.030 mmol) was dissolved in 1 mL of ethanol. To this solution was added 1,6-diiodoperfluorohexane (0.015 g, 0.030 mmol) in 1 mL of ethanol. The resulting solution was allowed for slow evaporation in a 2 dram borosilicate vial at room temperature. Colorless plate-shaped crystals were obtained after two days. Dec.81 ˚C.

2.2.3 Single Crystal X-ray Crystallography

Data were collected on Bruker Kappa APEX II systems using Mo Kα radiation and APEX2 software.[22] Initial cell constants were found by small widely separated "matrix" runs. Data collection strategies were determined using COSMO.[23] Scan speed and scan width were chosen based on scattering power and peak rocking curves. All datasets were collected at – 153 °C using an Oxford Cryostream low-temperature device. Unit cell constants and orientation matrix were improved by least-squares refinement of reflections "thresholded" from the entire dataset. Integration was performed with SAINT,[24] using this improved unit cell as a starting point. Precise unit cell constants were calculated in SAINT from the final merged dataset. Lorenz and polarization corrections were applied. Multi-scan absorption corrections were performed with SADABS.[25] Data were reduced with SHELXTL.[26] The structures were solved in all cases by direct methods without incident. The molecules were fully ordered, no solvent was present, and no constraints or restraints were applied. **A_6D_6** crystallized in the polar space group *Pca*2_1;

this dataset was treated for racemic twinning, with the scale factor refining to 0.36(2). In all cases except for **A$_6$D$_6$**, both the diamide acceptor and the diiodo donor molecule sit on crystallographic inversion centers. Excepting **A$_4$D$_6$**, **A$_6$D$_6$**, and **A$_6$D$_2$**, coordinates for the amide hydrogen were allowed to refine (attempted refinement in the other structures did not give meaningful results). All other hydrogen atoms were located in idealized positions and were treated with a riding model.

2.3 Results

Initial co-crystal screening was achieved through solvent-assisted grinding[27] experiments followed by IR spectroscopic characterization.[28] However all 4x5 possible donor-acceptor combinations were also subjected to co-crystal synthesis from solution since the perfluorinated iodoalkanes are volatile and can evaporate during a grinding process. All solids obtained in this way were analyzed using IR spectroscopy (Table 2.1) to establish if a co-crystal had formed, and crystals suitable for single-crystal diffraction were grown by slow-evaporation at ambient conditions. A total of fifteen of the twenty reactions produced co-crystals based on IR spectroscopy and thirteen of those yielded crystals suitable for single-crystal X-ray diffraction. The only acceptor that failed to produce any co-crystals with **D$_2$**-**D$_8$** was the smallest acceptor molecule, **A$_0$**, which inevitably came out of solution as the monohydrate (the structure of which has previously been reported).[19] Repeated attempts using different donor-acceptor ratios and solvents failed to produce co-crystals of **A$_0$**.

2.3.1 Characterization by IR spectroscopy

The distinction between reaction and no reaction of the twenty experiments was made based on the shifts of modes in the infrared region associated primarily with C-F bonds of the halogen bond donors and C-H bonds of the acceptors, Table 2.1.

2.3.2 Crystal structure descriptions

Hydrogen-bond geometries for all co-crystals are reported in Table 2.2.

Table 2.1 IR stretching frequencies (cm^{-1}) of the solids produced by combining **A_8-A_0** with **D_2-D_8**

	D_2 (1144,1096, 833, 685) cm^{-1}		**D_4 (1192, 1134, 1041) cm^{-1}**		**D_6 (1200, 1141, 1087) cm^{-1}**		**D_8 (1200, 1145,1053, 965) cm^{-1}**	
	Co-crystal (cm^{-1})	Δ (cm^{-1})	Co-crystal (cm^{-1})	Δ (cm^{-1})	Co-crystal (cm^{-1})	Δ (cm^{-1})	Co-crystal (cm^{-1})	Δ (cm^{-1})
A_8	1136 1090 827	-8 -5 -6	1189 1140 1045	-3 +6 +4	1191 1132 1080	-8 -9 -7	1191 1153 1059	-9 -8 -6
A_6	1137 1090 700	-7 -6 +15	1197 1138 1046	+5 +4 +5	1180 1150 1084	-20 +9 -3	1208 1143 1056	-8 -1 +3
A_4	1145 1090	+1 -6	1184 1122	-8 -12	1192 1132 1085	-8 -9 -2	1144 1056	-1 +3
A_2	-		1188 1126 1044	-4 -8 +3	1214 1079	+14 -8	1214 1057 962	+14 +4 -3
A_0	-		-		-		-	

Table 2.2 Hydrogen bond geometries for **A_2·D_4**, **A_2·D_6**, **A_2·D_8**, **A_4·D_2**, **A_4·D_4**, **A_4·D_6**, **A_4·D_8**, **A_6·D_2**, **A_6·D_6**, **A_6·D_8**, **A_8·D_2**, **A_8·D_4**, **A_8·D_6**

Structure	D-H···A (Å)	d(D-H)/Å	d(H···A)/Å	d(D···A)/Å	<(DHA)/º
A_2·D_4[i]	N(17)-(17)...O(17)#3	0.83(3)	1.99(3)	2.779(2)	159(3)
A_2·D_6[ii]	N(17)-(17)...O(17)#3	0.811(18)	2.026(19)	2.8117(15)	163.2(18)
A_2·D_8[iii]	N(17)-(17)...O(17)#3	0.84(4)	2.01(4)	2.817(3)	162(3)
A_4·D_2[iv]	N(2)-H(2N)...O(1)#3	0.830(15)	2.036(15)	2.8565(19)	170(2)
A_4·D_4[v]	N(2)-H(2N)...O(1)#3	0.844(17)	2.040(19)	2.866(3)	166(3)
A_4·D_6[vi]	N(17)-H(17)...O(17)#3	0.84(3)	2.01(3)	2.845(2)	170(2)
A_4·D_8[vii]	N(17)-H(17)...O(17)#3	0.84(3)	2.01(3)	2.845(2)	170(2)
A_6·D_2[viii]	N(17)-H(17)...O(17)#3	0.88	2.11	2.958(3)	161.8
A_6·D_6[ix]	N(17)-H(17)...O(17)#2 N(27)-H(27)...O(27)#3	0.88 0.88	2.03 1.98	2.883(6) 2.823(5)	164.5 158.6
A_6·D_8[x]	N(17)-H(17)...O(17)#3	0.79(3)	2.21(3)	2.994(2)	169(3)
A_8·D_2[xi]	N(17)-H(17)...O(17)#3	0.79(3)	2.21(3)	2.980(2)	164(3)
A_8·D_4[xii]	N(17)-(17)...O(17)#3	0.81(2)	2.18(2)	2.9736(14)	167.9(18)
A_8·D_6[xiii]	N(17)-(17)...O(17)#3	0.88(3)	2.12(3)	2.983(2)	166(3)

Symmetry transformations used to generate equivalent atoms

i) #1 -x,-y,-z+2 #2 -x+1,-y+1,-z+1 **ii)** #1 -x,-y+2,-z #2 -x+1,-y+1,-z+2 **iii)** #1 -x+1,-y+2,-z+2 #2 -x,-y+1,-z **iv)** #1 -x+2,-y+2,-z+1 #2 -x+3/2,-y+3/2,-z **v)** #1 -x,-y,-z+1 #2 -x+1,-y+2,-z+2 **vi)** #1 -x,-y+2,-z #2 -x+1/2,-y+3/2,-z+1 **vii)** #1 -x,-y,-z+1 #2 -x+1/2,-y-1/2,-z+2 **viii)** #1 -x+2,-y+1,-z #2 -x+1,-y+2,-z+1 **ix)** #1 x+1/2,-y+1,z **x)** #1 -x+2,-y+1,-z #2 -x+1,-y,-z+1 **xi)** #1 -x+2,-y,-z+1 #2 -x+1,-y,-z **xii)** #1 -x-1,-y+1,-z #2 -x,-y+1,-z+1 **xiii)** #1 -x+2,-y,-z+1 #2 -x+1,-y,-z

2.3.3 Crystal Structures

2.3.3.1 Crystal structures of $A_2 \cdot D_4$, $A_2 \cdot D_6$ and *$A_2 \cdot D_8$*

The supramolecular reaction between **A2** and **D4**, **D6** and **D8** yielded co-crystals with 1:1 stoichiometry driven by I···N (py) halogen-bond interactions resulting in infinite 1-D chains (Figure 2.6). Adjacent acceptor molecules are oriented in an orthogonal manner which results in doubly interpenetrated (4,4) networks where each molecule interacts with four nearest neighbors via N-H···O=C hydrogen bonding interactions producing a 3-D network, Figure 2.7.

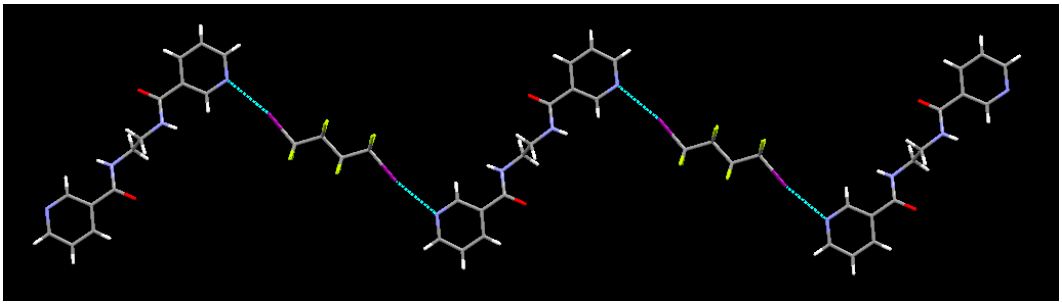

Figure 2.6 Infinite 1-D chains formed via I···N halogen bonds in the crystal structure of **$A_2 \cdot D_4$**

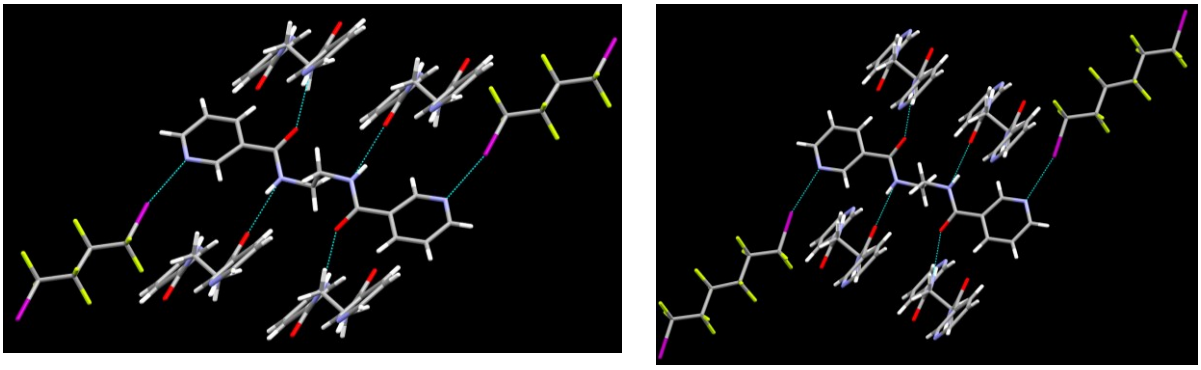

(a) (b)

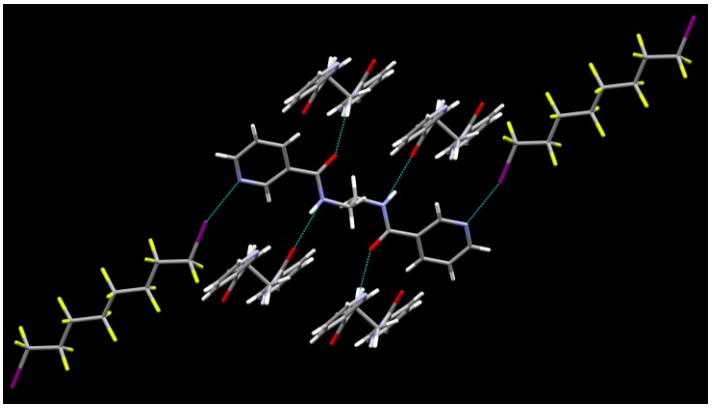

(c)

Figure 2.7 Part of the crystal structure showing doubly interpenetrated (4,4) network in (a) **A$_2$·D$_4$** (b) **A$_2$·D$_6$** and (c) **A$_2$·D$_8$**

2.3.3.2 Crystal structures of A$_4$·D$_2$, A$_4$·D$_6$ and A$_4$·D$_8$

The crystal structures of **A$_4$·D$_2$**, **A$_4$·D$_6$** and **A$_4$·D$_8$** are similar in that they are all 1:1 co-crystals of **A$_4$** and the given aliphatic halogen-bond donor. In every case, I···N (py) halogen bonds are driving the co-crystal synthesis and lead to infinite chains (Figure 2.8). Adjacent acceptors are oriented in an orthogonal manner which results in doubly interpenetrated (4,4) networks where each molecule interacts with four nearest neighbors via N-H···O=C hydrogen bonding interactions producing a 3-D network (Figure 2.9).

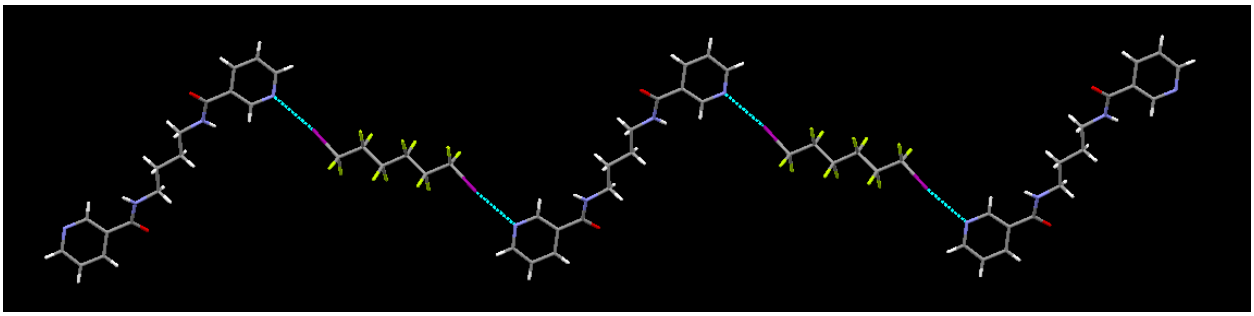

Figure 2.8 Infinite 1-D chains formed via I···N halogen bonds in the crystal structure of **A$_4$·D$_6$**

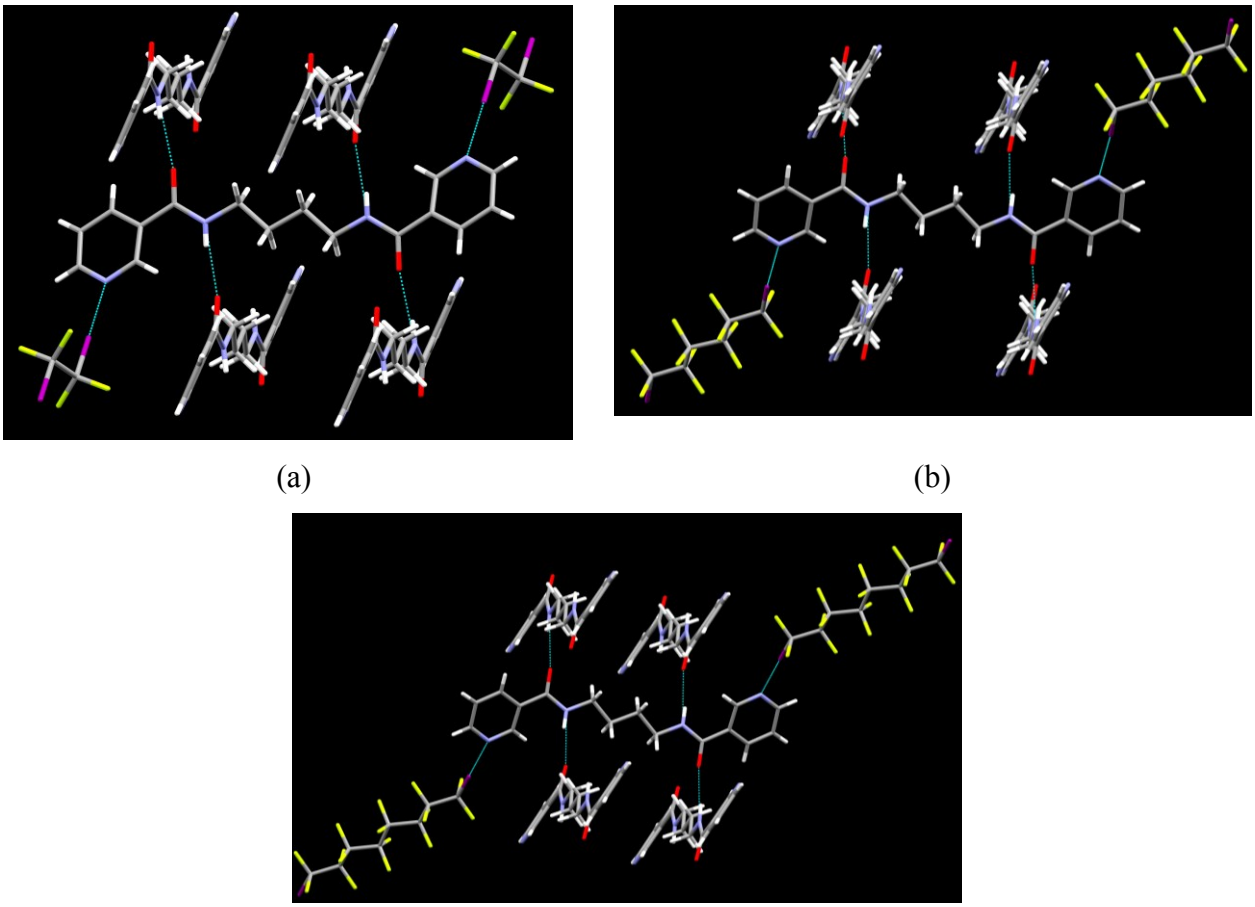

(a) (b)

(c)

Figure 2.9 Part of the crystal structure showing doubly interpenetrated (4,4) network in (a) **$A_4 \cdot D_4$** (b) **$A_4 \cdot D_6$** and (c) **$A_4 \cdot D_8$**

2.3.3.3 Crystal structure of $A_4 \cdot D_4$

The crystal structure determination of **$A_4 \cdot D_4$** confirmed the formation of a 1:1 co-crystal driven by I···N (py) halogen bonds to form infinite chains. However, the ligand arrangement is different than in **$A_4 \cdot D_2$**, **$A_4 \cdot D_6$** and **$A_4 \cdot D_8$**, and in **$A_4 \cdot D_4$**, as self-complementary N-H···O=C hydrogen-bonding interactions produce a 2-D sheet-like architecture, Figure 2.10.

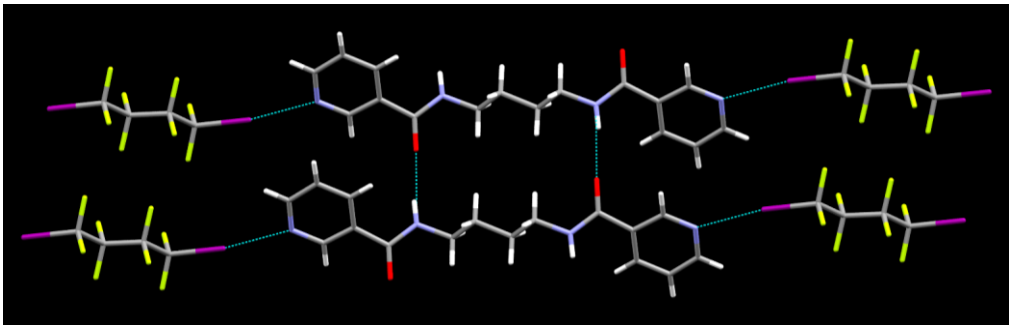

Figure 2.10 The 2-D sheet-like architecture of **A$_4$·D$_4$** constructed via I···N (py) and C=O···N-H interactions

2.3.3.4 Crystal structures of A$_6$·D$_2$, A$_6$·D$_6$ and *A$_6$·D$_8$*

The reaction between **A$_6$** and the aliphatic halogen-bond donors show co-crystal formation with 1:1 stoichiometry through I···N (py) and N-H···O=C synthons. The 1-D motifs created by I···N (py) halogen bonds between alternating molecules of **A$_6$** and **D** are accompanied by orthogonal self-complementary N-H···O=C hydrogen bonds resulting in buckled 2-D motifs where adjacent acceptors are arranged in a layered array (Figure 2.11).

2.3.3.5 Crystal structures of A$_8$·D$_2$, A$_8$·D$_4$ and *A$_8$·D$_6$*

The crystal structures of **A$_8$·D$_2$**, **A$_8$·D$_4$** and **A$_8$·D$_6$** showed 1:1 co-crystal formation between **A$_8$** and the halogen-bond donors. The interaction between the acceptor and the donors result in the formation of 1-D chains using I···N (py) halogen-bonds which in turn organize into 2-D layers via inter chain N-H···O=C amide-amide hydrogen bonds (Figure 2.12).

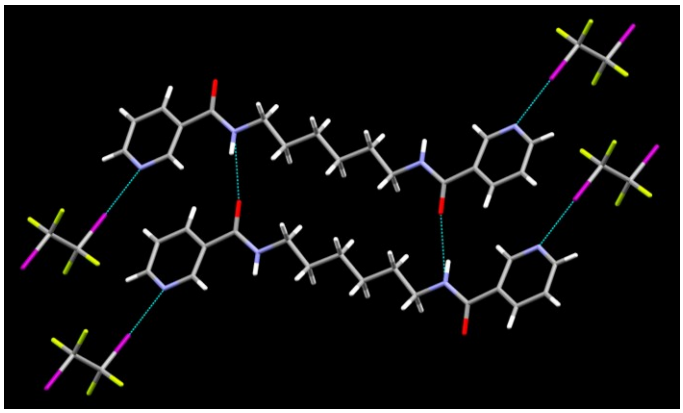

(a)

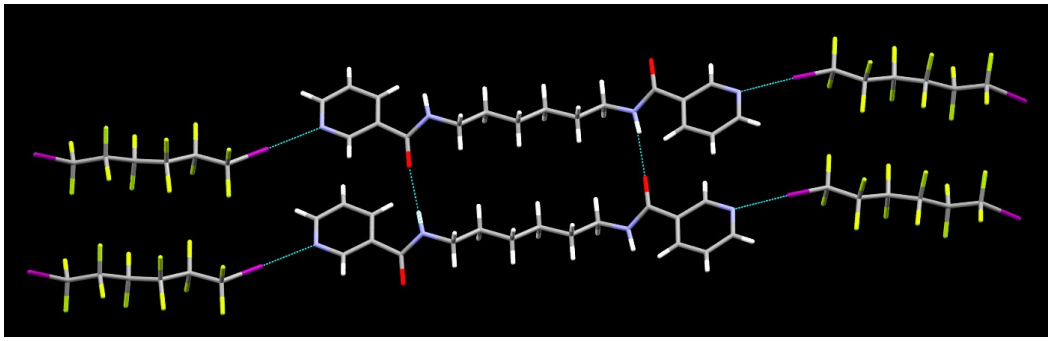

(b)

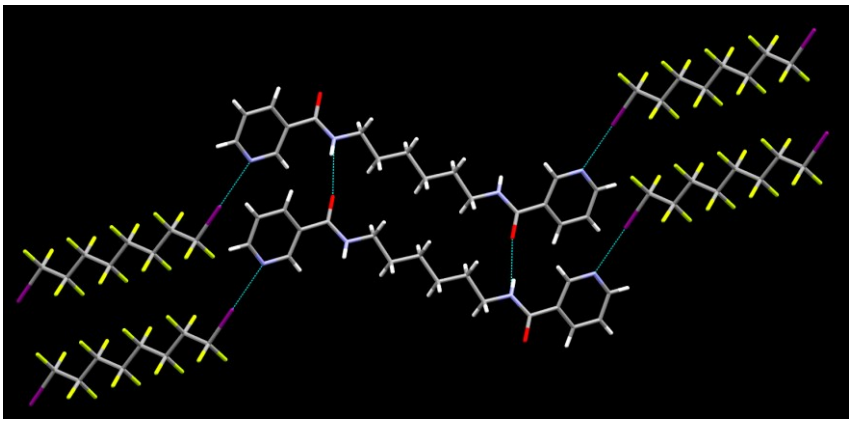

(c)

Figure 2.11 2-D layered motifs in (a) **A$_6$·D$_2$**, (b) **A$_6$·D$_6$** and (c) **A$_6$·D$_8$**

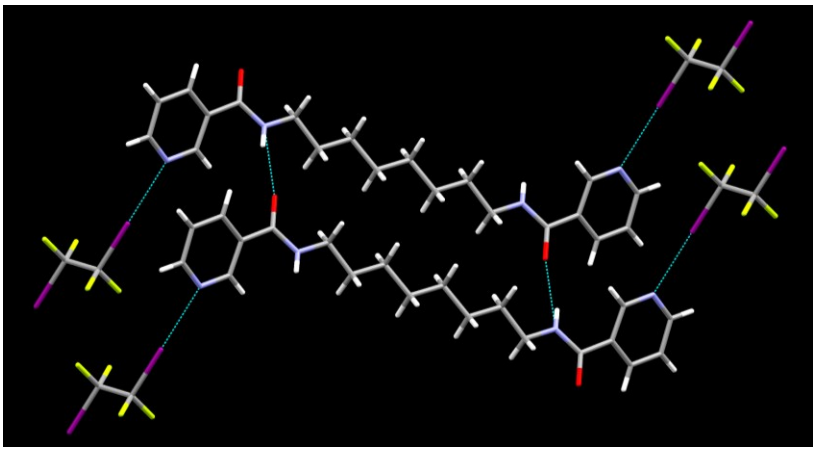

(a)

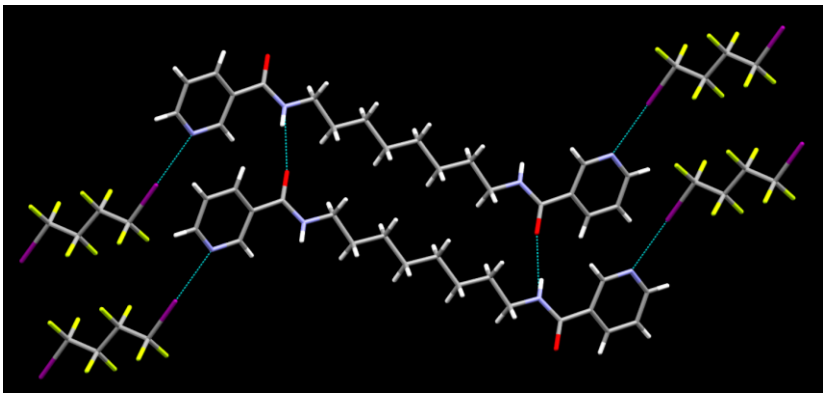

(b)

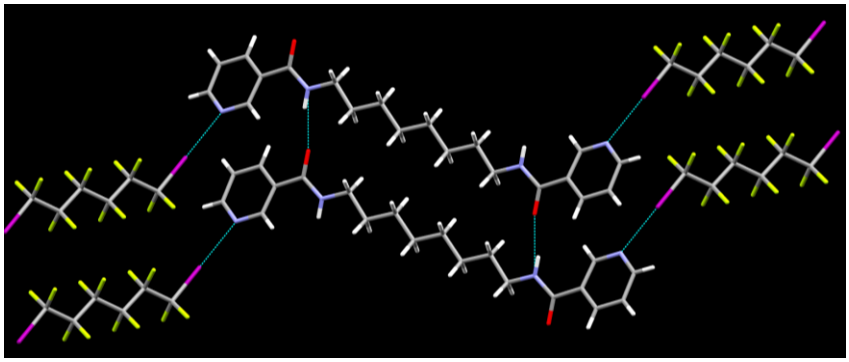

(c)

Figure 2.12 2-D layered motifs in (a) $\mathbf{A_8 \cdot D_2}$, (b) $\mathbf{A_8 \cdot D_4}$ and (c) $\mathbf{A_8 \cdot D_6}$

2.4 Discussion

2.4.1 Characterization of co-crystals through IR spectroscopy

Formation of halogen bonds was detected by IR spectroscopy since the vibrational frequencies and strength change upon a non-covalent interaction.[29] In the halogen bonded co-crystals, characteristic IR bands moved to both higher as well as to lower wavenumbers, with relatively small changes (Table 2.1). The C-F bands were red-shifted when compared to the same modes present in the pure perfluoroiodoalkanes in 2/3 of the co-crystals obtained. The magnitude of the red-shifts were in the 5-15 cm^{-1} range and may be a consequence of the charge transfer component of the XB. In the remaining co-crystals, the C-F modes were blue-shifted by 1-14 cm^{-1}. Our results are comparable with literature data which indicate that about 70% of co-crystals of perfluoroiodoalkanes display red-shifts of their relevant C-F modes (appearing at approximately 1218 and 1048 cm^{-1}, respectively).[30] In the remaining cases, the C-F bands were shifted to higher wave-numbers upon co-crystal formation with relatively small changes.[31]

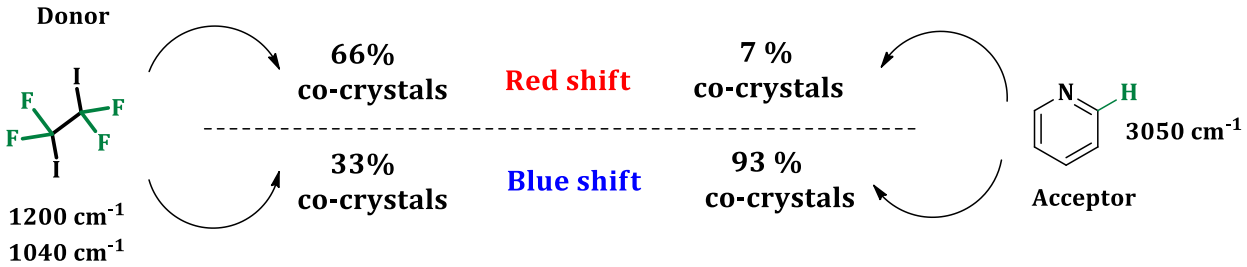

Figure 2.13 Summary of the red shifts and blue shifts observed in the co-crystals with respect to the donor and acceptor

The vibrational modes of the N-heterocyclic XB acceptor moiety is also affected by halogen-bond formation. The C-H stretching modes associated with the pyridine ring (**A8**; 3039 cm^{-1}, **A6**; 3046 cm^{-1}, **A4**; 3073 cm^{-1}, **A2**; 3073 cm^{-1}) became less intense and blue shifted; 3049-3053 cm^{-1} for **A8** co-crystals, 3050-3052 cm^{-1} for **A6** co-crystals, 3078-3085 cm^{-1} for **A4** co-crystals, and 3084-3089 cm^{-1} for **A2** co-crystals. Other characteristic vibrations of the pyridine ring (at 1470 cm^{-1} and 1240 cm^{-1}) were also blue-shifted by 5-10 cm^{-1} in the co-crystals relative to their positions in the pure acceptors. These changes are attributed to a slightly reduced electron density in the pyridine ring due to the electron-donating pair role that the pyridine moiety plays in halogen bonding.[32]

2.4.2 Melting point analysis of the co-crystals

All the co-crystals decomposed upon heating by first releasing the relatively volatile halogen-bond donor, followed by melting of the remaining pure acceptor (Table 2.3).

Table 2.3 Decomposition points and melting points of the co-crystals

	Decomposition point (˚C)	Melting point (˚C)
$A_8 \cdot D_2$	72	150-152
$A_8 \cdot D_4$	79	151-153
$A_8 \cdot D_6$	81	150-151
$A_6 \cdot D_2$	78	157-159
$A_6 \cdot D_6$	81	158-160
$A_6 \cdot D_8$	86	158-159
$A_4 \cdot D_2$	95	202-203
$A_4 \cdot D_4$	101	204-205
$A_4 \cdot D_6$	76	204-206
$A_4 \cdot D_8$	125	201-203
$A_2 \cdot D_4$	89	220-221
$A_2 \cdot D_6$	86	221-222
$A_2 \cdot D_8$	99	218-219

The temperatures at which the halogen-bond donors are “evicted” from the crystals, are to some extent related to the molecular weight of the donor . The co-crystals decomposed with the following decomposition temperature ranges **A_8** (72-89 ˚C), **A_6** (78-86 ˚C), **A_4** (76-125 ˚C) and **A_2** (86-99 ˚C) where in each case, the highest temperature in each series, is associated with the co-crystal of the heaviest perfluorinated halogen-bond donor and vice versa within each of the four series (Figure 2.14).

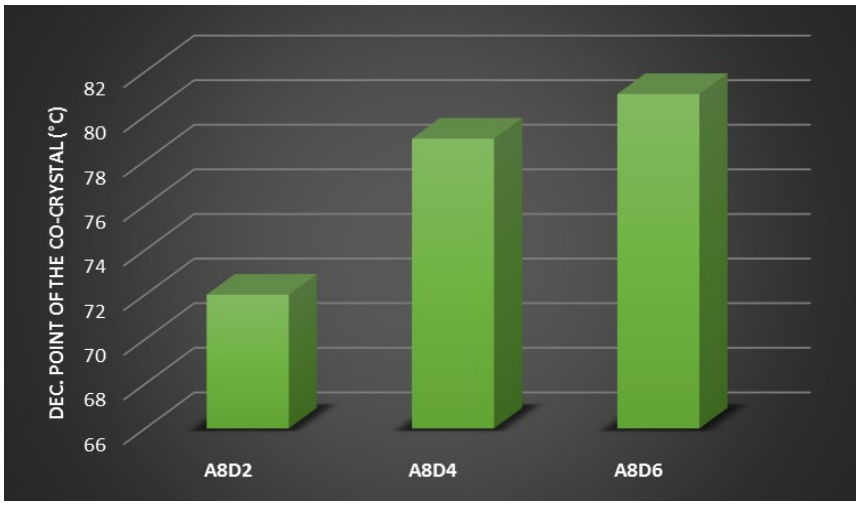

(a)

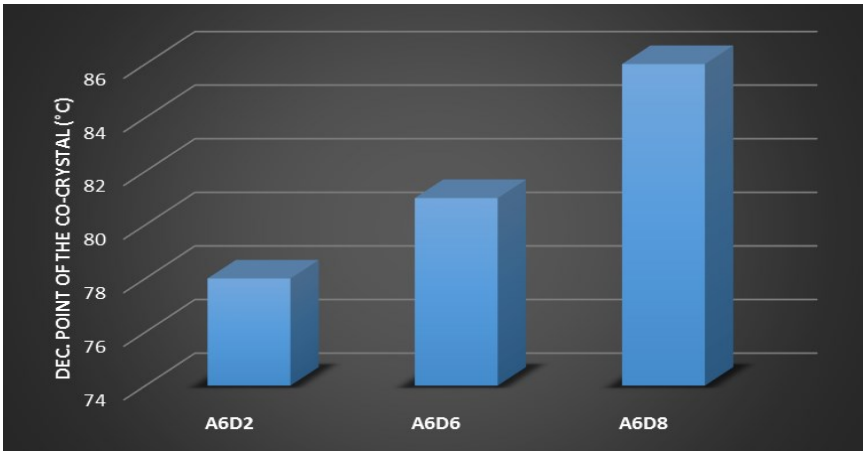

(b)

Figure 2.14 Decomposition profile of the co-crystals with respect to (a) **A_8** and (b) **A_6**

There is a possibility for stabilizing volatile XB donors within a crystalline lattice by combining them with a suitable acceptor which may have significant impact on practical application for transport and storage of volatile perfluorinated alkanes (Figure 2.15).[33] For example, the co-crystals of **A_8** are stabilized by 93°C, 88°C and 55°C respectively compared to the pure donor molecules.

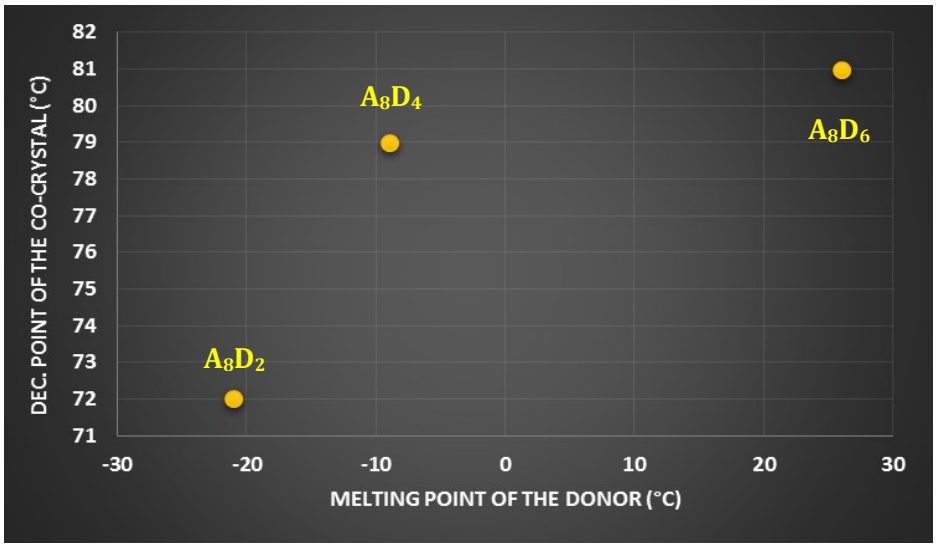

(a)

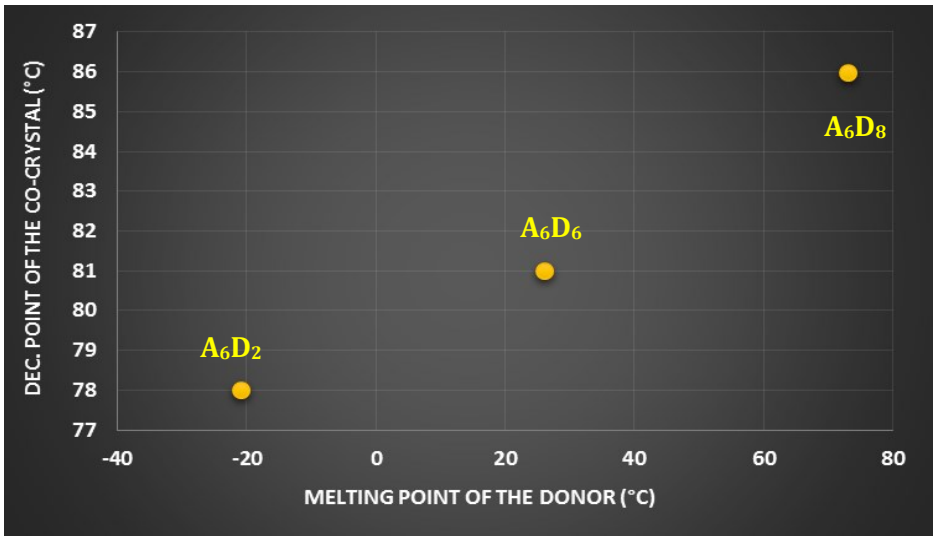

(b)

Figure 2.15 Correlation between the melting point of the donor and decomposition temperature of the co-crystals of (a) **A8** and (b) **A6**

2.4.3 Structural view of the co-crystals compared to the ligands by themselves

When the structures of the ligands **A8**-**A2** by themselves are taken into consideration, each molecule contains two conventional hydrogen-bond donors, the N-H groups, and four hydrogen-bond acceptor sites, the C=O and N(py) moieties. However in the three known structures (**A4**, **A6** and **A8**), the self-complementary N-H···O=C amide-amide synthons are the only observed

hydrogen bonds, and the pyridine moieties do not engage in any structure-directing conventional hydrogen bonds. However, the amide-amide interactions do produce two different motifs, a layered ribbon-like architecture in **A6** and **A8** and a doubly-interpenetrated orthogonal network in **A4**, (Figure 2.16).[20, 34] The crystal structure of **A2** is still unknown, and **A0** appears as a monohydrate.[19]

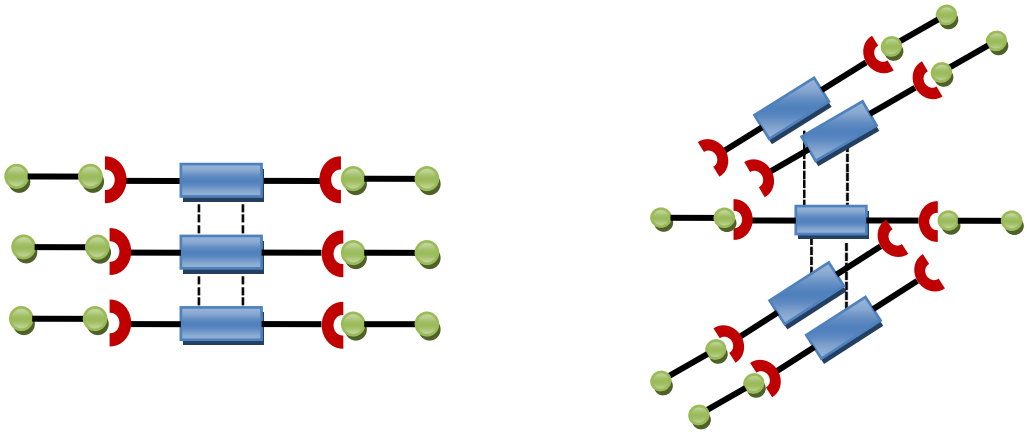

(a) (b)

Figure 2.16 Adjacent *bis*-acetamides are arranged either in a layered (a) or in an orthogonal (b) manner

The hydrogen-bonded co-crystals of $\mathbf{A}_n$ that are reported up to date have been synthesized with carboxylic acids as the donor using O-H···N(py) interactions. Within each binary lattice, the self-complementary C=O···N-H hydrogen bonds form layered ribbons between the adjacent *bis*-pyridineacetamides.[16] However this structural consistency is not seen in *bis*-acetamide co-crystals with aliphatic halogen-bond donors. For **A8** and **A6**, the layered motifs are present 6/6 times, for **A4** the layer is only present in one of the four examples, whereas all three of the co-crystals of **A2** contain the orthogonal *bis*-acetamide motif.

Based on these results, we propose that these *bis*-acetamidopyridine based hydrogen- and halogen-bonded co-crystals may be assembled in two-step processes. Each structure is constructed via two distinct synthons, where the hydrogen-bonded co-crystals are assembled via O-H···N(py) and amide···amide synthons and the C-I···N(py) and amide···amide interactions govern the assembly of the halogen-bonded co-crystals. The halogen-bonded co-crystals essentially display the same core as the *bis*-pyridines do by themselves which would suggest that the hydrogen-bond driven amide···amide interaction resulting in either a layer (for **A8** and **A6**) or orthogonal motif (in **A4**) is occurring as the first (or more favorable) step in the assembly process

which is then followed by the attachment of a halogen-bond donors to this 'core' via a C-I···N(py) bonds (Figure 2.17). This assembly process could be further explained by the DSC profile of the halogen-bonded co-crystals where we see two endothermic events, in which first endotherm correspond to dissociation of the halogen bond donor and the second endotherm correspond to the exact melting point of the API by itself (Appendix A).

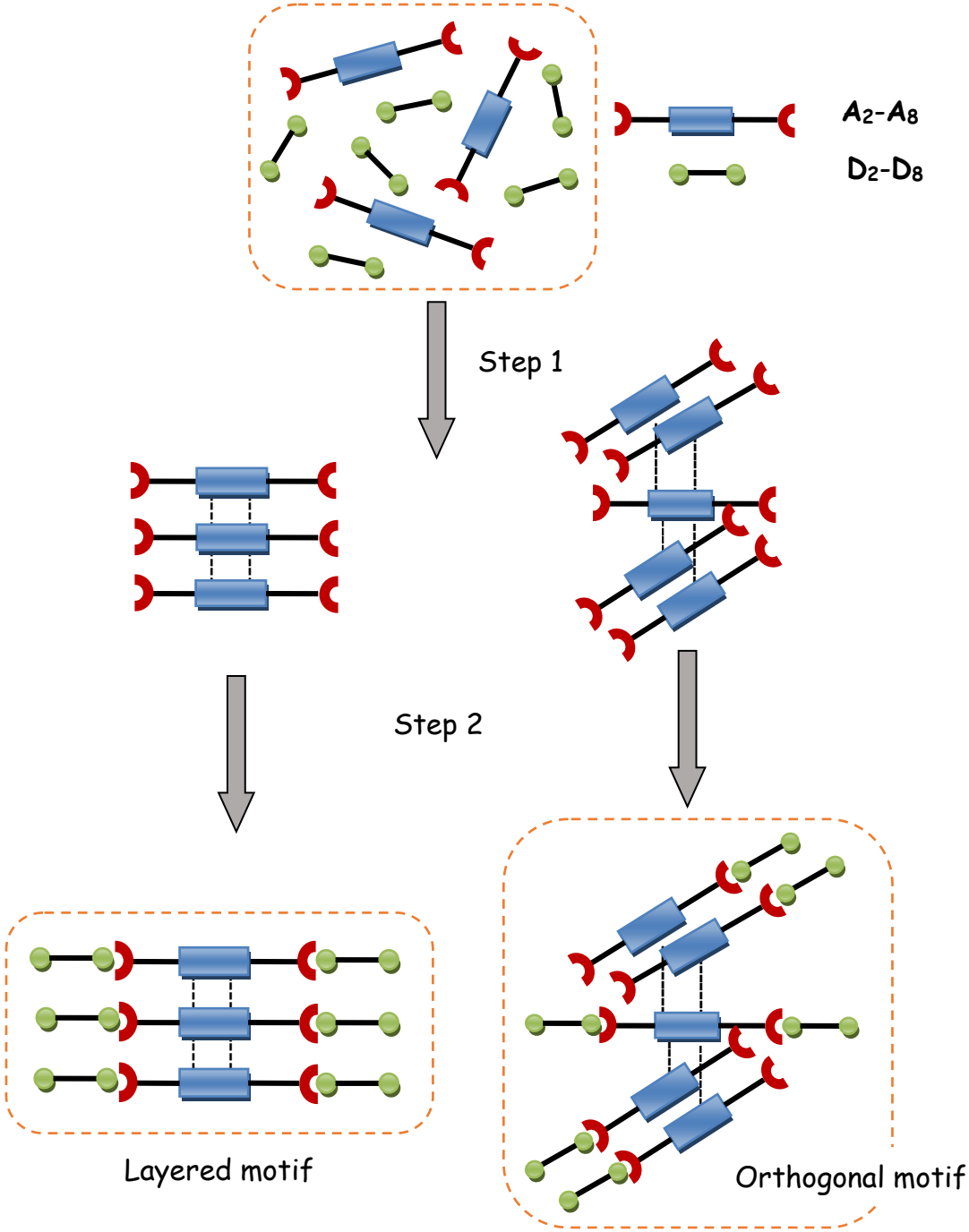

Figure 2.17 Step-wise self-assembly of halogen-bond driven supramolecular architectures

This hypothesis fits eight of the nine crystal structures of halogen-bonded co-crystals where the structure of the free *bis*-pyridine is known, with **A4**·**D4** being the outlier. Based on this hypothesis, we would expect an orthogonal amide···amide motif for the structure of **A2** but we have been unable to grow single-crystals of this compound after trying out many experimental conditions.

The fact that all the known hydrogen-bonded co-crystals of **A2**-**A8**, exhibit layered amide···amide motifs means a different process must be involved in an O-H···N bond driven co-crystal assembly. In this series of structures, the O-H···N(py) hydrogen bonding interaction takes place as the most favorable step to form chains of alternating hydrogen-bonds donors and acceptors, which is then followed by the self-assembly via the amide linkages to produce a 2-D layered arrangement (Figure 2.18). These chains are packed and oriented within 2-D layered architectures in such a way that anti-parallel dipoles aligned together and the polar, aromatic, and aliphatic moieties of neighboring chains are aggregated into distinct regions within each crystal. This process overcomes any possibility that the individual *bis*-pyridineacetamides arrange into an orthogonal geometry. The structural behavior of all known hydrogen-bonded co-crystal of **A2**-**A8** can be explained by this hypothesis. This assembly process could be explained by the DSC profile of the hydrogen bonded co-crystals which has only one endothermic event corresponding to the breakdown of the co-crystal (Appendix A).

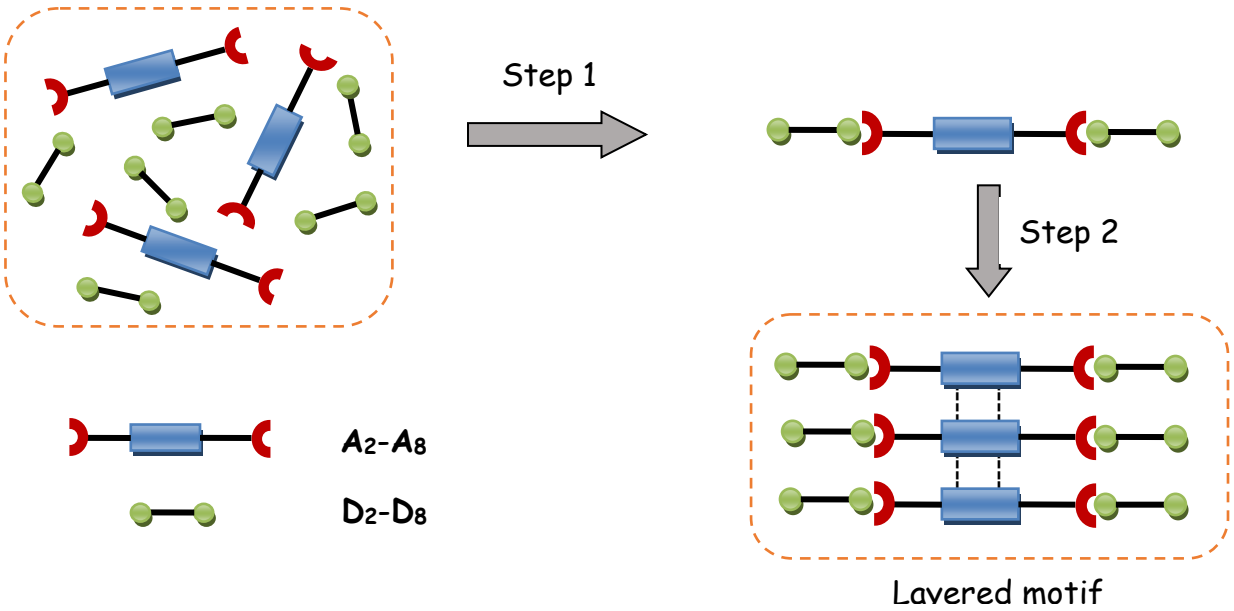

Figure 2.18 Step-wise self-assembly of hydrogen-bond driven supramolecular architectures

2.4.4 Correlation between the structure and the decomposition points of the co-crystals

The decomposition temperatures of the halogen bonded co-crystals correlate well with the type of ligand arrangement (layered vs. orthogonal) in the binary co-crystals. When the molecular weight of each halogen-bond donor is considered, the co-crystals of **A_4** and **A_2** display higher decomposition than those of **A_6** and **A_8** (Figure 2.19). This suggest that the volatile halogen-bond donors are held more firmly within the crystalline lattice due to their complex 3-D architecture in the co-crystals of **A_4** and **A_2**, so that the decomposition point gets higher. In contrast, the co-crystals of **A_6** and **A_8** are arranged into distinct columns where donors and acceptors are separated, facilitates the escape of the volatile halogen bond donors from the lattice more easily. In all cases, the final melting temperature was the melting point of the individual acceptor molecule indicating that only one of the two components remains.

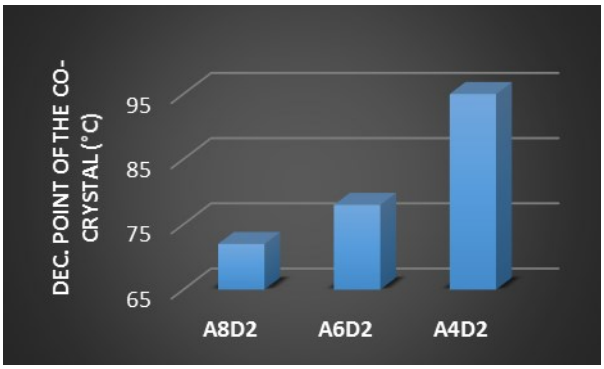

D_2

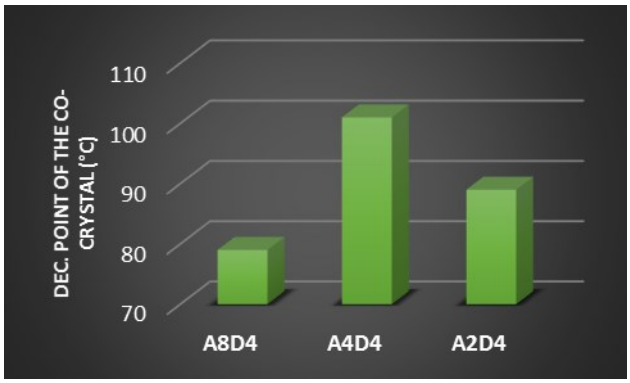

D_4

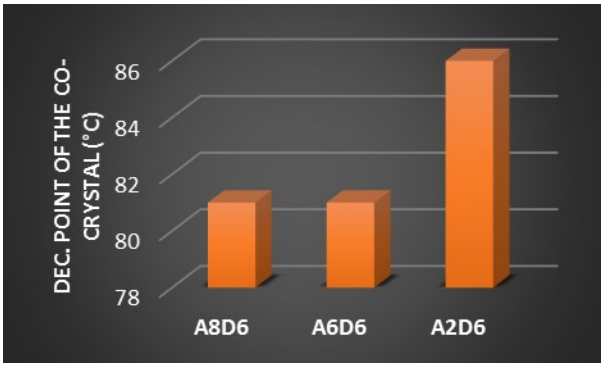

D_6

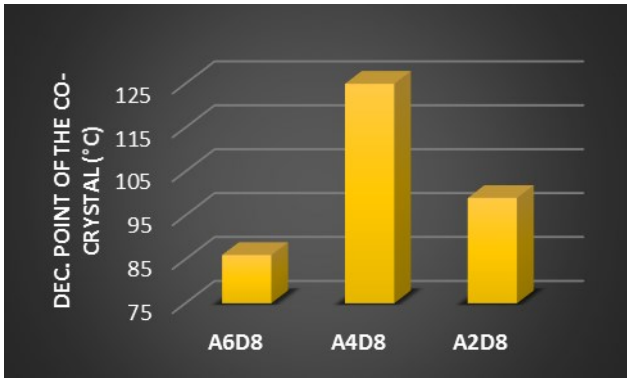

D_8

Figure 2.19 Decomposition temperature profiles with respect to the halogen bond donor

Since there were two different architectures observed for the halogen bonded co-crystals it is no longer possible to directly correlate physical properties with molecular properties. This is in contrast with the corresponding hydrogen-bonded co-crystals because they all displayed structural consistency with layered architectures where physical properties could be correlated well with the structural properties.[16]

2.5 Conclusion

Halogen bonding was successfully employed in synthesizing co-crystals of a series of *bis*-pyridine based pharmaceutical active ingredients using four iodoperfluoroalkanes. Thirteen of the supramolecular co-crystals driven by I···N(py) halogen bonds were compared with respect to the OH···N(py) driven hydrogen bonded co-crystals. The success rate was comparable with that of the hydrogen bonded analogues. However the structures of the halogen bonded co-crystals show two different architectures, layered vs orthogonal, depending on the relative orientation of the adjacent amide moieties and a two-step process is proposed as a way of rationalizing the observed structures. This study reveals that supramolecular architectures with high predictability and selectivity are possible by using appropriate hydrogen-bond and halogen-bond moieties that can operate in an independent manner. Also, volatile organic halogen bond donors can be substantially stabilized by incorporating them into a crystalline lattice.

2.6 References

1. (a) Shan, N.; Zaworotko, M. J. *Drug Discovery Today* **2008,** *13* (9–10), 440-446; (b) Schultheiss, N.; Newman, A. *Cryst. Growth Des.* **2009,** *9* (6), 2950-2967; (c) Jones, W.; Motherwell, W. D. S.; Trask, A. V. *MRS Bull.* **2006,** *31* (11), 875-879.

2. Nauha, E.; Kolehmainen, E.; Nissinen, M. *CrystEngComm* **2011,** *13* (21), 6531-6537.

3. (a) Yang, Z.; Li, H.; Huang, H.; Zhou, X.; Li, J.; Nie, F. *Propellants Explos. Pyrotech.* **2013,** *38* (4), 495-501; (b) Shen, J. P.; Duan, X. H.; Luo, Q. P.; Zhou, Y.; Bao, Q.; Ma, Y. J.; Pei, C. H. *Cryst. Growth Des.* **2011,** *11* (5), 1759-1765; (c) Landenberger, K. B.; Matzger, A. J. *Cryst. Growth Des.* **2010,** *10* (12), 5341-5347; (d) Bolton, O.; Simke, L. R.; Pagoria, P. F.; Matzger, A. J. *Cryst. Growth Des.* **2012,** *12* (9), 4311-4314; (e) Bolton, O.; Matzger, A. J. *Angew. Chem. Int. Ed.* **2011,** *50* (38), 8960-8963.

4. (a) Yan, Y.; Chen, J.-M.; Geng, N.; Lu, T.-B. *Cryst. Growth Des.* **2012,** *12* (5), 2226-2233; (b) Xu, L.-L.; Chen, J.-M.; Yan, Y.; Lu, T.-B. *Cryst. Growth Des.* **2012,** *12* (12), 6004-6011; (c) Shevchenko, A.; Miroshnyk, I.; Pietilä, L.-O.; Haarala, J.; Salmia, J.; Sinervo, K.; Mirza, S.; van Veen, B.; Kolehmainen, E.; Nonappa; Yliruusi, J. *Cryst. Growth Des.* **2013,** *13* (11), 4877-4884; (d) Good, D. J.; Rodríguez-Hornedo, N. *Cryst. Growth Des.* **2009,** *9* (5), 2252-2264; (e) Geng, N.; Chen, J.-M.; Li, Z.-J.; Jiang, L.; Lu, T.-B. *Cryst. Growth Des.* **2013,** *13* (8), 3546-3553; (f) Childs, S. L.; Kandi, P.; Lingireddy, S. R. *Mol. Pharm.* **2013,** *10* (8), 3112-3127.

5. (a) Prins, L. J.; Reinhoudt, D. N.; Timmerman, P. *Angew. Chem. Int. Ed.* **2001,** *40* (13), 2382-2426; (b) Desiraju, G. R. *Acc. Chem. Res.* **2002,** *35* (7), 565-573; (c) Archer, E. A.; Gong, H.; Krische, M. J. *Tetrahedron* **2001,** *57* (7), 1139-1159; (d) Aakeroy, C. B.; Seddon, K. R. *Chem. Soc. Rev.* **1993,** *22* (6), 397-407.

6. Metrangolo, P.; Neukirch, H.; Pilati, T.; Resnati, G. *Acc. Chem. Res.* **2005,** *38* (5), 386-395.

7. Legon, A. C. *Angew. Chem. Int. Ed.* **1999,** *38* (18), 2686-2714.

8. (a) Ouvrard, C.; Le Questel, J.-Y.; Berthelot, M.; Laurence, C. *Acta Crystallogr., Sect. B: Struct. Sci.* **2003,** *59* (4), 512-526; (b) Legon, A. C. *PCCP* **2010,** *12* (28), 7736-7747.

9. (a) Priimagi, A.; Cavallo, G.; Metrangolo, P.; Resnati, G. *Acc. Chem. Res.* **2013,** *46* (11), 2686-2695; (b) Metrangolo, P.; Resnati, G. *Chem. Eur. J.* **2001,** *7* (12), 2511-2519; (c) Metrangolo, P.; Meyer, F.; Pilati, T.; Resnati, G.; Terraneo, G. *Angew. Chem. Int. Ed.* **2008,** *47* (33), 6114-6127; (d) Baldrighi, M.; Cavallo, G.; Chierotti, M. R.; Gobetto, R.; Metrangolo, P.; Pilati, T.; Resnati, G.; Terraneo, G. *Mol. Pharm.* **2013,** *10* (5), 1760-1772.

10. (a) Nguyen, H. L.; Horton, P. N.; Hursthouse, M. B.; Legon, A. C.; Bruce, D. W. *J. Am. Chem. Soc.* **2003,** *126* (1), 16-17; (b) Chen, Y.; Yu, H.; Zhang, L.; Yang, H.; Lu, Y. *Chem. Commun.* **2014,** *50* (68), 9647-9649.

11. (a) Wang, F.; Ma, N.; Chen, Q.; Wang, W.; Wang, L. *Langmuir* **2007,** *23* (19), 9540-9542; (b) Shirman, T.; Kaminker, R.; Freeman, D.; van der Boom, M. E. *ACS Nano* **2011,** *5* (8), 6553-6563.

12. (a) Wilcken, R.; Zimmermann, M. O.; Lange, A.; Joerger, A. C.; Boeckler, F. M. *J. Med. Chem.* **2012,** *56* (4), 1363-1388; (b) Sirimulla, S.; Bailey, J. B.; Vegesna, R.; Narayan, M. *J. Chem. Inf. Model.* **2013,** *53* (11), 2781-2791; (c) Scholfield, M. R.; Zanden, C. M. V.; Carter, M.; Ho, P. S. *Protein Sci.* **2013,** *22* (2), 139-152; (d) Lu, Y.; Shi, T.; Wang, Y.; Yang, H.; Yan, X.; Luo, X.; Jiang, H.; Zhu, W. *J. Med. Chem.* **2009,** *52* (9), 2854-2862; (e) Lu, Y.; Liu, Y.; Xu, Z.; Li, H.; Liu, H.; Zhu, W. *Expert Opin. Drug Discovery* **2012,** *7* (5), 375-383; (f) Auffinger, P.; Hays, F. A.; Westhof, E.; Ho, P. S. *Proc. Nat. Acad. Sci. U.S.A.* **2004,** *101* (48), 16789-16794.

13. (a) Saha, B. K.; Nangia, A.; Jaskolski, M. *CrystEngComm* **2005,** *7* (58), 355-358; (b) Corradi, E.; Meille, S. V.; Messina, M. T.; Metrangolo, P.; Resnati, G. *Angew. Chem. Int. Ed.* **2000,** *39* (10), 1782-1786; (c) Aakeröy, C. B.; Schultheiss, N. C.; Rajbanshi, A.; Desper, J.; Moore, C. *Cryst. Growth Des.* **2008,** *9* (1), 432-441; (d) Aakeroy, C. B.; Panikkattu, S.; Chopade, P. D.; Desper, J. *CrystEngComm* **2013,** *15* (16), 3125-3136; (e) Aakeröy, C. B.; Fasulo, M.; Schultheiss, N.; Desper, J.; Moore, C. *J. Am. Chem. Soc.* **2007,** *129* (45), 13772-13773.

14. Aakeroy, C. B.; Desper, J.; Helfrich, B. A.; Metrangolo, P.; Pilati, T.; Resnati, G.; Stevenazzi, A. *Chem. Commun.* **2007,** (41), 4236-4238.

15. Aakeröy, C. B.; Chopade, P. D.; Desper, J. *Cryst. Growth Des.* **2011,** *11* (12), 5333-5336.

16. Aakeroy, C. B.; Forbes, S.; Desper, J. *CrystEngComm* **2014,** *16* (26), 5870-5877.

17. (a) Walsh, R. B.; Padgett, C. W.; Metrangolo, P.; Resnati, G.; Hanks, T. W.; Pennington, W. T. *Cryst. Growth Des.* **2001,** *1* (2), 165-175; (b) Han, N.; Zeng, Y.; Sun, C.; Li, X.; Sun, Z.; Meng, L. *J. Phys. Chem. A* **2014,** *118* (34), 7058-7065.

18. (a) Metrangolo, P.; Prasang, C.; Resnati, G.; Liantonio, R.; Whitwood, A. C.; Bruce, D. W. *Chem. Commun.* **2006,** (31), 3290-3292; (b) Metrangolo, P.; Panzeri, W.; Recupero, F.; Resnati, G. *J. Fluorine Chem.* **2002,** *114* (1), 27-33; (c) Metrangolo, P.; Carcenac, Y.; Lahtinen, M.; Pilati, T.; Rissanen, K.; Vij, A.; Resnati, G. *Science* **2009,** *323* (5920), 1461-1464; (d) Liantonio, R.; Metrangolo, P.; Pilati, T.; Resnati, G.; Stevenazzi, A. *Cryst. Growth Des.* **2003,** *3* (5), 799-803; (e) Farina, A.; Meille, S. V.; Messina, M. T.; Metrangolo, P.; Resnati, G.; Vecchio, G. *Angew. Chem. Int. Ed.* **1999,** *38* (16), 2433-2436; (f) Amico, V.; Meille, S. V.; Corradi, E.; Messina, M. T.; Resnati, G. *J. Am. Chem. Soc.* **1998,** *120* (32), 8261-8262.

19. Du, M.; Zhang, Z.-H.; Wang, X.-G.; Wu, H.-F.; Wang, Q. *Cryst. Growth Des.* **2006,** *6* (8), 1867-1875.

20. Sarkar, M.; Biradha, K. *Cryst. Growth Des.* **2005,** *6* (1), 202-208.

21. Murakami, Y.; Aoyama, Y.; Kikuchi, J.; Nishida, K. *J. Am. Chem. Soc.* **1982,** *104* (19), 5189-5197.

22. APEXII v2009. 5-1, © 2009, Bruker Analytical X-ray Systems, Madison, WI.

23. COSMO v1. 60, © 1999 - 2009, Bruker Analytical X-ray Systems, Madison, WI.

24. SAINT v7. 60a, © 1997 - 2008, Bruker Analytical X-ray Systems, Madison, WI.

25. SADABS v2008/1, © 2008, Bruker Analytical X-ray Systems, Madison, WI.

26. SHELXTL v2008/4, © 20080, Bruker Analytical X-ray Systems, Madison, WI.

27. (a) Braga, D.; Maini, L.; Grepioni, F. *Chem. Soc. Rev.* **2013,** *42* (18), 7638-7648; (b) Bowmaker, G. A. *Chem. Commun.* **2013,** *49* (4), 334-348.

28. (a) Aakeroy, C. B.; Schultheiss, N.; Desper, J.; Moore, C. *New J. Chem.* **2006,** *30* (10), 1452-1460; (b) Aakeroy, C. B.; Hussain, I.; Forbes, S.; Desper, J. *CrystEngComm* **2007,** *9* (1), 46-54.

29. Cragg, P. J. *Supramolecular chemistry: from biological inspiration to biomedical applications*. Springer Science and Business Media: 2010.

30. (a) Saccone, M.; Cavallo, G.; Metrangolo, P.; Pace, A.; Pibiri, I.; Pilati, T.; Resnati, G.; Terraneo, G. *CrystEngComm* **2013,** *15* (16), 3102-3105; (b) Fox, D. B.; Liantonio, R.; Metrangolo, P.; Pilati, T.; Resnati, G. *J. Fluorine Chem.* **2004,** *125* (2), 271-281; (c) Fox, D.; Metrangolo, P.; Pasini, D.; Pilati, T.; Resnati, G.; Terraneo, G. *CrystEngComm* **2008,** *10* (9), 1132-1136.

31. (a) Metrangolo, P.; Meyer, F.; Pilati, T.; Proserpio, D. M.; Resnati, G. *Chem. Eur. J.* **2007,** *13* (20), 5765-5772; (b) Dey, A.; Metrangolo, P.; Pilati, T.; Resnati, G.; Terraneo, G.; Wlassics, I. *J. Fluorine Chem.* **2009,** *130* (9), 816-823.

32. Priimagi, A.; Cavallo, G.; Forni, A.; Gorynsztejn–Leben, M.; Kaivola, M.; Metrangolo, P.; Milani, R.; Shishido, A.; Pilati, T.; Resnati, G.; Terraneo, G. *Adv. Funct. Mater.* **2012,** *22* (12), 2572-2579.

33. Aakeroy, C. B.; Wijethunga, T. K.; Benton, J.; Desper, J. *Chem. Commun.* **2015,** *51* (12), 2425-2428.

34. (a) Rajput, L.; Singha, S.; Biradha, K. *Cryst. Growth Des.* **2007,** *7* (12), 2788-2795; (b) Nguyen, T. L.; Fowler, F. W.; Lauher, J. W. *J. Am. Chem. Soc.* **2001,** *123* (44), 11057-11064; (c) Lauher, J. W.; Fowler, F. W.; Goroff, N. S. *Acc. Chem. Res.* **2008,** *41* (9), 1215-1229; (d) Coe, S.; Kane, J. J.; Nguyen, T. L.; Toledo, L. M.; Wininger, E.; Fowler, F. W.; Lauher, J. W. *J. Am. Chem. Soc.* **1997,** *119* (1), 86-93; (e) Chang, Y. L.; West, M. A.; Fowler, F. W.; Lauher, J. W. *J. Am. Chem. Soc.* **1993,** *115* (14), 5991-6000.

Chapter 3 - Effect of π-π interactions on hydrogen and halogen bond driven co-crystallization

3.1 Introduction

3.1.1 Background

Synthetic strategies involved in crystal engineering mainly rely on "supramolecular synthons";[1] recognition patterns between different functional groups that give rise to different crystal packing motifs in solid state. Hydrogen bonds and halogen bonds are the two primary tools that produce these supramolecular synthons due to their strength and directionality, and also owing to their ability to be fine-tuned electronically and geometrically.[2] Aromatic stacking interactions, even though a more subtle interaction in terms of consistency and robustness, has been widely recognized for directing the aggregation of aromatic molecules in the solid state. Furthermore these π-π stacking interactions can exert substantial effects on the crystallization of molecular species in the solid state when combined with hydrogen bonding and halogen bonding.[3]

The stacking interactions between aromatic interactions are proposed to have contributions from electrostatic and van der Waals forces, however the relative effect of each force on the interaction is still in debate.[4] The factors that contribute to the nature of the π-π stacking interactions was first defined by Hunter and Sanders in terms of an electrostatic model based on σ – π attractions, where the aromatic ring with a quadrupole moment with a partially positive charged σ framework is sandwiched between two negatively charged quadrupole moments with π electron density above and below the molecular plane (Figure 3.1).[5] Thus, the interaction between two such molecules would be repulsive between the approaching π clouds (Figure 3.2a). A set of point charges is used to represent the electrostatic charge distribution and the electrostatic force is calculated based on the sum of charge-charge interactions between the two π systems (Figure 3.2b). These electrostatic effects mainly determine the geometry of the interaction. The van der Waals contribution to the interaction indicated by the interplanar separation is proportional to the surface area of π overlap between the aromatic molecules and it mainly contributes to the magnitude of the stacking interactions. Cozzi and Siegel, in a related

study[6], proposed a polar/π electrostatic model to rationale the arene-arene interactions in terms of molecular quadrupole moments.

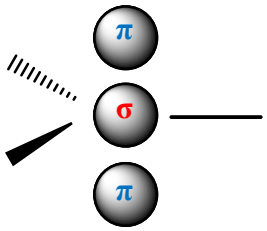

Figure 3.1 An sp^2 hybridized atom in a π-system[5]

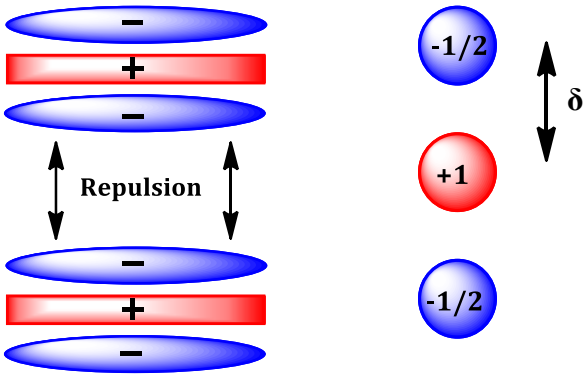

(a) (b)

Figure 3.2 (a) Interaction between two face-to-face π systems (b) electrostatic charge distribution of the π system[5]

Several geometries of the π-stacking interactions have been proposed based on the electrostatic component associated with the interaction in order to minimize the repulsive quadrupole-quadrupole interactions (Figure 3.3).[7] The edge-face, also known as CH-π interaction (Figure 3.3a) is usually observed with benzene in the solid state and aromatic residues in proteins.[8] In the off-set stacked arrangement (Figure 3.3b), which is commonly seen when the electron density of one or both the rings is reduced, has hydrophobic and van der Waals interactions prominent where the surface area is buried for the most part. The stacking interactions between DNA base pairs is governed by off-set stacking interactions.[9] The third geometry that a π system can display is face-to-face stacked orientation and it mostly occurs between π systems that have opposite quadrupoles in which the interactions become attractive (Figure 3.3c).

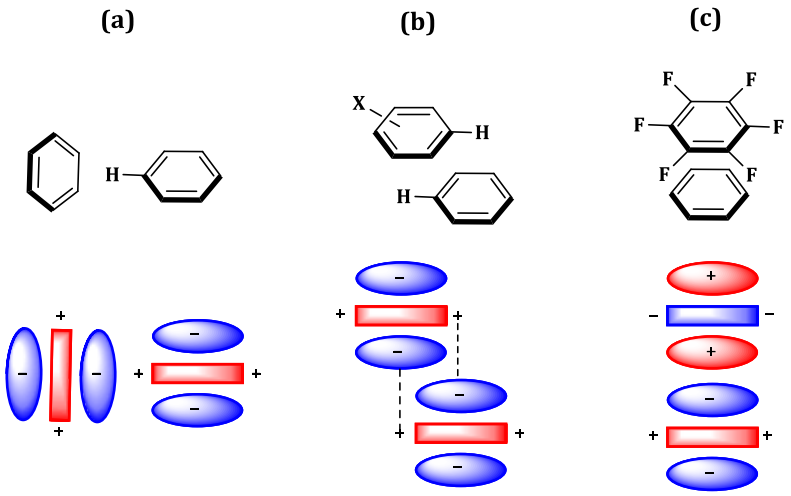

Figure 3.3 Geometries of aromatic interactions (a) edge-face (b) off-set stacked (c) face-to-face stacked[7]

A widely recognized association in this regard, is arene – perfluoroarene interactions where a pair of molecules comprise a face-to-face arrangement even though individual molecules arrange themselves in a herringbone (edge-face) pattern.[10] The π stacking interactions between such molecules are maximized with favorable quadrupole-quadrupole interactions which are comparable in magnitude but opposite in sign due to the electron withdrawing effect of the fluorinated ring. The arene-perfluoroarene interactions studied so far include, single aromatic rings and their derivatives (benzene vs hexafluorobenzene) or fused-ring poly aromatic compounds such as naphthalene, anthracene, phenanthrene and their fluorinated analogues.[11]

The crystal structure of benzene and hexafluorobenzene complex is composed of infinite parallel stacks of alternating **Ar(H)** and **Ar(F)** sequences of molecules suggesting that this is a reliable synthon in designing co-crystals (Figure 3.4).[12] Also, the complexes between hexafluorobenzene and various benzene derivatives (aromatic hydrocarbons and aromatic amines) and fused ring polyaromatic molecules also reveal face-to-face stacked conformation due to electrostatic contributions of the stacking interactions.[13]

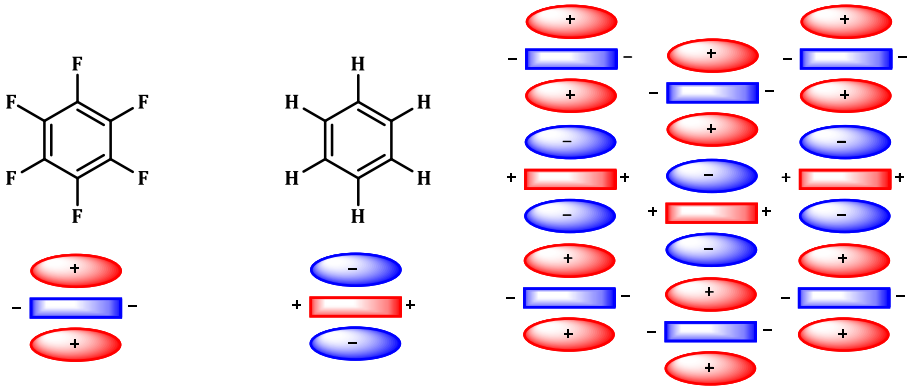

Figure 3.4 Schematic showing (a) quadrupoles of benzene and hexafluorobenzene and (b) the arrangement of parallel stacks of opposite charges[12]

The crystallization patterns of polynuclear aromatic hydrocarbons are classified into four basic structural types based on symmetry, C···C and C···H interactions and energetic criteria (Figure 3.5).[14] The simplest packing arrangement is herringbone motif where the C···H non-bonded interactions are between the nearest non-parallel neighbors. In the sandwich herringbone packing, the herringbone is made up of sandwich-like diads employed by C···C interactions and C···H interactions between parallel molecules. The third type is a flattened-out herringbone called γ structure in which the C···C interactions occur between parallel translated molecules. The fourth type contains 'graphitic' planes and is labeled a β structure stabilized by C···C interactions.[15]

However, when polynuclear aromatic hydrocarbons are combined with fluorinated analogues of arenes, infinite stacks of mixed parallel alternating arenes and perfluoroarenes are observed instead of the herringbone structure. These are not columnar, but slipped, and can be explained using several intermolecular parameters (Figure 3.6).[16]

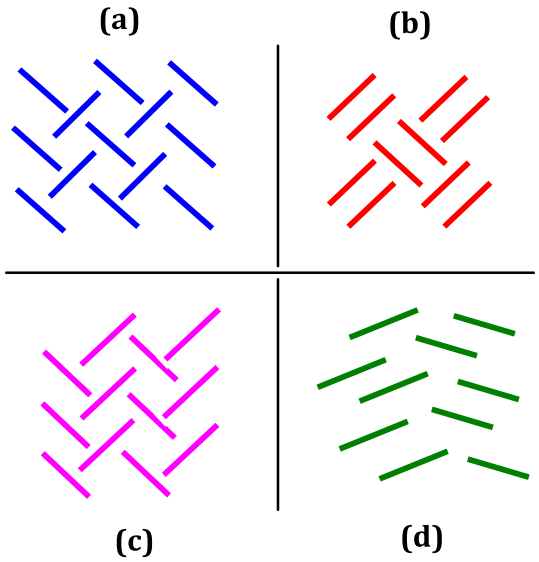

Figure 3.5 Schematics showing the packing arrangements of the four basic crystal packing of aromatic hydrocarbons (a) herringbone, (b) sandwich herringbone, (c) γ-structure and (d) β-structure

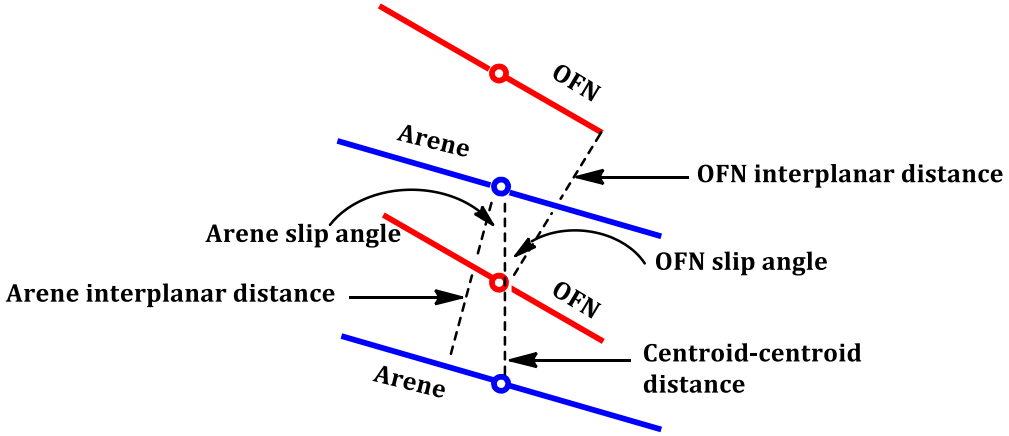

Figure 3.6 The schematic showing the intermolecular parameters to define the arene-perfluoroarene slipped parallel arrangements[16]

The packing mode between octafluoronaphthalene (OFN) and naphthalene, anthracene, phenanthrene, pyrene, triphenylene all show mixed stacks of alternating OFN and arene molecules, that are slipped (Figure 3.6) [13, 17] (defined by slip angle, 1.2-6.4˚ for OFN molecules and 1.5-9.1˚ for arene molecules) and the molecular planes of OFN-OFN and arene-arene are parallel to each other. Figure 3.7 shows packing diagram of OFN·anthracene and the intermolecular H···F distances are lower than the sum of the van der Waals radii. The dihedral

angles of the molecular planes of the above stated pairs range from 0.4-2.7˚. The inter-centroid distance between OFN-OFN and arene-arene are the same within the stack and is in the range of 6.73-6.81 Å which decreases with the increasing size of the polyarene.[16]

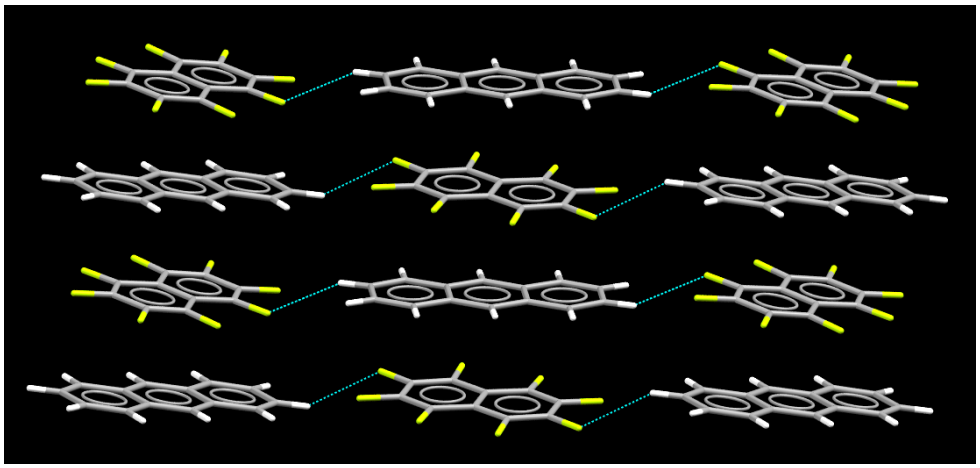

Figure 3.7 The packing diagram of OFN·naphthalene and the C-H···F-C distances are shown by dashed lines[16]

Fluorination of phenyl substituents lead to an increase of the displaced face-to-face contacts, limiting the edge-face interactions. The C–F group (‘‘organic fluorine’’) ‘‘… hardly ever accepts hydrogen bonds”[18] however form C–H···F-C weak interactions between neighboring fluorinated phenyl rings and non-fluorinated phenyl rings (Figure 3.8a). Also, fluorination facilitates F···F interactions that are weak due to the low polarizability of fluorine (Figure 3.8b).[19] These F···F interactions can be classified into two categories named, type I; which involves close packing and does not form stabilizing interactions and type II; which is formed through polarization of fluorine atoms. C-F···π interactions is another possibility that can influence the conformation and crystal packing in fluorinated systems.[20] These C-F···π interactions occur between electronegative fluorine and electropositive center of an aromatic ring (Figure 3.8c).

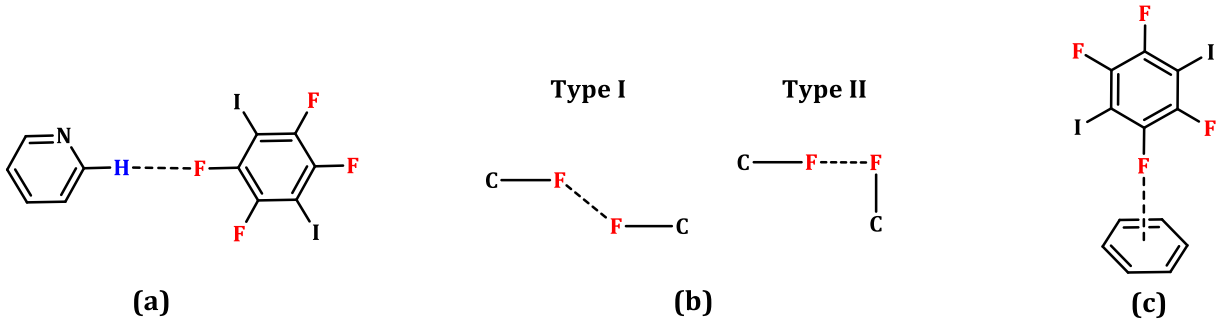

Figure 3.8 (a) C–H···F-C interactions (b) F···F interactions (c) C-F···π interactions

π stacking interactions are extensively studied as homomeric interactions between single aromatic units, however only a couple of studies have reported on the influence of these π-π interactions on binary systems. The interplay between hydrogen bonds and π-π interactions are studied in construction of different supramolecular assemblies.[21] Li *et al.* explored the importance of mutual influence between halogen bonds and π-π interactions in crystal packing.[22] To date, nothing has been reported on how π-π interactions affect the packing and stability of the hydrogen bonded and halogen bonded supramolecular architectures.

3.1.2 Stacking interactions in co-crystals of fluorinated and non-fluorinated hydrocarbons: Goals

In Chapter 2 we discussed the structural arrangements of a series of *bis*-acetamides (**A8**-**A0**) (Figure 3.9) with respect to aliphatic halogen bond donors. Herein we report a systematic structural study using aromatic halogen-bond donors and aromatic hydrogen bond donors to examine the effect of π-π interactions on the orientation of these chains of *bis*-acetamides in the binary co-crystals. This would potentially add insights into manipulation of supramolecular architectures in solid state with combined non-covalent interactions.

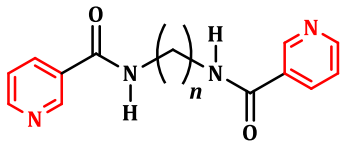

n = 8, 6, 4, 2, 0

Figure 3.9 3-Pyridyl *bis*-acetamides n = 8 (**A8**), 6 (**A6**), 4 (**A4**), 2 (**A2**), 0 (**A0**)

Two robust synthons are used in preparing these binary co-crystals, the OH(phenol)···N (py) hydrogen bonds and I···N (py) halogen bonds. The library of halogen and hydrogen bond donors contain fluorinated bromo and iodo halogen bond donors and *bis*-phenols are shown in Figure 3.10. The 3-pyridyl *bis*-acetamides are co-crystallized with these library of halogen bond donors in order to study the influence of the aromatic back bone on the structural arrangement of the co-crystals.

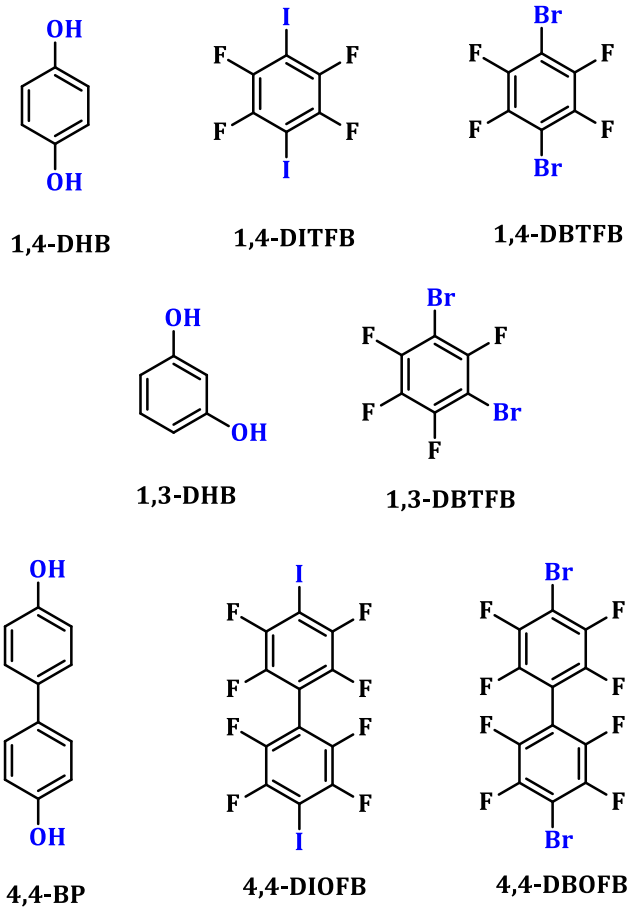

Figure 3.10 Scheme representing hydrogen- and halogen bond donor molecules, **1,4-DHB, 1,4-DITFB, 1,4-DBTFB, 1,3-DHB, 1,3-DBTFB, 4,4-BP**, **4,4-DIOFB** and **4,4-DBOFB**

We intend to address the following questions in this chapter.

i) Are aromatic hydrogen- and halogen bond donors capable of making the same robust architectures as discussed in Chapter 2?

ii) How does the weak aromatic interactions come into play in this process?

iii) Do fluorinated and non-fluorinated aromatics behave differently in the assembly of supramolecular architectures? Does fluorine segregation affect the crystal packing in the binary co-crystals?

iv) Can differences in crystal packing of fluorinated and non-fluorinated single components homomeric interactions be translated to the structure of binary co-crystals?

3.2 Experimental

3.2.1 Synthesis

All chemicals were purchased from were purchased from Aldrich, Combi blocks, Alfa Aeser and used without further purification. The ligands **A_8-A_0** were synthesized using the procedure reported in Chapter 2. ^1H, and ^{19}F NMR spectra were recorded on a Varian Unity plus 400 MHz or 200 MHz spectrometer in $CDCl_3$ or DMSO-d_6. Melting points/decomposition points were determined using Fisher-Johns melting point apparatus and are uncorrected. Infrared spectroscopy analysis was carried out using Nicolet 380 FT-IR with a digital resolution of 0.9 cm^{-1} and data processed using software, Omnic 8.0 © 1992-2008 Thermo Fisher Scientific Inc.

3.2.1.1 Synthesis of 4,4-octafluorodiiodobiphenyl, 44DIOFB

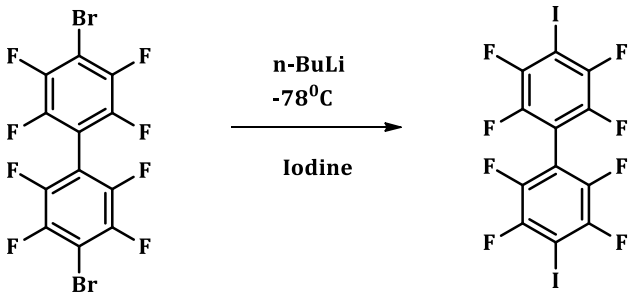

To an oven dried round bottomed flask purged with nitrogen, added 4,4-octaflurodibromobiphenyl (3.52 g, 7.72 mmol) and sealed with a rubber septum. Freshly distilled THF (150 mL) was added to the flask via cannula. This solution was then immersed in an dry ice-acetone bath (-78 ºC) for 5-7 minutes and afterwards *n*-butyl lithium, 1.6 M in hexanes (14.5 mL, 23.16 mmol) was slowly added through the septum under nitrogen upon which a white color solid starts to form. The solution was stirred for 20 minutes and afterwards iodine (5.87 g, 23.16 mmol) was added and the reaction mixture was slowly warmed up to room temperature. The reaction mixture was stirred overnight at room temperature and quenched with a saturated sodium thiosulfate solution to give a clear solution. The product was extracted with methylene chloride and dried over magnesium sulfate. The solvent removed under vacuum and to yield the crude **44DIOFB** as white solid. Recrystallization from methylene chloride:methanol 1:1 mixture produced colorless rod shaped crystals of **44DIOFB** with 64% yield. M.p. 142-144 ˚C (Reported M.p. 146-149 ˚C)[23] ^{19}F NMR (δ_F; 400 MHz, $CDCl_3$): 119.06 (m, 4F), 136.6 (m, 4F). IR: υ 1623, 1468, 1217, 953, 836, 715 cm^{-1}.

3.2.2 Synthesis of co-crystals

Bis-acetamide based ditopic acceptor ligands, **A$_0$**-**A$_8$** were subjected to co-crystallization experiments with a series of aromatic hydrogen and halogen bond donors: 1,4-dihydroxybenzene **14DHB**, 1,3-dihydroxybenzene **13DHB**, 4,4-bisphenol, **44BP** , 1,4-diiodotetrafluorobenzene **14DITFB**, 1,4-dibromotetrafluorobenzene **14DBTFB**, 1,3-dibromobenzene **13DBTFB**, 4,4-octafluorodiiodobiphenyl **44DIOFB**. Stoichiometric amounts of acceptor and the donor were mixed together and solvent assisted grinding were performed on all the 35 (5x7) combinations using a drop of methanol as the solvent until a solid paste was obtained. Single crystals suitable for X-ray diffraction were obtained by dissolving the solid paste from solvent assisted grinding in suitable solvents in borosilicate vials and carrying out slow evaporation (thirteen single crystals were obtained by using this method).

3.2.2.1 Synthesis of N,N-1,4-ethanediylbis-3-pyridinecarboxamide 4,4-bisphenol, A_2·44BP

N,N-1,2-Ethanediylbis-3-pyridinecarboxamide (0.010 g, 0.037 mmol) was dissolved in 1 mL of methanol. To this solution was added 4,4-bisphenol (0.007 g, 0.037 mmol) in 1 mL of methanol. The resulting solution was allowed for slow evaporation in a 2 dram borosilicate vial

at room temperature. Colorless prism-shaped crystals were obtained after five days. M.p. 225-227 ˚C.

3.2.2.2 Synthesis of N,N-1,4-butanediylbis-3-pyridinecarboxamide 1,4-dihydroxybenzene, A_4·1,4-DHB

N,N-1,4-Butanediylbis-3-pyridinecarboxamide (0.010 g, 0.032 mmol) was dissolved in 1 mL of methanol. To this solution was added 1,4-dihydroxybenzene (0.003 g, 0.032 mmol) in 1 mL of methanol. The resulting solution was allowed for slow evaporation in a 2 dram borosilicate vial at room temperature. Colorless plate-shaped crystals were obtained after two days. M.p. 216-218 ˚C.

3.2.2.3 Synthesis of N,N-1,4-butanediylbis-3-pyridinecarboxamide 4,4-bisphenol, A_4·44BP

N,N-1,4-Butanediylbis-3-pyridinecarboxamide (0.010 g, 0.032 mmol) was dissolved in 1 mL of methanol. To this solution was added 4,4-bisphenol (0.006 g, 0.032 mmol) in 1 mL of methanol. The resulting solution was allowed for slow evaporation in a 2 dram borosilicate vial at room temperature. Yellow color prism-shaped crystals were obtained after five days. M.p. 205-207˚C.

3.2.2.4 Synthesis of N,N-1,4-hexanediylbis-3-pyridinecarboxamide 4,4-bisphenol, A_6·44BP

N,N-1,6-Hexanediylbis-3-pyridinecarboxamide (0.010 g, 0.030mmol) was dissolved in 1 mL of methanol. To this solution was added 4,4-bisphenol (0.006 g, 0.030 mmol) in 1 mL of methanol. The resulting solution was allowed for slow evaporation in a 2 dram borosilicate vial at room temperature. Colorless plate-shaped crystals were obtained after three days. M.p. 192-195˚C.

3.2.2.5 Synthesis of N,N-1,4-octanediylbis-3-pyridinecarboxamide 1,4-dihydroxybenzene, A_8·1,4-DHB

N,N-1,8-Octanediylbis-3-pyridinecarboxamide (0.010 g, 0.028 mmol) was dissolved in 1 mL of methanol. To this solution was added 1,4-dihydroxybenzene (0.003 g, 0.028 mmol) in 1 mL of methanol. The resulting solution was allowed for slow evaporation in a 2 dram borosilicate vial at room temperature. Colorless plate-shaped crystals were obtained after seven days. M.p. 180-182 ˚C.

3.2.2.6 Synthesis of N,N-1,4-octanediylbis-3-pyridinecarboxamide 4,4-bisphenol, A_8·44BP

N,N-1,8-Octanediylbis-3-pyridinecarboxamide (0.010 g, 0.028 mmol) was dissolved in 1 mL of methanol. To this solution was added 4,4-bisphenol (0.005 g, 0.028 mmol) in 1 mL of methanol. The resulting solution was allowed for slow evaporation in a 2 dram borosilicate vial at room temperature. Colorless plate-shaped crystals were obtained after two days. M.p. 176-177 ˚C.

3.2.2.7 Synthesis of N,N-1,4-ethanediylbis-3-pyridinecarboxamide 1,4-diiodotetrafluorobenzene, A_2·1,4-DITFB

N,N-1,2-Ethanediylbis-3-pyridinecarboxamide (0.010 g, 0.037 mmol) was dissolved in 1 mL of methanol. To this solution was added 1,4-diiodotetrafluorobenzene (0.015 g, 0.037 mmol) in 1 mL of methanol. The resulting solution was allowed for slow evaporation in a 2 dram borosilicate vial at room temperature. Colorless prism-shaped crystals were obtained after seven days. Dec. 107 ˚C.

3.2.2.8 Synthesis of N,N-1,4-ethanediylbis-3-pyridinecarboxamide 1,4-dibromotetrafluorobenzene, A_2·1,4-DBTFB

N,N-1,2-Ethanediylbis-3-pyridinecarboxamide (0.010 g, 0.037 mmol) was dissolved in 1 mL of methanol. To this solution was added 1,4-dibromotetrafluorobenzene (0.011 g, 0.037 mmol) in 1 mL of methanol. The resulting solution was allowed for slow evaporation in a 2 dram borosilicate vial at room temperature. Colorless plate-shaped crystals were obtained after two days. Dec. 83˚C.

3.2.2.9 Synthesis of N,N-1,4-ethanediylbis-3-pyridinecarboxamide 4,4-diiodooctafluorobiphenyl, A_2·4,4-DIOFB

N,N-1,2-Ethanediylbis-3-pyridinecarboxamide (0.010 g, 0.037 mmol) was dissolved in 1 mL of methanol. To this solution was added 4,4-diiodooctafluorobiphenyl (0.020 g, 0.037 mmol) in 1 mL of methanol. The resulting solution was allowed for slow evaporation in a 2 dram borosilicate vial at room temperature. Colorless prism-shaped crystals were obtained after five days. Dec. 112˚C.

3.2.2.10 Synthesis of N,N-1,4-butanediylbis-3-pyridinecarboxamide 1,4-diiodotetrafluorobenzene, A_4*·1,4-DITFB*

N,N-1,4-Butanediylbis-3-pyridinecarboxamide (0.010 g, 0.032 mmol) was dissolved in 1 mL of methanol. To this solution was added 1,4-diiodotetrafluorobenzene (0.013 g, 0.032 mmol) in 1 mL of methanol. The resulting solution was allowed for slow evaporation in a 2 dram borosilicate vial at room temperature. Colorless prism-shaped crystals were obtained after two days. Dec. 94˚C.

3.2.2.11 Synthesis of N,N-1,4-butanediylbis-3-pyridinecarboxamide 1,4-dibromotetrafluorobenzene, A_4*·1,4-DBTFB*

N,N-1,4-Butanediylbis-3-pyridinecarboxamide (0.010 g, 0.032 mmol) was dissolved in 1 mL of methanol. To this solution was added 1,4-dibromotetrafluorobenzene (0.009 g, 0.032 mmol) in 1 mL of methanol. The resulting solution was allowed for slow evaporation in a 2 dram borosilicate vial at room temperature. Colorless prism-shaped crystals were obtained after five days. Dec. 79 ˚C.

3.2.2.12 Synthesis of N,N-1,4-butanediylbis-3-pyridinecarboxamide 1,3-dibromotetrafluorobenzene, A_4*·1,3-DBTFB*

N,N-1,4-Butanediylbis-3-pyridinecarboxamide (0.010 g, 0.032 mmol) was dissolved in 1 mL of methanol. To this solution was added 1,3-dibromotetrafluorobenzene (0.009 g, 0.032 mmol) in 1 mL of methanol. The resulting solution was allowed for slow evaporation in a 2 dram borosilicate vial at room temperature. Colorless plate-shaped crystals were obtained after seven days. Dec. 76˚C.

3.2.2.13 Synthesis of N,N-1,4-butanediylbis-3-pyridinecarboxamide 4,4-diiodooctafluorobiphenyl, A_4*·4,4-DIOFB*

N,N-1,4-Butanediylbis-3-pyridinecarboxamide (0.010 g, 0.032 mmol) was dissolved in 1 mL of methanol. To this solution was added 4,4-diiodooctafluorobiphenyl (0.017 g, 0.032 mmol) in 1 mL of methanol. The resulting solution was allowed for slow evaporation in a 2 dram borosilicate vial at room temperature. Colorless plate-shaped crystals were obtained after three days. M.p. 102-105 ˚C.

3.2.2.14 Synthesis of N,N-1,4-hexanediylbis-3-pyridinecarboxamide 1,4-diiodotetrafluorobenzene, *A_6·1,4-DITFB*

N,N-1,6-Hexanediylbis-3-pyridinecarboxamide (0.010 g, 0.030 mmol) was dissolved in 1 mL of methanol. To this solution was added 1,4-diiodotetrafluorobenzene (0.012 g, 0.030 mmol) in 1 mL of methanol. The resulting solution was allowed for slow evaporation in a 2 dram borosilicate vial at room temperature. Colorless prism-shaped crystals were obtained after five days. Dec. 87˚C.

3.2.2.15 Synthesis of N,N-1,4-hexanediylbis-3-pyridinecarboxamide 4,4-diiodooctafluorobiphenyl, *A_6·4,4-DIOFB*

N,N-1,6-Hexanediylbis-3-pyridinecarboxamide (0.010 g, 0.030 mmol) was dissolved in 1 mL of methanol. To this solution was added 4,4-diiodooctafluorobiphenyl (0.017 g, 0.030 mmol) in 1 mL of methanol. The resulting solution was allowed for slow evaporation in a 2 dram borosilicate vial at room temperature. Colorless prism-shaped crystals were obtained after two days. M.p. 152-154˚C.

3.3 Results

3.3.1 Crystal structure descriptions

A total of 15 crystal structures were obtained from solution experiments and the hydrogen bond geometries for all the co-crystals are shown in Table 3.1

Table 3.1 Hydrogen bond geometries for **A_2·4,4-BP**, **A_2·1,4-DITFB**, **A_2·1,4-DBTFB**, **A_2·4,4-DIOFB**, **A_4·1,4-DHB**, **A_4·4,4-BP**, **A_4·1,4-DITFB**, **A_4·1,3-DBTFB**, **A_4·1,4-DBTFB**, **A_4·4,4-DIOFB**, **A_6·4,4-BP**, **A_6·1,4-DITFB**, **A_6·4,4-DIOFB**, **A_8·1,4-DHB**, **A_8·4,4-BP**

Structure	D-H···A (Å)	d(D-H)/Å	d(H···A)/Å	d(D···A)/Å	<(DHA)/º
A_2·44BP [i]	N(17)-H(17)...O(37)	0.87(2)	1.95(2)	2.8091(15)	167.6(16)
	N(37)-H(37)...O(17)#4	0.911(18)	1.941(19)	2.8311(16)	165.0(15)
	O(51A)-H(51A)...N(11)	0.97(6)	1.85(5)	2.75(3)	153(5)
	O(51B)-H(51B)...N(11)	0.95(6)	1.85(5)	2.72(3)	150(6)
A_2·1,4-DITFB [ii]	N(17)-H(17)...O(17)#3	0.80(2)	2.04(2)	2.8037(16)	161(2)
A_2·1,4-DBTFB [iii]	N171-H171...N112#5	0.88	2.13	2.910(3)	147.5
	N172-H172...O171#6	0.88	2.05	2.814(2)	144.4
A_2·44DIOFB [iv]	N(17)-H(17)...O(27)#3	0.88	2.00	2.7710(18)	145.1
	N(27)-H(27)...O(47)	0.88	1.95	2.7790(18)	156.7
	N(47)-H(47)...O(17)#4	0.88	1.95	2.7742(18)	154.7
A_4·14DHB [v]	N(17)-H(17)...O(27)#3	0.902(12)	2.022(12)	2.9078(11)	166.8(11)
	N(27)-H(27)...O(17)#4	0.894(12)	2.016(12)	2.8957(11)	167.4(11)
	O(41)-H(41)...N(11)	0.846(16)	1.920(16)	2.7430(13)	163.7(15)
	O(51)-H(51)...N(21)	0.904(15)	1.865(15)	2.7411(13)	162.6(13)
A_4·44BP [vi]	N(17)-H(17)...O(27)#3	0.898(14)	2.028(14)	2.9096(11)	166.6(12)
	N(27)-H(27)...O(17)#4	0.894(14)	2.012(14)	2.8952(11)	169.3(12)
	O(41)-H(41)...N(11)	0.879(17)	1.912(17)	2.7460(13)	157.8(15)
	O(51)-H(51)...N(21)	0.913(16)	1.846(16)	2.7354(14)	164.3(14)
A_4·1,4-DITFB [vii]	N(17)-H(17)...O(17)#3	0.74(2)	2.23(2)	2.9630(15)	170(2)
A_4·1,3-BTFB [viii]	N171-H171...O174#5	0.88	1.96	2.816(7)	163.7
	N172-H172...O173#5	0.88	1.99	2.824(7)	157.8
	N173-H173...O171#6	0.88	2.00	2.856(7)	162.6
	N174-H174...O172#6	0.88	1.99	2.850(7)	163.7
A_4·1,4-DBTFB [ix]	N(17)-H(17)...O(17)#3	0.80(2)	2.08(2)	2.8684(16)	169.5(19)
A_4·44DIOFB [x]	N(17)-H(17)...O(27)#1	0.87(4)	2.13(4)	2.904(3)	149(4)
	N(27)-H(27)...O(17)#2	1.01(4)	1.99(4)	2.947(3)	157(3)
A_6·44BP [xi]	N(17)-H(17)...O(27)#3	0.880(12)	2.032(12)	2.8992(9)	168.1(11)
	N(27)-H(27)...O(17)#4	0.872(12)	2.058(12)	2.9141(9)	166.9(11)
	O(41)-H(41)...N(11)	0.928(14)	1.837(14)	2.7374(11)	162.9(12)
	O(51)-H(51)...N(21)	0.885(14)	1.898(14)	2.7510(11)	161.3(13)
A_6·14DITFB [xii]	N(17)-H(17)...N(11)#3	0.88	2.09	2.896(4)	152.8
A_6·44DIOFB [xiii]	N(17)-H(17)...O(17)#3	0.82(2)	2.16(2)	2.971(2)	173(2)
	N(37)-H(37)...O(37)#4	0.83(2)	2.15(2)	2.963(2)	167(2)
A_8·14DHB [xiv]	O(31)-H(31)...N(11)	1.05(5)	1.74(5)	2.750(5)	162(4)
	N(17)-H(17)...O(17)#3	0.94(5)	2.00(5)	2.927(4)	168(4)
A_8·44BP [xv]	N(17)-H(17)...O(27)#3	0.866(14)	2.066(14)	2.9193(13)	168.1(13)
	N(27)-H(27)...O(17)#4	0.851(14)	2.062(15)	2.9028(13)	169.1(14)
	O(41)-H(41)...N(11)	0.834(17)	1.966(17)	2.7503(15)	156.3(16)
	O(51)-H(51)...N(21)	0.879(17)	1.883(17)	2.7365(15)	163.3(15)

Symmetry transformations used to generate equivalent atoms

i) #1 -x,-y,-z+1 #2 -x+1,-y+1,-z+1 #3 -x+1,-y+2,-z+2 #4 x,y+1,z **ii)** #1 -x+1,-y,-z+1 #2 -x,-y+1,-z+2 #3 x,-y+1/2,z+1/2 **iii)** #1 -x-1,-y,-z #2 -x+2,-y,-z+1 #3 -x+2,-y+1,-z #4 -x+2,-y+1,-z+1 #5 x-1,y,z #6 -x+1,-y,-z **iv)** #1 -x+1/2,-y-1/2,-z+1 #2 -x,y,-z+3/2 #3 -x+1/2,y+1/2,-z+1/2 #4 -x+1/2,-y+1/2,-z+1 **v)** #1 -x+2,-y+1,-z #2 -x-1,-y,-z+2 #3 -x+1,-y,-z+1 #4 -x,-y+1,-z+1 **vi)** #1 -x,-y,-z+2 #2 -x+1,-y+3,-z #3 -x+1,-y+1,-z+1 #4 -x,-y+2,-z+1 **vii)** #1 -x+1,-y+1,-z+2 #2 -x,-y+2,-z #3 -x+1,y-1/2,-z+3/2 **viii)** #1 -x+1,y+1/2,-z+1/2 #2 -x+1,y-1/2,-z+1/2 #3 -x+1,-y+2,-z+1 #4 -x+1,-y+1,-z+1 #5 x-1,-y+3/2,z-1/2 #6 x+1,y,z **ix)** #1 -x+1,-y+2,-z+1 #2 -x+1/2,-y+3/2,-z #3 x,-y+1,z-1/2 **x)** #1 x,y-1,z #2 x-1,y,z **xi)** #1 -x,-y-1,-z #2 -x+1,-y+2,-z+2 #3 -x+1,-y,-z+1 #4 -x,-y+1,-z+1 **xii)** #1 -x+1,-y,-z+1 #2 -x+2,-y,-z #3 x+1/2,-y+1/2,z+1/2 **xiii)** #1 -x-2,-y+1,-z-1 #2 -x+3,-y,-z+2 #3 x-1,y,z #4 x+1,y,z **xiv)** #1 -x+1,-y+2,-z+1 #2 -x+2,-y,-z #3 x+1,y,z **xv)** #1 -x,-y-1,-z #2 -x+1,-y+2,-z+2 #3 -x+1,-y,-z+1 #4 -x,-y+1,-z+1

3.3.2 Crystal structures

3.3.2.1 Crystal structures of A_2·14DITFB, A_4·14DITFB and A_6·14DITFB

The crystal structures of **A_2·14DITFB** and **A_4·14DITFB** show halogen bond formation resulting 1-D infinite chains which are then cross-linked in an orthogonal manner forming 3-D doubly interpenetrated (4,4) networks (Figure 3.11 a and b). However, the crystal structure of **A_6·14DITFB** does not display the expected amide ladder, instead two major interactions are responsible for the formation of the 3-D co-crystal; C=O···I halogen bonds and N-H···N hydrogen bonds (Figure 3.11 c).

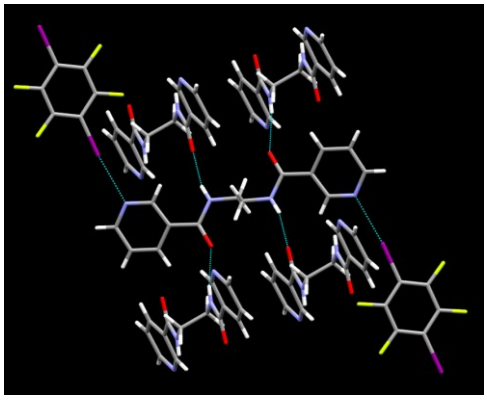

(a)

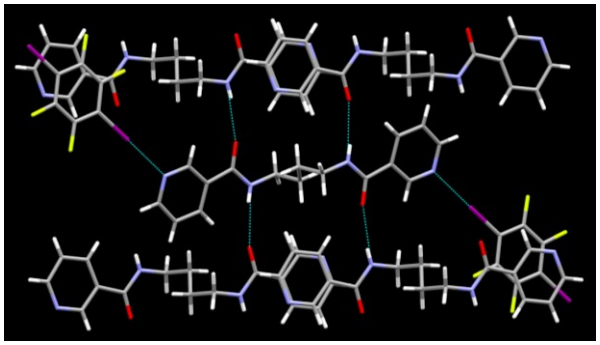

(b)

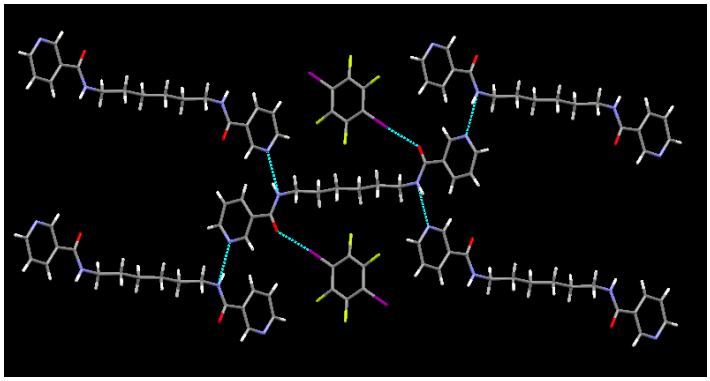

(c)

Figure 3.11 Hydrogen and halogen bond formation in the co-crystals (a) **A_2·14DITFB** (b) **A_4·14DITFB** (c) **A_6·14DITFB**

In **A_2·14DITFB** the **14DITFB** molecules form infinite columns in *bc* plane organizing themselves into a γ-structure (Figure 3.12 a). In contrast assembly of parallel stacks of off-set **14DITFB** molecules are seen in **A_6·14DITFB** (Figure 3.12 b). Neither structure show stacking between the donor and acceptor. However, in **A_4·14DITFB**, face-to-face stacking of infinite planar parallel layers of alternate pyridine and **14DITFB** molecules is observed, Figure 3.13 (mean interplanar separation ~ 3.38 - 3.39 Å).

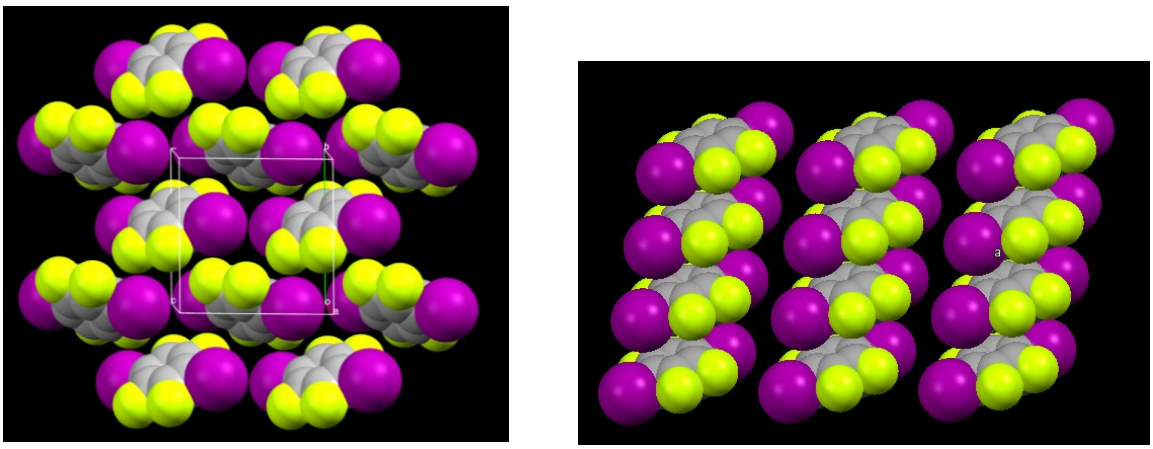

(a) (b)

Figure 3.12 Space filling model representing crystal packing of **14DITFB** molecules in the crystal lattice of (a) **A_2·14DITFB** (b) **A_6·14DITFB**

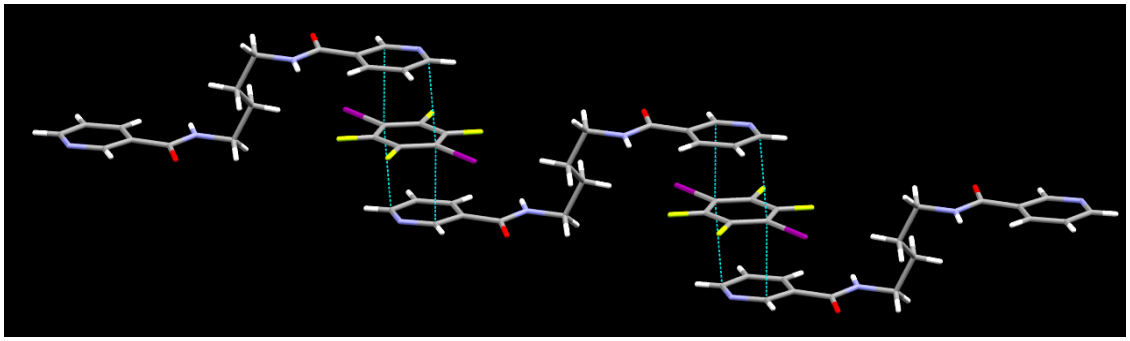

Figure 3.13 Face-to-face stacking in **A₄·14DITFB**

3.3.2.2 Crystal structure of A_2·14DBTFB and A_4·14DBTFB

A₄·14DBTFB arrange into a 4,4 3-D network with halogen bonds and self-complementary amide linkages Figure 3.14 a. The crystal structure of **A₂·14DBTFB**, however does not display the amide ladder, instead several interactions are responsible for the formation of the co-crystal. Br···N(py) and Br···O=C halogen bonds make infinite 1-D chains and N-H···N(py), N-H···O=C hydrogen bonds yield a 3D network Figure 3.14 b. The **14DBTFB** molecules organize into a γ-structure with infinite columns, along *bc* plane in **A₄·14DBTFB** and *ab* and *ac* planes in **A₂·14DBTFB** (Figure 3.15). Further, off-set stacking interactions were observed between **A₂** molecules in **A₂·14DBTFB** (Figure 3.16).

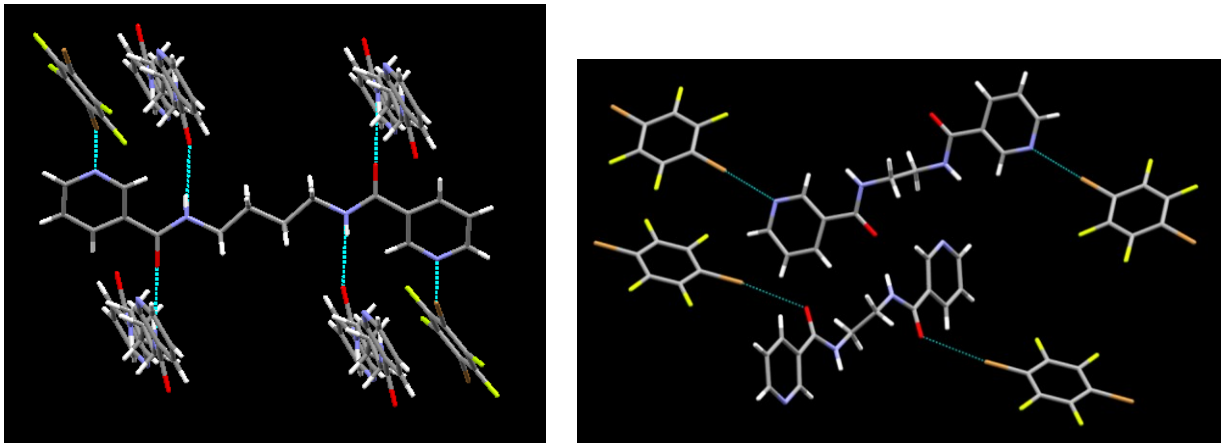

(a) (b)

Figure 3.14 (a) Infinite 1D chains produced by halogen bonds (b) space filling model representing the γ structure of **14DBTFB** molecules

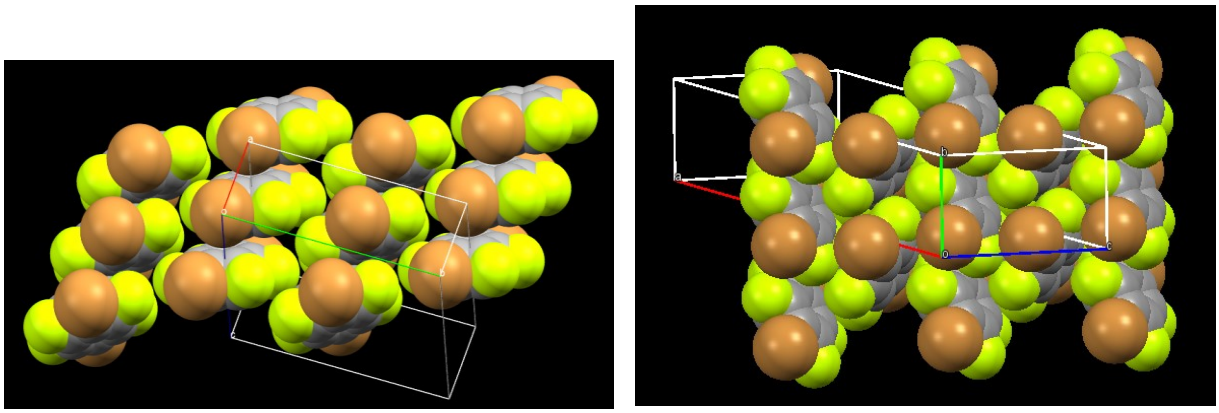

(a) (b)

Figure 3.15 Space filling model representing γ-structure of **14DBTFB** molecules in the crystal lattice of (a) **A_2·14DBTFB** (b) **A_4·14DBTFB**

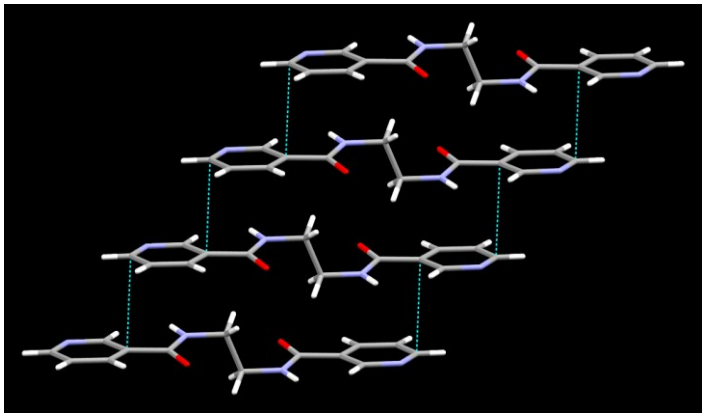

Figure 3.16 Off-set stacking interactions between **A_2** molecules in **A_2·14DBTFB**

3.3.2.3 Crystal structure of A_2·44DIOFB, A_4·44DIOFB, A_6·44DIOFB

All three crystal structures show I···N(py) halogen bonds and amide linkages in the lattice (Figure 3.18). Stacking interactions between the donor and the acceptor could be observed in all three cases (Figure 3.18). Edge-face interactions are seen between **44DIOFB** and **A_2** molecules with a mean distance of 3.06 Å and 3.00 Å which is less than sum of van der Waals radii, 3.17 Å (Figure 3.18 a). Face-to-face stacking interactions are present between **A_4** and **44DIOFB** molecules (Figure 3.18 b) similar to **A_4·14DITFB**. There are edge-face stacking interactions between **A_6** and **44DIOFB** with a separation of 3.00 Å (Figure 3.18 c).

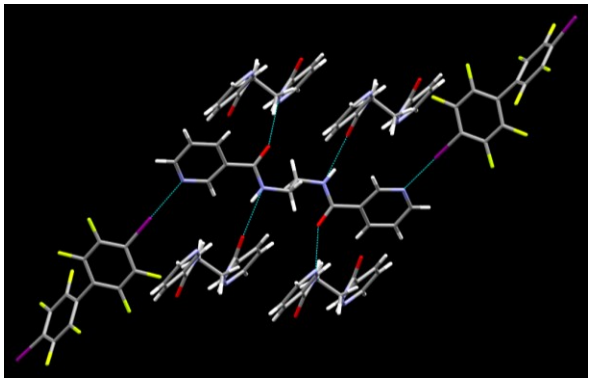

(a)

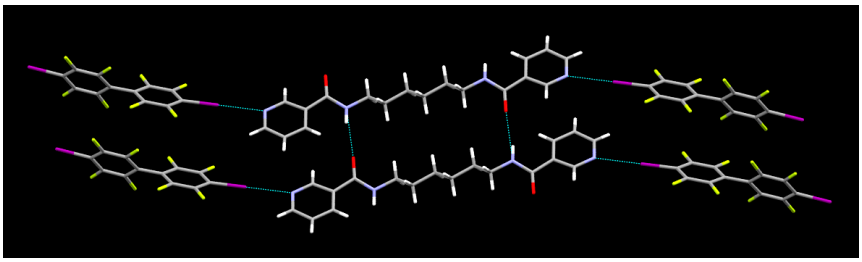

(b)

Figure 3.17 I···N(py) halogen bonds and amide linkages in (a) **A_2·44DIOFB** and (b) **A_6·44DIOFB**

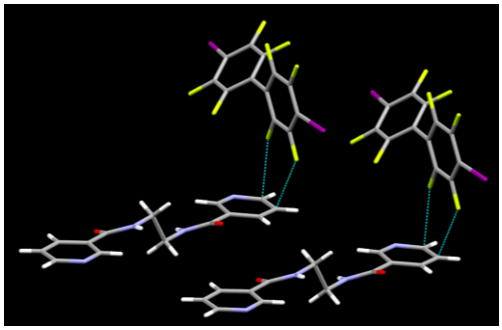

(a)

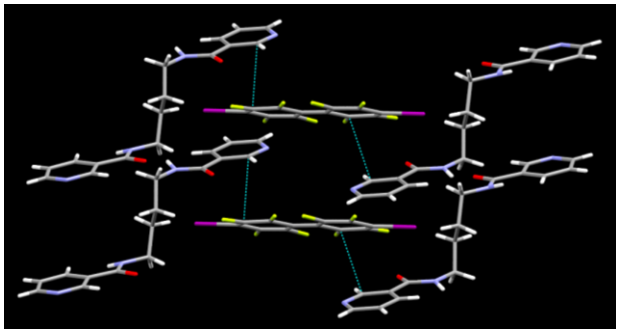

(b)

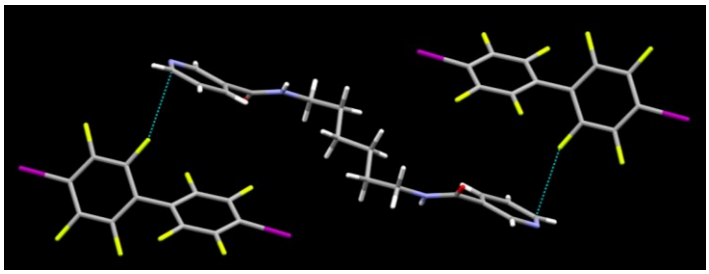

(c)

Figure 3.18 (a) Edge-face interactions in **A_2·44DIOFB** (b) face-to-face interactions in **A_4·44DIOFB** (c) edge-face interactions in **A_6·44DIOFB**

The **14DIOFB** molecules, form a γ-structure in **A_2·44DIOFB** in the *bc* plane arranging into infinite columns (Figure 3.19 a), parallel stacks in the *ab* plane forming off-set stacking interactions in **A_4·44DIOFB** crystal lattice (Figure 3.19 b) and a γ-structure in **A_6·44DIOFB** in the *ab* plane, Figure 3.19 c.

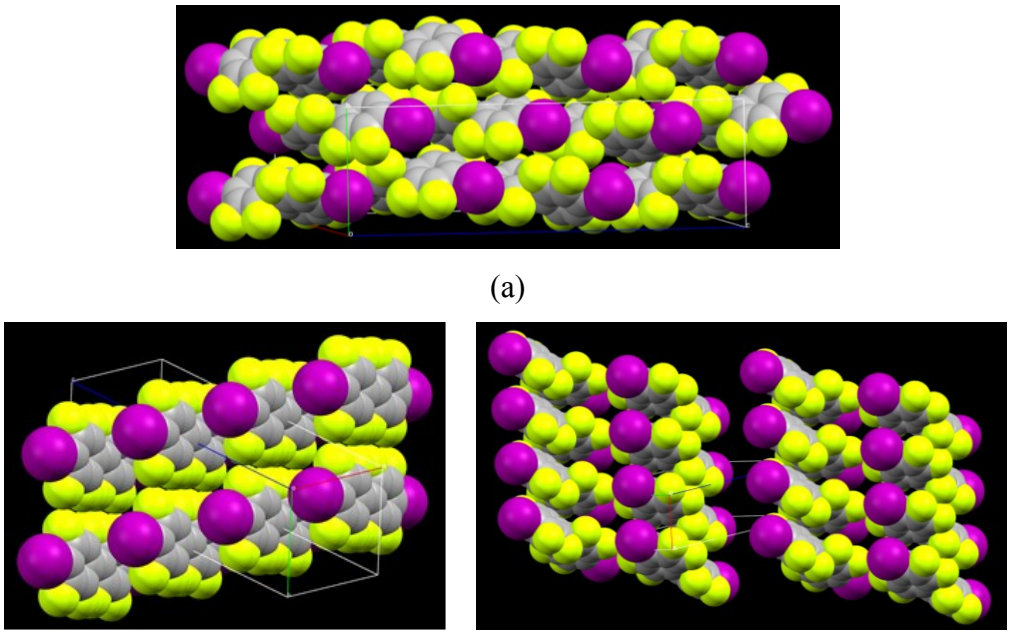

(a) (b) (c)

Figure 3.19 Space filling representation of **44DIOFB** molecules in (a) **A_2·44DIOFB** γ-structure along the *bc* plane (b) **A_4·44DIOFB** - parallel stacks in the *ab* plane forming off-set stacking (c) **A_6·44DIOFB** γ-structure along the *ab* plane

3.3.2.4 Crystal structure of A_4·13DBTFB

The crystal structure of **A_4·13DBTFB** shows Br···N(py) halogen bond formation and C=O···H-N hydrogen bonds to form doubly interpenetrated (4,4) network (Figure 3.20 a). The **13DBTFB** molecules form a γ-structure along the *b* direction extending into columns in the *ac* plane (Figure 3.20 b). Neither the individual **A_4** molecules nor **A_4** and **13DBTFB** molecules had stacking interactions.

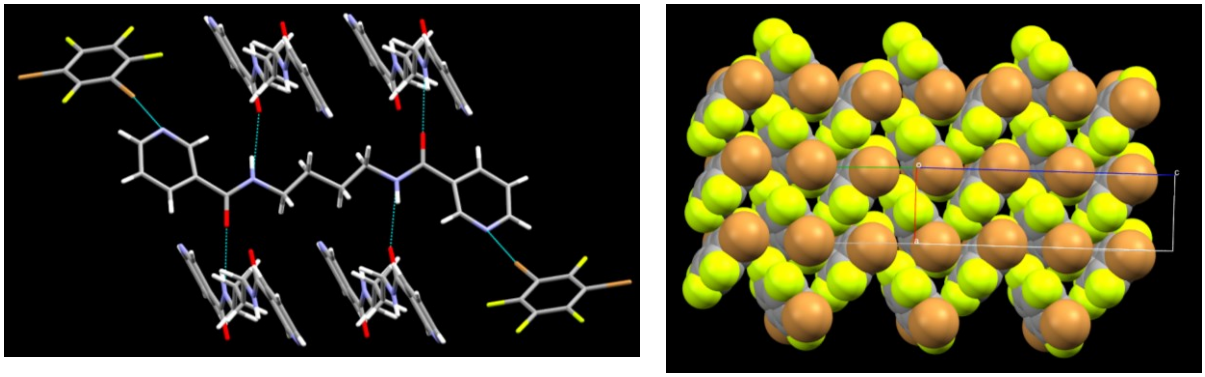

(a) (b)

Figure 3.20 (a) Interpenetrated 3-D network formed by Br···N(py) halogen bonds and C=O···H-N hydrogen bonds (b) space filling model representing the γ-structure formed between individual **13DBTFB** molecules.

3.3.2.5 Crystal structure of A_4·14DHB and A_8·14DHB

The crystal structure of **A_4·14DHB** shows OH···N (py) and N-H···O=C hydrogen bonding to produce 1-D infinite chains which are then cross-linked to form 2-D network (Figure 3.21 a). The **14DHB** molecules in **A_4·14DHB**, stack to form a γ-structure along the *c* direction extending into 2-D columns in the *ab* plane, Figure 3.22 a. In **A_8·14DHB**, the **14DHB** molecules are arranged in parallel stacks along the *a* direction forming infinite columns in the *ab* plane with off-set stacking (Figure 3.22 b). Also, there are off-set π-π stacking interactions between **A_4** molecules in **A_4·14DHB** (Figure 3.23). No stacking interactions observed between the donor and the acceptor.

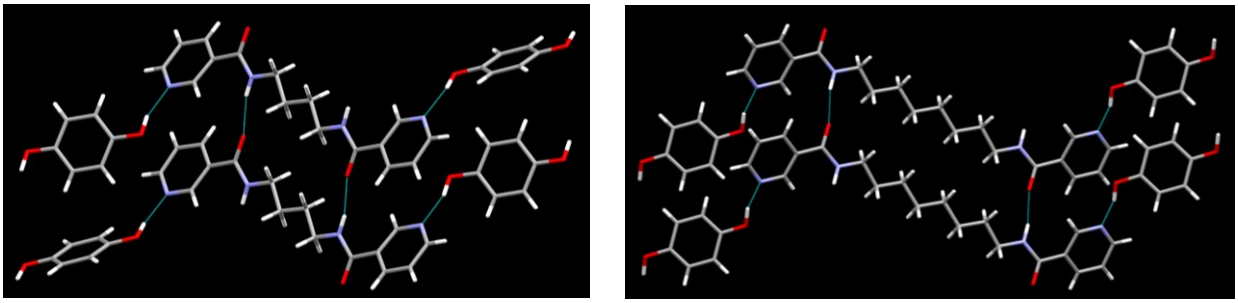

(a) (b)

Figure 3.21 1-D chains formed via OH···N hydrogen bonds which are extended into 2-D amide ladder via C=O···H-N hydrogen bonds

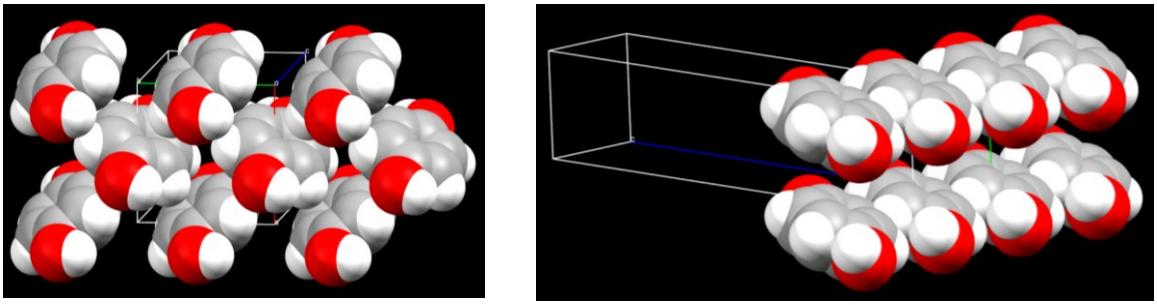

(a) (b)

Figure 3.22 Space filling model representing the arrangement of **14DHB** molecules (a) γ-structure in **A₄·14DHB** (b) parallel stacks forming off-set stacking in **A₈·14DHB**

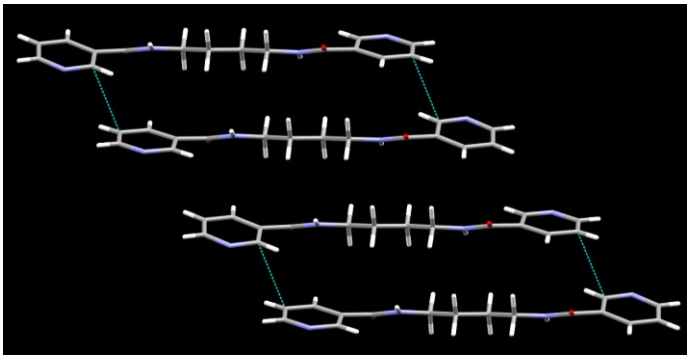

Figure 3.23 Off-set stacking interactions between **A₄** molecules in the crystal lattice of **A₄·14DHB**

3.3.2.6 Crystal structure of *A_2·44BP,* *A_4·44BP,* *A_6·44BP,* *A_8·44BP*

All four crystal structures show OH···N (py) hydrogen bonds and 1-D infinite chains which are then oriented in an orthogonal manner resulting in a (4,4) network in **A₂·44BP** (Figure 3.24 a) and 2-D amide ladders in **A₄·44BP**, **A₆·44BP** and **A₈·44BP** (Figure 3.24 bcd). As far as the packing of **44BP** molecules goes, in **A₂·44BP**, the **44BP** rings arrange into infinite parallel stacks in the *ab* plane as shown in Figure 3.25 a. The **44BP** molecules in all other three structures form a herringbone structure along the *c* direction stacking into columns in the *ab* plane (Figure 3.25 bcd).

The ligands in **A₄·44BP**, **A₆·44BP** and **A₈·44BP** interact with each other via off-set stacking interactions (Figure 3.26) with a separation of 3.37 Å, 3.37 Å and 3.389 Å respectively. In **A₂·44BP**, where there are no stacking interactions between **44BP** molecules, edge-face stacking interactions are observed between **A₂** and **BP** with a separation of 2.73 Å, Figure 3.27.

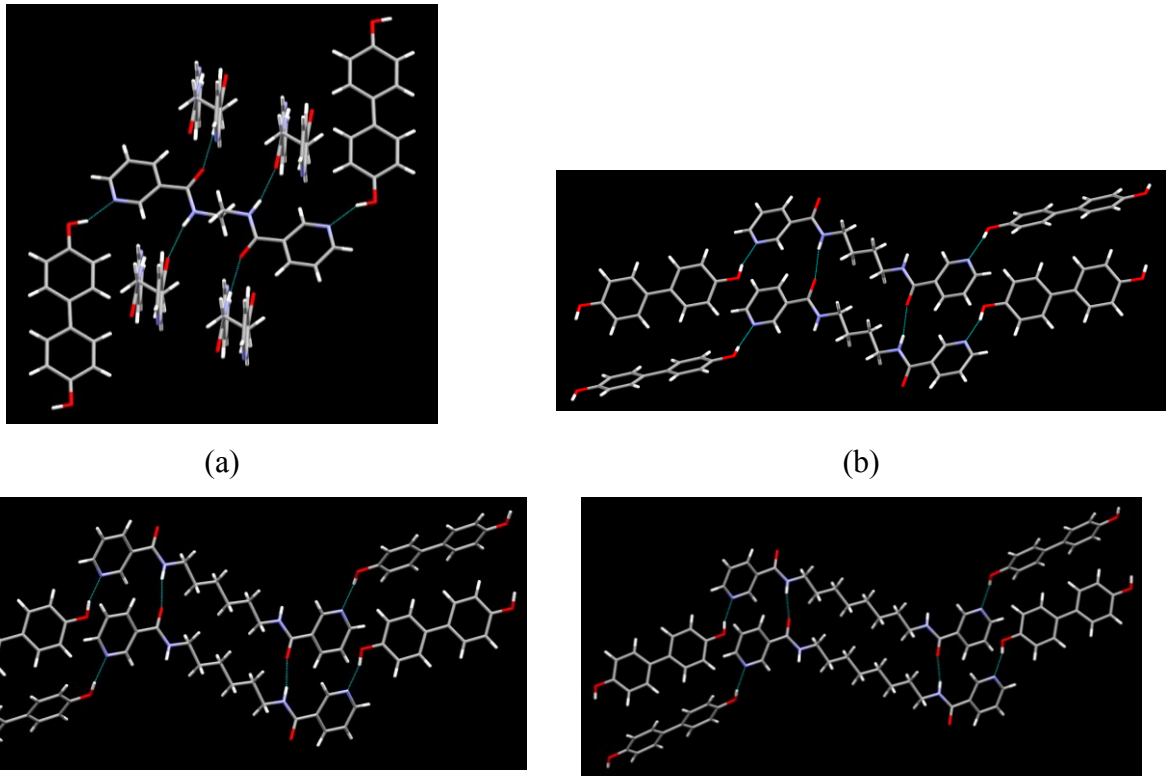

(a) (b)

(c) (d)

Figure 3.24 Part of the crystal structure showing OH···N (py) and C=O···N-H hydrogen bonding interactions resulting (a) (4,4) network in **A_2·44BP** and amide ladder in (b) **A_4·44BP** (c) **A_6·44BP and** (d) **A_8·44BP**

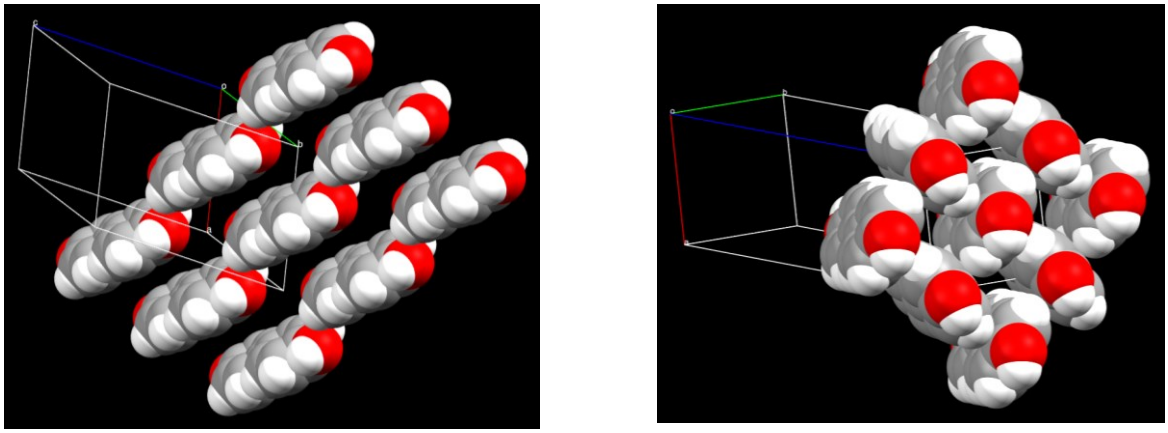

(a) (b)

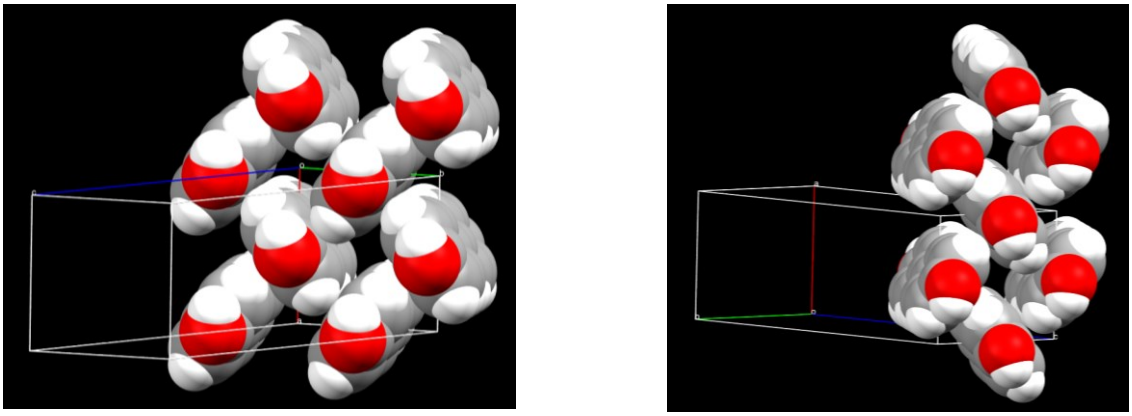

(c) (d)

Figure 3.25 Space filling representation of **44BP** molecules (a) parallel stacks in **A_2·44BP** (b)(c)(d) herringbone structure in **A_4·44BP, A_6·44BP** and **A_8·44BP**

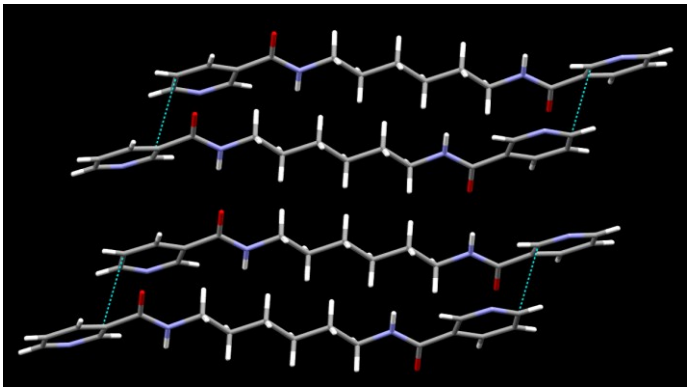

Figure 3.26 Off-set stacking interactions between **A_6**

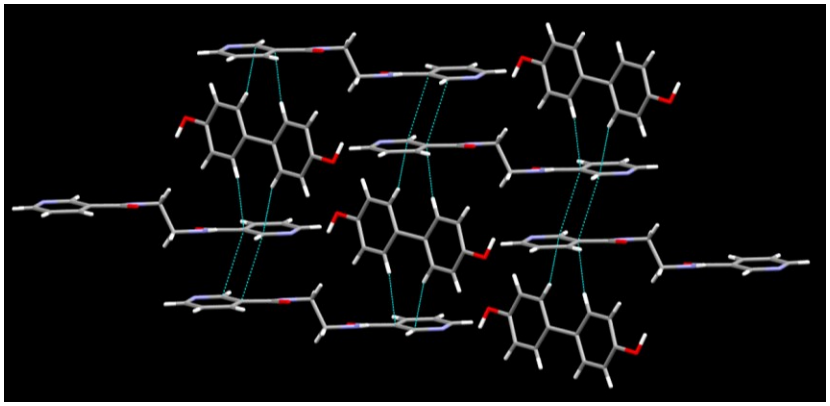

Figure 3.27 Edge-face stacking interactions between **A_2** and **44BP**

3.4 Discussion

3.4.1 Characterization by IR spectroscopy

3.4.1.1 Halogen bonded co-crystals

The distinction between reaction and no reaction of the 25 experiments that we carried out, was made based on shifts of various modes in the infrared region associated primarily with C-F bonds of the halogen bond donors (Table 3.2) and C-H bonds of the acceptors. As discussed in Chapter 2, we observed both red shifts and blue shifts of IR bands of the co-crystals with these aromatic halogen bond donors. 14/25 experiments show co-crystal formation with a red shift in the range of (1-20 cm^{-1}) due to the charge transfer from the pyridine ring during halogen-bond formation. Our results are in accordance to the literature data, where the stretching modes of the co-crystals shift to lower wave numbers due to halogen-bond formation.[24]

Table 3.2 IR stretching frequencies (cm^{-1}) of halogen bonded co-crystals of ligands **A_0-A_8**

	14DITFB (1456,938, 757) cm^{-1}		**14DBTFB (1480, 952,786) cm^{-1}**		**13DBTFB (1488,1083,895, 742) cm^{-1}**		**44DIOFB (1468, 954,715) cm^{-1}**		**44DBOFB (1463, 956,720) cm^{-1}**	
	Co-crystal (cm^{-1})	Δ (cm^{-1})	Co-crystal (cm^{-1})	Δ (cm^{-1})	Co-crystal (cm^{-1})	Δ (cm^{-1})	Co-crystal (cm^{-1})	Δ (cm^{-1})	Co-crystal (cm^{-1})	Δ (cm^{-1})
A_8	1458 937 756	+2 -1 -1	1473 957 787	-7 +5 +1	1485 1086 894	-3 +3 -1	1467 945	-1 -9	1465 960 714	+2 +4 -6
A_6	1461 941 758	+5 +3 +1	1472 944	-8 -8	1486 1080 895	-2 -3 0	1465 952 717	-3 -2 +2	1467 956 717	+4 0 -3
A_4	1455 935 750	-1 -3 -7	1474 954 784	-6 +2 -2	1480 1072 891	-8 -11 -4	1448 944 713	-20 0 0	1466 956 718	+3 0 -2
A_2	1453 942 756	-3 +4 -1	1476 952 789	-4 0 +3	1482 1083 898	-6 0 +3	1459 952 715	-9 -2 0	1467 957 705	+4 +1 -15
A_0	1460 936 754	+4 -2 -3	1482 952 787	+2 0 +1	1486 1084 898	-2 +1 +3	1464 952 716	-4 -2 +1	1464 956 721	+1 0 +1

Among the halogen bond donors, **44DBOFB** does show co-crystal formation with blue shifts in the IR, however it did not form co-crystals from solution experiments as the donor always precipitated as a single component. The ligand, **A_0** precipitate as a monohydrate in the solution experiments.

3.4.1.2 Hydrogen bonded co-crystals

The solids obtained from the grinding experiments of each of the four ligands with the three aromatic hydrogen bond donors were analyzed via IR spectroscopy paying particular attention to intermolecular OH···N hydrogen bonding interactions. However the broad stretches that appear near 2500 and 1900 cm^{-1} were not very prominent for the phenolic OH unlike for carboxylic acid in most of the cases. Grinding experiments of **A_0 – A_8** with **13DHB** always gave a sticky solid, which was evidence of a reaction taking place and these showed prominent OH···N interactions in the IR spectrum, Figure 3.28. The vibrational modes of the N-heterocyclic XB acceptor moiety was taken into consideration when determining a positive co-crystal event, because the C-H stretching modes (~3073-3039 cm^{-1}) and other characteristic vibrations (~1470 cm^{-1}) associated with the pyridine ring are also affected by hydrogen bond formation due to the reduced electron density in the pyridine ring. This is reflected by a blue shift of these stretches by 2-14 cm^{-1} wave numbers, Table 3.3.

.

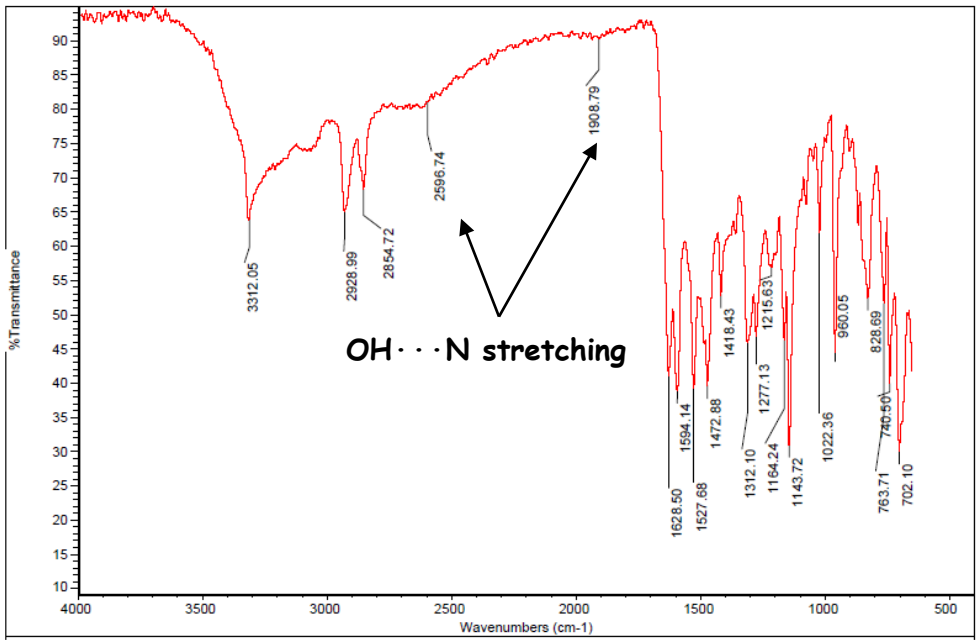

Figure 3.28 IR spectrum of **A_8·13DHB** grinding showing OH···N hydrogen bonding

Table 3.3 IR stretching frequencies (cm^{-1}) of hydrogen bonded co-crystals of ligands **A_0-A_8**

Ground mixture	OH···N (cm^{-1}) (1800-2500)	C-H(py) (cm^{-1}) **A_8**; 3039 ,1474 **A_6**; 3046, 1476 **A_4**; 3073, 1476 **A_2**; 3073, 1475 **A_0**; 3075, 1476	
A_0·13DHB	-	3078	1474
A_0·14DHB	-	3075	1477
A_0·44BP	2486, 1854	3074	1480
A_2·13DHB	2647,1960	3077	1473
A_2·14DHB	-	3079	1463
A_2·44BP	-	3087	1481
A_4·13DHB	2560,1920	-	1486
A_4·14DHB	-	3086	1473
A_4·44BP	2450, 1980	3072	1477
A_6·13DHB	2520,1850	3054	1471
A_6·14DHB	-	-	1473
A_6·44BP	2500,1980	3052	1474
A_8·13DHB	2590, 1950	-	1473
A_8·14DHB	-	-	-
A_8·44BP	-	3042	1476

3.4.2 Do aromatics produce the same robust architectures as aliphatic donors?

The *bis*-acetamide ligand consists of two HB/XB acceptors (Figure 3.29a) which gives the HB/XB donor two options, pyridine N and carbonyl O. In Chapter 2 we demonstrated that, with aliphatic ditopic halogen bond donors, the pyridine N atom acts as the only halogen bond acceptor while the amide produces self-complementary hydrogen bonds (Figure 3.29b).

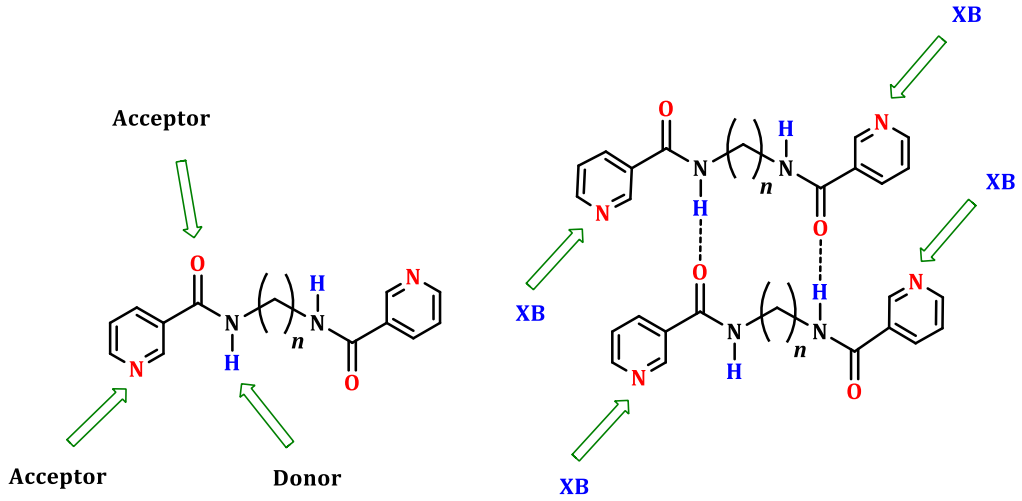

(a) (b)

Figure 3.29 (a) Possible donor and acceptor sites of *bis*-acetamide ligand (b) binding preferences observed in Chapter 2

With aromatic hydrogen and halogen-bond donors, pyridine N, 6/8 times acts as the halogen bond acceptor and 8/8 times as the hydrogen bond acceptor (Figure 3.30). Therefore, the results are in agreement with Chapter 2 and aromatic hydrogen and halogen bond donors are capable of making the same robust architectures. In the remaining cases, 2/8 times (**A_6·14DITFB**, Figure 3.11c and **A_2·14DBTFB**, Figure 3.14b), carbonyl O acts as the halogen bond acceptor disrupting the amide linkage based network Figure 3.30a.

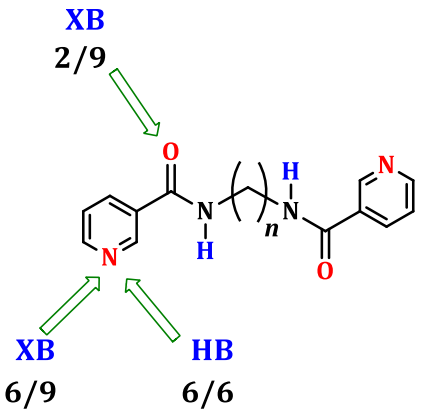

Figure 3.30 Illustration of the success rate of (a) halogen bond (XB) formation and (b) hydrogen bond (HB) formation with N(py) and C=O

3.4.3 Structural role played by aromatic stacking interactions

The stacking interactions between aromatic components is classified into three main categories as edge-face, off-set stacked and face-to-face interactions, where the aromatic-aromatic interactions between the donor (D) and the acceptor (A) could possibly stack into one or more different categories (Figure 3.31). The edge-face interactions are further categorized under four main crystal packing types, Figure 3.32. Based on the crystal packing of all 15 crystal structures, we analyzed each structure individually to determine the stacking interactions between acceptors, between donors and between acceptor and donor molecules.

3.4.3.1 Halogen-bonded co-crystals

The results shows that aromatic donor molecules tend to stack together by themselves into separate 2-D columns within the crystal lattice via stacking interactions. In halogen bonded co-crystals 89% of the structures show stacking between fluorinated donor molecules. From this 89%, edge-face stacking (γ-structure) seems to be the most stable packing arrangement giving rise to 75% of the structures. Off-set stacking interactions are observed for 25% of the time of the structures. We only observe 44% stacking interactions between the donor and the acceptor (edge-face and face-to-face stacking) and only 11% stacking interactions between the acceptor molecules. Figure 3.33 and Table 3.4 summarizes these results.

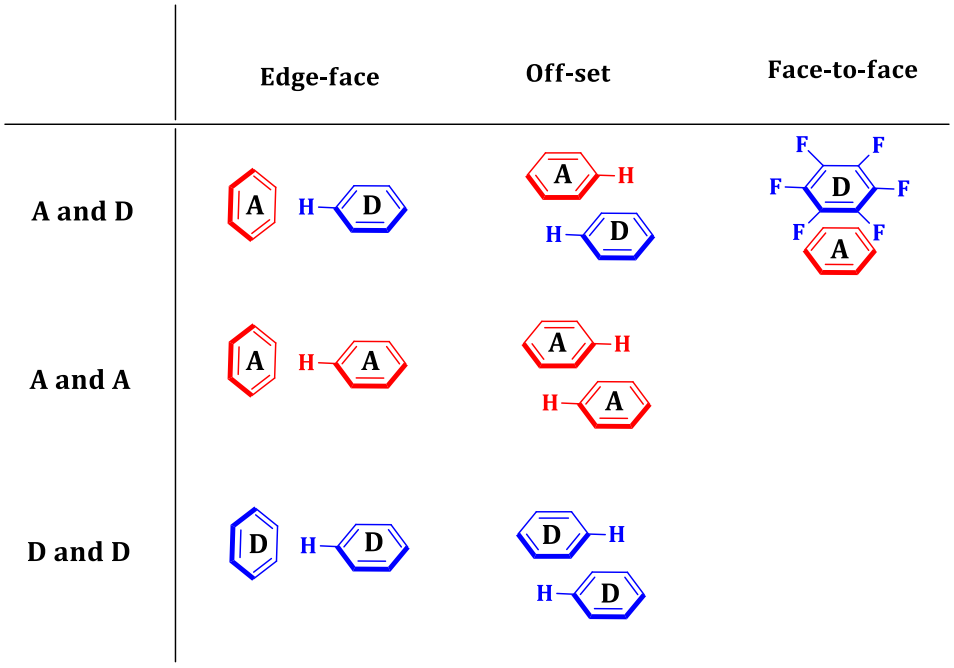

Figure 3.31 Different possibilities of stacking between the donor (D) and the acceptor (A)

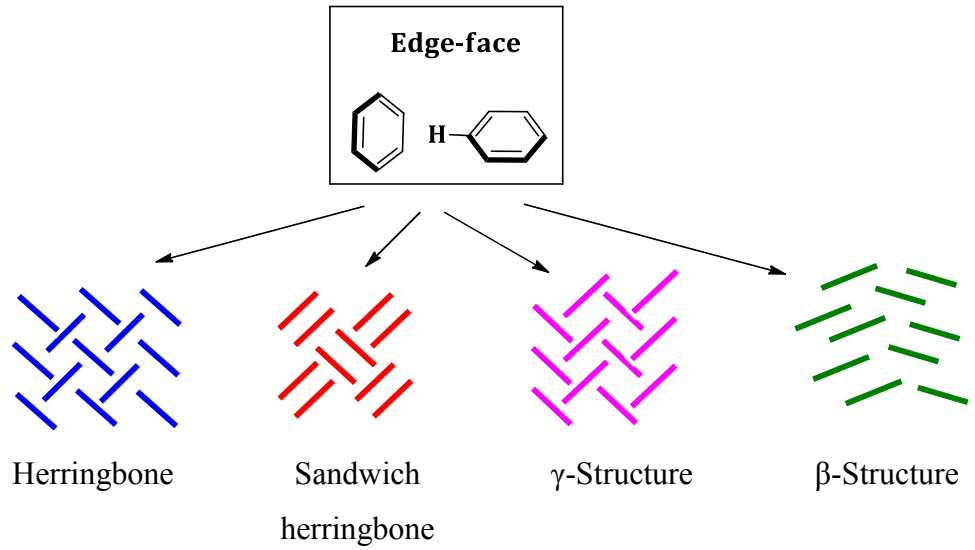

Figure 3.32 The basic structural types of edge-face stacking

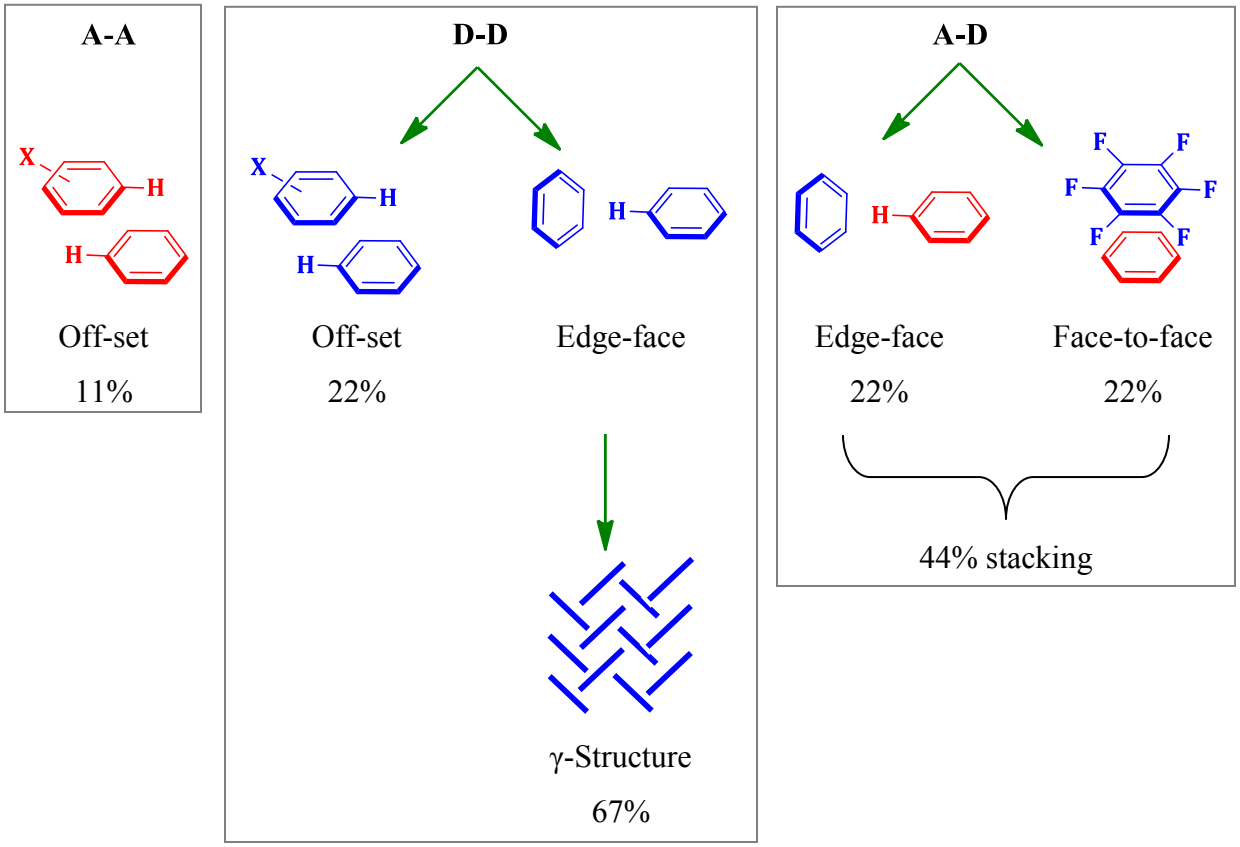

Figure 3.33 Halogen bonded co-crystals - stacking interactions between A-A, D-D and A-D

Table 3.4 Halogen bonded co-crystals - stacking interactions between A-A, D-D and A-D

Structure	A-A	D-D	A-D
A_2·14DITFB	No stacking	Edge-face (γ-structure)	No stacking
A_4·14DITFB	No stacking	No stacking	Face-to-face
A_6·14DITFB	No stacking	Off-set stacking	No stacking
A_2·14DBTFB	Off-set stacking	Edge-face (γ-structure)	No stacking
A_4·14DBTFB	No stacking	Edge-face (γ-structure)	No stacking
A_4·13DBTFB	No stacking	Edge-face (γ-structure)	No stacking
A_2·44DIOFB	No stacking	Edge-face (γ-structure)	Edge-face
A_4·44DIOFB	No stacking	Off-set stacking	Face-to-face
A_6·44DIOFB	No stacking	Edge-face (γ-structure)	Edge-face
Overall results	**11 % stacking**	**89% stacking** (67% γ-structure 22% off-set stacking)	**44% stacking**

3.4.3.2 Effect of fluorination on crystal packing

The fluorinated aromatic halogen bond donors influence crystal packing via three types of fluorine contacts in these co-crystals, listed in Table 3.5. Edge-face stacking interactions are mostly governed by C-F···C contacts, between the donor and the acceptor. C-F···H-C contacts are the most frequently observed contacts between the donor and the C-H(py) of the acceptor (Figure 3.34a). C-F···F-C contacts are responsible for packing of the aromatic halogen bond donors into off-set arrangement or a γ-structure. Both type I and type II fluorine contacts or either one was observed in the crystal packing (Figure 3.34b).

Table 3.5 Fluorine contacts of the co-crystals

Co-crystal	Type of F contact/s
A_2·14DITFB	C-F···H-C
A_4·14DITFB	C-F···H-C
A_6·14DITFB	C-F···H-C
A_2·14DBTFB	C-F···C
A_4·14DBTFB	C-F···H-C C-F···F-C
A_4·13DBTFB	C-F···H-C C-F···F-C C-F···C
A_2·44DIOFB	C-F···C
A_4·44DIOFB	C-F···C
A_6·44DIOFB	C-F···C C-F···F-C C-F···H-C

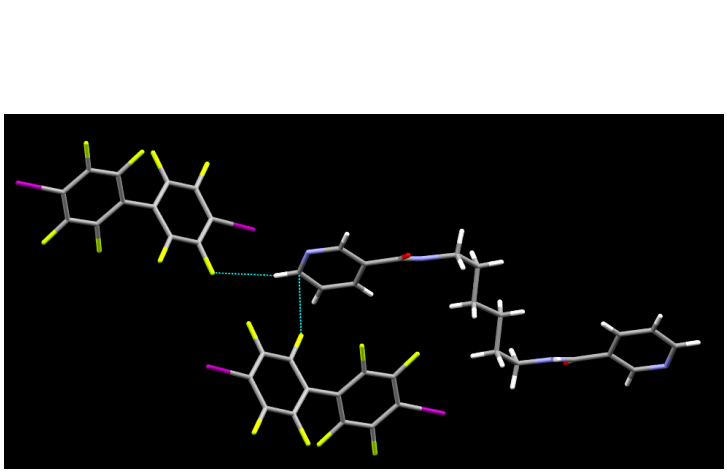

(a)

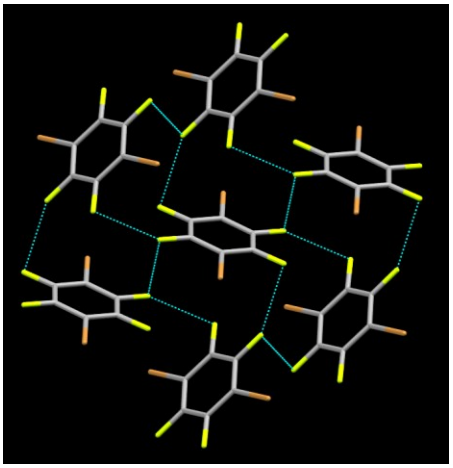

(b)

Figure 3.34 (a) C-F···C contacts and C-F···H-C contacts in **A_6·44DIOFB** (b) type I and type II C-F···F-C contacts between **14DBTFB** molecules in **A_4·14DBTFB**

3.4.3.3 Hydrogen-bonded co-crystals

In the case of hydrogen-bonded co-crystals, again we see 100% stacking between the donor molecules, 66% edge-face (50% herringbone and 17% γ-structure) stacking, being the most stable packing arrangement and 33% off-set stacking interactions. Stacking between acceptor molecules seemed to be favorable with the hydrogen bonded co-crystals (83% off-set stacking), however, stacking between A-D is furthermore only 17%, similar to the halogen bonded co-crystals.

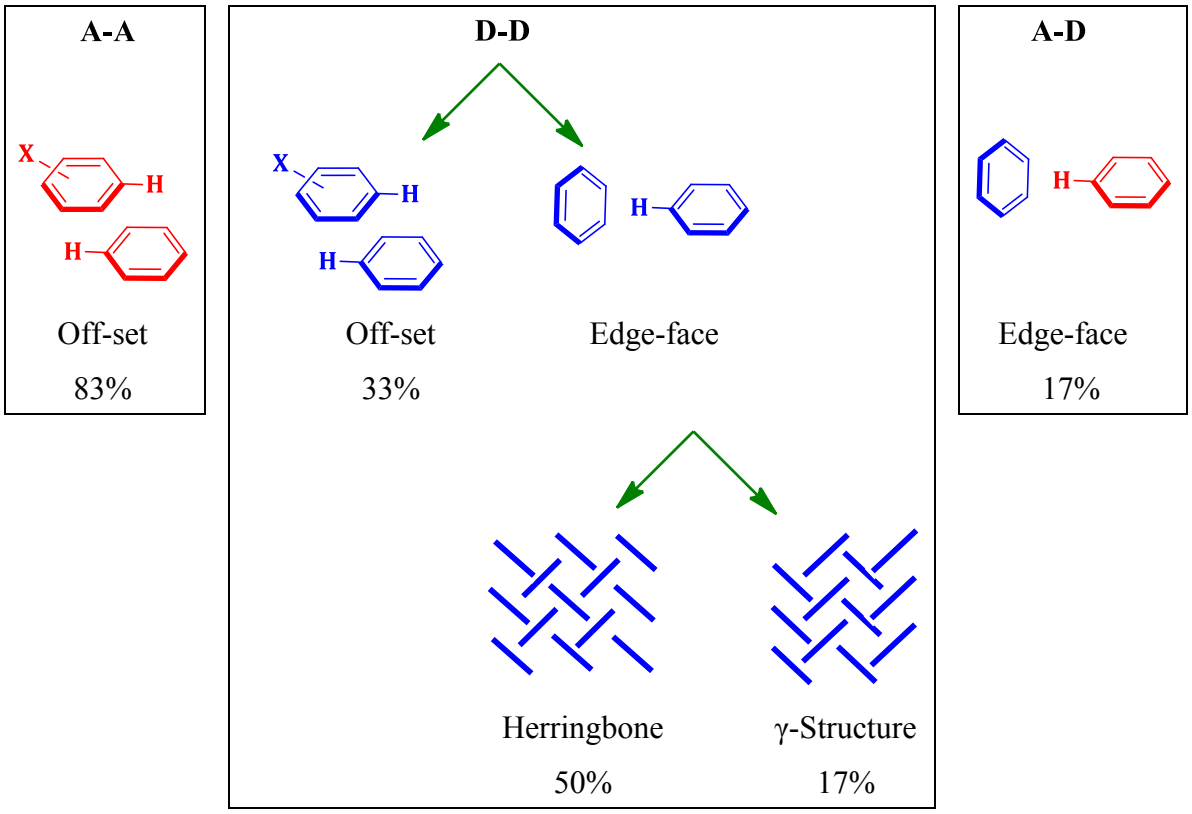

Figure 3.35 Hydrogen bonded co-crystals - stacking interactions between A-A, D-D and A-D

3.4.3.4 How does our system compare with literature data?

Even though it may be expected in this binary system, that the electron rich pyridine ring interacts with the electron deficient halogen bond donors via face-to-face stacking as the most stable crystal packing arrangement, we observe only 2/9 of the structures following this behavior. On the other hand, the packing arrangement of the single donors are reproduced in the binary co-crystal system as the herringbone structure or the γ-structure. Reported to date, the face-to-face stacking of electron rich and electron deficient aromatic rings occurs for most single

component assemblies[25] as well as for binary co-crystal assemblies.[21-22, 26] In these cases the shapes of arene and perfluoroarene molecules were geometrically close matched or moderately different. Moreover, Gdaniec *et al*[26c] showed that, some degree of size and shape compatibility between the supramolecular substrates is necessary to allow effective aryl–perfluoroaryl stacking within the molecular complexes. The ligands **A_0-A_8**, in which the pyridine rings are separated by methylene units, are not compatible in size, shape and geometry with that of the individual donor molecules in order to undergo face-to-face stacking interactions, thus the donor molecules adopt the most favorable crystal packing arrangement that they can achieve, which is a γ-type packing in the binary co-crystal lattice with the aid of weak F contacts. Similar results were observed with hydrogen bonded co-crystals where stacking between the donor and the acceptor was minimum, and the aromatic hydrogen donors adopt either a herringbone or a γ-structure as the most stable packing arrangement reproduced in the crystal lattice presumably due to the lack of size, shape and geometric complementarity between the donor and the acceptor.

Table 3.6 Hydrogen bonded co-crystals - stacking interactions between A-A, D-D and A-D

Structure	A-A	D-D	A-D
A_4-14DHB	Off-set stacking	Edge-face (γ-structure)	No stacking
A_8-14DHB	No stacking	Off-set stacking	No stacking
A_2-44BP	Off-set stacking	Off-set stacking	Edge-face
A_4-44BP	Off-set stacking	Edge-face (herringbone)	No stacking
A_6-44BP	Off-set stacking	Edge-face (herringbone)	No stacking
A_8-44BP	Off-set stacking	Edge-face (herringbone)	No stacking
Overall results	**83% stacking**	**100% stacking** (33% Off-set stacking 17% γ-structure 50% herringbone)	**17% stacking**

The weak F contacts do affect the crystal packing as the A-D stacking is higher in halogen-bonded co-crystals compared to the hydrogen-bonded co-crystals. The C-F···C and C-F···H-C contacts assist the face-to-face and edge-face interactions between the donor and the acceptor of the halogen-bonded co-crystals, which the hydrogen-bonded co-crystals are not privileged of during crystal packing. Thus aggregation between the individual donor and acceptor molecules dominates in the hydrogen bonded co-crystals.

3.5 Conclusion

Our results demonstrate that aromatic hydrogen- and halogen bond donors are capable of forming robust supramolecular architectures via OH···N(py) and I···N(py) synthons, similar to the aliphatic hydrogen- and halogen bond donors. The weak aromatic interactions come into play during the assembly of the co-crystals by aggregation of the individual aromatic donors and acceptors into 2-D columns rather than stacking interactions between the donor and the acceptor. This reveals that effective stacking interactions between donor-acceptor pair can only occur by having some degree of size, shape and geometric compatibility between the two molecules. Fluorine aggregation affect the crystal packing, thus the stacking interactions between A-A, D-D and A-D differs in halogen bonded and hydrogen bonded co-crystals. Given that no stacking interactions take place between the donor and the acceptor, the homomeric interactions between the single components can be thus translated into the structure of the binary co-crystals.

3.6 References

1. Desiraju, G. R. *Angew. Chem. Int. Ed. Engl.* **1995,** *34* (21), 2311-2327.

2. (a) Saccone, M.; Cavallo, G.; Metrangolo, P.; Pace, A.; Pibiri, I.; Pilati, T.; Resnati, G.; Terraneo, G. *CrystEngComm* **2013,** *15* (16), 3102-3105; (b) Rissanen, K. *CrystEngComm* **2008,** *10* (9), 1107-1113; (c) Reynisson, J.; McDonald, E. *J. Comput. Aided Mol. Des.* **2004,** *18* (6), 421-431.

3. Swierczynski, D.; Luboradzki, R.; Dolgonos, G.; Lipkowski, J.; Schneider, H.-J. *Eur. J. Org. Chem.* **2005,** *2005* (6), 1172-1177.

4. Martinez, C. R.; Iverson, B. L. *Chem. Sci.* **2012,** *3* (7), 2191-2201.

5. Hunter, C. A.; Sanders, J. K. M. *J. Am. Chem. Soc.* **1990,** *112* (14), 5525-5534.

6. Cozzi, F.; Cinquini, M.; Annunziata, R.; Dwyer, T.; Siegel, J. S. *J. Am. Chem. Soc.* **1992,** *114* (14), 5729-5733.

7. Waters, M. L. *Curr. Opin. Chem. Biol.* **2002,** *6* (6), 736-741.

8. (a) Perutz, M. F.; Fermi, G.; Abraham, D. J.; Poyart, C.; Bursaux, E. *J. Am. Chem. Soc.* **1986,** *108* (5), 1064-1078; (b) McGaughey, G. B.; Gagné, M.; Rappé, A. K. *J. Biol. Chem.* **1998,** *273* (25), 15458-15463.

9. (a) Tuma, J.; Connors, W. H.; Stitelman, D. H.; Richert, C. *J. Am. Chem. Soc.* **2002,** *124* (16), 4236-4246; (b) Wheeler, S. E.; Bloom, J. W. G. *J. Phys. Chem. A* **2014,** *118* (32), 6133-6147.

10. Gavezzotti, A.; Desiraju, G. R. *Acta Crystallogr., Sect. B: Struct. Sci.* **1988,** *44* (4), 427-434.

11. (a) Kilbinger, A. F. M.; Grubbs, R. H. *Angew. Chem.* **2002,** *114* (9), 1633-1636; (b) Collings, J. C.; Batsanov, A. S.; Howard, J. A. K.; Marder, T. B. *Cryst. Eng.* **2002,** *5* (1), 37-46; (c) Smith, C. E.; Smith, P. S.; Thomas, R. L.; Robins, E. G.; Collings, J. C.; Dai, C.; Scott, A. J.; Borwick, S.; Batsanov, A. S.; Watt, S. W.; Clark, S. J.; Viney, C.; Howard, J. A. K.; Clegg, W.; Marder, T. B. *J. Mater. Chem.* **2004,** *14* (3), 413-420; (d) Dai, C.; Nguyen, P.; B. Marder, T.; B. Marder, T.; J. Scott, A.; Clegg, W.; Viney, C.; Viney, C. *Chem. Commun.* **1999,** (24), 2493-2494.

12. Hunter, C. A.; Lawson, K. R.; Perkins, J.; Urch, C. J. *J. Chem. Soc., Perk. Trans. 2* **2001,** (5), 651-669.

13. Collings, J. C.; Roscoe, K. P.; Robins, E. G.; Batsanov, A. S.; Stimson, L. M.; Howard, J. A. K.; Clark, S. J.; Marder, T. B. *New J. Chem.* **2002,** *26* (12), 1740-1746.

14. Desiraju, G. R.; Gavezzotti, A. *Acta Crystallogr., Sect. B: Struct. Sci.* **1989,** *45* (5), 473-482.

15. Desiraju, G. R.; Gavezzotti, A. *J. Chem. Soc., Chem. Commun.* **1989,** (10), 621-623.

16. Collings, J. C.; Roscoe, K. P.; Thomas, R. L.; Batsanov, A. S.; Stimson, L. M.; Howard, J. A. K.; Marder, T. B. *New J. Chem.* **2001,** *25* (11), 1410-1417.

17. Potenza, J.; Mastropaolo, D. *Acta Crystallogr., Sect. B: Struct. Sci.* **1975,** *31* (10), 2527-2529.

18. Dunitz, J. D.; Taylor, R. *Chem. Eur. J.* **1997,** *3* (1), 89-98.

19. Pauling, L. C. The Nature of the Chemical Bond. *Documentary History* 1960.

20. Prasanna, M. D.; Guru Row, T. N. *Cryst. Eng.* **2000,** *3* (2), 135-154.

21. Piotrkowska, B.; Gdaniec, M.; Milewska, M. J.; Polonski, T. *CrystEngComm* **2007,** *9* (10), 868-872.

22. Li, H.; Lu, Y.; Liu, Y.; Zhu, X.; Liu, H.; Zhu, W. *PCCP* **2012,** *14* (28), 9948-9955.

23. Deacon, G.; Smith, R. *Aust. J. Chem.* **1982,** *35* (8), 1587-1597.

24. (a) Walsh, R. B.; Padgett, C. W.; Metrangolo, P.; Resnati, G.; Hanks, T. W.; Pennington, W. T. *Cryst. Growth Des.* **2001,** *1* (2), 165-175; (b) Syssa-Magale, J.-L.; Boubekeur, K.; Palvadeau, P.; Meerschaut, A.; Schollhorn, B. *CrystEngComm* **2005,** *7* (50), 302-308.

25. Cozzi, F.; Bacchi, S.; Filippini, G.; Pilati, T.; Gavezzotti, A. *Chem. Eur. J.* **2007,** *13* (25), 7177-7184.

26. (a) Ebrahimi, A.; Habibi, M.; Sadat Neyband, R.; Reza Gholipour, A. *PCCP* **2009,** *11* (48), 11424-11431; (b) Meejoo, S.; Kariuki, B. M.; Harris, K. D. M. *Chemphyschem* **2003,** *4* (7), 766-769; (c) Gdaniec, M.; Jankowski, W.; Milewska, M. J.; Połoñski, T. *Angew. Chem.* **2003,** *115* (33), 4033-4036.

Chapter 4 - Simultaneous hydrogen bonding and halogen bonding as synthon mimics of each other

4.1 Introduction

Crystal engineering involves the self-assembly of designed molecular species to form predictable supramolecular architectures with complementary size, shape and positioning of the functional groups to maximize the intermolecular interactions. In this regard, halogen bonding, a specific, directional and strong interaction that gives rise to robust supramolecular architectures, can complement the opportunities presented by hydrogen bonding.[1] Strong halogen bonds can be achieved via electron withdrawing substituents attached to the halogen atom resulting in a more positive electrostatic potential of the "σ hole". Iodoperfluoroalkanes (Chapter 2) and fluorinated aromatic compounds (Chapter 3) have been used as powerful halogen bond donors for constructing reliable synthons. In addition to fluorine substitution, the hybridization of the carbon atom bound to the halogen atom also contributes to the effectiveness of the halogen bond donor; the strength of the halogen bond donor usually follows as C(*sp*)-X > C(sp^2)-X > C(sp^3)-X making the *sp*-hybridized carbon bound halogen to be the strongest halogen bond donor (Figure 4.1).[2] Furthermore, C(*sp*)-X has a comparable electrostatic potential compared to its fluorinated analogue (Figure 4.2). In a competitive scenario, where an activated and a non-activated iodine atom are present on the same molecular backbone, the C(*sp*)-X moiety is the better halogen bond donor (Figure 4.3).[3]

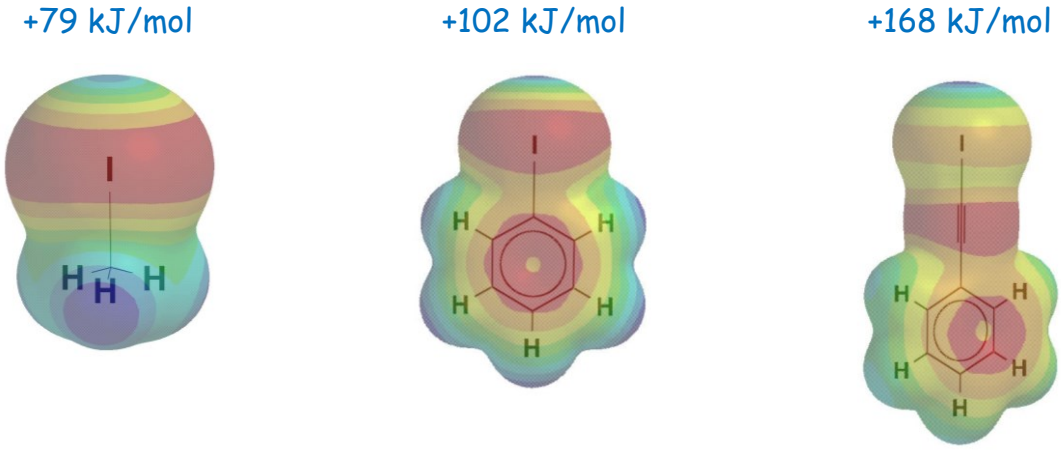

Figure 4.1 Molecular electrostatic potentials of C(sp^3)-I, C(sp^2)-I and C(*sp*)-I

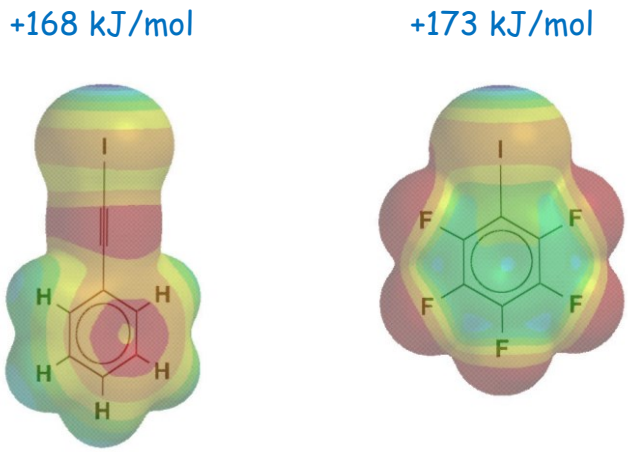

Figure 4.2 Comparison between C(*sp*)-I and fluorinated analogue

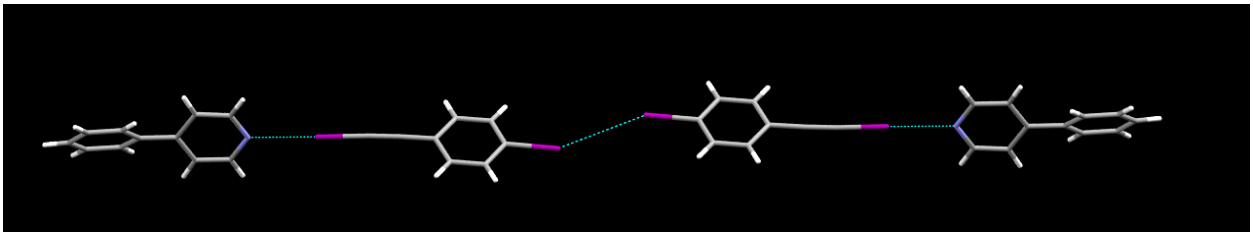

Figure 4.3 Selectivity of the halogen bonding between C(*sp*)-I and C(sp^2)-I

Halogen bond strength also depends on the polarizability of the C(*sp*)-halogen which increases down the periodic table C(*sp*)-Cl < C(*sp*)-Br < C(*sp*)-I indicated by the calculated molecular electrostatic potentials (Figure 4.4). The ability of C(*sp*)-I to form strong halogen bonds has been used in designing pharmaceutical co-crystals[4] and in functional materials and devices.[5]

Similarly functionalized hydrogen atoms also participate in "non-conventional" hydrogen bonds due to its acidity, which is around pK_a of 25. The hydrogen bond donor ability of the fluorinated hydrogen and acetylene hydrogen are illustrated by the high positive electrostatic potential along the terminal of the covalent C-H vector compared to the non-activated or C(sp^2)-H (Figure 4.5). Based upon molecular electrostatic potentials, it is evident that C(*sp*)-H has a higher positive potential than C(*sp*)-Br and C(*sp*)-H and C(*sp*)-I have comparable charges. Due to this positive potential, C(sp)-H has been utilized in supramolecular synthons as synthetic tools in designing discrete supramolecular architectures in solid state (Figure 4.6).[6]

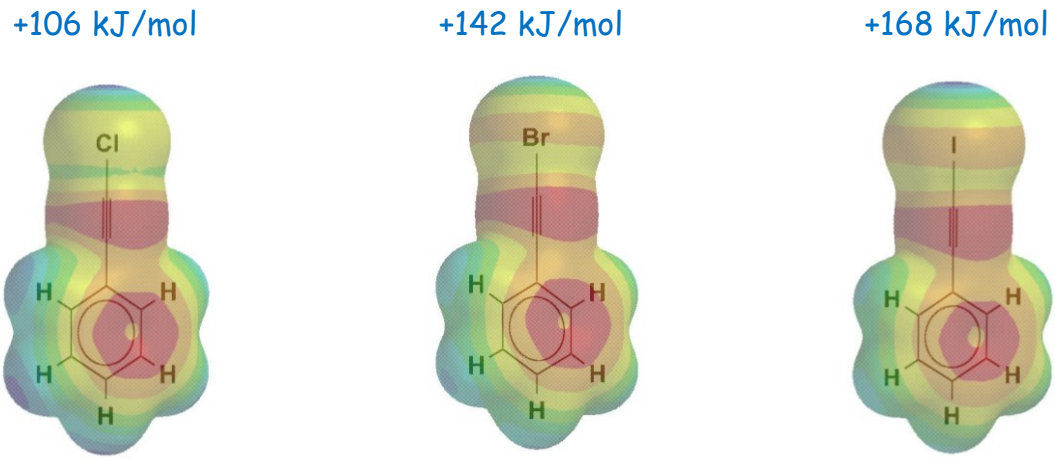

Figure 4.4 Molecular electrostatic potential charges of the C(*sp*)-Cl, C(*sp*)-Br and C(*sp*)-I based on DFT calculation

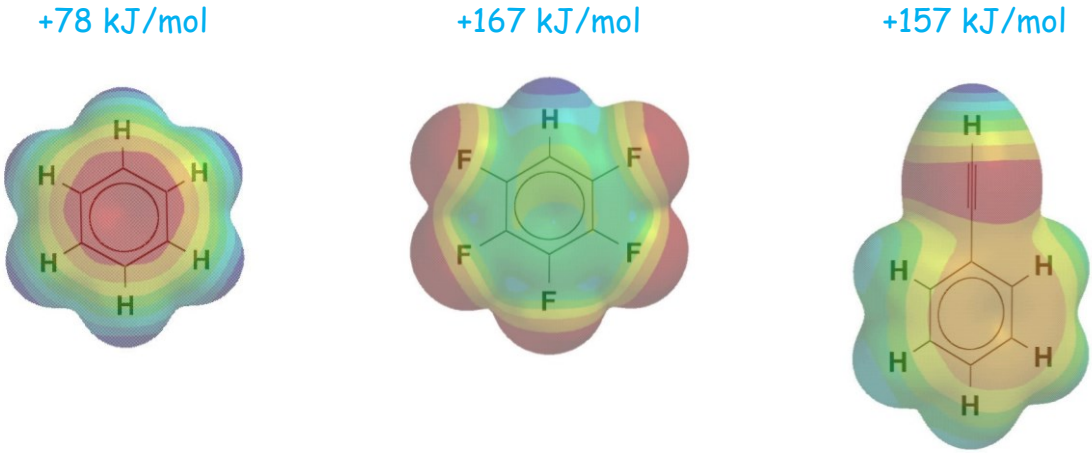

Figure 4.5 Molecular electrostatic potential charges of the C(sp^2)-H and C(*sp*)-H based on DFT calculation

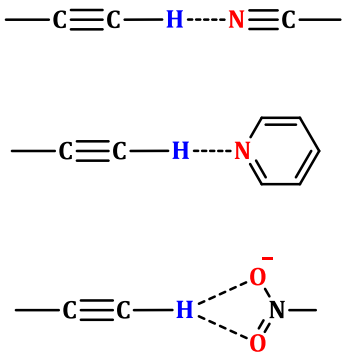

Figure 4.6 Synthons based on C(*sp*)-H

Hydrogen and iodine atoms are far apart in the periodic table and display dramatic differences in chemical and electronic properties (Table 4.1). However, when they are activated with similar functionality and geometry, they possess similar charges. Thus similarly functionalized hydrogen and iodine atoms playing the role of hydrogen-bond and halogen-bond donors of the same shape and geometry, could give rise to identical architectures in the solid state despite the fact that the iodine atom is about 40-50 times larger than the hydrogen atom and they obviously display drastically different electronic structures. Therefore, we wanted to explore whether these two atoms of radically different size and chemical characteristics nevertheless can display "synthon mimicry" in the solid state.

Table 4.1 Comparison of the properties of hydrogen and iodine[7]

	Hydrogen	Iodine
Atomic weight (amu)	1.0079	126.90
Atomic radius (Å)	0.25	1.40
Atomic volume (Å)^3	0.065	11.49
Electron configuration	$1s^2$	[Kr] $4d^{10}$ $5s^2$ $5p^5$
1st Ionization energy (kJ/mol)	1312	1008

In fact, the "synthon mimicry" of organic halogen and ethynyl groups,-C-X and -C≡C-H has been studied as they possess isostruturality due to their similar charge distribution and volume (Figure 4.7).[8] The interchangeability of the -C-X and -C≡C-H functionalities has realized isostructural supramolecular assemblies with reproducible topological identity in cyclic and finite architectures (Figure 4.8).[9]

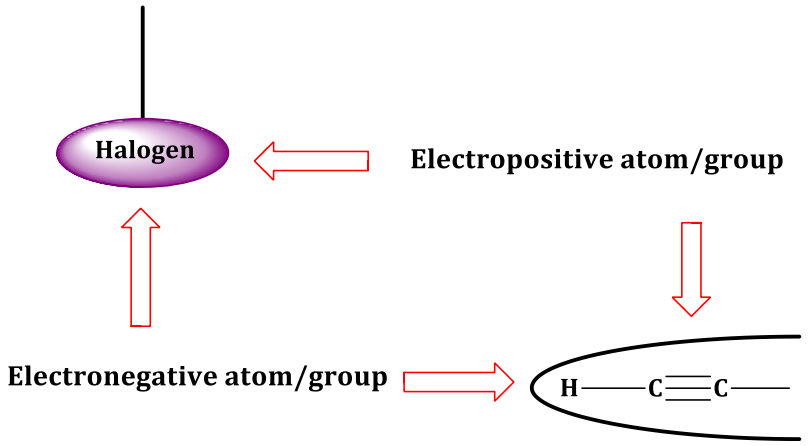

Figure 4.7 Charge distribution of the -C-X and -C≡C-H groups[8]

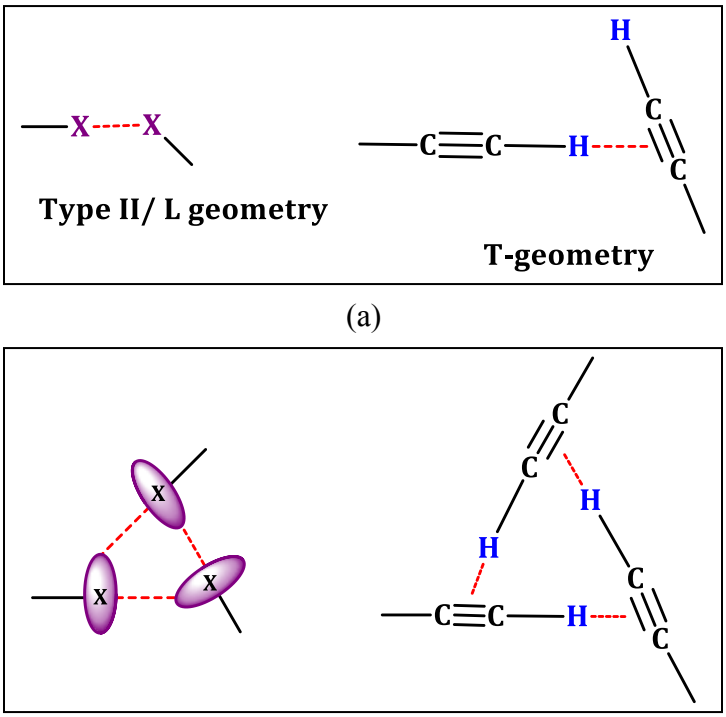

(a)

(b)

Figure 4.8 Similar architectures realized by -C-X and -C≡C-H groups[9] (a) halogen-halogen type II geometry is mimicked by T-geometry of -C≡C-H (b) halogen trimer synthon is mimicked by -C≡C-H trimer synthon

Further, if XB and HB pairs could produce structurally similar architectures, it would confirm that the electrostatic component possessed by both HB and XB is crucial in solid state crystal engineering. In order to explore this idea we eliminated the conventional hydrogen bond

donors such as carboxylic acids, phenols, oximes, amines and amides due to their inherent different geometric features and selected ethynyl hydrogen, C(*sp*)-H as the hydrogen bond donor as it has the same basic molecular shape as ethynyl iodine, C(*sp*)-I. We incorporated these hydrogen bonding, C(*sp*)-H and halogen bonding, C(*sp*)-I functionalities into the same backbone to study the possible interchangeability of the two functionalities in the solid state. We employed a 2-aminopyrimidine moiety as the source of a reliable supramolecular structural backbone thanks to its propensity to form ribbon-like architectures via self-complementary NH···N hydrogen bonds. (Figure 4.5).[10]

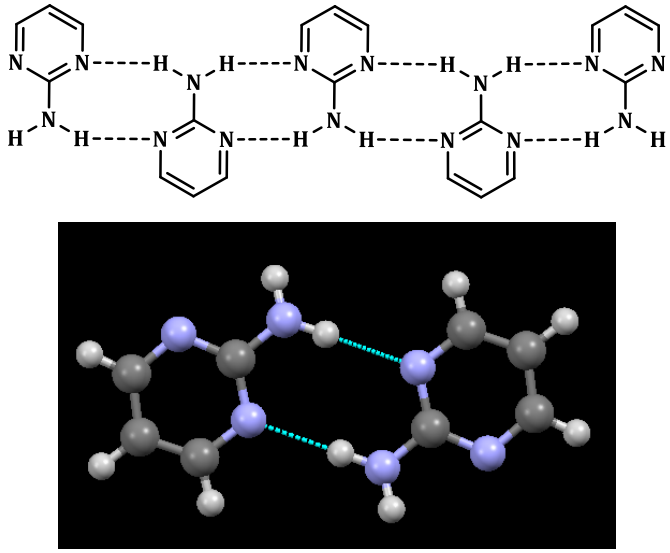

Figure 4.9 2-aminopyrimidines making ribbon-like architectures via N-H···N hydrogen bonds

The 2-aminopyrimidines were functionalized with C(*sp*)-H (**Hpym**) and C(*sp*)-I (**Ipym**) (Figure 4.10 a) to examine how they individually behave in the solid state via the expected C-X···π (X=H/I) synthons (Figure 4.10 b) which is well recognized in acetylene and iodoacetylene derivatives.[9c] Also, the possible interchangeability of these C(*sp*)-H and C(*sp*)-I synthetic vectors was evaluated with the help of suitable halogen/hydrogen bond acceptor.

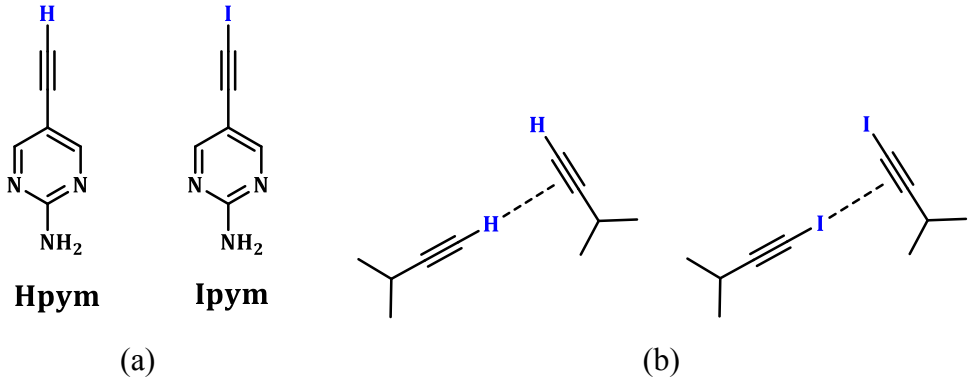

Figure 4.10 (a) Functionalized 2-aminopyrimidines (b) C-H···π and C-I···π synthons expected to form between the individual **Hpym** and **Ipym** molecules

An effective way of probing these structural consequences of hydrogen bonds and halogen bonds is through the use of co-crystallizations and to investigate this idea, several symmetric ditopic acceptors were chosen in order to study the binding preferences and possible synthon interchangeability of **Hpym** and **Ipym**, (Figure 4.11).

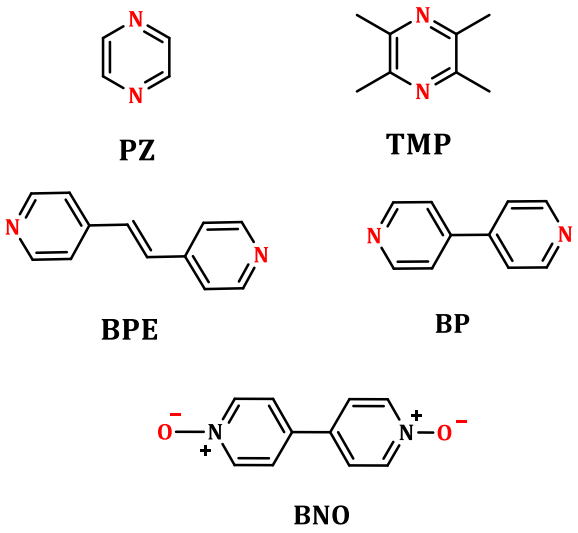

Figure 4.11 Symmetric ditopic acceptor molecules

The main objectives in this chapter are:

i. To determine how the ligands by themselves behave in the solid state
ii. To examine whether those interactions be disrupted by combining **Hpym** and **Ipym** with a strong acceptor
iii. To investigate the interchangeability of **Hpym** and **Ipym** in the co-crystals
iv. To establish if two atoms of radically different size and chemical characteristics nevertheless can display "synthon mimicry" in the solid state

4.2 Experimental

4.2.1 Synthesis

Tetramethyl pyrazine (TMP), 1,2-*bis*(4-pyridyl)ethylene (BPE), pyrazine (PZ), 4,4-bipyridyl were purchased from Sigma Aldrich and 4,4'-bipyridyl N,N'-dioxide (BNO) from Acros Organics. Column chromatography was carried out on silica gel (150 Å pore size) from Analtech, Inc. ^{1}H and ^{13}C NMR spectra were recorded on a Varian Unity plus 400 MHz spectrometer in $CDCl_3$. Data is expressed in parts per million (ppm) downfield shift from tetramethylsilane as internal reference and are reported as position (in ppm). Melting point/decomposition point determination was performed using Fisher-Johns melting point apparatus and are uncorrected. Infrared spectroscopy analysis was carried out using Nicolet 380 FT-IR with a digital resolution of 0.9 cm^{-1}. Data were analyzed using software, Omnic 8.0 © 1992-2008 Thermo Fisher Scientific Inc.

4.2.1.1 Synthesis of 5-bromo-2-aminopyrimidine[11]

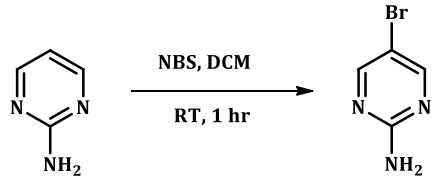

A solution of N-bromosuccinimide (5.2 g, 29.2 mmol) dissolved in methylene chloride (100 mL) was added dropwise to a solution of 2-aminopyrimidine (2.36 g, 24.8 mmol) dissolved in methylene chloride (50 mL) kept over an ice bath. After addition, the ice bath was removed and the reaction mixture was stirred at room temperature for 1 hr. Upon completion, the reaction was quenched with 10% sodium bicarbonate and 10% sodium sulfite solution. The mixture was

filtered and the precipitate washed with water twice and dried to yield a white powder. (3.7 g, 86.2 %). M.p. > 250 ºC (Reported M.p. 245 ºC)[12]; ^{1}H NMR (δH; 200 MHz, $CDCl_3$): 8.31 (s, 2H), 5.09 (br, 2H).

4.2.1.2 Synthesis of 2-amino-5-trimethylsilanylethynylpyrimidine[13]

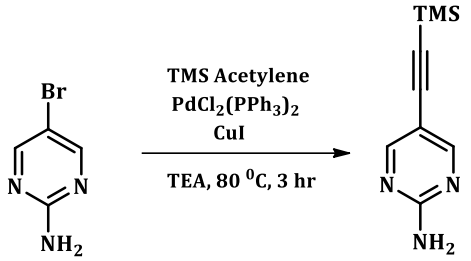

5-Bromo-2-aminopyrimidine (2.0 g, 11.5 mmol) was dissolved in triethylamine (30 mL) and degassed by bubbling nitrogen through the reaction mixture. TMS-acetylene (2.82 g, 28.7 mmol), $PdCl_2(PPh_3)_2$ (0.81 g, 1.15 mmol) and CuI (0.438 g, 2.30 mmol) were added and the mixture was refluxed at 70 ºC overnight. The solvent was removed by evaporation and the residue dissolved in diethyl ether (200 mL), washed with 1 M HCl (50 mL) and brine (50 mL). The organic layer was separated and dried over anhydrous magnesium sulfate. The solvent was removed on a rotary evaporator and the residue was chromatographed on silica with hexane: ethyl acetate mixture as eluent to obtain a light brown colored powder. Upon recrystallization from methylene chloride, colorless crystals were obtained, (1.4 g, 63.6 %). ^{1}H NMR (δH; 200 MHz, $CDCl_3$): 8.40 (s, 2H), 5.21 (br, 2H), 0.26 (s, 9H).

4.2.1.3 Synthesis of 2-amino-5-ethynylpyrimidine (HPym)[10]

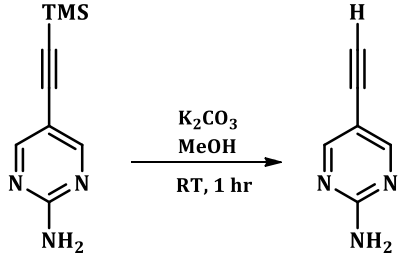

2-Amino-5-trimethylsilanylethynylpyrimidine (1.3 g, 6.8 mmol) and potassium carbonate (0.99 g, 7.20 mmol) were stirred in methanol at room temperature for 2 hrs. Upon completion, the solvent was removed by rotary evaporation and the residue dissolved in diethyl ether and washed with water (2 x 50 mL). The combined organic layers were dried over anhydrous magnesium sulfate and concentrated via rotary evaporation to obtain the product, **Hpym** as

yellow crystalline solid. (0.69 g, 85.1%). Dec. 148 ˚C. ^{1}H NMR (δH; 200 MHz, $CDCl_3$): 8.41 (s, 1H), 5.23 (br, 2H), 3.19 (s, 1H); IR: υ 3280, 3241, 2753, 2530, 2350, 2170, 2104, 1659, 1588, 1476, 1080, 939, 798 cm^{-1}.

4.2.1.4 Synthesis of 2-amino-5-iodoethynylpyrimidine (IPym)[14]

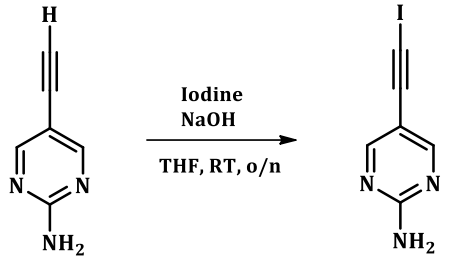

To a solution of 2-amino-5-ethynylpyrimidine (0.5 g, 4.2 mmol) dissolved in THF (50 mL), added dropwise simultaneously a concentrated solution of iodine in methanol (1.407 g, 5.54 mmol) and a 10% sodium hydroxide solution over 30 min, vigorously stirring. The mixture was stirred overnight, and quenched with 100 mL water upon which a light yellow color precipitate forms. The filtered solid washed with sodium bisulfite solution afforded pure pale yellow color powder of **Ipym**, (0.82 g, 79.7%). Dec. 160 ˚C. ^{1}H NMR (δH; 200 MHz, $CDCl_3$): 8.38 (s, 1H), 5.21 (br, 2H). IR: υ 3308, 3163, 2956, 2702, 2158, 1649, 1587, 1525, 1493, 1368, 1219, 1069, 942, 796 cm^{-1}.

4.2.2 Synthesis of co-crystals

The co-crystals were synthesized using solvent assisted grinding[15] where the two hydrogen and halogen bond donor molecules, **Hpym** and **Ipym** were mixed in a 2:1 molar ratio with each of the five ditopic acceptor molecules and ground together using a drop of methanol until a solid paste was obtained. The resulting solid from each of the ten reactions (2x5) were analyzed using attenuated total reflectance (ATR) FTIR spectrometry for the confirmation of co-crystal formation. Based on the result of the grinding experiment, if the IR showed that a reaction has occurred, the solid paste was dissolved in methanol or methanol:THF mixture in 2 dram borosilicate vials and allowed for slow evaporation at room temperature. The single crystals suitable for X-ray diffraction were again analyzed by IR for the confirmation of co-crystal formation. By this method, four single crystals confirmed to be co-crystals and two single crystals confirmed to be **Hpym** by itself and **Ipym** by itself were obtained.

4.2.2.1 Synthesis of 2-amino-5-ethynylpyrimidine·tetramethylpyrazine, HPym·TMP

2-Amino-5-ethynylpyrimidine (HPym) (0.010 g, 0.084 mmol) and tetramethylpyrazine (TMP) (0.034 g, 0.25 mmol) were dissolved in methanol in a 2 dram borosilicate vial and allowed for slow evaporation at ambient conditions. After seven days colorless plate shaped crystals were obtained. Dec. 112 ˚C.

4.2.2.2 Synthesis of 2-amino-5-ethynylpyrimidine·1,2-bis(4-pyridyl)ethylene, HPym·BPE

2-Amino-5-ethynylpyrimidine (HPym) (0.010 g, 0.084 mmol) and 1,2-bis(4-pyridyl)ethylene (BPE) (0.046 g, 0.25 mmol) were dissolved in methanol in a 2 dram borosilicate vial and allowed for slow evaporation at ambient conditions. After five days gold color plate shaped crystals were obtained. M.p. 135-137 ˚C.

4.2.2.3 Synthesis of 2-amino-5-iodoethynylpyrimidine·tetramethylpyrazine, IPym·TMP

2-Amino-5-iodoethynylpyrimidine (IPym) (0.010 g, 0.041 mmol) and tetramethylpyrazine (TMP) (0.003 g, 0.020 mmol) were dissolved in methanol: THF 1:1 mixture in a 2 dram borosilicate vial and allowed for slow evaporation at ambient conditions. After three days colorless plate shaped crystals were obtained. M.p. 108-110 ˚C.

4.2.2.4 Synthesis of 2-amino-5-iodoethynylpyrimidine·1,2-bis(4-pyridyl)ethylene, IPym·BPE

2-Amino-5-iodoethynylpyrimidine (IPym) (0.010 g, 0.041 mmol) and 1,2-bis(4-pyridyl)ethylene (BPE) (0.004 g, 0.020 mmol) were dissolved in methanol:THF 1:1 mixture in a 2 dram borosilicate vial and allowed for slow evaporation at ambient conditions. After two days colorless plate shaped crystals were obtained. Dec. 171℃.

4.2.3 Single Crystal X-ray Crystallography

X-ray data were collected on a Bruker APEX II CCD diffractometer at 120 K using, a fine-focus molybdenum Kα tube. Data were collected using APEX2[16] software. Initial cell constants were found by small widely separated “matrix” runs. Scan speed and scan width were chosen based on scattering power and peak rocking curves.

Unit cell constants and orientation matrix were improved by least-squares refinement of reflections thresholded from the entire dataset. Integration was performed with SAINT[17] using this improved unit cell as a starting point. Precise unit cell constants were calculated in SAINT

from the final merged dataset. Lorenz and polarization corrections were applied. All datasets were corrected for absorption using SADABS[18] Laué symmetry, space group, and unit cell contents were found with XPREP.

Data were reduced with SHELXTL.[19] The structures were solved in all cases by direct methods without incident. Except where indicated, hydrogens were assigned to idealized positions and were allowed to ride. Heavy atoms were refined with anisotropic thermal parameters. Absorption correction was carried out on all datasets.

Ipym - The molecule sits on a crystallographic mirror plane. All hydrogens were located in idealized positions. Attempts to account for the residual electron density in the vicinity of the iodine, either with more sophisticated absorption correction or with molecular disorder, were unsuccessful.

Ipym·TMP - The asymmetric unit contains one alkyne and one half-pyrazine. All hydrogens were located in idealized positions.

Ipym·BPE - The asymmetric unit contains one alkyne and one half-ethylene. Coordinates of the amine hydrogens H32A & H32B were allowed to refine.

Hpym·TMP - The asymmetric unit contains one alkyne and one half-pyrazine. The two unique methyl groups were rotationally disordered and were each treated as two species. All hydrogens were located in idealized positions. Coordinates of the amine hydrogens H12A & H12B and the ethynyl hydrogen H18 were allowed to refine.

Hpym·BPE - The asymmetric unit contains two alkynes and two half-ethylenes. These molecules were grouped into two different residues for consistent numbering. One of the two half-ethylenes was disordered and was modeled as two species. Geometries of the two species were restrained with the "SAME" command and thermal parameters were pairwise constrained with the "EADP" command. For both residues, coordinates of the amine hydrogens H12A & H12B and the ethynyl hydrogen H18 were allowed to refine.

Hpym - The molecule sits on a crystallographic mirror plane. Coordinates of the unique amine hydrogen H11 were allowed to refine.

4.2.4 Molecular electrostatic potential charge calculations

Molecular electrostatic potential calculations for **Hpym** and **Ipym** were performed using Spartan '10 (Wavefunction, Inc., Irvine, CA) (Figure 4.12). The geometry optimization of the molecules were done using DFT with B3LYP procedure and 6-311+G** basis set, where a positive point charge in the vacuum was used to determine the maximum value of the potential, V(r), corresponding to the depth of the σ-hole on each halogen atom surface (0.002 e/au isosurface). The numbers indicate the interaction energy (kJ/mol) between particular point of the molecule and the surface of the positive point probe. A negative number corresponding to negative charge and positive number corresponding to positive charge which represents the electrostatic potential on the atoms.

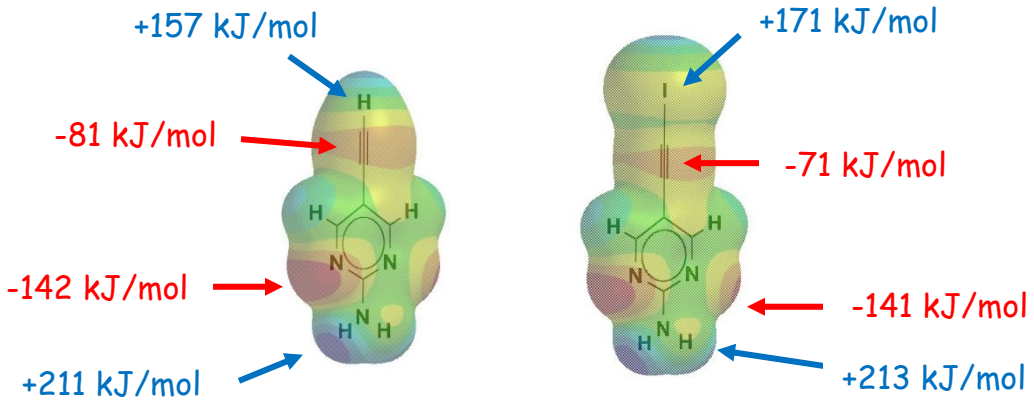

Figure 4.12 MEP surface charge calculations for Hpym and Ipym; numbers represent the electrostatic potential on hydrogen atom and iodine atom

4.3 Results

4.3.1 Characterization by IR spectroscopy

Formation of a co-crystal was established by carefully comparing the IR spectrum of the ground solid mixture with the IR spectra of the pure donor and the acceptor. The C≡C (2100-2200 cm^{-1}) bond stretch was analyzed which is directly affected by the presence of a halogen bond (Table 4.2). The shifts of other stretches corresponding to either donor or the acceptor is also taken into consideration and the results are tabulated and used as a basis when determining a successful co-crystal event.

Table 4.2 FT-IR significant bands from solvent-assisted grinding experiments and the frequencies are expressed in wavenumbers, (cm^{-1})

	Original	PZ	TMP	BP	BPE	BNO
Hpym	2170	2155	2152	2151	2167	2162
	2108	2106	2100	2096	2098	2105
	1659	1660	1650	1654	1643	1660
	1080	1064	1064	1068	1065	1083
	798	797	796	799	795	797
Ipym	2159	2157	2155	2150	2153	2159
	1649	1651	1648	1654	1651	1653
	1587	1589	1589	1587	1582	1590
	1544	1546	1547	1546	1542	1546
	1525	1527	1528	1528	1521	1526
	796	797	794	801	794	799

4.3.2 Crystal structures

A total of four co-crystal structures were obtained along with the crystal structures of **Hpym** and **Ipym**. The hydrogen bond geometries for **Hpym**, **Ipym** and the co-crystals are presented in Table 4.3.

Table 4.3 Hydrogen bond geometries for **Hpym, Ipym, HPym·TMP, HPym·BPE, IPym·TMP** and **IPym·BPE**

Structure	D-H···A (Å)	d(D-H)/Å	d(H···A)/Å	d(D···A)/Å	<(DHA)/º
Hpym[i]	N(11)-H(11)...N(12)#2	0.929(13)	2.108(13)	3.0342(10)	175.2(10)
Ipym[ii]	N(12)-H(12A)...N(11)#2	0.90	2.22	3.075(8)	158.2
HPym·TMP[iii]	N(12)-H(12A)...N(11)#2 N(12)-H(12B)...N(13)#3 C(18)-H(18)...N(31)	0.890(16) 0.882(16) 0.943(16)	2.174(16) 2.176(16) 2.414(16)	3.0642(16) 3.0575(17) 3.3375(18)	177.7(13) 178.3(13) 166.2(14)
HPym·BPE[iv]	N121-H12A1...N112 N122-H12A2...N111 N121-H12B1...N131#3 N122-H12B2...N132#4 C181-H181...N21A1 C182-H182...N212	0.925(17) 0.912(18) 0.868(18) 0.848(18) 0.952(17) 0.941(17)	2.295(18) 2.144(18) 2.323(18) 2.192(18) 2.341(18) 2.277(18)	3.2169(17) 3.0562(17) 3.1905(18) 3.0381(18) 3.280(2) 3.2090(19)	174.1(14) 178.4(16) 176.8(16) 175.3(16) 169.0(15) 170.5(15)
IPym·TMP[v]	N(32)-H(32A)...N(31)#2 N(32)-H(32B)...N(33)#3	0.88 0.88	2.15 2.18	2.999(3) 3.004(4)	161.5 155.4
IPym·BPE[vi]	N(32)-H(32A)...N(31)#2 N(32)-H(32B)...N(33)#3	0.81(3) 0.82(3)	2.21(3) 2.27(3)	3.014(2) 3.088(2)	176(3) 178(3)

Symmetry transformations used to generate equivalent atoms: **i)** #1 x,-y+1/2,z #2 -x+2,-y+1,-z, **ii)** #1 -x+1,y,z #2 -x+3/2,-y+1/2,-z+1, **iii)** #1 -x,-y,-z+1 #2 -x+1,-y+3,-z #3 -x+2,-y+2,-z, **iv)** #1 -x+4,-y-1,-z #2 -x-2,-y+2,-z+2 #3 -x+2,-y+1,-z+1 #4 -x,-y,-z+1 **v)** #1 -x+2,-y,-z+1 #2 -x-1,-y+1,-z #3 -x,-y+2,-z, **vi)** #1 -x+1,-y+1,-z-1 #2 -x+2,y+1/2,-z+5/2 #3 -x+2,y-1/2,-z+5/2

4.3.2.1 Crystal structure of 2-amino-5-iodoethynylpyrimidine, Ipym

The crystal structure of **Ipym** shows that the aminopyrimidine moiety of the individual molecules form a ribbon-like arrangement via self-complementary NH···N interactions. These ribbons further extend to a 2-D network via perpendicular C(*sp*)-I···π interactions (Figure 4.13). The pyrimidine rings are offset stacked and arranged in an anti-parallel fashion (Figure 4.14).

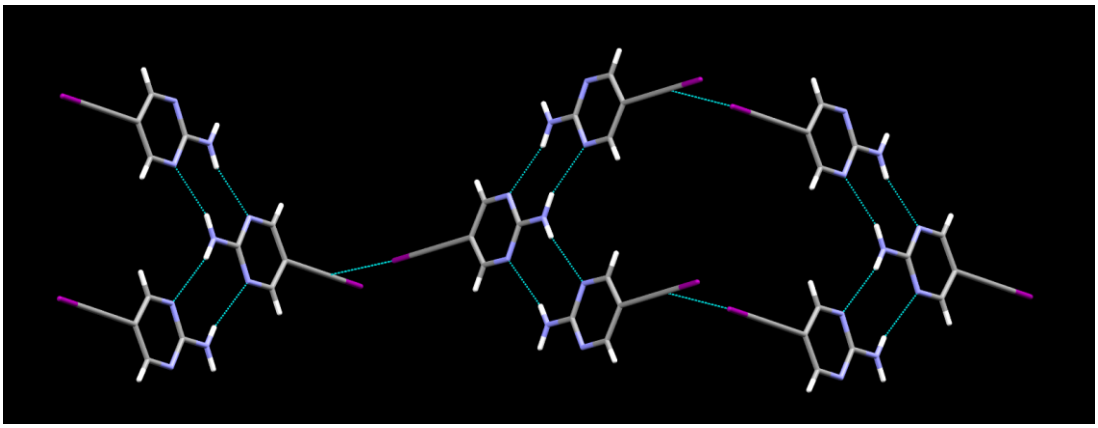

Figure 4.13 Primary interactions in the crystal structure of **Ipym**, the self-complementary NH···N interactions which makes ribbons and extension of the ribbons via C(*sp*)-I···π interactions

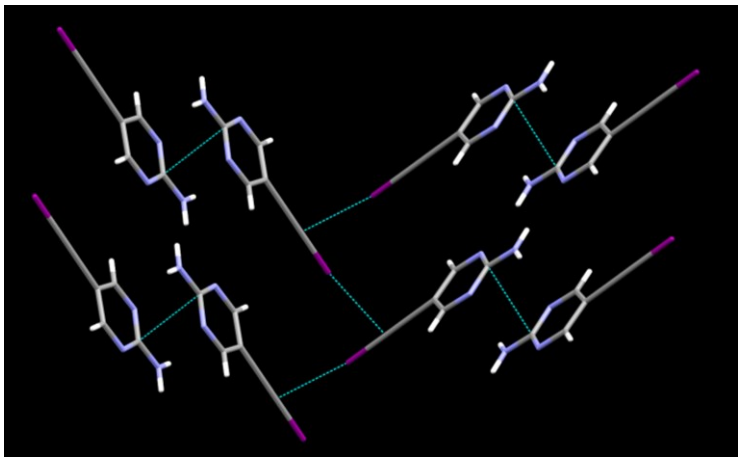

Figure 4.14 Offset stacked pyrimidine units in the crystal of **Ipym**

4.3.2.2 Crystal structure of 2-amino-5-ethynylpyrimidine, Hpym

In the structure of **Hpym** itself, a ribbon-like architecture is formed between 2-aminopyrimidine moieties via NH···N self-complementary interactions (Figure 4.15). The structure is different than **Ipym** in which the ribbons are extended via C(*sp*)-H···N hydrogen bonding interactions (Figure 4.15). The structure involves off-set stacks of pyrimidine units that are arranged in a parallel fashion (Figure 4.16).

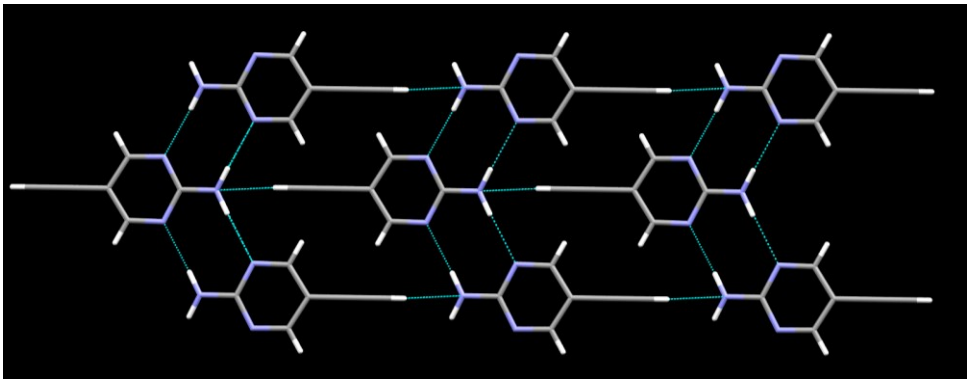

Figure 4.15 Part of the crystal structure of **Hpym** showing N-H···N interactions and C(sp)-H···N interactions

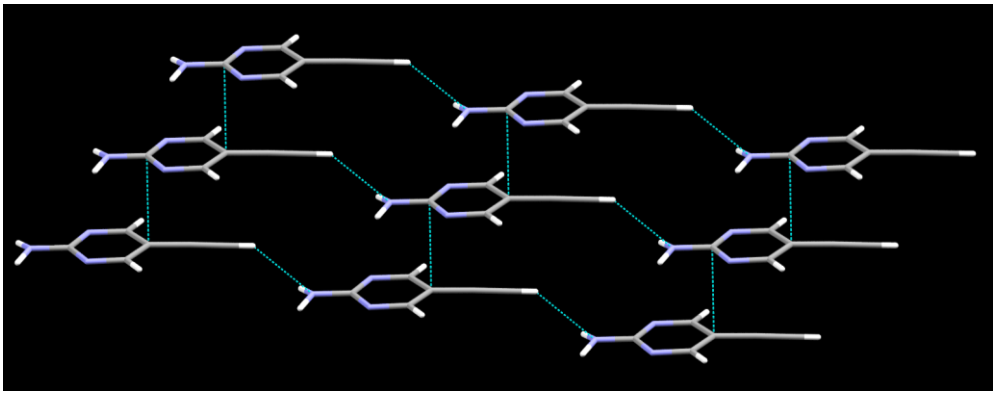

Figure 4.16 Off-set stacks of pyrimidine units that are arranged in parallel fashion

4.3.2.3 Crystal structure of 2-amino-5-iodoethynylpyrimidine·tetramethylpyrazine, IPym·TMP

The structure determination of **IPym·TMP** showed a 1:1 co-crystal with self-complementary NH···N synthons forming ribbon-like architecture. These ribbons are further cross-linked by C*(sp)*-I···N halogen bonds (Figure 4.17).

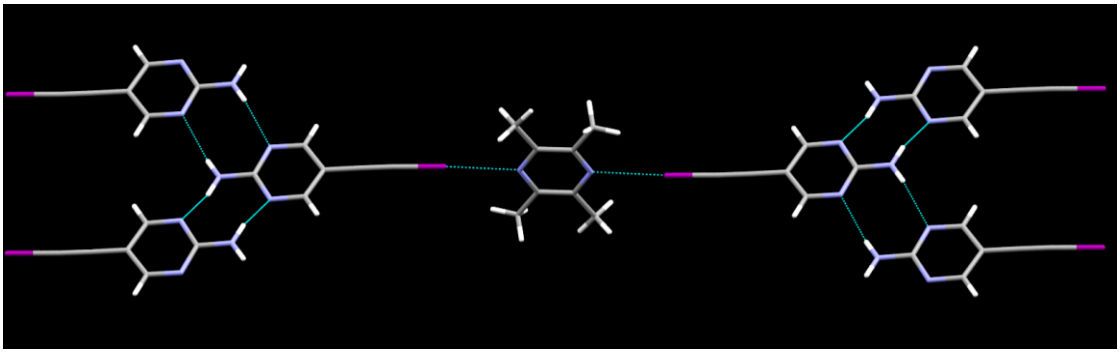

Figure 4.17 The primary N-H···N interactions that form ribbons and C*(sp)*-I···N halogen bonds that cross-links the ribbons

4.3.2.4 Crystal structure of 2-amino-5-ethynylpyrimidine·tetramethylpyrazine, HPym·TMP

When 2-amino-5-ethynylpyrimidine was combined with tetramethylpyrazine, the structure determination showed 1:1 co-crystal formation similar to the structure of **IPym·TMP**. The ribbon-like architecture was consistent and formed via NH···N synthons further cross-linked via C*(sp)*-H···N hydrogen bonds instead of C*(sp)*-I···N halogen bonds in **IPym·TMP** (Figure 4.18).

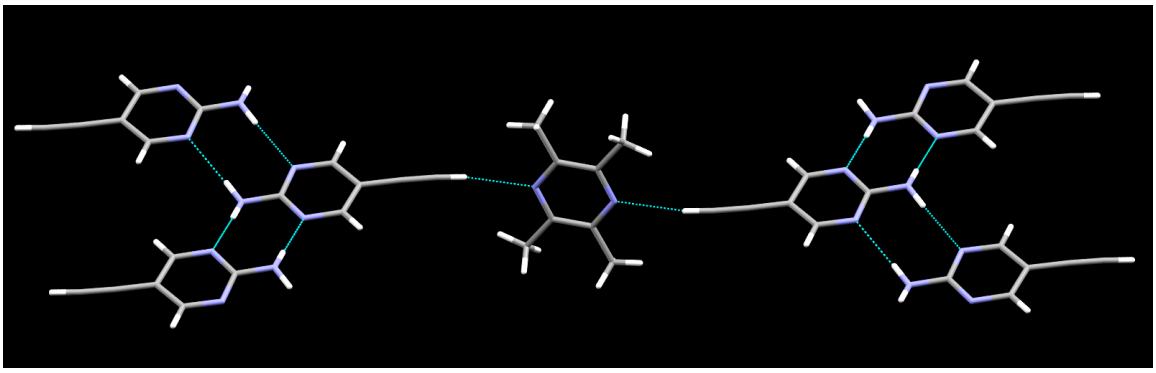

Figure 4.18 The primary N-H···N interactions that form ribbons and C*(sp)*-H···N hydrogen bonds that cross-links the ribbons

4.3.2.5 Crystal structure of 2-amino-5-iodoethynylpyrimidine·1,2-bis(4-pyridyl)ethylene, IPym·BPE

The crystal structure of **IPym·BPE** showed similar behavior (with 1:1 stoichiometry), where symmetry related self-complementary NH···N synthons produce a ribbon like architecture. The C*(sp)*-I···N halogen bonds crosslink the pyrimidine molecules into infinite chains (Figure 4.19).

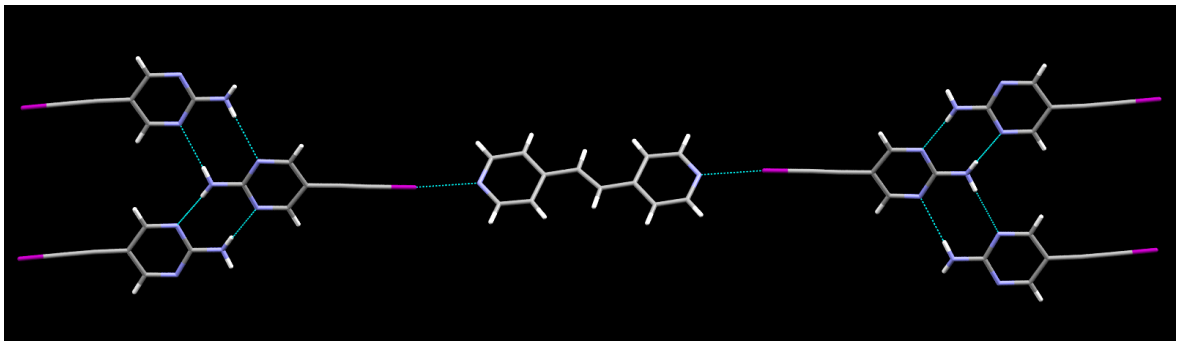

Figure 4.19 The extended 2-D network formed via self-complementary N-H···N interactions and C*(sp)*-I···N halogen bonds

4.3.2.6 Crystal structure of 2-amino-5-ethynylpyrimidine·1,2-bis(4-pyridyl)ethylene, HPym·BPE

When 2-amino-5-ethynylpyrimidine was combined with 1,2-*bis*(4-pyridyl)ethylene, the structure determination showed 1:1 co-crystal similar to the structure of **IPym·BPE**. The ribbon-like architecture is consistent and formed via NH···N synthons that are further cross-linked via C*(sp)*-H···N hydrogen bonds instead of C*(sp)*-I···N halogen bonds in IPym·BPE (Figure 4.20).

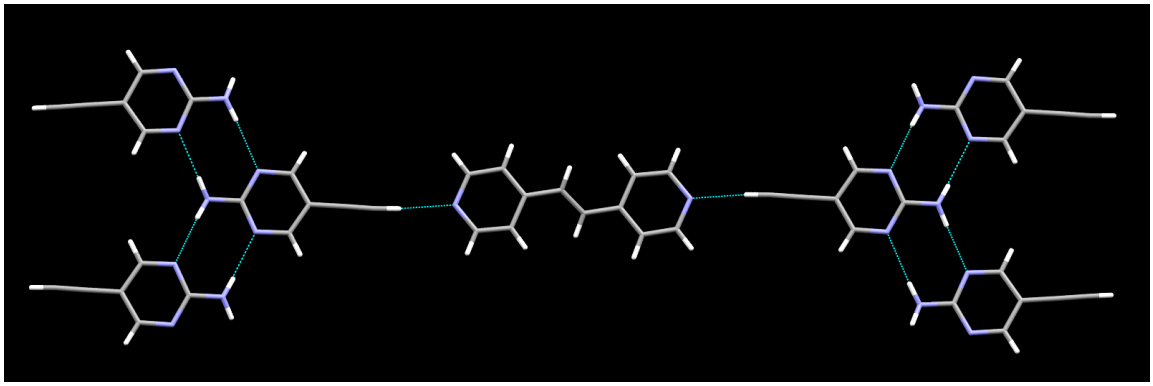

Figure 4.20 The structural roles of C(*sp*)-H···N hydrogen bonding and self-complementary N-H···N hydrogen bonding in **HPym·BPE** co-crystal

4.4 Discussion

4.4.1 Characterization of the co-crystals from IR spectroscopy

Systematic analysis of the IR spectra is a good way of characterizing co-crystal formation since the vibrational frequency and the bond strength changes as a result of new non-covalent interactions. The identification of co-crystal formation was done by carefully analyzing the IR spectra of the ground solid mixture or the single crystals that are formed and comparing them with the IR spectra of the individual donor and acceptor molecules. The C-I stretch was not within the range of our instrument. The C(*sp*)-H stretch that shows up around 3300 cm^{-1} is very weak and its precise position could not be identified with **Hpym** or **Hpym** based co-crystals. Therefore, the most telling characterization was based on the shift of the stretch corresponding to the C≡C in **Hpym** and **Ipym** (2170 and 2158 cm^{-1} respectively). In addition, C═C stretching bands (1400 – 1500 cm^{-1} and 1200 – 1300 cm^{-1}), C-H in-plane bending modes (900 – 1000 cm^{-1}) and C-H out-of-plane bending modes (750 – 850 cm^{-1}) from both donor and acceptor were taken into consideration. A successful co-crystal formation was confirmed when the IR spectra of the ground solid mixture or the single crystals consist of stretches from both the donor and the acceptor and the magnitude of the shift of the IR bands are 2 cm^{-1} or more. An example of IR spectra of co-crystals **IPym·TMP** and **HPym·TMP** and their corresponding starting materials are shown in Figure 4.21 and Figure 4.22.

The grinding experiments showed 100% co-crystal formation from the IR spectral analysis, based on the red shifts of the halogen / hydrogen bond donor and blue shifts of the halogen / hydrogen bond acceptor molecules. The C≡C in **Hpym** (2170 cm^{-1}) and **Ipym** (2159 cm^{-1}) is diagnostic of the presence of halogen bonding or hydrogen bonding where a significant red shift is observed in all the co-crystals as iodoalkyne and acetylene proton are directly involved in co-crystal formation (2157, 2155, 2150, 2153, 2158 cm^{-1} in **Ipym** co-crystals and 2155, 2152, 2151, 2167, 2162 cm^{-1} in **Hpym** co-crystals). The symmetric ring stretching modes of **BPE** (975 cm^{-1}), **TMP** (986 cm^{-1}), **BNO** (1020 cm^{-1}), **PZ** (972 cm^{-1}), **BP** (1026 cm^{-1}) are blue shifted and the C(sp^2)-H stretching modes of the heterocyclic ring (above 3000 cm^{-1}) have become less intense and blue shifted, indicative of co-crystal formation (Figure 4.2) consistent with literature data.[20] These changes are attributed to the $n \rightarrow \sigma^*$ electron density donation from the heterocyclic ring to the electropositive iodine or hydrogen atom.

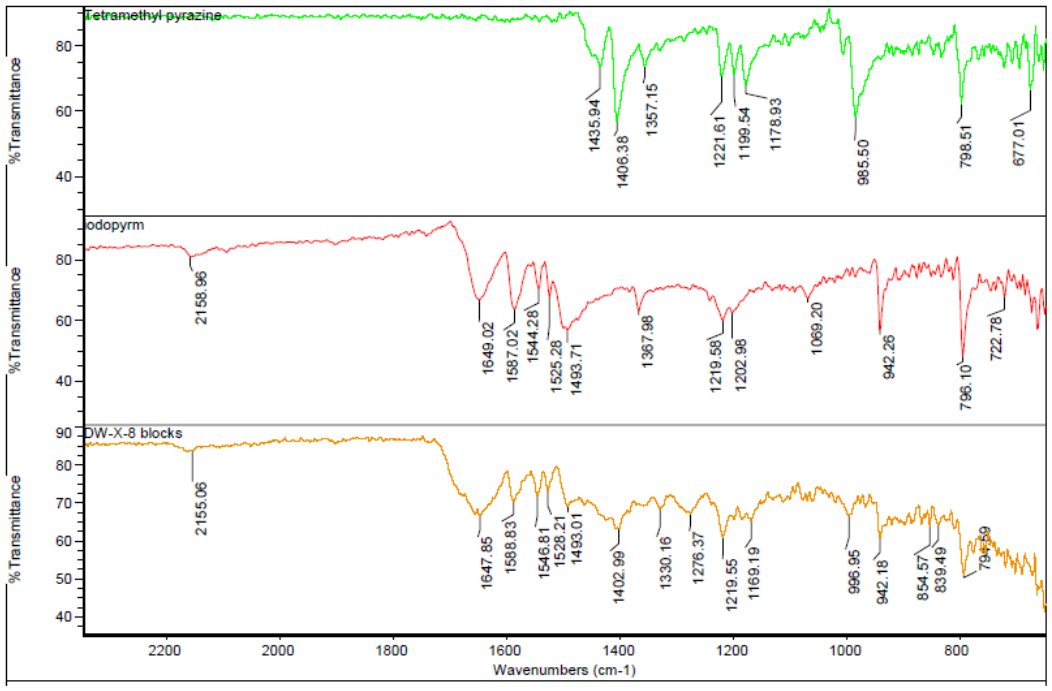

Figure 4.21 The comparison of the IR spectra of **IPym·TMP** (orange) with pure **TMP** (green) and **Ipym** (red).

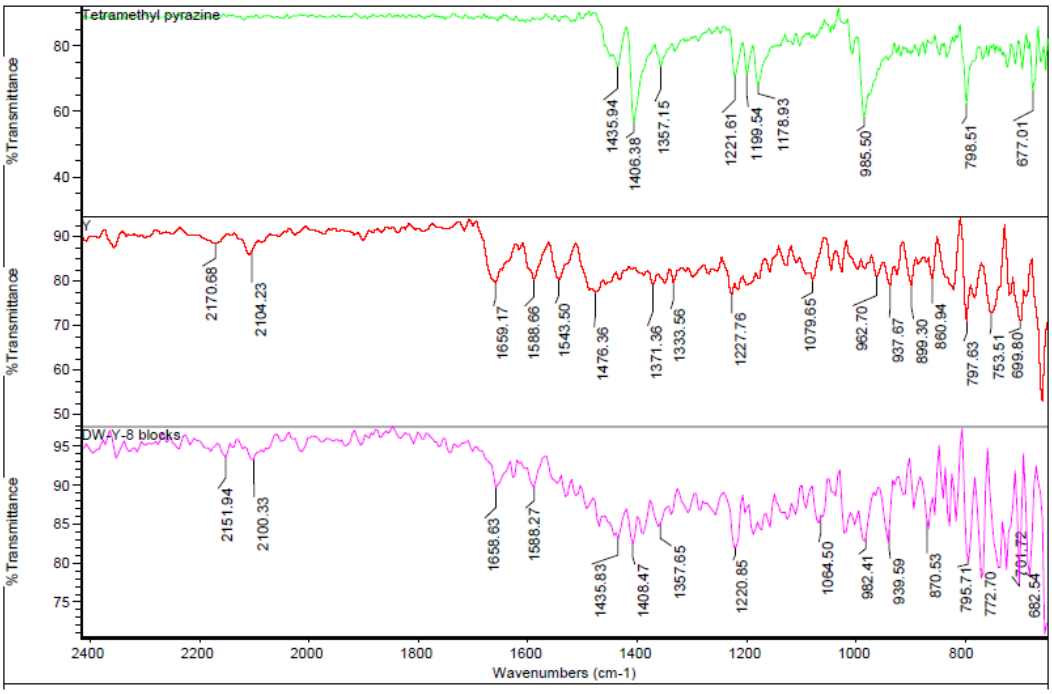

Figure 4.22 The comparison of the IR spectra of **HPym·TMP** (pink) with pure **TMP** (green) and **Hpym** (red).

The magnitude of the shifts of C═C and C-H modes are relatively small and showed either a red shift or blue shift. This is in agreement with literature and can be explained since the C═C and C-H bonds are not directly involved in C-X···N (X=I/H) hydrogen bonds or halogen bonds and could be affected by the nearest neighbors during crystal packing.[3]

4.4.2 Interchangeability of ethynyl iodine and ethynyl hydrogen

In order to assess the interchangeability of ethynyl iodine and ethynyl hydrogen, we need to carefully look at the crystal structures of **Hpym** and **Ipym** themselves and their co-crystals in detail.

4.4.2.1 Behavior of the ligand by itself, Hpym and Ipym

Both **Hpym** and **Ipym** have two acceptor sites and one donor site (Figure 4.23) and these give an idea of possible synthons in each individual molecule.

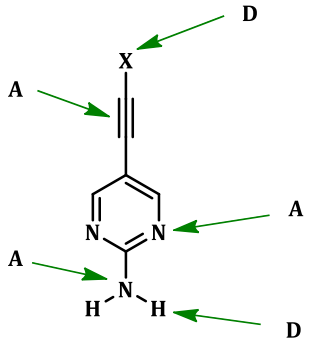

Figure 4.23 The possible donor and acceptor sites in **Hpym** and **Ipym** (D – donor, A – acceptor)

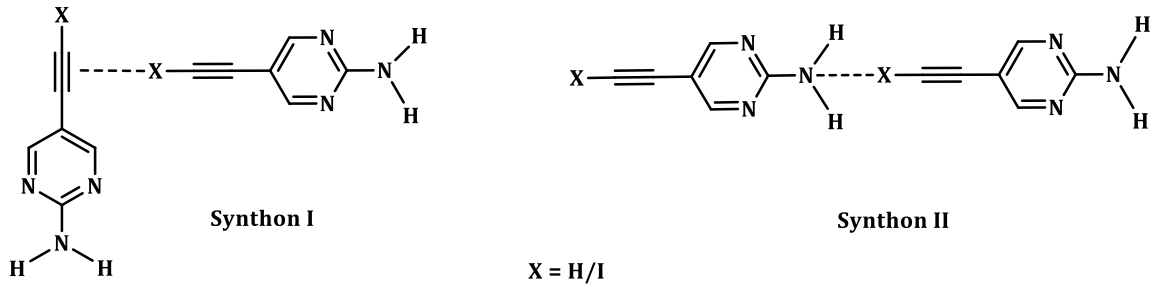

Figure 4.24 The two possible synthons that can result from the interactions

The crystal structure of **Ipym** shows a self-complementary ribbon-like architecture involving the 2-aminopyrimidine moiety. However, the main interest is paid to the haloethynyl moiety which displays synthon I (Figure 4.24), where the σ hole on the iodine atom forms a halogen bond with the π electron cloud of the C≡C (which acts as halogen bond acceptor) of the adjacent molecule. The I···C distance is 3.38 Å, shorter than sum of van der Waals radii (3.68 Å) and the interaction is almost perpendicular to the triple bond axis, 82.5°. The C-I···C≡C angle is 171.5 Å suggesting a linear strong halogen bond between the σ hole and the π electron cloud. This (T-shaped) triple bond centroid perpendicular halogen bonding leads the ribbons to zig-zag chains. Crystal packing of **Ipym** is also controlled by off-set stacked pyrimidine units that are arranged in an anti-parallel fashion (Figure 4.14). The interplanar distance (3.38 Å) is smaller than the sum of van der Waals radii (3.40 Å) indicating that π stacking interactions also play a role in crystal packing.

The same T-shaped C-H···π interactions are known to occur in terminal alkynes to form zig-zag type chains, in which the distance of C-H···π ranges from 2.56 – 3.58 Å and the C-H···C≡C angle is linear with 180±10°.[9a, 9b, 21] However, the ethynyl hydrogen of **Hpym** exhibit synthon II in which the hydrogen bond is formed between the electropositive hydrogen and the amino N atom (Figure 4.24). The distance of C-H···N is 2.71 Å which is slightly less than sum of van der Waals radii (2.75 Å) and the C≡C-H···N angle is 139.4°. The π stacking interactions contribute to the crystal packing in **Hpym** as well given the interplanar distance 3.32 Å is shorter than sum of van der Waals radii (3.34 Å) where the pyrimidine units off-set stack in parallel fashion (Figure 4.16).

Hpym and **Ipym** possess two different synthons, based on MEP charge calculations, the amine N is the better acceptor than the comparatively less electronegative electron cloud on the C≡C triple bond. However, the bigger size of the iodine atom may prohibit it from reaching the amine N lone pair due to steric factor and therefore, interacts with the π electron cloud of the C≡C triple bond. Hydrogen atom on the other hand is small and can easily access the amine N atom to form C-H···N hydrogen bonds.

4.4.3 Comparison of hydrogen and halogen bonded co-crystals of Hpym and Ipym

Both **IPym·TMP** and **HPym·TMP** exhibit the same structural behavior where C(*sp*)-I···N halogen bonds and C(*sp*)-H···N hydrogen bonds crosslink the pyrimidine molecules into infinite chains indicating the synthon mimicry of C(*sp*)-I···N halogen bonds and C(*sp*)-H···N hydrogen bonds. This structural similarity was reproducible when **Hpym** and **Ipym** were co-crystalized with a different acceptor, **BPE** which again points that C(*sp*)-H···N hydrogen bonds can act as C(*sp*)-I···N synthon mimics (Figure 4.25).

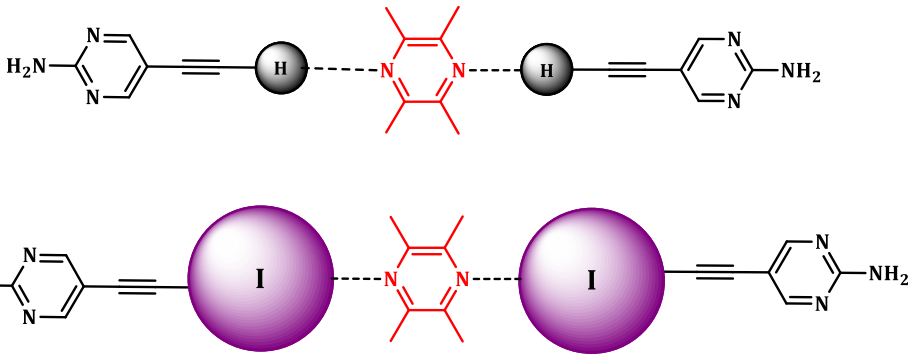

HPym·TMP and **IPym·TMP**

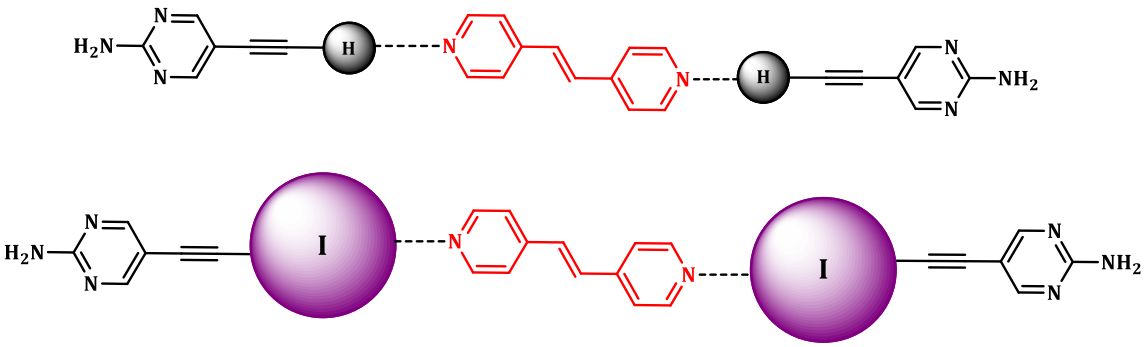

HPym·BPE and **IPym·BPE**

Figure 4.25 Representation of **IPym** and **HPym** interacting with two acceptors, **TMP** and **BPE**

In each case, halogen bonding occurs with C*(sp)*-I···N distances 2.897(2) Å and 2.7859(17) Å for **TMP** and **BPE**, respectively (Table 4.4), which are considerably shorter than sum of van der Waal radii for nitrogen (1.55 Å) and iodine (1.98 Å) atoms. The C*(sp)*-H···N distance in structures 2.414(16) Å in **Hpym·TMP** and 2.341(18) Å, 2.277(18) Å in **Hpym·BPE** are also shorter than sum of van der Waal radii for nitrogen (1.55 Å) and hydrogen (1.20 Å).

Table 4.4 Key geometric parameters in structures **Hpym** and **Ipym**

Structure	C-I···N (Å)	C-I···N (°)
Ipym·TMP	2.897(2)	176.76(11)
Ipym·BPE	2.7859(17)	175.11(7)
	C-H···N (Å)	**C-H···N (°)**
Hpym·TMP	2.414(16)	166.2(14)
Hpym·BPE	2.341(18)	169.0(15)
		170.5(15)

When the co-crystal structures of **Hpym** and **Ipym** are analyzed more closely (Table 4.5), **Ipym·TMP** and **Hpym·TMP** are isostructural with the same space group with triclinic crystal system. **Ipym·BPE** and **Hpym·BPE** has different monoclinic and triclinic structures with P2(1)/c and P-1 space group respectively. The density of **Ipym·TMP** and **Ipym·BPE** is higher than **Hpym·TMP** and **Hpym·BPE** as expected due to the high atomic mass of iodine.

Table 4.5 Co-crystal structural comparison between **Hpym** and **Ipym**

	Space group	Crystal system	Volume (Å^3)	Density (g/cm^3)
Ipym·TMP	P-1	Triclinic	560.46(8)	1.855
Hpym·TMP	P-1	Triclinic	502.2(3)	1.238
Ipym·BPE	P2(1)/c	Monoclinic	1200.9(2)	1.859
Hpym·BPE	P-1	Triclinic	1033.84(18)	1.351

4.4.4 Structural comparison with CSD

A search for relevant analogous structures in CSD revealed two pairs of molecules with the same acceptor, 4,4-bipyridine with the hydrogen and halogen bond donors 1,4-bisethynylbenzene (RUXMAZ)[22] and 1,4-diiodoethynylbenzene (MB1201)[23]. The co-crystals of **Ipym** and **Hpym** are compared with the reported co-crystals, RUXMAZ and MB1201 (Figure 4.26).

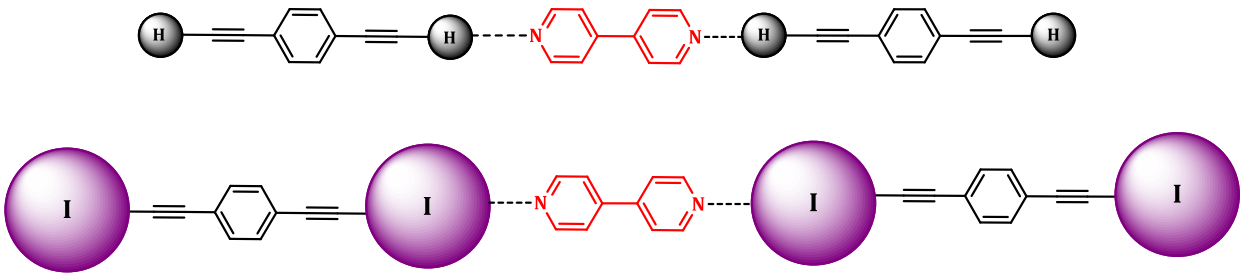

Figure 4.26 Representation of the co-crystals RUXMAZ and MB1201

The co-crystal of 1,4-bisethynylbenzene and 4,4-bipyridine exhibits C*(sp)*-H···N hydrogen bonds, the distance of C-H···N is 2.264 Å which is slightly less than sum of van der Waals radii (2.75 Å) and the C-H···N angle is 174.9°. The co-crystal of 1,4-diiodoethynylbenzene and 4,4-bipyridine shows C*(sp)*-I···N halogen bonds, the distance of C-I···N is 2.759 Å which is slightly less than sum of van der Waals radii (3.53 Å) and the C-I···N angle is 174.9° (Table 4.6). The geometric parameters are in agreement with the co-crystals of **Hpym** and **Ipym**.

Table 4.6 Key geometric parameters in structures RUXMAZ and MB1201

Structure	C-I···N (Å)	C-I···N (°)
RUXMAZ	2.759	174.9
	C-H···N (Å)	**C-H···N (°)**
MB1201	2.264	174.9

The chains of both hydrogen bonded and halogen bonded assemblies arrange in such a way that alternate molecules stack together to form the infinite layers of molecules (Figure 4.27). This shows that both hydrogen bonded and halogen bonded assemblies possess analogous behavior to each other and that C(*sp*)-I···N halogen bonds and C(*sp*)-H···N hydrogen bonds act as synthon mimics of each other.

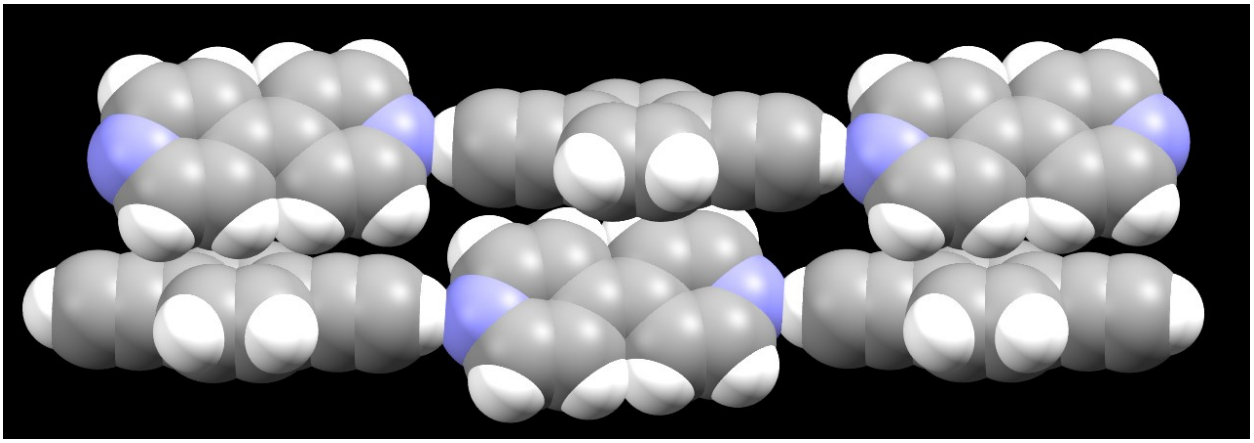

(a)

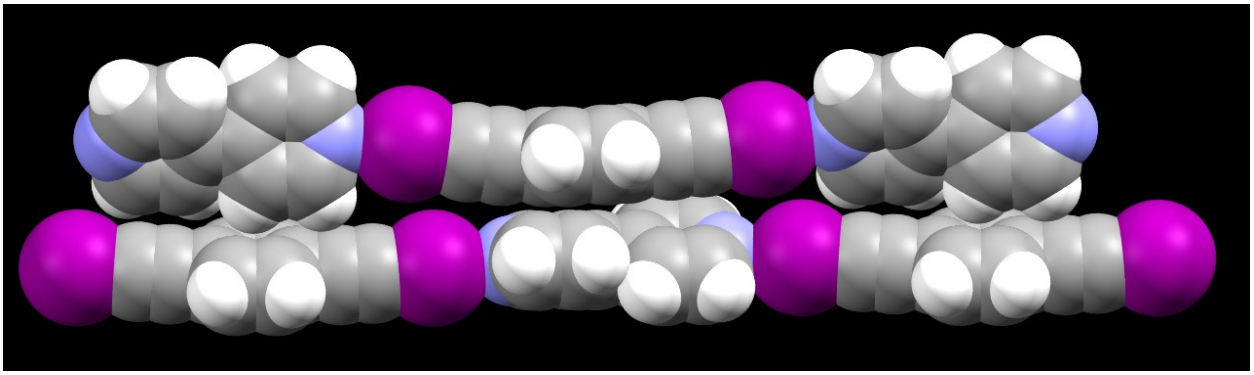

(b)

Figure 4.27 Space filling representation of a portion of the crystal structure (a) The C-H···N hydrogen bonded assembly between 1,4-bisethynylbenzene and 4,4-bipyridine in RUXMAZ (b) The C-I···N halogen bonded assembly between 1,4-bisiodoethynylbenzene and 4,4-bipyridine MB1201

4.5 Conclusions

Our charge calculations and experimental structural data demonstrate that hydrogen atoms and iodine atoms connected to an *sp* hybridized carbon atom act as hydrogen and halogen bond donors. 2-aminopyrimidine backbone provides robust and reliable self-complementary NH···N synthon to investigate the interchangeability of the hydrogen bonding and halogen bonding.

(i) The individual ligands **Hpym** and **Ipym** behave differently to one another; hydrogen of one **Hpym** binds with the amine nitrogen of another molecule which is the best acceptor

whereas the iodine in **Ipym** binds with the π electron cloud of another **Ipym** molecule due to its bigger size hindering the access to the amine nitrogen.

(ii) However, by combining the ligands with a strong acceptor disrupts the homomeric interactions between individual molecules and creates supramolecular assemblies using C(*sp*)-H···N hydrogen bonds and C(*sp*)-I···N halogen bonds.

(iii) Despite the fact that hydrogen and iodine atoms possess drastically different physical and chemical characteristics with respect to each other, they share a common electrostatic potential which could potentially influence non-covalent interaction geometries in solid state. We have been able to prove that ethynyl proton is capable of acting as a synthon mimic of ethynyl iodine by interchangeable C(*sp*)-H···N hydrogen bonds and C(*sp*)-I···N halogen bonds.

The versatility of halogen bonding has been recognized in light responsive functional materials where low-molecular-weight halogen-bonded polymeric complexes were found to be exceptionally efficient and reproducible. These low-molecular-weight halogen-bonded polymeric complexes facilitate the mass transport which increases the dynamics towards equilibrium, compared to high molecular weight complexes.[20a, 24] Possible interchangeability of C(*sp*)-H···N hydrogen bonds and C(*sp*)-I···N halogen bonds provides opportunities to employ C(*sp*)-H···N hydrogen bonds in the place of C(*sp*)-I···N halogen bonds which enables even lower molecular weight photoresponsive supramolecular complexes. The structural similarities offered by these synthons also proves that, by replacing the I atom by a H atom, the macroscopic properties (i.e. mass) of a system can be modulated, without changing the integrity of the system. Haloprogin, an antifungal agent, has been exploited in terms of designing new solid forms using halogen bond based co-crystal design.[4b] The employed C(*sp*)-I···N synthons can be replaced by C(*sp*)-H···N hydrogen bonds (Figure 4.28) to realize same structural motifs with less density offered by the H atom.

The findings of our study provide interesting design strategies for functional materials and drug design with the aid of C(*sp*)-H···N synthon in the place of C(*sp*)-I···N synthon to create low weight and less density materials.

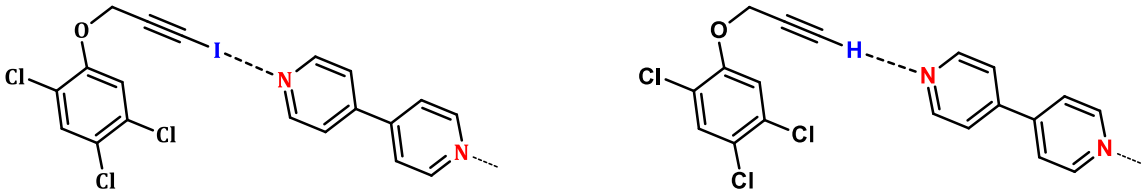

Figure 4.28 Interchangeability of the C(*sp*)-I···N and C(*sp*)-H···N synthons in haoprogin co-crystals

4.6 References

1. Metrangolo, P.; Neukirch, H.; Pilati, T.; Resnati, G. *Acc. Chem. Res.* **2005,** *38* (5), 386-395.

2. (a) Zou, J.-W.; Jiang, Y.-J.; Guo, M.; Hu, G.-X.; Zhang, B.; Liu, H.-C.; Yu, Q.-S. *Chem. Eur. J.* **2005,** *11* (2), 740-751; (b) Bouchmella, K.; Boury, B.; Dutremez, S. G.; van der Lee, A. *Chem. Eur. J.* **2007,** *13* (21), 6130-6138.

3. Aakeröy, C. B.; Baldrighi, M.; Desper, J.; Metrangolo, P.; Resnati, G. *Chem. Eur. J.* **2013,** *19* (48), 16240-16247.

4. (a) Baldrighi, M.; Cavallo, G.; Chierotti, M. R.; Gobetto, R.; Metrangolo, P.; Pilati, T.; Resnati, G.; Terraneo, G. *Mol. Pharm.* **2013,** *10* (5), 1760-1772; (b) Baldrighi, M.; Bartesaghi, D.; Cavallo, G.; Chierotti, M. R.; Gobetto, R.; Metrangolo, P.; Pilati, T.; Resnati, G.; Terraneo, G. *CrystEngComm* **2014,** *16* (26), 5897-5904.

5. (a) Yamamoto, H. M.; Yamaura, J.-I.; Kato, R. *J. Am. Chem. Soc.* **1998,** *120* (24), 5905-5913; (b) Yamamoto, H. M.; Maeda, R.; Yamaura, J.-I.; Kato, R. *J. Mater. Chem.* **2001,** *11* (4), 1034-1041; (c) M. Yamamoto, H.; Yamaura, J.-i.; Kato, R. *J. Mater. Chem.* **1998,** *8* (1), 15-16; (d) Ghassemzadeh, M.; Harms, K.; Dehnicke, K. *Chem. Ber.* **1996,** *129* (2), 259-262; (e) Barres, A.-L.; El-Ghayoury, A.; Zorina, L. V.; Canadell, E.; Auban-Senzier, P.; Batail, P. *Chem. Commun.* **2008,** (19), 2194-2196; (f) González, L.; Gimeno, N.; Tejedor, R. M.; Polo, V.; Ros, M. B.; Uriel, S.; Serrano, J. L. *Chem. Mater.* **2013,** *25* (22), 4503-4510.

6. (a) West, K.; Wang, C.; Batsanov, A. S.; Bryce, M. R. *J. Org. Chem.* **2006,** *71* (22), 8541-8544; (b) J. Langley, P.; Hulliger, J.; Thaimattam, R.; R. Desiraju, G. *New J. Chem.* **1998,** *22* (12), 1307-1309.

7. http://periodictable.com/Elements/053/data.html

8. Saha, B. K.; Nangia, A. *Cryst. Growth Des.* **2007,** *7* (2), 393-401.

9. (a) Weiss, H.-C.; Blaser, D.; Boese, R.; M. Doughan, B.; M. Haley, M. *Chem. Commun.* **1997,** (18), 1703-1704; (b) Weiss, H.-C.; Boese, R.; Weiss, H.-C.; L. Smith, H.; M. Haley, M. *Chem. Commun.* **1997,** (24), 2403-2404; (c) M. A. Robinson, J.; M. Kariuki, B.; D. M. Harris, K.; Philp, D. *J. Chem. Soc., Perk. Trans. 2* **1998,** (11), 2459-2470; (d) Robinson, J. M. A.; Kariuki, B. M.; Gough, R. J.; Harris, K. D. M.; Philp, D. *J. Solid State Chem.* **1997,** *134* (1), 203-206; (e) Robinson, J. M. A.; Philp, D.; Harris, K. D. M.; Kariuki, B. M. *New J. Chem.* **2000,** *24* (10), 799-806.

10. Scheinbeim, J.; Schempp, E. *Acta Crystallogr., Sect. B: Struct. Sci.* **1976,** *32* (2), 607-609.

11. Rajbanshi, A. supramolecular interactions from small-molecule selectivity to molecular capsules. Kasas State University, May, 2010

12. Zhang, Y.-J.; Shen, L.-L.; Cheon, H.-G.; Xu, Y.-N.; Jeong, J.-H. *Arch. Pharmacal Res.* **2014,** *37* (5), 588-599.

13. Jude, H.; Sinclair, D. J.; Das, N.; Sherburn, M. S.; Stang, P. J. *J. Org. Chem.* **2006,** *71* (11), 4155-4163.

14. Fellig, J.; Barnes, J. R.; Rachlin, A. I.; O'Brien, J. P.; Focella, A. *J. Agric. Food. Chem.* **1970,** *18* (1), 78-80.

15. Friščić, T.; Trask, A. V.; Jones, W.; Motherwell, W. D. S. *Angew. Chem. Int. Ed.* **2006,** *45* (45), 7546-7550.

16. APEX2 v2013.10.0 © 2005 - 2013, Bruker AXS, Madison, WI.

17. APEX2 v2013.10.0 © 2005 - 2013, Bruker AXS, Madison, WI.

18. APEX2 v2013.10.0 © 2005 - 2013, Bruker AXS, Madison, WI.

19. APEX2 v2013.10.0 © 2005 - 2013, Bruker AXS, Madison, WI.

20. (a) Priimagi, A.; Saccone, M.; Cavallo, G.; Shishido, A.; Pilati, T.; Metrangolo, P.; Resnati, G. *Adv. Mater.* **2012,** *24* (44), OP345-OP352; (b) Priimagi, A.; Cavallo, G.; Forni, A.; Gorynsztejn–Leben, M.; Kaivola, M.; Metrangolo, P.; Milani, R.; Shishido, A.; Pilati, T.; Resnati, G.; Terraneo, G. *Adv. Funct. Mater.* **2012,** *22* (12), 2572-2579; (c) Fox, D.; Metrangolo, P.; Pasini, D.; Pilati, T.; Resnati, G.; Terraneo, G. *CrystEngComm* **2008,** *10* (9), 1132-1136.

21. (a) Steiner, T. *J. Chem. Soc., Chem. Commun.* **1995,** (1), 95-96; (b) Eaton, P. E.; Galoppini, E.; Gilardi, R. *J. Am. Chem. Soc.* **1994,** *116* (17), 7588-7596; (c) Benghiat, V.; Leiserowitz, L.; Schmidt, G. M. J. *J. Chem. Soc., Perk. Trans. 2* **1972,** (12), 1769-1772; (d) Benghiat, V.; Leiserowitz, L. *J. Chem. Soc., Perk. Trans. 2* **1972,** (12), 1772-1778.

22. Bosch, E. *Cryst. Growth Des.* **2010,** *10* (8), 3808-3813.

23. Michele Baldrighi, Private Communication

24. (a) Houbenov, N.; Milani, R.; Poutanen, M.; Haataja, J.; Dichiarante, V.; Sainio, J.; Ruokolainen, J.; Resnati, G.; Metrangolo, P.; Ikkala, O. *Nat Commun* **2014,** *5*; (b) Virkki, M.; Tuominen, O.; Forni, A.; Saccone, M.; Metrangolo, P.; Resnati, G.; Kauranen, M.; Priimagi, A. *J. Mater. Chem. C* **2015,** *3* (13), 3003-3006.

Chapter 5 - Halogen bond driven anion recognition and coordination using bishaloethynyl compounds

5.1 Introduction

Anions play an important role in most biological, environmental and chemical processes.[1] Some examples include phosphate ions in nucleic acids and ATP,[2,3] nitrates and phosphates in agricultural industry,[4] pertechnetate ions as radiopharmaceuticals[5] and halides in organic synthesis.[6] However, an excess of anions can have deleterious effects on the environment such as eutrophication of lakes,[7] accumulation of radioactive materials[8] and also on health issues such as cystic fibrosis.[9] Anion recognition is challenging for several reasons. First, anions are larger than their isoelectronic cations, therefore, the charge density is low and the electrostatic potential is thus less effective. Secondly, at low pH the anions can get protonated and compete with the selective recognition process. Therefore, the design of hosts for anions need to be carefully tailored to achieve high selectivity and high affinity.

Anion recognition has been achieved using a vast number of receptors through hydrogen bonding,[10] metal-coordination,[11] anion – π interactions[12] and ionic bonds with positively charged receptors (polyammonium, guanidinium, and imidazolium cations).[13] Halogen bonding interactions which occur between a halogen atom and an electronegative atom has drawn particular interest as a potential tool in anion coordination in solid state supramolecular chemistry. The increased electron density on the halogen bond acceptor increases the Lewis basicity and thus make strong and directional halogen bonds. Therefore, anions are better halogen bond acceptors than neutral species, having greater binding affinity towards halogen bond donors.[14]

Iodoperfluoroalkanes being inherently good electron acceptors, have been effectively directing the halogen bonded assemblies in anion driven recognition process, giving rise to many applications. For example, ω-Diiodoperfluoroalkanes which are useful intermediates for the synthesis of fluoro-containing resins, elastomers, and surfactants, have been employed for separation and purification process using anion coordination.[15] Also, iodoperfluoroalkanes find applications in radioactive waste management via anion coordination in cryptation, extraction, and recovery in the fluorous phase of radioactive metal cations[16] and development of selective ion channels or dynamic porous materials.[17] Likewise, the design and synthesis of

iodofluoroarenes based halogen bond receptors has been reported with applications in anion binding.[18]

The supramolecular architectures of halogen bond based anion coordination can be classified into two main groups in order to identify the number of halogen bonds formed by a given anion depending on the composition of the system, the structure of interacting components, and the overall geometric and electronic requirements in the crystal packing. Therefore, the XB based anionic assemblies fall into either heteromeric two-component systems or heteromeric three-component systems (Figure 5.1).[19]

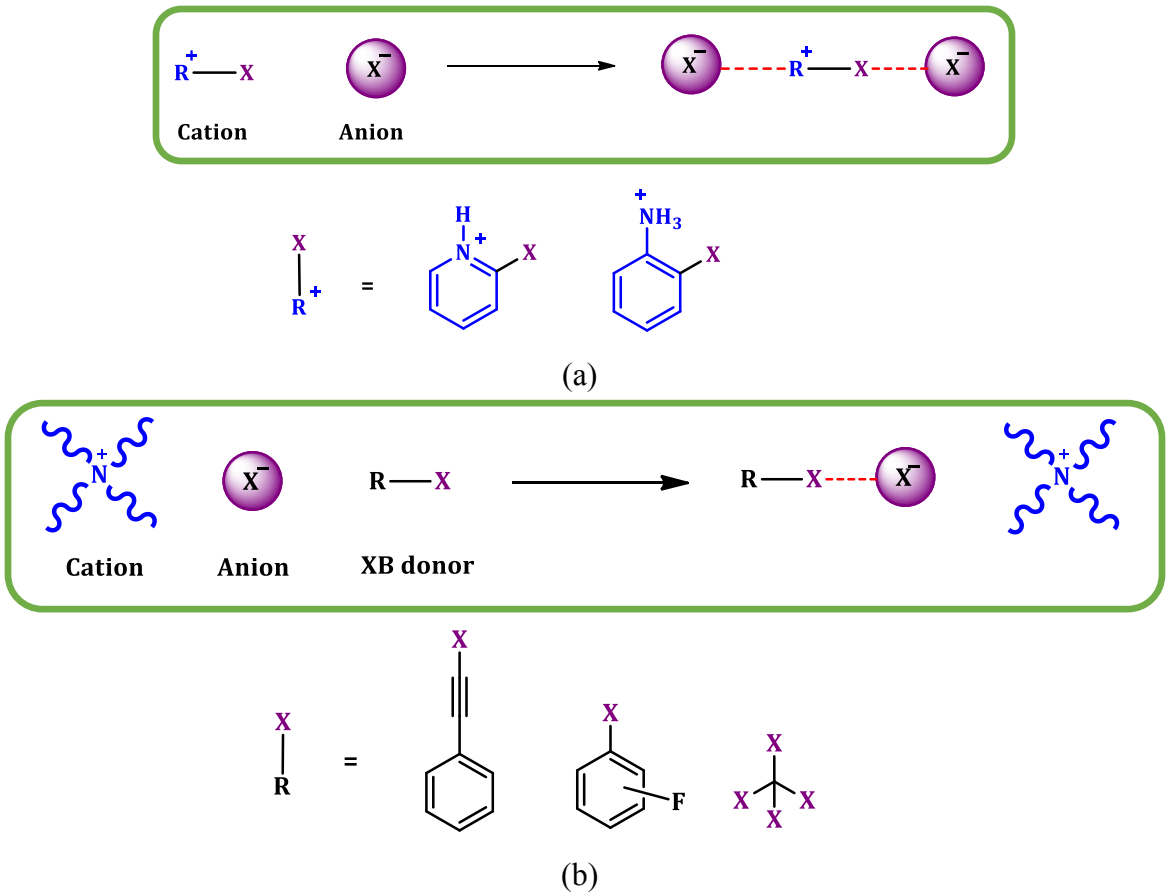

Figure 5.1 (a) Heteromeric two-component system (b) Heteromeric three-component system in XB based anion coordination

In heteromeric two-component systems, the positive and negative charges of the crystal lattice are balanced by the number of halogen bonds formed by the anion, therefore, the anion play the role of the XB-acceptor and the halogenated organic cation acts as the XB-donor moiety (Figure 5.1a). In heteromeric three-component systems, weakly coordinating cations are

employed, and halogen bonding takes place between an anion and a XB donor while the cation does not participate (Figure 5.1b), therefore, these systems are better tailored to study the ability of the anions to template the XB-donor partner(s).

Halides are spherical anions that can be tailored to form a variety of halogen bonded supramolecular architectures. The topology of the halogen bonded (XB) supramolecular halide ion is strictly dependent on the number of halogen bonds formed, the geometry around the anion and the nature and size of the counter cation.[19]

The number of halogen bonds formed by a given halide is a key factor in anion coordination. It can vary as a function of the composition of the system, the molecular structure of the donor sites, and the overall geometric and electronic requirements in the crystal packing. Halides usually have a moderate bias and therefore, frequently give rise to two or three halogen bonds,[18a, 20] but careful crystal engineering can make the halide form other coordination numbers (CN), (Figure 5.2).[21]

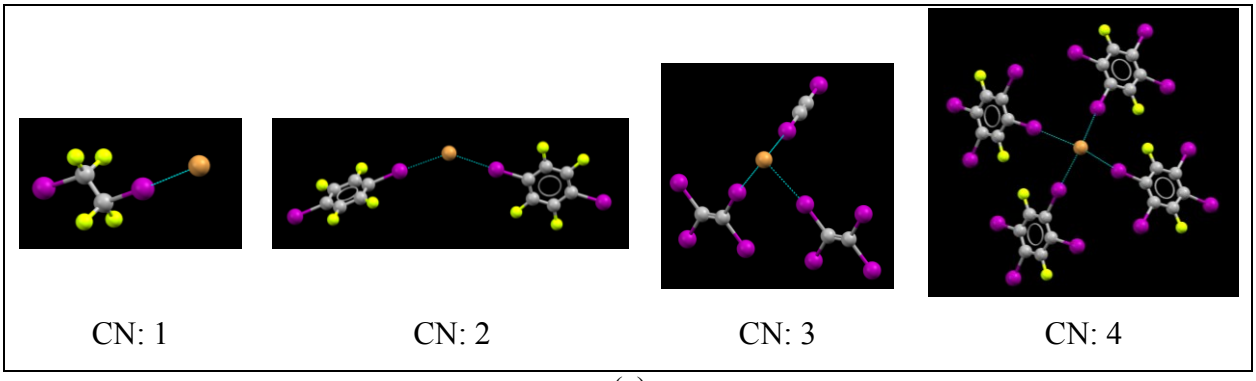

(a)

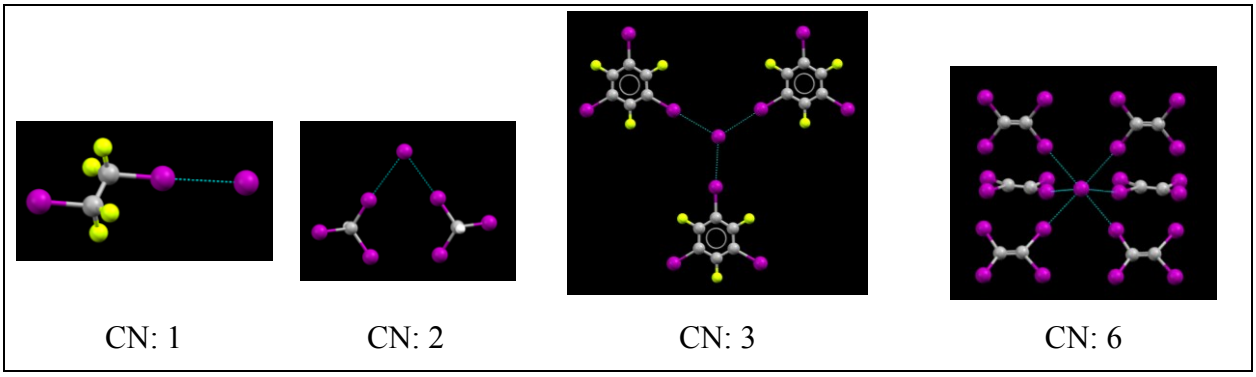

(b)

Figure 5.2 Different coordination numbers around (a) bromides[14, 21f, 22] and (b) iodides[21f, 23]

The geometry around the halide ion, (Ar)R–X···Y$^-$···X–R(Ar) varies from 60º-180º (Figure 5.3) which is different to the high linearity of the angle formed in the covalent bond and the halogen bond formed by the XB donor atom, Y$^-$···X–R(Ar).[19] The cation nature and size also influence the topology of the halogen bonded anion assembly. The anion tends to act as an XB acceptor and forms a greater number of halogen bonds when the anion is paired with a weakly coordinating cations.[24]

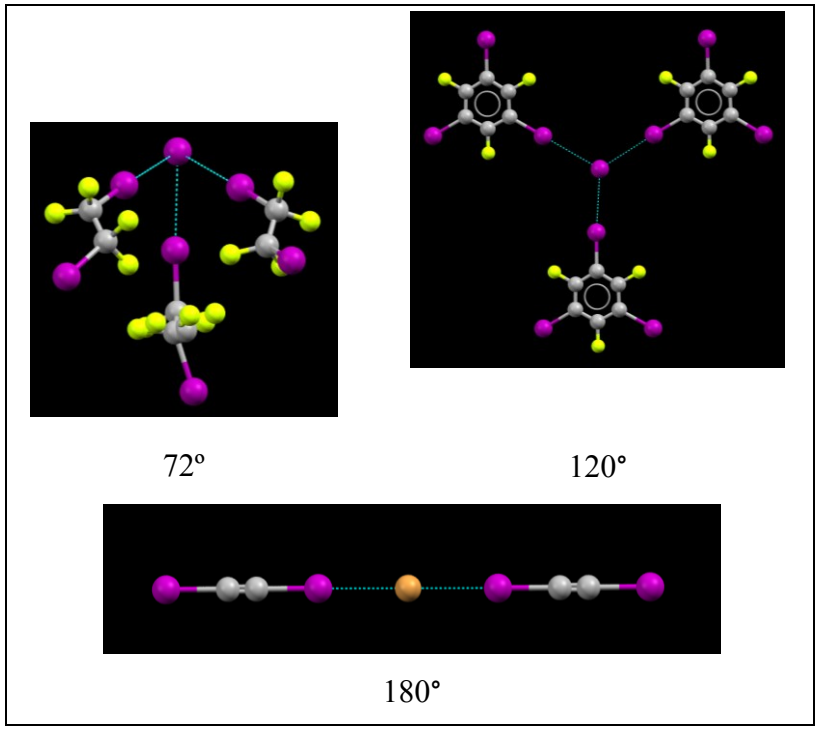

Figure 5.3 Different coordination geometries around iodides[23b, 25] and bromides[21f]

The haloperfluoroarenes are reliable and robust tectons in anion binding and coordination.[24] The crystal structures reported are heteromeric three component systems where the cation acts as the weakly coordinating species, iodide or bromide as the halogen bond acceptor and the haloperfluoroarene as the halogen bond donor. These supramolecular assembly can be arranged in two different ways, first, the fluorinated aromatic rings can aggregate (Chapter 3) away from the cations and anions (Figure 5.4a) and secondly there is no fluorine aggregation and all three components are mixed together in the crystal lattice (Figure 5.4b).

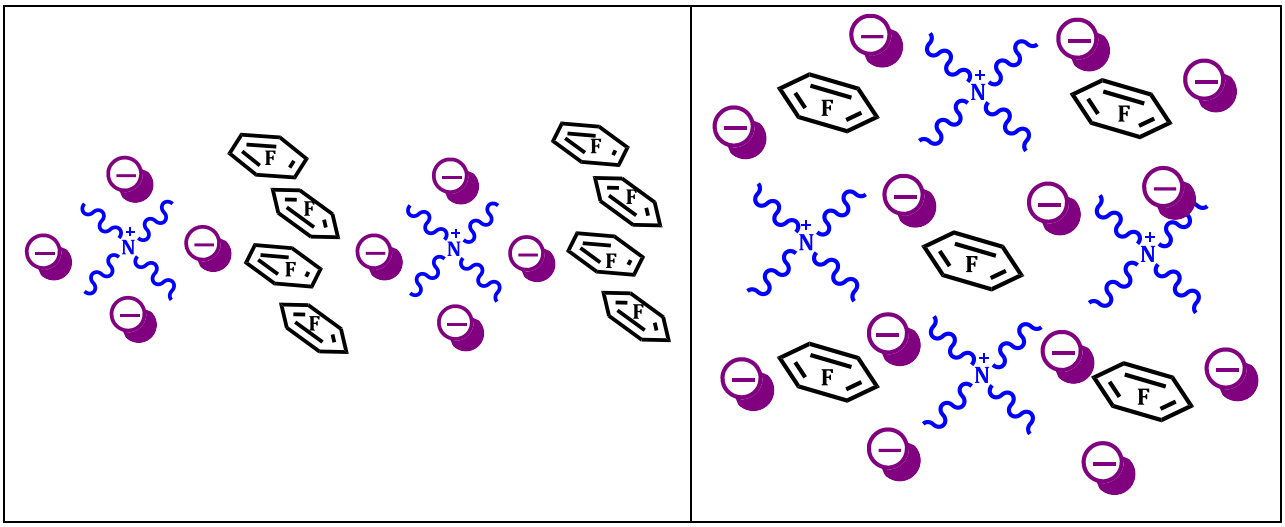

Figure 5.4 The possible arrangements of halogen bond driven anion supramolecular assembly (a) fluorine aggregated assembly (b) cation, anion and the donor assorted arrangement

As demonstrated in Chapter 4, a halogen atom next to an *sp* hybridized C atom also acts as a halogen bond donor and similarly functionalized 1,4-*bis*(iodoethynyl)benzene) and derivatives have been utilized in anion based halogen bonds for introducing molecular conductors containing supramolecular assemblies (Figure 5.5).[21f, 26]

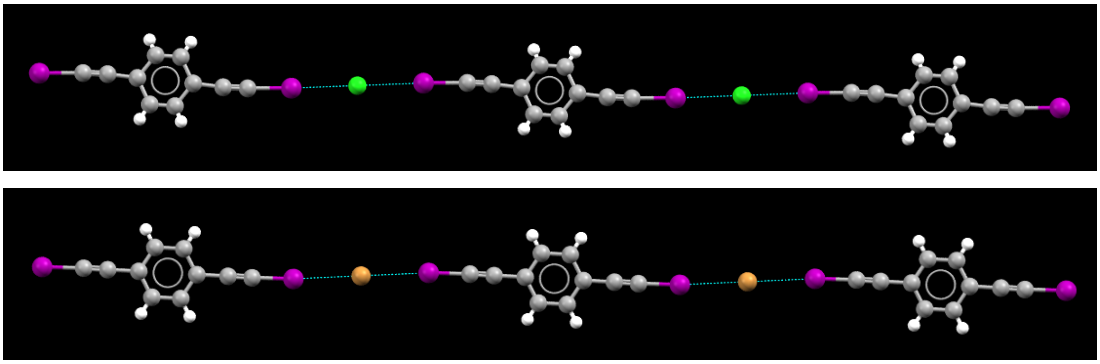

Figure 5.5 1,4-*bis*(iodoethynyl)benzene) forming halogen bonds with Cl^- and Br^- ions

However, very little work with 1,4-*bis*(haloethynyl)benzene derivatives on anion binding has been reported to date. Since haloethynyl moiety is an alternative halogen bond donor candidate for anion binding, it is useful to investigate the binding preferences of this functionality towards different anions. Also, it is interesting to explore the similarities and/or

differences of these 1,4-*bis*(haloethynyl)benzene - anion driven supramolecular assemblies with respect to the perfluoroarene systems.

Thus, in this current study we investigate the halogen bonding capability of three 1,4-*bis*(haloethynyl)benzene analogous, **CEB** (1,4-*bis*(chloroethynyl)benzene), **BEB** (1,4-*bis*(bromoethynyl)benzene) and **IEB** (*1,4-bis*(iodoethynyl)benzene) (Figure 5.6) towards a series of anions. **IEBP** (4,4'-*bis*(iodoethynyl)-1,1'-biphenyl) analogue was also used as an iodine donor since **IEB** has issues with co-crystallization.

Since heteromeric three component systems can be better tailored towards anion recognition, with no limitations on anion coordination and geometry, a series of tetraalkylammonium salts are chosen as the anions of interest, due to the weakly coordinating nature of the tetraalkylammonium cation (Figure 5.7). There are two iodide salts, seven bromide salts, and one chloride salt in the series.

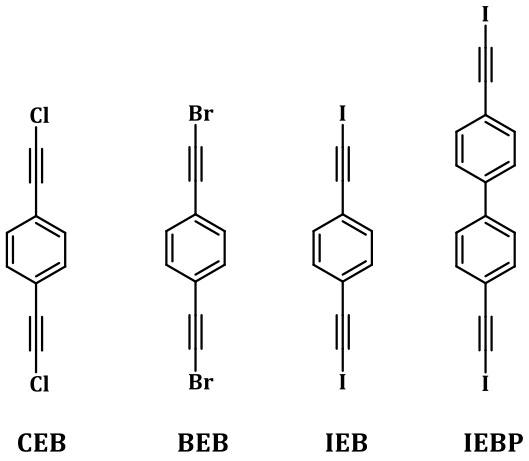

Figure 5.6 1,4-*bis*(haloethynyl)benzene derivatives as symmetric ditopic halogen bond donors

In this chapter we will attempt to answer the following questions:

i) Are 1,4-*bis*(haloethynyl)benzene derivatives capable of forming halogen bonds to halide anions?

ii) Is there a selectivity towards anion recognition that can be achieved from **CEB** vs. **BEB** vs. **IEB**?

iii) Do we observe aromatic π stacking interactions or mixed cation-anion based assembly with these 1,4-*bis*(haloethynyl)benzene derivatives based anion coordination ? Do F···F contacts have any effect in the fluorinated aromatic halogen bond based coordination which does not appear in the former case?

iv) How is the topology of the halogen bonded anion influenced by the number of halogen bonds formed (coordination number), the geometry around the anion and the cation nature and size?

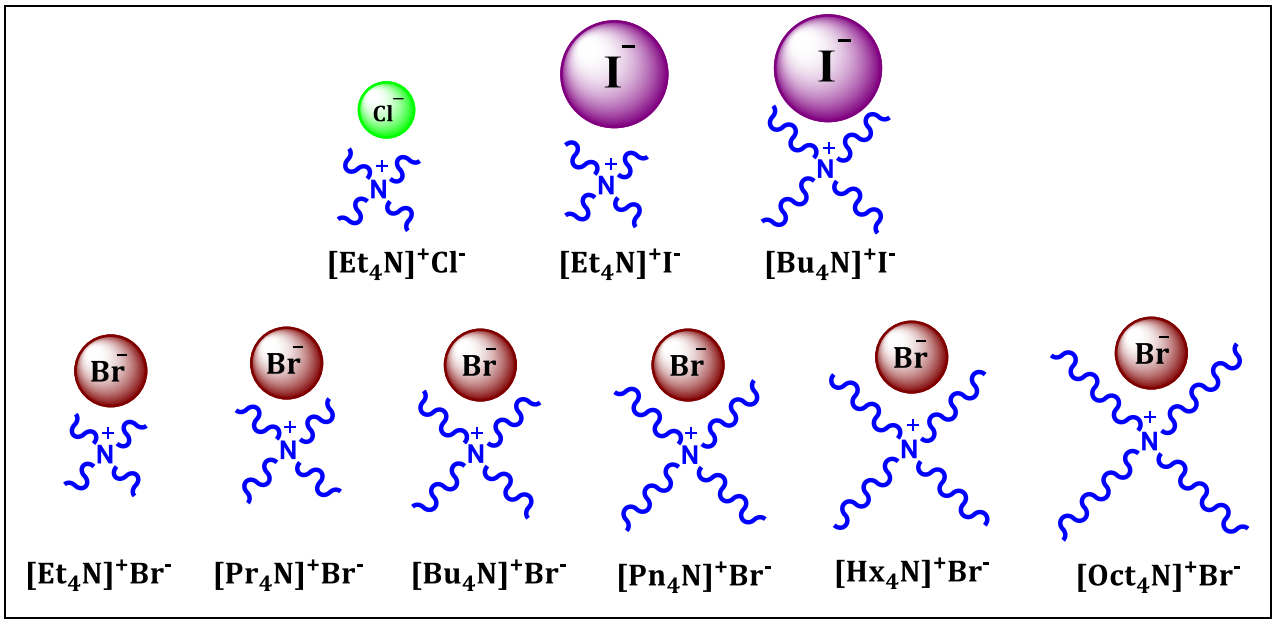

Figure 5.7 Series of tetraalkylammonium halides acting as halogen bond acceptors in this study

5.2 Experimental

5.2.1 Synthesis

All the tetraalkylammonium salts were purchased from Sigma Aldrich, Acros Organics. Column chromatography was carried out on silica gel (150 Å pore size) from Analtech, Inc. ^{1}H and ^{13}C NMR spectra were recorded on a Varian Unity plus 400 MHz spectrometer in $CDCl_3$. Data is expressed in parts per million (ppm) downfield shift from tetramethylsilane as internal reference and are reported as position (in ppm). Melting point/decomposition point determination was done using Fisher-Johns melting point apparatus and are uncorrected. Infrared spectroscopy analysis was carried out using Nicolet 380 FT-IR with a digital resolution of 0.9 cm^{-1}. Data were analyzed using software, Omnic 8.0 © 1992-2008 Thermo Fisher Scientific Inc.

5.2.1.1 Synthesis of 1,4-bis((trimethylsilyl)ethynyl)benzene[27]

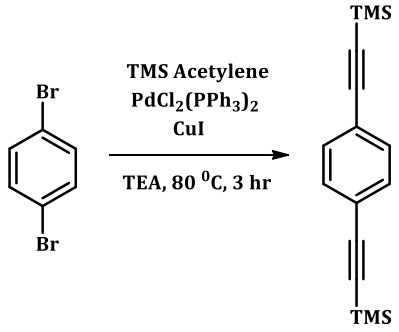

1,4-Dibromobenzene (8.2 g, 34.7 mmol) was dissolved in triethylamine (250 mL) and degassed by bubbling nitrogen through the reaction mixture. TMS-acetylene (6.81 g, 69.4 mmol), $PdCl_2(PPh_3)_2$ (2.43 g, 3.47 mmol) and CuI (1.32 g, 6.94 mmol) were added and the mixture was heated under reflux at 70 ºC overnight. The solvent was removed by evaporation and the residue was dissolved in diethyl ether (500 mL), washed with 1 M HCl (100 mL) and brine (100 mL). The organic layer was separated and dried over anhydrous magnesium sulfate. The solvent was removed on a rotary evaporator and the residue was chromatographed on silica with hexane: ethyl acetate mixture as eluent to obtain a light brown colored powder. The crude product was purified by flash column chromatography with hexanes as the eluent, to give pure 1,4-*bis*((trimethylsilyl)ethynyl)benzene as colorless crystalline powder (7.3 g, 77.8 %). ^{1}H NMR (δH; 200 MHz, $CDCl_3$): 7.39 (s, 4H), 0.25 (s, 18H).

5.2.1.2 Synthesis of 1,4-bis(ethynyl)benzene[28]

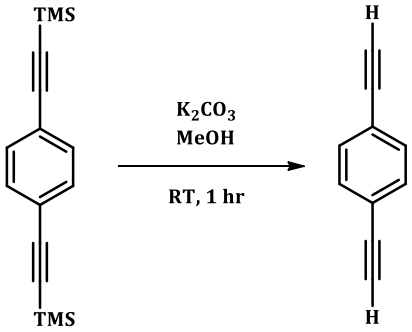

1,4-*Bis*((trimethylsilyl)ethynyl)benzene (2.3 g, 8.5 mmol) and potassium carbonate (1.23 g, 8.92 mmol) were stirred in methanol at room temperature for 2 hrs. Upon completion, the solvent was removed by rotary evaporation and the residue dissolved in diethyl ether and washed with water (2 x 50 mL). The combined organic layers were dried over anhydrous magnesium sulfate and concentrated via rotary evaporation to obtain the product, 1,4-*bis*(ethynyl)benzene, as

a yellow crystalline solid. (0.99 g, 93%). ^{1}H NMR (δH; 200 MHz, $CDCl_3$): 7.45 (s, 4H), 3.18 (s, 2H). IR (Zn ATR crystal): υ 2192, 1904, 1656, 1499, 1399, 1263, 1176, 1098, 826 cm^{-1}.

5.2.1.3 Synthesis of 1,4-bis(iodoethynyl)benzene, IEB[29]

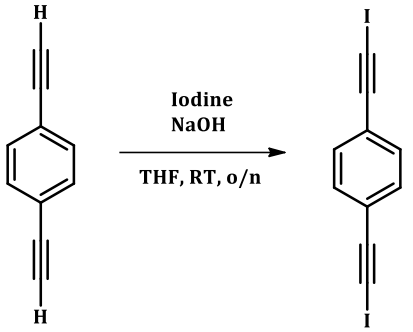

To a solution of 1,4-*bis*(ethynyl)benzene (0.85 g, 6.73 mmol) dissolved in methanol (50 mL), added dropwise simultaneously a concentrated solution of iodine in methanol (2.25 g, 8.87 mmol) and a 10% sodium hydroxide solution over 30 min, vigorously stirring. The mixture was stirred overnight, and quenched with 100 mL water upon which a light yellow color precipitate forms. The filtered solid washed with sodium bisulfite solution afforded orange color powder of **IEB**, (2.19 g, 86%). Dec.124 ˚C. ^{1}H NMR (δH; 200 MHz, $CDCl_3$): 7.37 (s, 4H). IR (Zn ATR crystal): υ 2162, 1905, 1786, 1698, 1599, 1362, 1212, 1181, 1116, 1028, 904 cm^{-1}.

5.2.1.4 Synthesis of 4,4'-bis((trimethylsilyl)ethynyl)-1,1'-biphenyl[27]

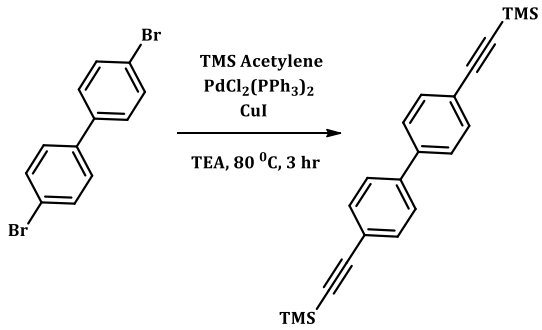

4,4'-Dibromo-1,1'-biphenyl (4.05 g, 12.9 mmol) was dissolved in triethylamine (150 mL) and degassed by bubbling nitrogen through the reaction mixture. TMS-acetylene (2.54 g, 25.9 mmol), $PdCl_2(PPh_3)_2$ (0.90 g, 1.29 mmol) and CuI (0.49 g, 2.58 mmol) were added and the mixture was refluxed at 70 ºC overnight. The solvent was removed by evaporation and the residue dissolved in diethyl ether (250 mL), was washed with 1 M HCl (100 mL) and brine (100 mL). The organic layer was separated and dried over anhydrous magnesium sulfate. The solvent

was removed on a rotary evaporator and the residue was chromatographed on silica with hexane: ethyl acetate mixture as eluent to obtain a light brown colored powder. The crude product was purified by flash column chromatography with hexanes as the eluent, to give pure 4,4'-*bis*((trimethylsilyl)ethynyl)-1,1'-biphenyl as colorless crystalline powder (3.59 g, 80.4 %). ^{1}H NMR (δH; 200 MHz, $CDCl_3$): 7.61-7.65 (m, 8H), 0.22 (s, 18H).

5.2.1.5 Synthesis of 4,4'-diethynyl-1,1'-biphenyl[28]

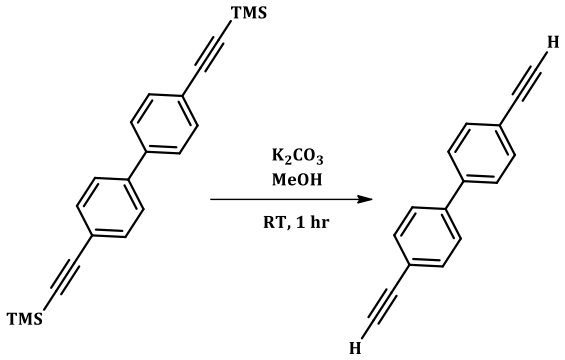

4,4'-*Bis*((trimethylsilyl)ethynyl)-1,1'-biphenyl (3.4 g, 9.8 mmol) and potassium carbonate (1.42 g, 10.28 mmol) were stirred in methanol at room temperature for 2 hrs. Upon completion, the solvent was removed by rotary evaporation and the residue dissolved in diethyl ether and washed with water (2 x 50 mL). The combined organic layers were dried over anhydrous magnesium sulfate and concentrated via rotary evaporation to obtain the product, 4,4'-diethynyl-1,1'-biphenyl, as a yellow crystalline solid. (1.72 g, 87%). ^{1}H NMR (δH; 200 MHz, $CDCl_3$): 7.54-7.60 (m, 8H), 3.16 (s, 2H).

5.2.1.6 Synthesis of 4,4'-bis(iodoethynyl)-1,1'-biphenyl, IEBP[29]

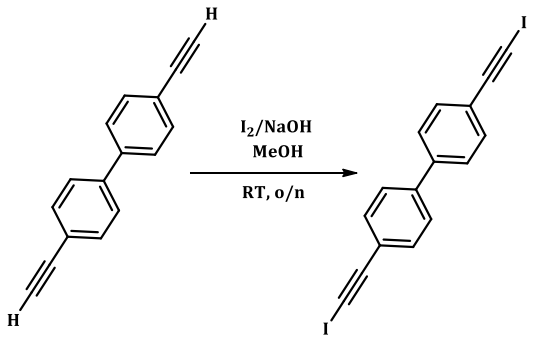

To a solution of 4,4'-diethynyl-1,1'-biphenyl (1.5 g, 7.4 mmol) dissolved in methanol (50 mL), added a concentrated solution of iodine in methanol (2.47 g, 9.75 mmol) and a 10% sodium hydroxide solution over 30 min, under vigorous stirring. The mixture was stirred overnight, and

quenched with 100 mL water upon which a light yellow color precipitate forms. The filtered solid washed with sodium bisulfite solution afforded orange color powder of **IEBP** (2.75 g, 82%). Dec.182 ˚C. ^{1}H NMR (δH; 200 MHz, $CDCl_3$): 7.50-7.56 (m, 8H) IR (Zn ATR crystal): υ 3033, 2916, 2159, 1920, 1605, 1486, 1431, 1392, 1220, 1004, 822 cm^{-1}.

5.2.1.7 Synthesis of 1,4-bis(chloroethynyl)benzene, *CEB*[30]

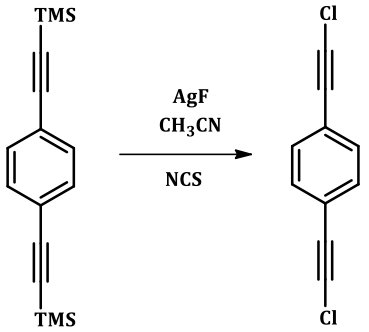

1,4-*Bis*((trimethylsilyl)ethynyl)benzene (2.4 g, 8.87 mmol) and AgF (2.25 g, 17.74 mmol) was placed in round-bottomed flask and CH_3CN (200 mL) was added. The mixture was stirred under purging nitrogen for 20 minutes. The flask was wrapped in aluminum foil and under dark conditions, NCS (2.37 g, 17.74 mmol) was added. The mixture was stirred for overnight at room temperature after which time it was passed through a 2 cm plug of silica gel. The solvent was removed by rotary evaporation. The resulting residue was dissolved in Et_2O and washed with H_2O (50 mL). The organic part was separated, dried with Na_2SO_4 and the solvent was removed under vacuum to yield off white powder of **CEB** in 54 % yield (0.93 g, 4.79 mmol). Dec. 89 °C; ^{1}H NMR (δH; 200 MHz, $CDCl_3$): 7.40 (s, 4H) IR (Zn ATR crystal): υ 2214, 1904, 1664, 1643, 1541, 1404, 1325, 1287, 1236, 1017, 957, 864 cm^{-1}.

5.2.1.8 Synthesis of 1,4-bis(bromoethynyl)benzene, BEB[30]

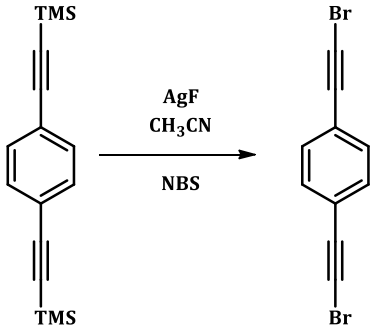

1,4-*Bis*((trimethylsilyl)ethynyl)benzene (1.5 g, 5.54 mmol) and AgF (1.61 g, 11.08 mmol) was placed in round-bottomed flask and CH_3CN (200 mL) was added. The mixture was stirred under purging nitrogen for 20 minutes. The flask was wrapped in aluminum foil and under dark conditions, NBS (1.97 g, 11.08 mmol) was added. The mixture was stirred for overnight at room temperature after which time it was passed through a 2 cm plug of silica gel. The solvent was removed by rotary evaporation. The resulting residue was dissolved in Et_2O and washed with H_2O (50 mL). The organic part was separated, dried with Na_2SO_4 and the solvent was removed under vacuum to yield brown color crystals of **BEB** in 57 % yield (0.89 g, 3.13 mmol). M.p. 103˚C. ^{1}H NMR (δH; 200 MHz, $CDCl_3$): 7.39 (s, 4H). IR (Zn ATR crystal): υ 2192, 1906, 1779, 1659, 1502, 1483, 1400, 1362, 1264, 1102, 1017, 826, 743 cm^{-1}.

5.2.2 Synthesis of co-crystals

The halogen bond donor molecules, **CEB**, **BEB**, **IEB** and **IEBP** were subjected to co-crystallization experiments with ten different tetraalkyl ammonium salts. We used two iodides, tetraethyl ammonium iodide **$[Et_4N]^+I^-$** and tetrabutyl ammonium iodide **$[Bu_4N]^+I^-$**, six bromides, tetraethyl ammonium bromide **$[Et_4N]^+Br^-$**, tetrapropyl ammonium bromide **$[Pr_4N]^+Br^-$**, tetrabutyl ammonium bromide **$[Bu_4N]^+Br^-$**, tetrapentyl ammonium bromide **$[Pn_4N]^+Br^-$**, tetrahexyl ammonium bromide **$[Hx_4N]^+Br^-$**, tetraoctyl ammonium bromide **$[Oct_4N]^+Br^-$**, and didodcyldimethyl ammonium bromide **$[Dod_4Me_2N]^+Br^-$** and one chloride, tetraethyl ammonium chloride **$[Et_4N]^+Cl^-$**.

The co-crystals were synthesized using solvent assisted grinding[31] where the halogen bond donors were mixed in a 1:5 stoichiometric ratio with each of the ten different tetraalkyl ammonium salts and ground together using a drop of methanol until a solid paste was obtained. The resulting solid from each of the 40 reactions (4x10) were analyzed using attenuated total reflectance (ATR) FTIR spectrometry for the confirmation of co-crystal formation. The solid paste was dissolved in methanol or methanol:THF mixture in 2 dram borosilicate vials and allowed for slow evaporation at room temperature. The single crystals suitable for X-ray diffraction were again analyzed by IR for the confirmation of co-crystal formation. By this method, ten single crystals that are confirmed to be co-crystals.

5.2.2.1 Synthesis of 1,4-bis(iodoethynyl)benzene tetrapropyl ammonium bromide

IEB·[Pr$_4$N]$^+$Br$^-$

1,4-Bis(iodoethynyl)benzene (**IEB**) (0.010 g, 0.026 mmol) and tetrapropyl ammonium bromide, **[Pr$_4$N]$^+$Br$^-$** (0.021 g, 0.079 mmol) were dissolved in methanol in a 2 dram borosilicate vial and allowed for slow evaporation at ambient conditions. After eight days colorless plate shaped crystals were obtained. Dec. 87 ˚C.

5.2.2.2 Synthesis of 1,4-bis(iodoethynyl)benzene tetrabutyl ammonium bromide

IEB·[Bu$_4$N]$^+$Br$^-$

1,4-Bis(iodoethynyl)benzene (**IEB**) (0.010 g, 0.026 mmol) and tetrabutyl ammonium bromide, **[Bu$_4$N]$^+$Br$^-$** (0.025 g, 0.079 mmol) were dissolved in methanol in a 2 dram borosilicate vial and allowed for slow evaporation at ambient conditions. After five days colorless plate shaped crystals were obtained. Dec.102 ˚C.

5.2.2.3 Synthesis of 1,4-bis(iodoethynyl)benzene tetrabutyl ammonium iodide IEB·[Bu$_4$N]$^+$I$^-$

1,4-Bis(iodoethynyl)benzene (**IEB**) (0.010 g, 0.026 mmol) and tetrabutyl ammonium iodide, **[Bu$_4$N]$^+$I$^-$** (0.029 g, 0.079 mmol) were dissolved in methanol in a 2 dram borosilicate vial and allowed for slow evaporation at ambient conditions. After five days colorless plate shaped crystals were obtained. Dec. 115˚C.

5.2.2.4 Synthesis of 4,4'-bis(iodoethynyl)-1,1'-biphenyl tetraethyl ammonium iodide

IEBP·[Et$_4$N]$^+$I$^-$

4,4'-Bis(iodoethynyl)-1,1'-biphenyl (**IEBP**) (0.010 g, 0.022 mmol) and tetraethyl ammonium iodide, **[Et$_4$N]$^+$I$^-$** (0.028 g, 0.11 mmol) were dissolved in methanol in a 2 dram borosilicate vial and allowed for slow evaporation at ambient conditions. After five days colorless plate shaped crystals were obtained. Dec. >200 ˚C.

5.2.2.5 Synthesis of 4,4'-bis(iodoethynyl)-1,1'-biphenyl tetrabutyl ammonium iodide

IEBP·[Bu$_4$N]$^+$I$^-$

4,4'-Bis(iodoethynyl)-1,1'-biphenyl (**IEBP**) (0.010 g, 0.022 mmol) and tetrabutyl ammonium iodide, **[Bu$_4$N]$^+$I$^-$** (0.041 g, 0.11 mmol) were dissolved in methanol in a 2 dram borosilicate vial and allowed for slow evaporation at ambient conditions. After five days colorless plate shaped crystals were obtained. M.p. 132-135 ˚C.

5.2.2.6 Synthesis of 4,4'-bis(iodoethynyl)-1,1'-biphenyl tetrapropyl ammonium bromide *IEBP·[Pr$_4$N]$^+$Br$^-$*

4,4'-Bis(iodoethynyl)-1,1'-biphenyl (**IEBP**) (0.010 g, 0.022 mmol) and tetrapropyl ammonium bromide, **[Pr$_4$N]$^+$Br$^-$** (0.029 g, 0.11 mmol) were dissolved in methanol in a 2 dram borosilicate vial and allowed for slow evaporation at ambient conditions. After five days colorless plate shaped crystals were obtained. Dec. 155 ˚C.

5.2.2.7 Synthesis of 4,4'-bis(iodoethynyl)-1,1'-biphenyl tetrabutyl ammonium bromide *IEBP·[Bu$_4$N]$^+$Br$^-$*

4,4'-Bis(iodoethynyl)-1,1'-biphenyl (**IEBP**) (0.010 g, 0.022 mmol) and tetrabutyl ammonium bromide, **[Bu$_4$N]$^+$Br$^-$** (0.035 g, 0.11 mmol) were dissolved in methanol in a 2 dram borosilicate vial and allowed for slow evaporation at ambient conditions. After five days colorless plate shaped crystals were obtained. M.p. 124-126 ˚C.

5.2.2.8 Synthesis of 4,4'-bis(iodoethynyl)-1,1'-biphenyl tetrapentyl ammonium bromide *IEBP·[Pn$_4$N]$^+$Br$^-$*

4,4'-Bis(iodoethynyl)-1,1'-biphenyl (**IEBP**) (0.010 g, 0.022 mmol) and tetrapentylammonium bromide, **[Pn$_4$N]$^+$Br$^-$** (0.042 g, 0.11 mmol) were dissolved in methanol:THF 1:1 mixture in a 2 dram borosilicate vial and allowed for slow evaporation at ambient conditions. After five days colorless plate shaped crystals were obtained. M.p. 89-92 ˚C.

5.2.2.9 Synthesis of 4,4'-bis(iodoethynyl)-1,1'-biphenyl tetraoctyl ammonium bromide *IEBP·[Oct$_4$N]$^+$Br$^-$*

4,4'-Bis(iodoethynyl)-1,1'-biphenyl (**IEBP**) (0.010 g, 0.022 mmol) and tetraoctylammonium bromide **[Oct$_4$N]$^+$Br$^-$** (0.060 g, 0.11 mmol) were dissolved in methanol:THF 1:1 mixture in a 2 dram borosilicate vial and allowed for slow evaporation at ambient conditions. After five days colorless plate shaped crystals were obtained. M.p. ˚C.

5.2.2.10 Synthesis of 4,4'-bis(iodoethynyl)-1,1'-biphenyl didodecyldimethyl ammonium bromide *IEBP·[Dod$_2$Me$_2$N]$^+$Br$^-$*

4,4'-Bis(iodoethynyl)-1,1'-biphenyl (**IEBP**) (0.010 g, 0.022 mmol) and didodecyldimethyl ammonium bromide **[Dod$_2$Me$_2$N]$^+$Br$^-$** (0.050 g, 0.11 mmol) were dissolved in methanol:THF 1:1 mixture in a 2 dram borosilicate vial and allowed for slow evaporation at

ambient conditions. After five days colorless plate shaped crystals were obtained. M.p. 120-122˚C.

5.3 Results

5.3.1 Characterization by IR spectroscopy

The results of the co-crystallization reactions were screened using IR spectroscopy, paying particular interest to the diagnostic alkynyl group of the halogen bond donor. Usually the occurrence of a halogen bond results in a red shift of the C≡C bond when the iodoethynyl moiety is halogen bonded to a halide.[32] The results of the grinding experiments between the halogen bond donors, **CEB**, **BEB**, **IEB** and **IEBP** and the halogen bond acceptors are shown in Table 5.1.

Table 5.1 C≡C IR stretching frequencies of the supramolecular complexes

	CEB (2214 cm^{-1})	**BEB** (2192 cm^{-1})	**IEB** (2162 cm^{-1})	**IEBP** (2159 cm^{-1})
$[Et_4N]^+I^-$	2212 (-2)	2196 (+4)	2159 (-3)	2157 (-2)
$[Bu_4N]^+I^-$	2216 (+2)	2193 (+1)	2158 (-4)	2151 (-8)
$[Et_4N]^+Br^-$	2213 (-1)	2191 (-1)	2155 (-7)	2158 (-1)
$[Pr_4N]^+Br^-$	2215 (+1)	2186 (-6)	2159 (-3)	2145 (-14)
$[Bu_4N]^+Br^-$	2212 (-2)	2189 (-3)	2155 (-7)	2151 (-8)
$[Pn_4N]^+Br^-$	2214 (0)	2192 (0)	2152 (-10)	2156 (-3)
$[Hx_4N]^+Br^-$	2212 (-2)	2195 (+3)	2156 (-6)	2154 (-5)
$[Dod_4Me_2N]^+Br^-$	2215 (+1)	2186 (-6)	2163 (+1)	2155 (-4)
$[Oct_4N]^+Br^-$	2216 (+2)	2190 (-2)	2155 (-7)	2159 (0)
$[Et_4N]^+Cl^-$	2214 (0)	2197 (+5)	2149 (-13)	2147 (-12)
Success rate	50%	70%	90%	80%

5.3.2 Crystal structures

5.3.2.1 Crystal structures of IEB·[Bu$_4$N]$^+$Br$^-$ and IEB·[Bu$_4$N]$^+$I$^-$

Single crystal X-ray diffraction analysis revealed that **IEB·[Bu$_4$N]$^+$Br$^-$** and **IEB·[Bu$_4$N]$^+$I$^-$** are isostructural and crystallize in the P2_1/c space group, that anion and the XB donor are present in a 1:2 ratio. XBs occur between **IEB** and iodide and bromide anions, which behave as bidentate XB acceptors (Figure 5.8). The halide coordination sphere is completed by HB contacts with H atoms belonging to the cation alkyl chains, one contact in **IEB·[Bu$_4$N]$^+$Br$^-$** and three contacts in **IEB·[Bu$_4$N]$^+$I$^-$** (Figure 5.8). The distance between the XB donor and acceptor is 3.464 Å in **IEB·[Bu$_4$N]$^+$I$^-$** and 3.267 Å for **IEB·[Bu$_4$N]$^+$Br$^-$** (~ 16-17% reduction of the sum of van der Waals radii of I and the Pauling ionic radius of I^- and Br^-) and the C(18)−I(1)···I$^-$(3) and C(22)−I(1)···Br$^-$(1) angles are 174° and 176º respectively.

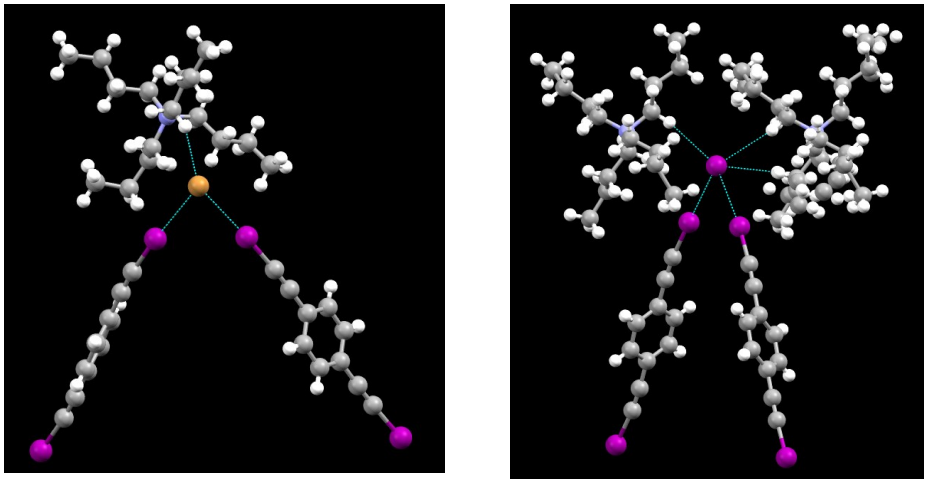

(a) (b)

Figure 5.8 Bonding pattern around halide anions in the co-crystals (a) **IEB·[Bu$_4$N]$^+$Br$^-$** and (b) **IEB·[Bu$_4$N]$^+$I$^-$**

The halogen bonded bidentate halide anions form infinite chains in a zig-zag type arrangement angles spanning 73º and 75º for **IEB·[Bu$_4$N]$^+$I$^-$** and **IEB·[Bu$_4$N]$^+$Br$^-$** respectively where the tetrabutylammonium cations sit perfectly between the zig-zag chains sandwiched between the aromatic XB donor where it is pinned by electrostatic interactions and weak C-H···π interactions. The overall crystal packing for the two assemblies are the same Figure 5.9.

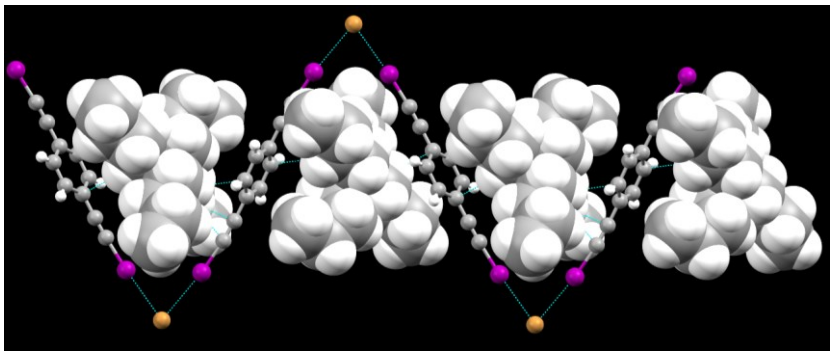

(a)

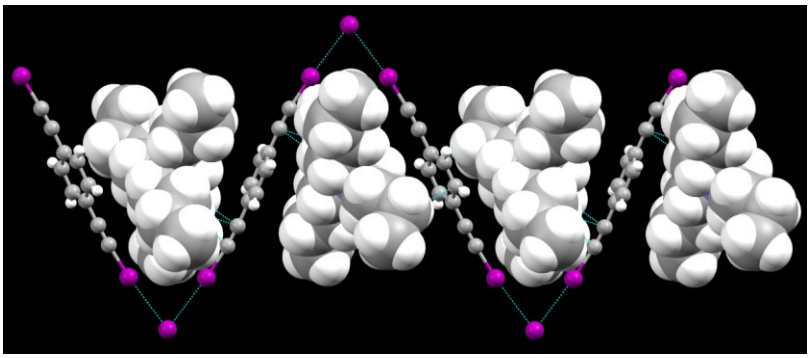

(b)

Figure 5.9 Overall packing in (a) **IEB·[Bu$_4$N]$^+$Br$^-$** and (b) **IEB·[Bu$_4$N]$^+$I$^-$** . Anionic networks are in ball-stick style while cations are in spacefill style.

5.3.2.2 Crystal structures of *IEBP·[Bu$_4$N]$^+$Br$^-$* and *IEBP·[Bu$_4$N]$^+$I$^-$*

IEBP·[Bu$_4$N]$^+$Br$^-$ crystallizes in the P-1 space group and shows a disordered structure with 1:2 stoichiometry with two iodo compounds and one quaternary ammonium bromide ions. Also, there are two orientations present as shown by the thermal ellipsoid plot, Figure 5.10 a. There are two halogen bonds between I and the Br$^-$, which behaves as a bidentate halogen bond acceptor and there are two C-H···Br$^-$ short contacts are seen from the alkyl chain of the cation Figure 5.11 a.

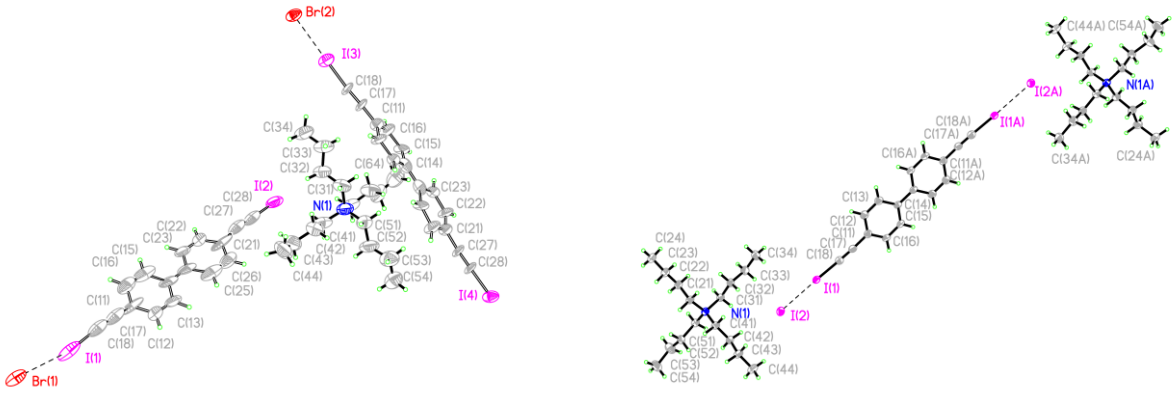

(a) (b)

Figure 5.10 Thermal ellipsoid plot (50% probability level) and the labeling scheme of the supermolecules (a) **IEBP·[Bu$_4$N]$^+$Br$^-$** (b) **IEBP·[Bu$_4$N]$^+$I$^-$**

X-ray analysis confirmed that the **IEBP·[Bu$_4$N]$^+$I$^-$** ratio is 1:2 (Figure 5.10 b), with an interplay of XB and HB creating a sphere around the iodide ion, (Figure 5.11 b). The iodide anion acts as a monodentate donor, forming a dianionic [I$^-$··· IEBP··· I$^-$] species.

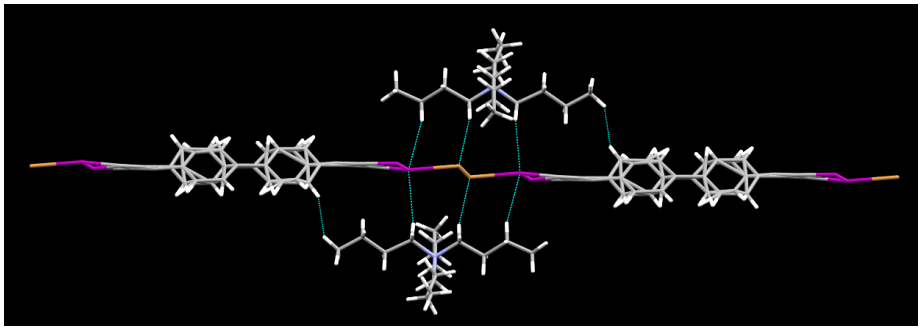

(a)

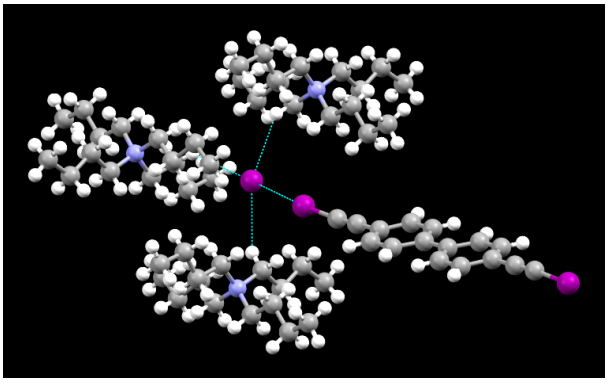

(b)

Figure 5.11 Bonding pattern around halide anions in the co-crystals (a) **IEBP·[Bu$_4$N]$^+$Br$^-$** and (b) **IEBP·[Bu$_4$N]$^+$I$^-$** shown in ball-stick style

5.3.2.3 Crystal structures of IEB·[Pr$_4$N]$^+$Br$^-$ and IEBP·[Pr$_4$N]$^+$Br$^-$

The single crystal X-ray diffraction of **IEB·[Pr$_4$N]$^+$Br$^-$** and **IEBP·[Pr$_4$N]$^+$Br$^-$** reveals that the propylammonium bromide forms two halogen bonds with both the halogen bond donors, **IEB** and **IEBP**. Two cations are coordinating to the bromide ion via HB contacts in both structures, Figure 5.12. Both XBs are short, linear, and similar in their geometrical parameters. Br$^-$···I distances are 3.188 Å for **IEB·[Pr$_4$N]$^+$Br$^-$** and 3.198Å for **IEBP·[Pr$_4$N]$^+$Br$^-$** (around 17-19% reduction of the sum of van der Waals radii of the interacting atoms) and angles, C22–I1···Br$^-$1 and C18–I1···Br$^-$1 are 176° and 176° respectively.

We observe in both the structures that, **IEB** and **IEBP** halogen bond with the bromide ion making infinite zig-zag chains with angles of 139º and 79º respectively. In the crystal structure of **IEBP·[Pr$_4$N]$^+$Br$^-$**, the tetrapropylammonium cations sit in the center of the zig-zag chains formed with the aid of C-H···π contacts (Figure 5.13 a), but in the case of **IEB·[Pr$_4$N]$^+$Br$^-$**, the tetrapropylammonium cations are moved slightly out of the zig-zag chains so that the overall crystal packing consists of alternating anionic and cationic layers (Figure 5.13 b).

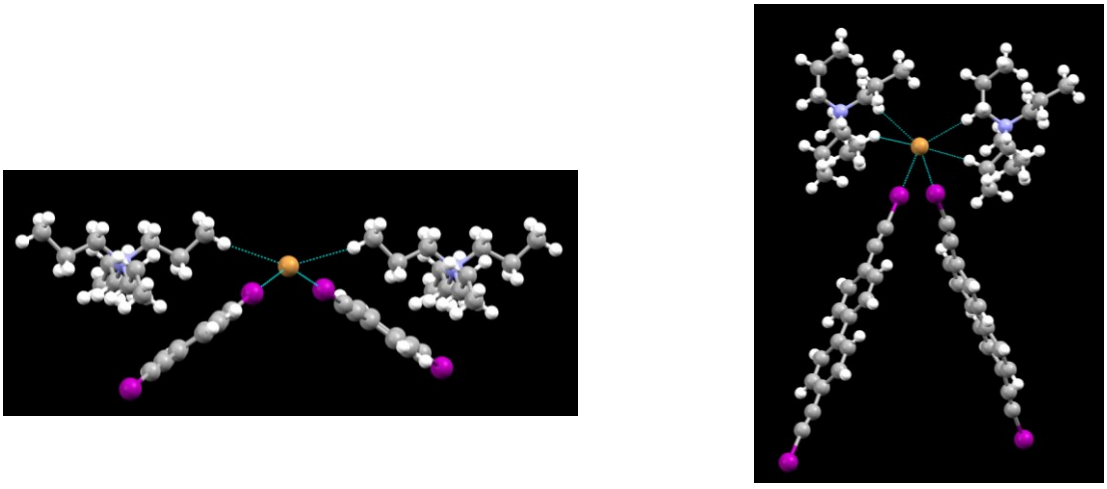

(a) (b)

Figure 5.12 Bonding pattern around halide anions in the co-crystals (a) **IEB·[Pr$_4$N]$^+$Br$^-$** and (b) **IEBP·[Pr$_4$N]$^+$Br$^-$**

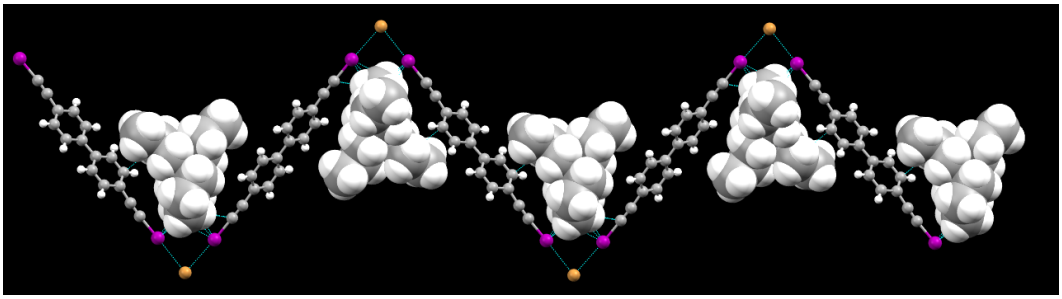

(a)

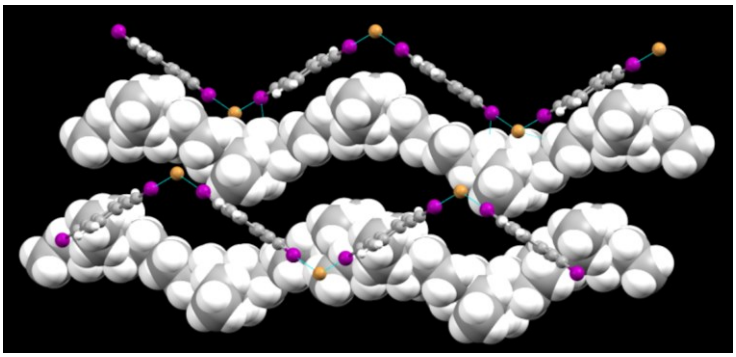

(b)

Figure 5.13 Overall packing in (a) **IEBP·[Pr$_4$N]$^+$Br$^-$** and (b) **IEB·[Pr$_4$N]$^+$Br$^-$**. The cations are displayed in spacefill style.

5.3.2.4 Crystal structures of IEBP·[Et$_4$N]$^+$I$^-$

In the crystal structure of **IEBP·[Et$_4$N]$^+$I$^-$**, there are three alkynes and three ammonium iodides in the asymmetric unit, Figure 5.14 a. The anions are closely associated with the alkyne and form three different zig-zag infinite chains of I$^-$···I-alkyne-biphenyl-alkyne-I··· I$^-$ assembly. The iodide acts as a bidentate acceptor forming two halogen bonds with **IEBP** with I···Br$^-$···I coordination angle of 162º. The halogen bonds are linear with C-I···I$^-$ angle of 179º and C-I···I$^-$ distance of 3.403 Å. The ammonium ions are not interacting with the iodide instead make short contacts with **IEBP** using C-H···π interactions (Figure 5.14 b).

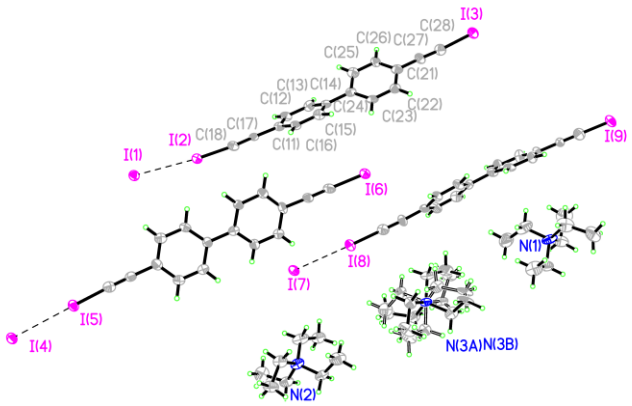

(a)

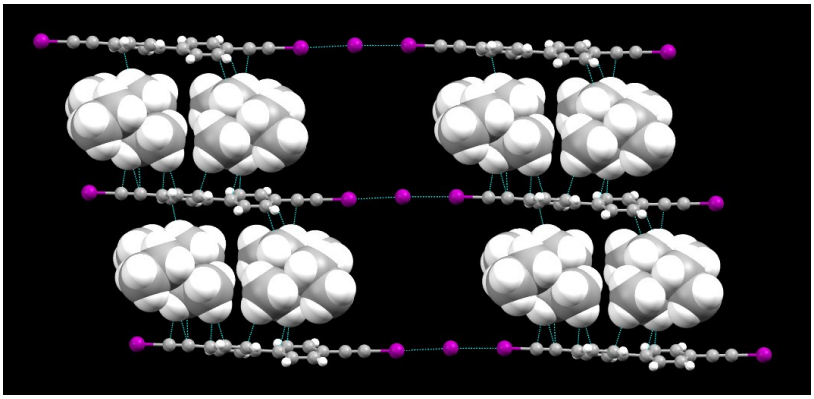

(b)

Figure 5.14 (a) Thermal ellipsoid plot (50% probability level) and the labeling scheme of the supermolecule (b) Overall packing and the bonding pattern around the iodide ion, the tetraethylammonium cation is displayed in spacefill style.

5.3.2.5 Crystal structure of IEBP·[Pn$_4$N]$^+$Br$^-$

The crystal structure of **IEBP·[Pn$_4$N]$^+$Br$^-$** show a halogen bond with an I···Br$^-$ distance of 3.174 Å (20% reduction of the sum of van der Waals radii) and C18−I1···Br$^-$ angle of 176° and undergo HB contact with the cation alkyl chains (Figure 5.15a). The halogen bonding between **IEBP** and Br$^-$ has an angle of 76º forming infinite zig-zag chains and the tetrapentylammonium cations stick in between the chains (Figure 5.15b).

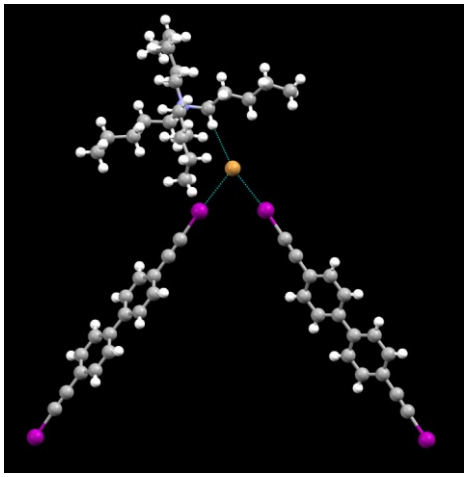

(a)

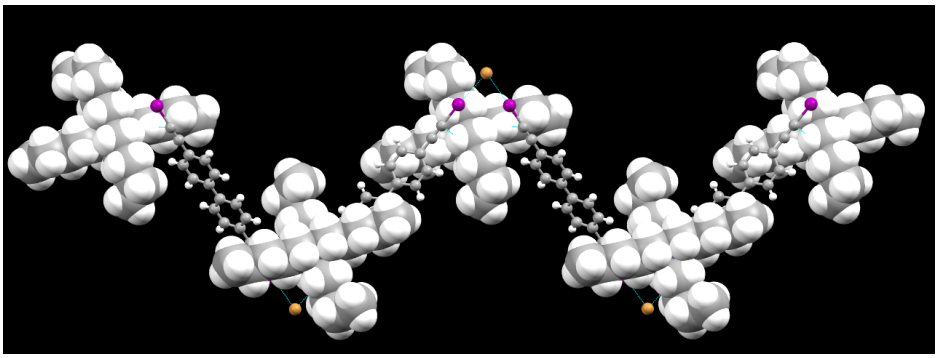

(b)

Figure 5.15 (a) Bonding pattern around halide anions in the co-crystal (b) Overall packing and the bonding pattern around the bromide ion, the tetrapentylammonium cation is displayed in spacefill style.

5.3.2.6 Crystal structure of IEBP·[Oct$_4$N]$^+$Br$^-$

The single crystal XRD analysis of **IEBP·[Oct$_4$N]$^+$Br$^-$** confirmed the formation of a 1:1 complex in which bromide functions as a ditopic XB acceptor and interacts at each end with two molecules of **IEBP** via to Br···N XBs (Figure 5.16a). The Br$^-$···I distance is 3.184 Å, which is about 19% shorter than sum of van der Waals radii and the C18−I1···Br$^-$ angle is 176º. The bromide ion makes two hydrogen bonds with the alkyl protons of two cations and the coordination angle around the bromide anion is 158º, which makes zig-zag type infinite chains similar to previous structures. The tetraoctylammonium cations make alternate chains along and in between the zig-zag chains (Figure 5.16b).

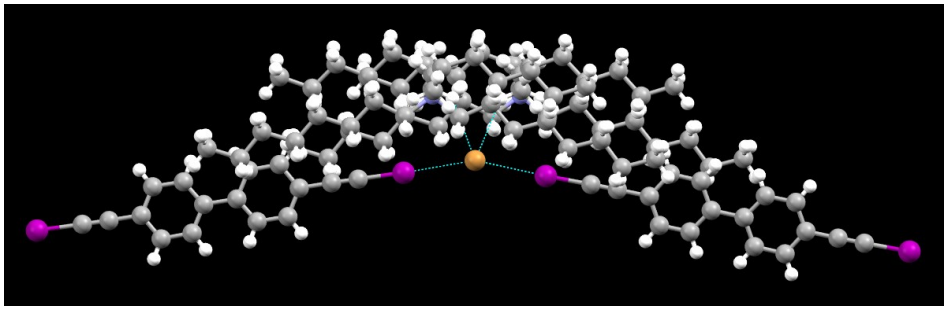

(a)

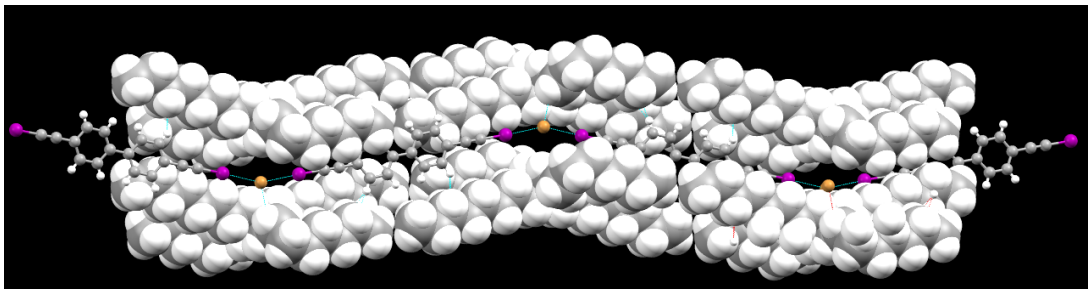

(b)

Figure 5.16 (a) Bonding pattern around halide anions in the co-crystal (b) Overall packing and the bonding pattern around the bromide ion, the tetrapentylammonium cation is displayed in spacefill style.

5.3.2.7 Crystal structure of IEBP·[Me$_2$Oct$_2$N]$^+$Br$^-$

The crystal structure of **IEBP·[Me$_2$Oct$_2$N]$^+$Br$^-$** shows that Br$^-$ is halogen bonded to the iodine with a Br$^-$···I distance of 3.20 Å (19% reduction of the sum of van der Waals radii) and C18−I1···Br$^-$ angle of angle of 177°, and undergo one HB contact with the cation alkyl chains (Figure 5.17a). The halogen bonding between **IEBP** and Br$^-$ makes a coordination angle of 75º forming infinite zig-zag chains and the tetrapentylammonium cations form alternate parallel chains along with the rows of polymeric chains between the halide and the **IEBP** molecules, via CH···π interactions (Figure 5.17b).

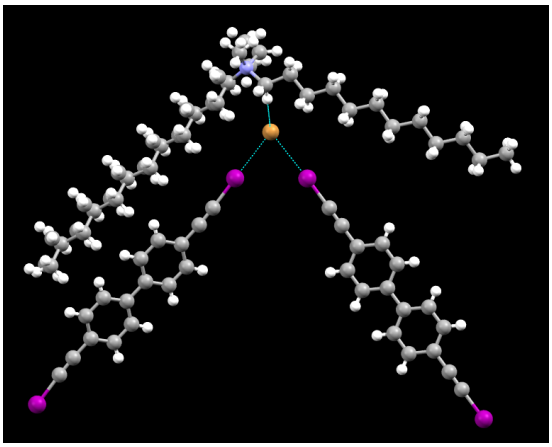

(a)

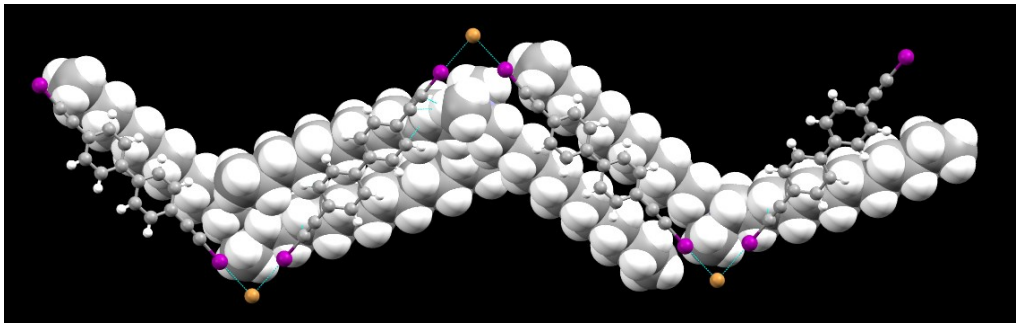

(b)

Figure 5.17 (a) Bonding pattern around halide anions in the co-crystal (b) Overall packing and the bonding pattern around the bromide ion, the cation is displayed in spacefill style.

5.4 Discussion

5.4.1 Characterization of the co-crystals from IR spectroscopy

Involvement of the haloalkynyl fragment with a strong electron density-donor site in the co-crystal formation was evidenced by the red shifts of the stretching band of the C≡C bond. The stretching bands of the C≡C bond of the pure **CEB**, **BEB** and **IEB** appear around 2214 cm^{-1}, 2192 cm^{-1} and 2162 cm^{-1} respectively and these bands are closely monitored as an event of co-crystal formation. An example of a positive co-crystal hit between **IEB** and $[\mathbf{Bu_4N}]^+\mathbf{I}^-$ is shown in (Figure 5.18) where the C≡C bond stretch at 2162 cm^{-1} red shifts to 2157 cm^{-1}. About 48% of the successful grinding experiments displayed a red shift for the halogen bond donor, however,

about 16% of the results revealed blue shifts of the C≡C bond stretch, which are also counted as a positive co-crystal event whenever the shift is greater than two wavenumbers.

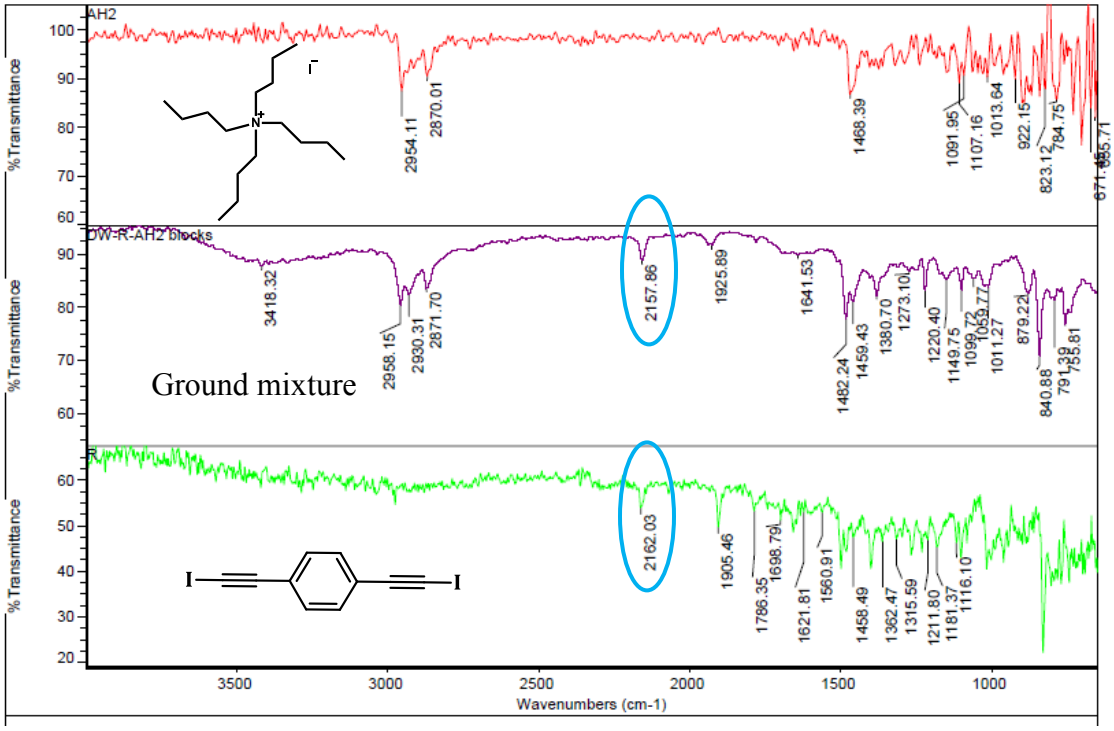

Figure 5.18 The comparison of the IR spectra of **IEB**·$[Bu_4N]^+I^-$ with pure **IEB** and $[Bu_4N]^+I^-$

The halogen bond donors **CEB**, **BEB** and **IEB** (**IEBP**) all showed positive co-crystal events with grinding experiments, even though only the iodine donors, **IEB** and **IEBP** were able to give rise single crystals suitable for X-ray diffraction. The co-crystallization attempts of **BEB** failed precipitating the ligand by itself even after increasing the stoichiometric amount of the anion to five fold. All the halogen atoms may, in principle, function as XB donor sites, however, the strength of the interaction is heavily influenced by the polarizability of the halogen atom. Based on our grinding experiments, **CEB** showed 50% success, **BEB** 70% and **IEB** (**IEBP**) 85% success towards anion binding, Table 5.1. Also, the red shifts ($\Delta\bar{\upsilon}$) observed for **CEB** was less compared to the red shifts observed for **BEB** and **IEB** (**IEBP**). This result is consistent with the fact that halogen bond strength depends on the polarizability of the C(*sp*)-halogen atom which increases down the column following the trend C(*sp*)-Cl < C(*sp*)-Br < C(*sp*)-I indicated by the molecular electrostatic potentials (Figure 4.4) demonstrated in Chapter 4.

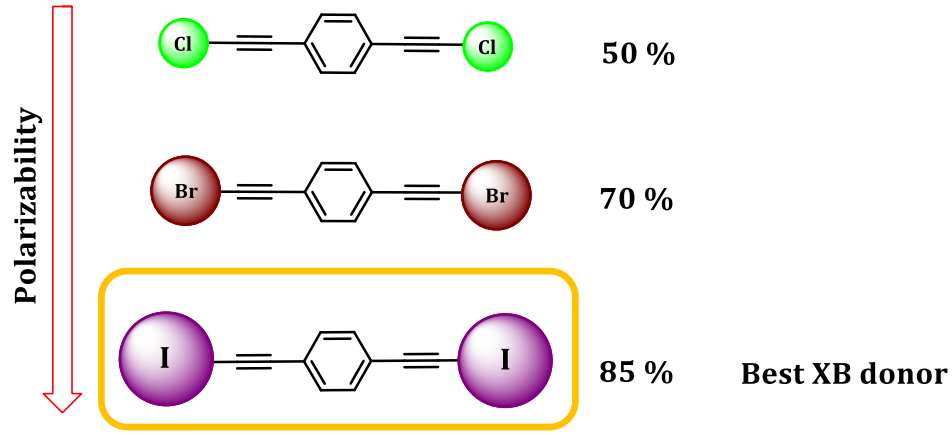

Figure 5.19 Highest polarizable atom makes the best XB donor based on the IR results

FTIR spectroscopy of co-crystals showed red-shifted triple bond stretching modes from 2162 cm^{-1} in pure **IEB** through 2159 cm^{-1} (-3) in $[Et_4N]^+I^-$ and to 2155 cm^{-1} (-7) in $[Et_4N]^+Br^-$ and to 2149 cm^{-1} (-13) in $[Et_4N]^+Cl^-$ which clearly indicates the electron acceptor ability of the anions following in the trend $Cl^- > Br^- > I^-$. Based on overall grinding results of **IEB** and **IEBP** iodine donors, the highest maximum red shifts are observed for bromide and chloride ions (Table 5.1) consistent with reported data,[32b] implying that bromides and chlorides are better acceptors than iodides due to the high charge density possessed by bromides and chlorides.

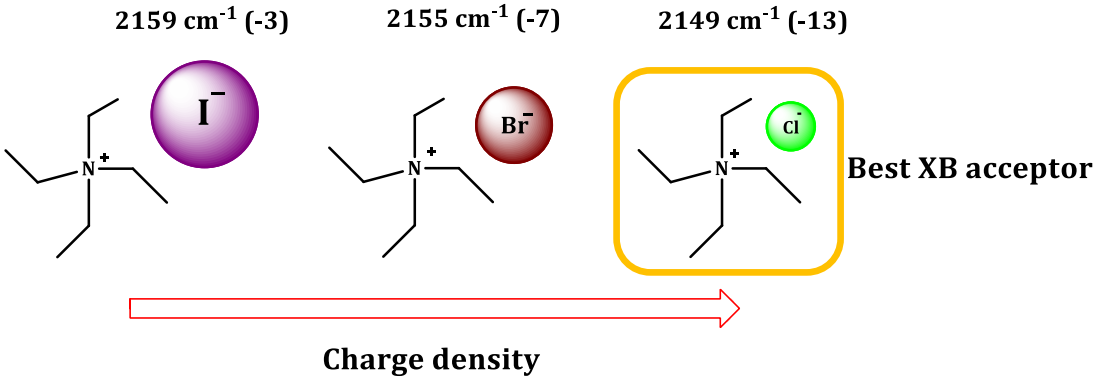

Figure 5.20 Anion with the highest charge density makes the best XB acceptor based on IR results

5.4.2 Comparison of the structures with diiodotetrafluorobenzene based anion coordinated structures

A detailed systematic study of the anion coordination ability of 1,4-*bis*(iodethynyl)benzene compounds has not been performed to date. Hence in this section our new crystal structures are analyzed to explore whether they could act as reliable and robust tectons for anion coordination. Furthermore, these halogen bond based anion coordinated supramolecular architectures of 1,4-*bis*(iodethynyl)benzene derivatives are examined in terms of how they compare with previously reported crystallographic data. For this purpose, the analogous anion coordinated 1,4-diiodotetrafluoro benzene (DITFB) supramolecular assemblies are taken into account, as these have been explored as means of anion coordination and anion-templated assembly process. Moreover, structures are evaluated with respect to the trends in aromatic π stacking interactions, coordination number of the anion, geometry around the anion and effect of the counter cation.

5.4.2.1 Effect of aromatic π stacking interactionson the halogen bond driven anion coordination supramolecular assemblies

All the crystal structures reported in this chapter are heteromeric three component system where the tetraalkyl ammonium cation plays virtually no active role, as far as XB is concerned. No aromatic π stacking interactions is seen and all three components are mixed together in the crystal lattice. As far as the overall crystal packing is considered, either the tetraalkylammonium cations sit in between the zig-zag chains sandwiched between the aromatic XB donor where it is pinned by electrostatic interactions and weak C-H···π interactions (Figure 5.21a) or they form alternate chains along with the rows of polymeric halide···XB zig-zag chains with the use of CH···π interactions (Figure 5.21b).

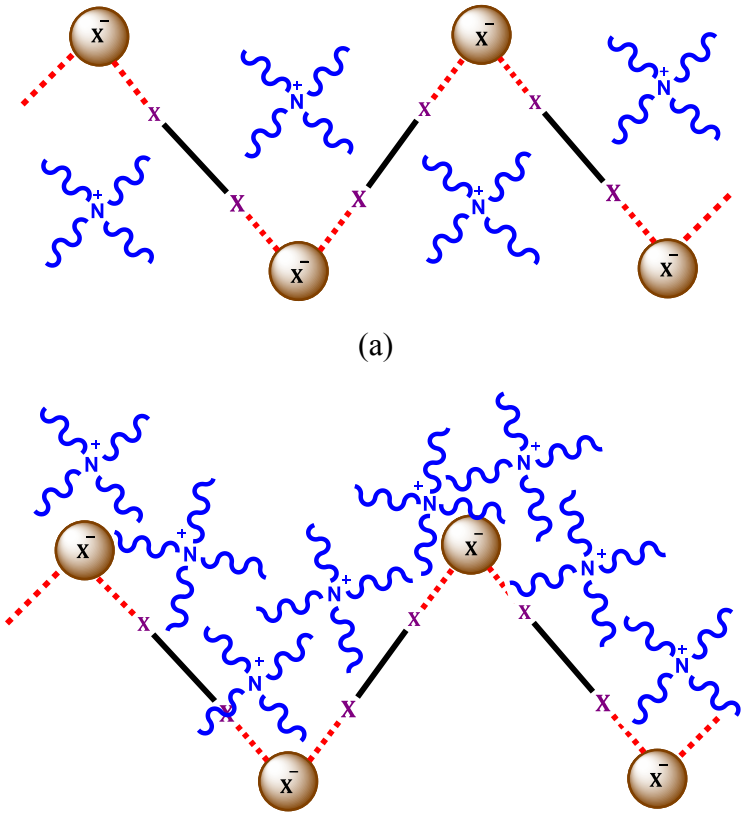

(a)

(b)

Figure 5.21 Overall packing arrangements of the co-crystals

On the other hand the analogous DITFB co-crystals reported in the CSD (CSD REFCODE: GIXGAV, GIXGEZ, GIXGUP, MAHCIJ and OHOVUD) show π stacking interactions within the crystal lattice via F···F interactions (Figure 5.22a). Therefore, in the case of *bis*-haloethynyl donors, the CH···π interactions and electrostatic interactions from slightly diffuse positive and negative charges, dominate over aromatic π stacking interactions as shown in Figure 5.22b. The π electron cloud of the triple bond act as a good electron donor which plays a role in the secondary interactions. However, the electrostatic interactions may not be powerful enough to overcome the aromatic π stacking interactions governed by F···F contacts between the DITFB molecules in the arrangement.

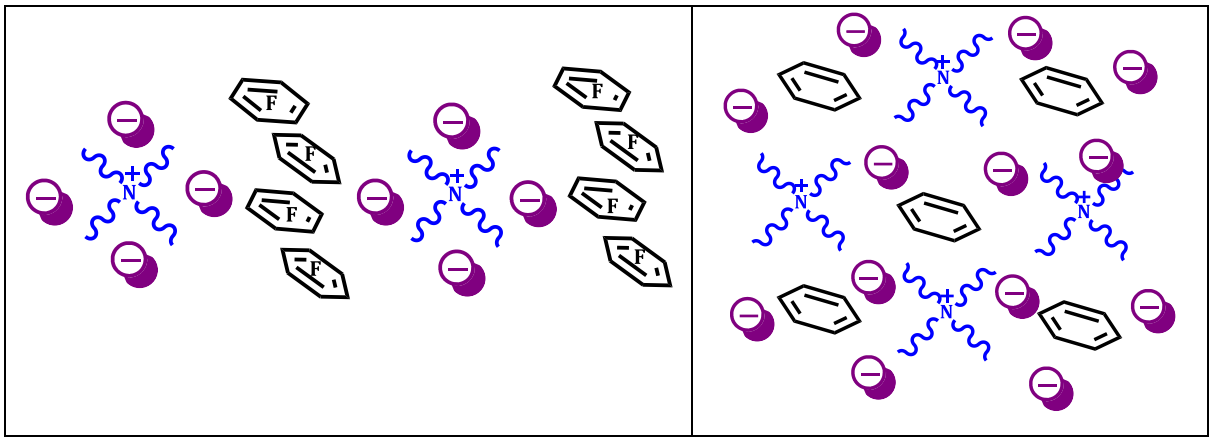

Figure 5.22 Schematic picture showing the packing arrangement of (a) DITFB co-crystals (b) 1,4-*bis*-haloethynyl co-crystals

5.4.2.2 Coordination number of the anion

Based on the ten crystal structures (Table 5.2), we tried to find trends in the coordination number around the anion with respect to the analogous DITFB co-crystals. In this case, the number of halogen bonds are counted as the coordination number neglecting the HB contacts from the tetra alkylammonium cation. Out of the ten crystal structures, all seven bromides have a coordination number of two. Also, 2/3 of the iodide based crystal structures show a coordination number of two and only 1/3 involves in a coordination number of one. Altogether 9/10 structures of bromides and iodides have a preference for forming two halogen bonds regardless of the counter cation (Figure 5.23).

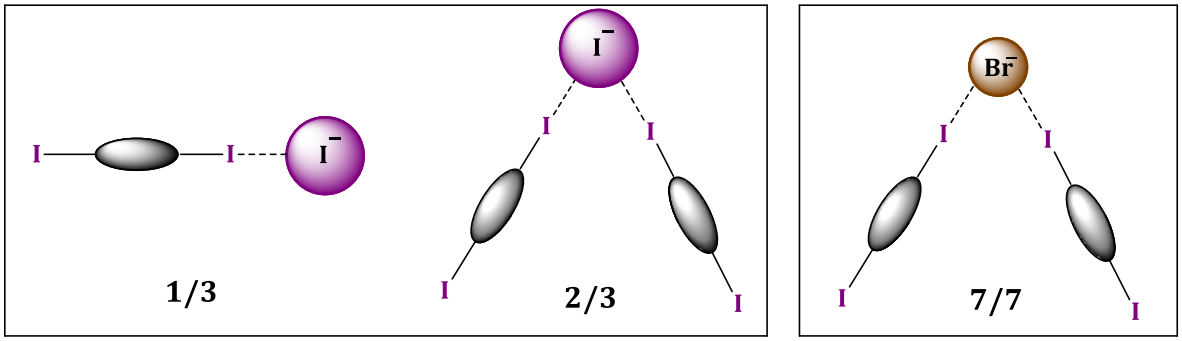

Figure 5.23 Summary of the coordination numbers formed by iodides and bromides

Table 5.2 Coordination numbers (number of XBs formed), HB contacts around the anion and the I···X^-··· I (º) angle X^- = Br^- or I^-

Crystal Structures	Coordination number	HB contacts around the anion	I···X^-··· I (º)
IEB·$[Bu_4N]^+Br^-$	2	1	75.12
IEB·$[Bu_4N]^+I^-$	2	3	73.43
IEB·$[Pr_4N]^+Br^-$	2	2	139.60
IEBP·$[Bu_4N]^+Br^-$	2	2	-
IEBP ·$[Bu_4N]^+I^-$	1	3	-
IEBP ·$[Et_4N]^+I^-$	2	0	162.18
IEBP ·$[Pr_4N]^+Br^-$	2	4	79.82
IEBP ·$[Pn_4N]^+Br^-$	2	1	76.82
IEBP ·$[Oct_4N]^+Br^-$	2	2	157.69
IEBP ·$[Me_2Oct_2N]^+Br^-$	2	1	75.32

This results are in agreement with the analogous ditopic DITFB based co-crystals, previously reported by Viger-Gravel *et al*,[33] where 2/3 of the structures, the bromides have a coordination number of two regardless of the counter cation (Figure 5.24).

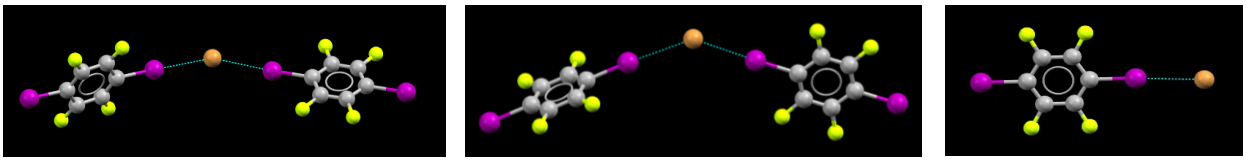

DITFB·$[Bu_4N]^+Br^-$ DITFB·$[Bu_4P]^+Br^-$ DITFB·$[EtPh_3P]^+Br^-$

Figure 5.24 Halogen bonding contacts between bromide ion and DITFB[33]

Iodides when halogen bonded to ditopic aliphatic or aromatic halogen bond donors are known to form two halogen bonds, reported by Casnati *et al* (Figure 5.25a)[20b] and Mele *et al* (Figure 5.25b).[18a] According to these results, it further proves that even with the fluorinated halogen bond donors, iodides have a bias towards formation of two halogen bonds regardless of the counter cation.

Comparison of all these previously reported structures to our results demonstrate that 1,4-*bis*-iodoethynyl functionality is a robust XB donor as good as fluorinated XB donors that can be utilized in anion coordination.

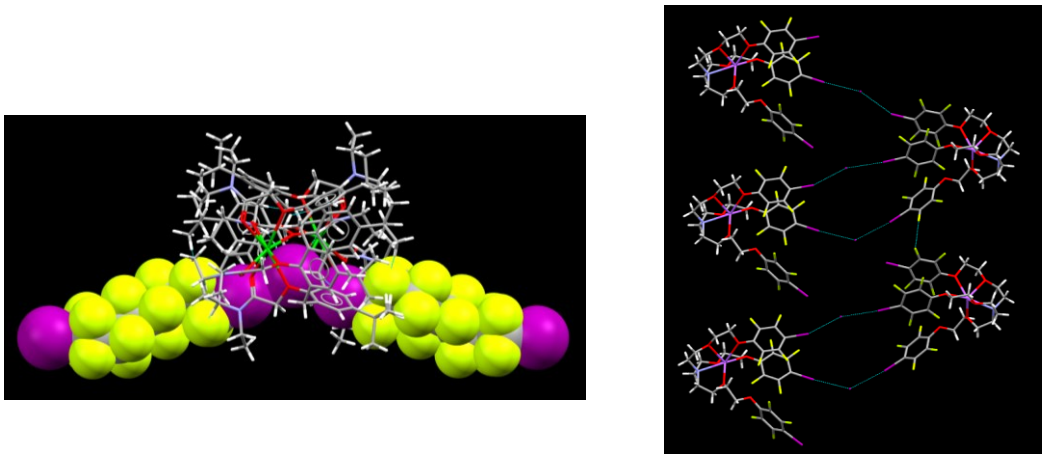

(a) (b)

Figure 5.25 (a) Iodide ion forming two halogen bonds with diiodoperfluorooctane shown in spacefil model[20b] (b) iodide ion forming 2 halogen bonds with the receptor bearing XB donors[18a]

5.4.2.3 Geometry around the anion

As the coordination number of the I^- or Br^- anions turned out to be two almost all the times when coordinated to these ditopic halogen bond donors, it is important to note that at all times the angles of either I···I^-···I or I···Br^-···I are observed in the range of either 70º-80º or 140º-160º (Figure 5.26). This observation is consistent with the analogous anion co-crystals of DITFB, when coordinated to Br^-, the most common I···Br^-···I angles observed are ~70º (Ex. CSD REFCODE: GIXGEZ) (Figure 5.27a)[34] and ~140º (Ex. CSD REFCODE: OHOWAK01) (Figure 5.27b)[22b].

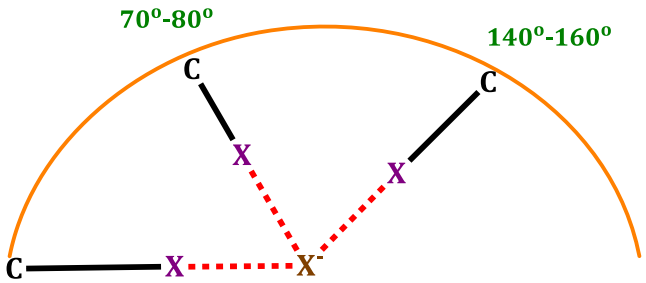

Figure 5.26 Variation of the observed X···X^-···X angles

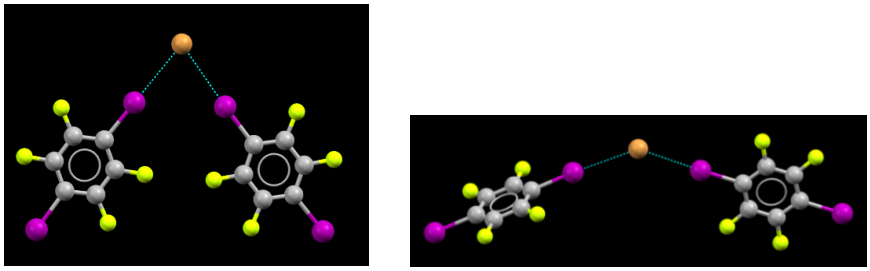

74.3° 139.2°

Figure 5.27 Examples showing the geometry around the bromide ion of the reported structures (a) GIXGEZ and (b) OHOWAK01[22b]

Another important point to consider here is that the size of the cation or the number of HB contacts it forms with the anion or the arrangement of the alkyl chains does not influence the geometry around the anion whether it is a bromide or an iodide (Figure 5.28). Therefore, regardless of the presence of the cation, only two angles are observed for iodides and bromides. The most common angle is 70º-80º which was shown by 5/8 structures. The remaining 3/8 structures has a coordination angle of 140º-160º (**IEBP·[Bu$_4$N]$^+$I$^-$** is a dianionic [I$^-$··· *p*BIBP··· I$^-$] species and **IEBP·[Bu$_4$N]$^+$I$^-$** is a disordered structure, which are not counted in considering the geometry).

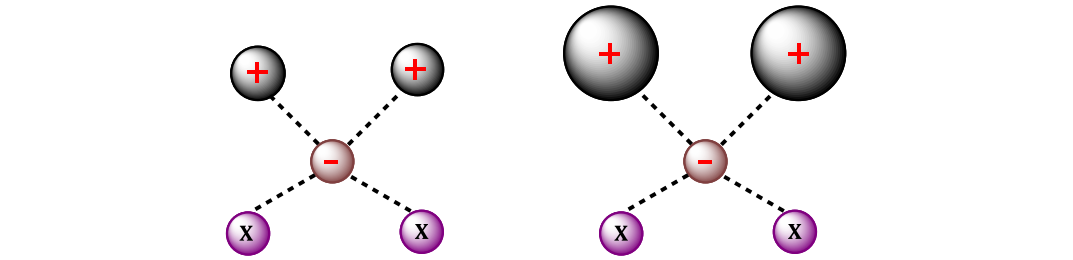

Size of the counter cation

Number of HB contacts

Figure 5.28 Schematics showing (a) the size of the counter cation (b) number of HB contacts doesn't have an effect on the X···X$^-$···X angle

However, when multitopic halogen bond donors are employed with iodides with different counter cations, the cation size has an effect on the coordination number and the geometry as illustrated by the bromoform co-crystals with the $[Me_4N]^+Br^-$, $[Et_4N]^+Br^-$ and $[Pr_4N]^+Br^-$ salts (Figure 5.29a).[21a] Furthermore, Metrangolo *et al*[23b] reported obtaining supramolecular assemblies with similar topology by using similar counter cations, i.e. 1,3,5-triiodotrifluorobenzene co-crystals of $[Et_4N]^+I^-$ and $[Et_4P]^+I^-$ (Figure 5.29b).

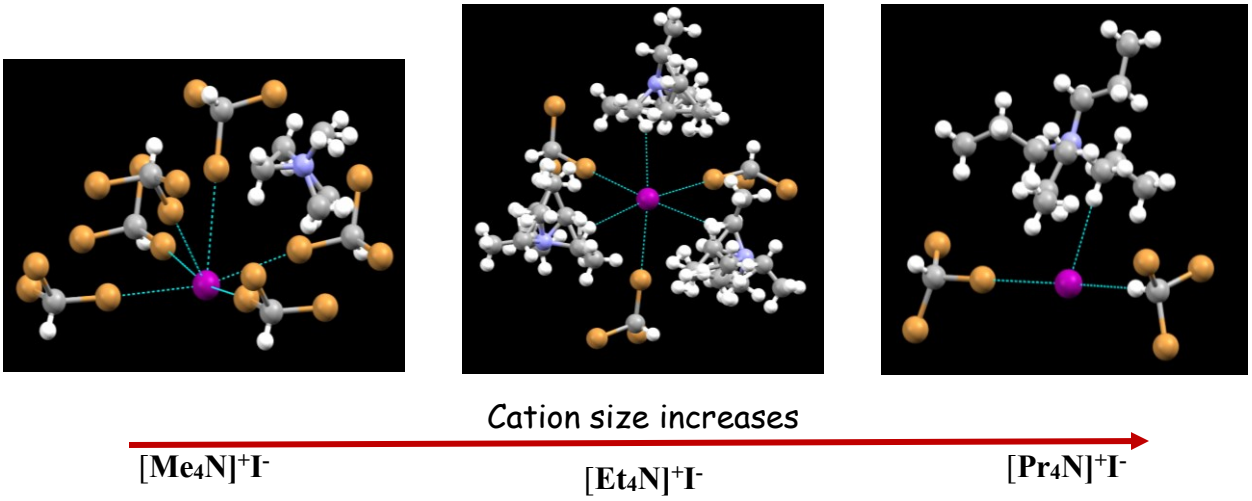

(a)

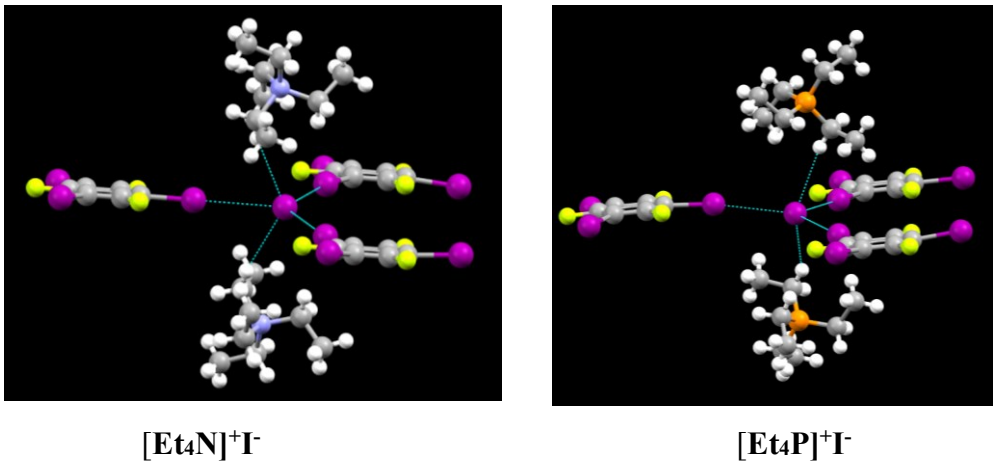

(b)

Figure 5.29 Effect of the size of the cation on the topology of the iodide ion

5.5 Summary and conclusion

We have successfully demonstrated, that the haloalkynyl moiety is a robust and reliable tecton for halogen bond based anion recognition. The effect of the halogen bond donor atom was studied using **CEB, BEB** and **IEB** and we observed the trend of XB donor ability Cl<Br<I and XB acceptor ability $I^-<Br^-<Cl^-$.

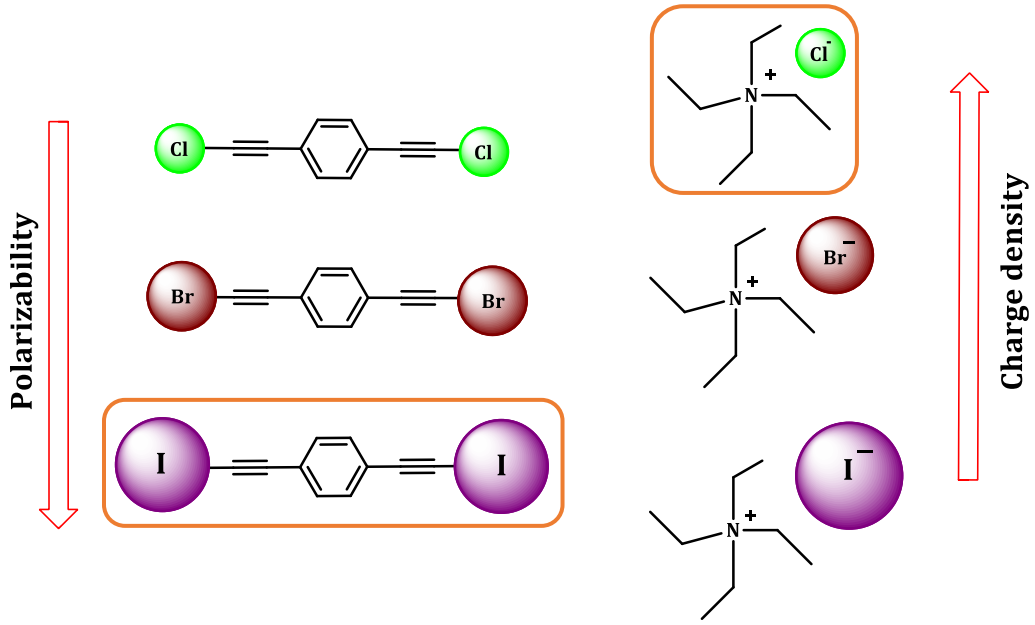

Figure 5.30 XB donor acceptor ability

All the crystal structures obtained with the iodine donors are heteromeric three component systems where the tetraalkyl ammonium cation did not play active role as far as XB is concerned. The aromatic donor molecules does not exhibit aromatic π stacking interactions within this anionic co-crystal lattice as opposed to the DITFB systems.

The topology of the anion center (Figure 5.31) is fixed to form two halogen bonds in almost all the structures, where it give rise to infinite polymeric zig-zag chains with either owing a X···X-···X angle in the range of 70º-80º or 140º-160º. The size of the tetralakyl ammonium cation or the HB contacts from the alkyl chains of the cation does not seem to affect either the coordination number of the anion or the geometry around the anion.

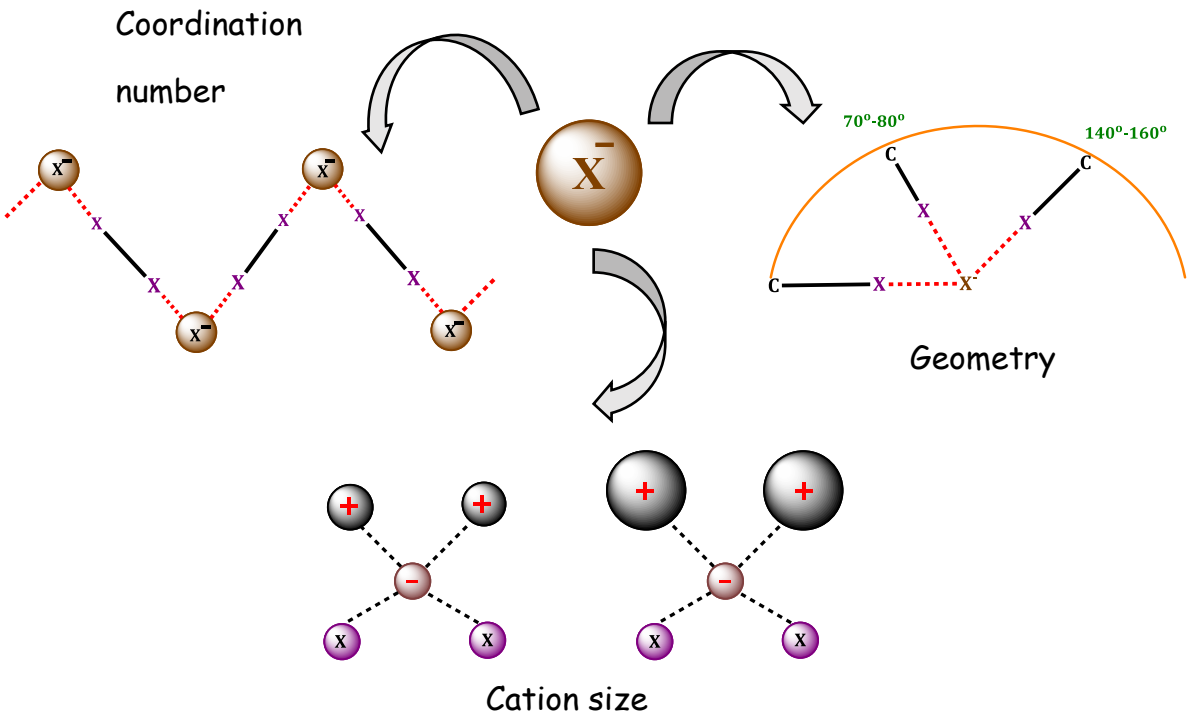

Figure 5.31 Topology of halide ion

This restricted coordination profile of the anion might be due to the balance between the nature of the halogen bond donor (number of halogen bond donor sites, the spatial arrangement of the donor sites, etc.) and the anion, which may arise from the general entropic factors.[22b] As the best way to investigate this concept further, halogen bond donors with multiple donor sites which are arranged in different geometry are proposed (Figure 5.32) as a continuation of this project. The synthesis and characterization of these iodine donors are already performed (NMR in Appendix A) and the co-crystal growth attempts with above mentioned alkyl ammonium halides are being pursued currently experimenting with different solvents and different methods.

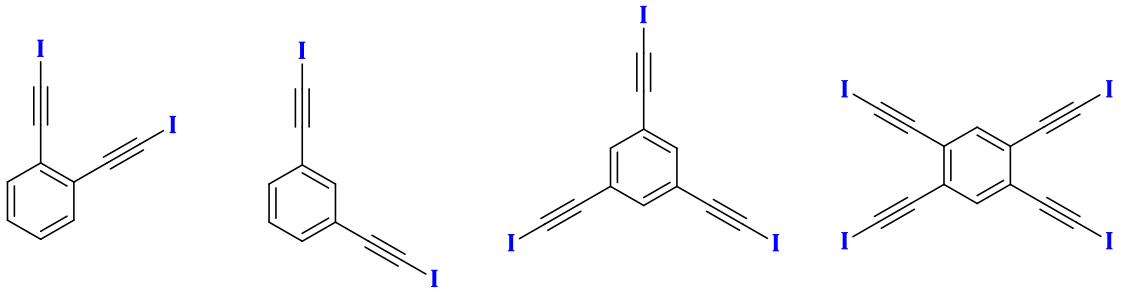

Figure 5.32 Proposed halogen bond donors with multiple sites and different geometry

As the haloalkynyl moiety is available in the anion recognition tool box as a new tecton, it allows to access various topologies of the anion coordination sphere. A comprehensive study of these new XB based systems will allow the advantage of having predictability in various different architectures. Consequently it invites the opportunities of these systems to be employed in tuning the physical properties of functional materials in near future.

5.6 References

1. (a) Bianchi, A.; Bowman-James, K.; Garcia-Espana, E. *Supramolecular Chemistry of Anions*. Wiley-VCH: New York, 1997; (b) Sessler, J. L.; Gale, P. A.; Won-Seob, C. *Anion Receptor Chemistry*. Royal Society of Chemistry: Cambridge, UK, 2006.

2. (a) Christianson, D. W.; Lipscomb, W. N. *Acc. Chem. Res.* **1989,** *22* (2), 62-69; (b) Puglisi, J. D.; Chen, L.; Frankel, A. D.; Williamson, J. R. *Proc. Natl. Acad. Sci. U. S. A.* **1993,** *90* (8), 3680-3684; (c) Berg, J. M. *Acc. Chem. Res.* **1995,** *28* (1), 14-19.

3. Ashcroft, F. M. *Ion Channels and Disease* Academic Press: San Diego and London, 2000.

4. http://www.ecifm.rdg.ac.uk/nutrient.htm

5. Ryo, U. Y.; Vaidya, P. V.; Schneider, A. B.; Bekerman, C.; Pinsky, S. M. *Radiology* **1983,** *148* (3), 819-822.

6. (a) Gupta, M. K.; O'Sullivan, T. P. *RSC Advances* **2013,** *3* (48), 25498-25522; (b) Kabalka, G. W.; Wu, Z.; Ju, Y. *J. Organomet. Chem.* **2003,** *680* (1–2), 12-22.

7. Moss, B. *Phil. Trans. R. Soc. B* **2008,** *363* (1491), 659-666.

8. Yamamoto, Y.; Nishiyama, Y.; Ono, Y.; Satoh, K.; Ohkawa, M.; Kawasaki, Y.; Tanabe, M. *Ann. Nucl. Med.* **1999,** *13* (5), 357-359.

9. Welsh, M. J. *FASEB J.* **1990,** *4* (10), 2718-25.

10. (a) Davis, A. P. *Coord. Chem. Rev.* **2006,** *250* (23–24), 2939-2951; (b) Chandrashekar, T. K.; Venkatraman, S. *Acc. Chem. Res.* **2003,** *36* (9), 676-691; (c) Lankshear, M. D.; Beer, P. D. *Acc. Chem. Res.* **2007,** *40* (8), 657-668; (d) Filby, M. H.; Steed, J. W. *Coord. Chem. Rev.* **2006,** *250* (23–24), 3200-3218; (e) Anzenbacher Jr, P.; Nishiyabu, R.; Palacios, M. A. *Coord. Chem. Rev.* **2006,** *250* (23–24), 2929-2938; (f) Sessler, J. L.; Davis, J. M. *Acc. Chem. Res.* **2001,** *34* (12), 989-997; (g) Gale, P. A. *Acc. Chem. Res.* **2006,** *39* (7), 465-475; (h) Misra, R.; Chandrashekar, T. K. *Acc. Chem. Res.* **2008,** *41* (2), 265-279; (i) Amendola, V.; Esteban-Gómez, D.; Fabbrizzi, L.; Licchelli, M. *Acc. Chem. Res.* **2006,** *39* (5), 343-353.

11. O'Neil, E. J.; Smith, B. D. *Coord. Chem. Rev.* **2006,** *250* (23–24), 3068-3080.

12. (a) Schottel, B. L.; Chifotides, H. T.; Dunbar, K. R. *Chem. Soc. Rev.* **2008,** *37* (1), 68-83; (b) Quiñonero, D.; Garau, C.; Rotger, C.; Frontera, A.; Ballester, P.; Costa, A.; Deyà, P. M. *Angew. Chem. Int. Ed.* **2002,** *41* (18), 3389-3392; (c) Robertazzi, A.; Krull, F.; Knapp, E.-W.; Gamez, P. *CrystEngComm* **2011,** *13* (10), 3293-3300.

13. (a) García-España, E.; Díaz, P.; Llinares, J. M.; Bianchi, A. *Coord. Chem. Rev.* **2006,** *250* (23–24), 2952-2986; (b) Schmuck, C. *Coord. Chem. Rev.* **2006,** *250* (23–24), 3053-3067; (c) Wichmann, K.; Antonioli, B.; Söhnel, T.; Wenzel, M.; Gloe, K.; Gloe, K.; Price, J. R.; Lindoy, L. F.; Blake, A. J.; Schröder, M. *Coord. Chem. Rev.* **2006,** *250* (23–24), 2987-3003; (d) Katayev, E. A.; Ustynyuk, Y. A.; Sessler, J. L. *Coord. Chem. Rev.* **2006,** *250* (23–24), 3004-3037.

14. Cavallo, G.; Metrangolo, P.; Meyer, F.; Pilati, T.; Resnati, G.; Terraneo, G. *Acta Crystallogr. Sect. E: Struct. Rep. Online* **2014,** *70* (1), o9-o10.

15. Metrangolo, P.; Carcenac, Y.; Lahtinen, M.; Pilati, T.; Rissanen, K.; Vij, A.; Resnati, G. *Science* **2009,** *323* (5920), 1461-1464.

16. Liantonio, R.; Metrangolo, P.; Pilati, T.; Resnati, G. *Cryst. Growth Des.* **2003,** *3* (3), 355-361.

17. Casnati, A.; Cavallo, G.; Metrangolo, P.; Resnati, G.; Ugozzoli, F.; Ungaro, R. *Chem. Eur. J.* **2009,** *15* (32), 7903-7912.

18. (a) Mele, A.; Metrangolo, P.; Neukirch, H.; Pilati, T.; Resnati, G. *J. Am. Chem. Soc.* **2005,** *127* (43), 14972-14973; (b) Sarwar, M. G.; Dragisic, B.; Sagoo, S.; Taylor, M. S. *Angew. Chem.* **2010,** *122* (9), 1718-1721.

19. Metrangolo, P.; Pilati, T.; Terraneo, G.; Biella, S.; Resnati, G. *CrystEngComm* **2009,** *11* (7), 1187-1196.

20. (a) Bock, H.; Holl, S. *Z. Naturforsch., B: Chem. Sci.* **2001,** *56* (2), 152-163; (b) Casnati, A.; Liantonio, R.; Metrangolo, P.; Resnati, G.; Ungaro, R.; Ugozzoli, F. *Angew. Chem. Int. Ed.* **2006,** *45* (12), 1915-1918.

21. (a) Rosokha, S. V.; Neretin, I. S.; Rosokha, T. Y.; Hecht, J.; Kochi, J. K. *Heteroat. Chem* **2006,** *17* (5), 449-459; (b) Lindeman, S. V.; Hecht, J.; Kochi, J. K. *J. Am. Chem. Soc.* **2003,** *125* (38), 11597-11606; (c) Nakamoto, T.; Wang, Q.; Miyazaki, Y.; Sorai, M. *Polyhedron* **2002,** *21* (12–13), 1299-1304; (d) Gattuso, G.; Pappalardo, A.; Parisi, M. F.; Pisagatti, I.; Crea, F.; Liantonio, R.; Metrangolo, P.; Navarrini, W.; Resnati, G.; Pilati, T.; Pappalardo, S. *Tetrahedron* **2007,** *63* (23), 4951-4958; (e) Ghassemzadeh, M.; Harms, K.; Dehnicke, K. *Chem. Ber.* **1996,** *129* (1), 115-120; (f) Yamamoto, H. M.; Yamaura, J.-I.; Kato, R. *J. Am. Chem. Soc.* **1998,** *120* (24), 5905-5913.

22. (a) Yamamoto, H. M.; Kato, R. *Chem. Lett.* **2000,** *29* (8), 970-971; (b) Abate, A.; Biella, S.; Cavallo, G.; Meyer, F.; Neukirch, H.; Metrangolo, P.; Pilati, T.; Resnati, G.; Terraneo, G. *J. Fluorine Chem.* **2009,** *130* (12), 1171-1177.

23. (a) Fox, D. B.; Liantonio, R.; Metrangolo, P.; Pilati, T.; Resnati, G. *J. Fluorine Chem.* **2004,** *125* (2), 271-281; (b) Metrangolo, P.; Meyer, F.; Pilati, T.; Resnati, G.; Terraneo, G. *Chem. Commun.* **2008,** (14), 1635-1637; (c) du Mont, W.-W.; Stenzel, V.; Jeske, J.; Jones, P. G.; Sebald, A.; Pohl, S.; Saak, W.; Baetcher, M. *Inorg. Chem.* **1994,** *33* (7), 1502-1505.

24. Cavallo, G.; Biella, S.; Lü, J.; Metrangolo, P.; Pilati, T.; Resnati, G.; Terraneo, G. *J. Fluorine Chem.* **2010,** *131* (11), 1165-1172.

25. Liantonio, R.; Metrangolo, P.; Meyer, F.; Pilati, T.; Navarrini, W.; Resnati, G. *Chem. Commun.* **2006,** (17), 1819-1821.

26. Yamamoto, H. M.; Maeda, R.; Yamaura, J.-I.; Kato, R. *J. Mater. Chem.* **2001,** *11* (4), 1034-1041.

27. Jude, H.; Sinclair, D. J.; Das, N.; Sherburn, M. S.; Stang, P. J. *J. Org. Chem.* **2006,** *71* (11), 4155-4163.

28. Rajbanshi, A. supramolecular interactions from small-molecule selectivity to molecular capsules. Kasas State University, May, 2010

29. Fellig, J.; Barnes, J. R.; Rachlin, A. I.; O'Brien, J. P.; Focella, A. *J. Agric. Food. Chem.* **1970,** *18* (1), 78-80.

30. Osowska, K.; Lis, T.; Szafert, S. *Eur. J. Org. Chem.* **2008,** *2008* (27), 4598-4606.

31. Friščić, T.; Trask, A. V.; Jones, W.; Motherwell, W. D. S. *Angew. Chem. Int. Ed.* **2006,** *45* (45), 7546-7550.

32. (a) Baldrighi, M.; Cavallo, G.; Chierotti, M. R.; Gobetto, R.; Metrangolo, P.; Pilati, T.; Resnati, G.; Terraneo, G. *Mol. Pharm.* **2013,** *10* (5), 1760-1772; (b) Baldrighi, M.; Bartesaghi, D.; Cavallo, G.; Chierotti, M. R.; Gobetto, R.; Metrangolo, P.; Pilati, T.; Resnati, G.; Terraneo, G. *CrystEngComm* **2014,** *16* (26), 5897-5904.

33. Viger-Gravel, J.; Leclerc, S.; Korobkov, I.; Bryce, D. L. *CrystEngComm* **2013,** *15* (16), 3168-3177.

34. Grebe, J.; Geiseler, G.; Harms, K.; Dehnicke, K. *Z. Naturforsch., B: Chem. Sci.* **1999,** *54*, 77.

Chapter 6 - Suitably functionalized cavitands as carriers of active ingredients

6.1 Introduction

Molecular recognition, a key concept employed in fundamental biological processes rely on complementary balance between size, shape and functional entities and is responsible for their unique behavior.[1] Parts of this concept is used in developing new strategies in modern supramolecular chemistry.[2] In this area, reversible non-covalent intermolecular forces provide a tool box for the supramolecular chemist as means of achieving enormous diversity in functional complementarity in supramolecular assemblies and architectures. Large synthetic receptors have offered high binding affinities,[3] remarkable selectivity,[4] high catalytic efficiency[5] and unique signaling systems.[6] Cavitands, bowl-shaped molecules that feature sizable concave surfaces hold prominent place in the history of these synthetic receptors.

Resorcin[4]arene based cavitands (Figure 6.1) were first introduced by Cram in 1980s as "molecules that contain enforced cavities large enough to accommodate simple molecules or ions".[7] Since then their popularity grew exponentially with particular attention of these molecules in numerous applications, for example, molecular catalysis,[8] molecular sensing,[9] stabilization of reaction intermediates,[10] as a reaction chamber,[11] gas encapsulation,[12] and as photosensitizers.[13] Furthermore, individual cavitand molecules can be self-assembled or covalently bound together to form capsules[10b, 14] or hexameric superbowl structures[15] which find applications due to the restricted inner space isolated from the bulk environment. The "nanospace" of these cavitands, capsules and superbowl structures have this unique well-defined size, volume and chemical characteristics that are well-suited for incorporating complementary guest molecules inside.

A resorcin[4]arene based cavitand exhibit a versatile scaffold with the possibility of achieving large variation in covalent modification in three different positions without altering the integrity of the cavitand framework (Figure 6.2). The lower end of a cavitand is termed as "feet" where covalent modification can be done to alter the solubility of the molecule.[16] The middle part of the molecule which constitutes the cavity is the "body" and is made up of four phenyl rings providing a π basic interior for capturing electron deficient guest molecules.[17] The methylene groups that are connecting the adjacent aromatic rings are the "bridging groups"

which are responsible for reducing the flexibility thus avoiding other possible conformations of the molecule. Bridging groups can be modified in order to alter the width or depth of the cavity.[7a, 18] The four positions on the rim of the cavity constitute the "upper rim" where most modifications can be performed to achieve cavitands decorated with a multitude of functional moieties. Our synthetic efforts will focus on functionalizing the upper rim (labeled X) while methylene bridges and the pentyl feet will not be altered Figure 6.2.

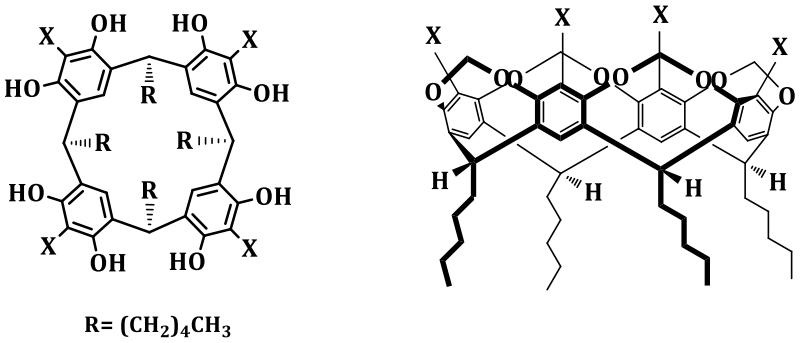

Figure 6.1 Resorcin[4]arene based cavitand scaffold; top view (left) right view (right)

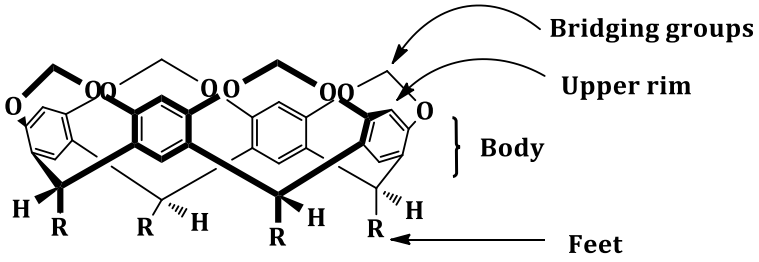

Figure 6.2 A resorcin[4]arene-based cavitand outlining the possible adaptable locations

A resorcin[4]arene-based cavitand, bearing four aromatic positions, upon functionalization, offer the advantage of binding four guest molecules per one host molecule. Moreover, the versatility offered by the cavitands creates opportunity for a wide range of guests that can be tailored towards a molecular recognition event. Reversibility is a key factor which needs to be achieved in any molecular recognition event and hydrogen bonding and halogen bonding have so far been the most promising supramolecular synthetic tools in the field of non-covalent synthesis.

6.1.1 Molecular recognition by upper rim functionalization

6.1.1.1 Hydrogen-bonded cavitands

Resorcin[4]arene based cavitands have been functionalized with hydrogen bond donors and acceptor moieties to impart hydrogen bonding capabilities. Hydrogen bond donors such as –COOH,[19] –OH,[20] –C(R)=NOH,[21] -NH_2,[22] -NHCOR[17a, 23] and hydrogen bond acceptors such as –pyridyl,[24] -pyrazole,[25] -C≡N[26] functionalities are reported with the major binding motifs as O-H···N, N-H···N, N-H···O bonding interactions (Figure 6.3). These synthons are employed in either guest binding of individual cavitands or dimeric hydrogen-bonded capsular assemblies.

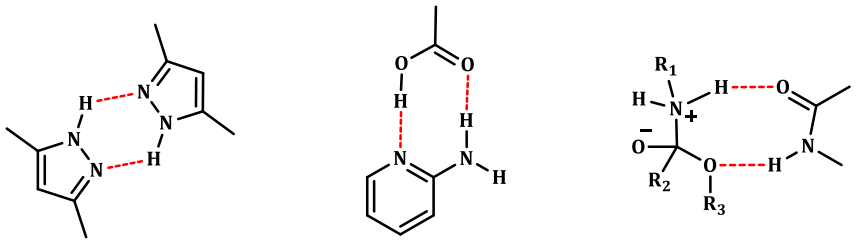

Figure 6.3 Schematic showing some examples of the observed synthons

6.1.1.2 Halogen-bonded cavitands

Employing halogen bonding functionalities is another way of decorating the rim of a cavitand, however, there are not many known examples of halogen bonded cavitands in the literature to date. Resorcin[4]arene cavitands, functionalized with fluorinated iodine donors assemble into a molecular capsule via halogen bonds is reported.[27] Tetraiodoethynyl resorcinarene cavitands are known to act as multivalent halogen bond donors towards neutral and anionic acceptors.[28] On the other hand, N-alkyl ammonium resorcinarene halides acting as halogen bond acceptors for perfluoroiodobenzene and bromotrichloro methane are also known.[29]

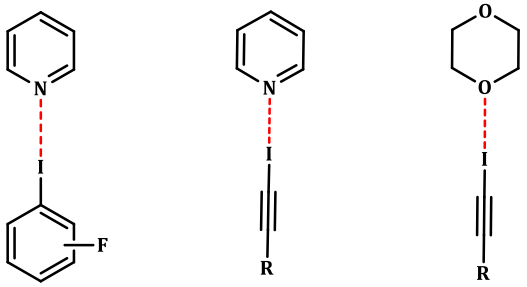

Figure 6.4 Schematic showing some examples of the observed synthons

6.1.2 Molecular recognition via cavity inclusion

The pre-organized hydrophobic interior of the cavitand is capable of encapsulating guests with high affinity and high selectivity. The structural complementarity between the host cavity and the guest is crucial in order for the molecular recognition to take place, where the size and shape of the guest determines the selectivity.

The aromatic walls that compose the cavity generate a polarizable π surface interior, and thereby has the potential to encapsulate and stabilize cations (by cation- π interactions),[30] molecules bearing a thin layer of positive charge such as C−H bonds (by CH- π interactions),[31] anionic species such as surfactants (sodium dodecyl sulfate, SDS),[32] and neutral species[33] are reported.

6.1.3 An approach for quantifying the molecular recognition event

Some of the major challenging tasks in supramolecular chemistry are, the design of large multicomponent systems with predictable stoichiometry and quantitative analysis of the intermolecular interaction of interest. Solid state experiments, i.e. FTIR analysis provide information to prove that the host and the guest of a particular system are interacting with each other, however, does not grant the stoichiometry or the strength of a binding event. Besides, single crystal growth of these larger systems suitable for X-ray diffraction is a major issue in supramolecular chemistry. The most common method to address this issue is the supramolecular titration method.

In this titration method, one component (i.e.guest) is incrementally titrated into the other component (i.e. host), by carefully monitoring the change of a physical property sensitive to the molecular recognition event, for example, the change in the resonance (NMR spectroscopy), the change in the absorbance (UV/fluorescence spectroscopy) etc. The data acquired from the titration is fit into non-linear binding curves to obtain the association constants K_a which is the basic criterion for evaluating the host-guest recognition process. In addition, free energy, ΔG can be calculated as expressing the favorability of the complexation and also the stoichiometry of the binding event can be determined by means of a Jobs plot.

6.1.4 Goals

The goals of this study are related to the fact that one cavitand molecule with the appropriate rim functionalization can act as a carrier of four guest molecules. We aim to design and synthesize cavitands with suitable upper rim functionalization and to study their binding ability towards a series of guest molecules. The guest have three options to bind to the cavitand via, 1) cavity inclusion, 2) upper rim binding, or 3) cavity inclusion and upper rim binding (Figure 6.5). The upper rim of the cavitand will be decorated with hydrogen bond and halogen bond donor and acceptor functionalities in order to evaluate their ability towards guest binding.

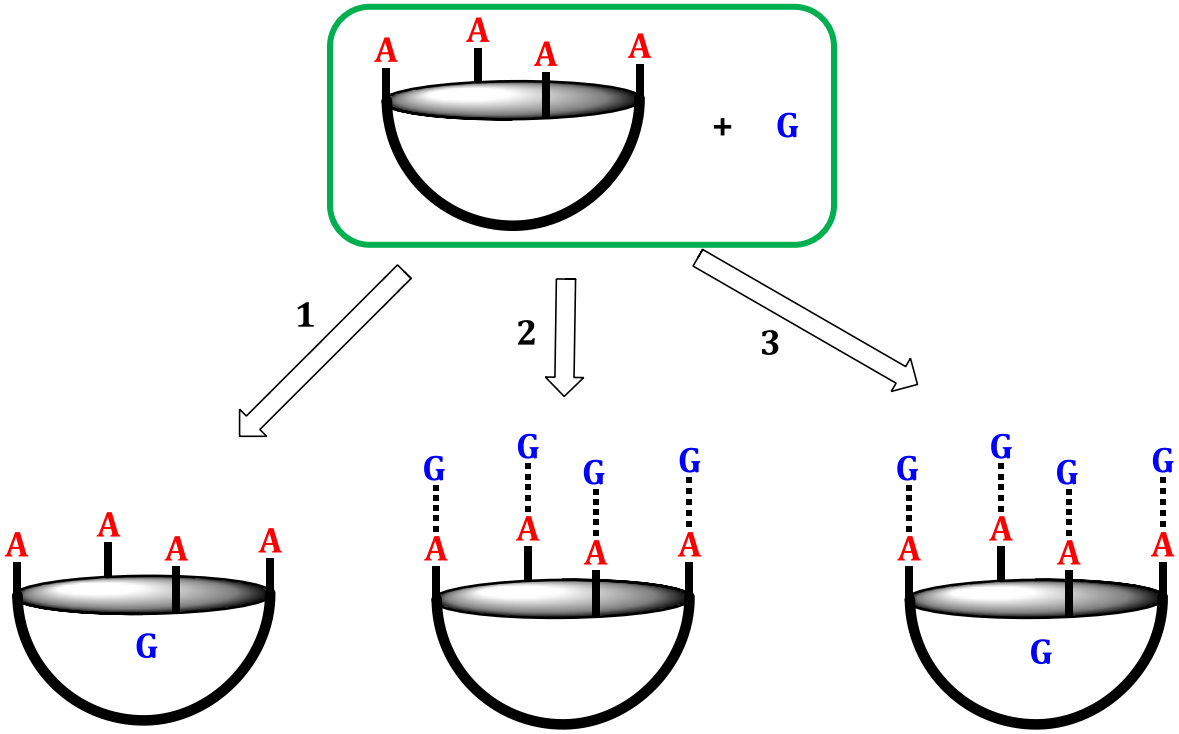

Figure 6.5 Cartoon representation showing the three possible modes of guest binding to the cavitand (A - binding site, G - guest)

The overall specific goals of this chapter are as follows-

i) To synthesize tetracarboxylic acid cavitand and tetraethynyl cavitand as hydrogen-bond (HB) donor functionalized cavitands and tetraiodoethynyl cavitand and tetrabromoethynyl cavitand as the halogen-bond (XB) donor functionalized cavitands

ii) To study the binding ability of these cavitands towards a series of active ingredients bearing HB/XB acceptor moieties

iii) To synthesize tetrapyridyl cavitand and tetra pyridyl-N-oxide cavitand as HB/XB acceptor functionalized cavitands

iv) To study the binding ability of these cavitands towards a series of active ingredients bearing HB/XB donor moieties

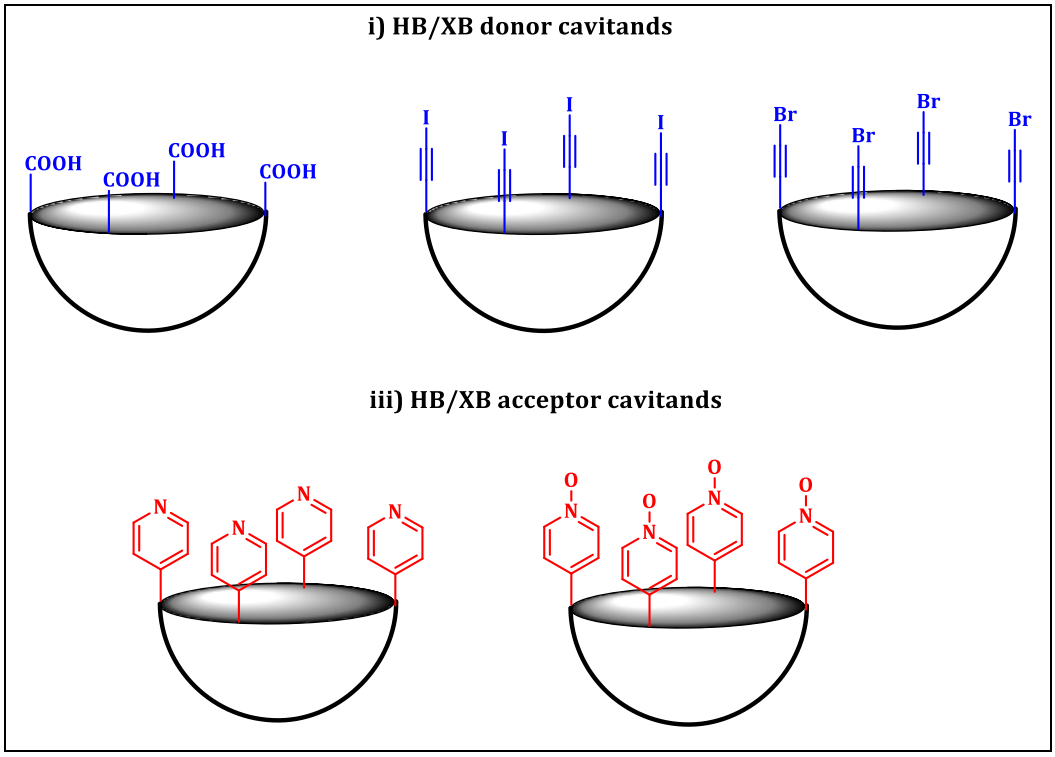

Figure 6.6 Target cavitands

6.2 Experimental

6.2.1 Synthesis

All chemicals were purchased from Aldrich, Fisher, TCI America, Oakwood products Inc. and the agrochemicals were from Syngenta crop protection, Inc. which were used without further purification unless otherwise noted. Column chromatography was carried out on silica gel (150 Å pore size) from Analtech, Inc. THF was distilled from sodium-benzophenone ketyl under an argon atmosphere. The ligands 3$\mathbf{A_8}$-3$\mathbf{A_0}$ and 4$\mathbf{A_8}$-4$\mathbf{A_0}$ were synthesized using the procedure reported in Chapter 2. Ibuprofen and naproxen were extracted from Advil and Aleve tablets. ^{1}H and ^{13}C NMR spectra were recorded on a Varian Unity plus 400 MHz spectrometer in $CDCl_3$ or DMSO. Data is expressed in parts per million (ppm) downfield shift from tetramethylsilane as

internal reference and are reported as position (in ppm). Variable temperature ^{1}H NMR experiments were carried out by cooling down the probe from 25 °C to 10 °C, 0 °C, -20 °C and -50 °C in $CDCl_3$. If not mentioned otherwise, all spectra were recorded at 25 °C. The residual solvent peak was used as the internal reference ($CDCl_3$: δH = 7.26 ppm, δC = 77.16 ppm; DMSO: δH = 2.56 ppm, δC = 53.32 ppm). The ^{1}H NMR spectra are reported as follows: chemical shift δ in ppm relative to TMS (δ = 0 ppm), multiplicity, coupling constant (J in Hz), number of protons. The resonance multiplicity is described as s (singlet), d (doublet), t (triplet), q (quartet) or m (multiplet). The determinations of melting points were carried out on Fisher-Johns melting point apparatus and are uncorrected. Infrared spectroscopy analysis was carried out using Nicolet 380 FT-IR with a digital resolution of 0.9 cm^{-1}. Data were analyzed using software, Omnic 8.0 © 1992-2008 Thermo Fisher Scientific Inc.

6.2.1.1 Synthesis of C-pentylcalix[4]resorcinarene, 1[34]

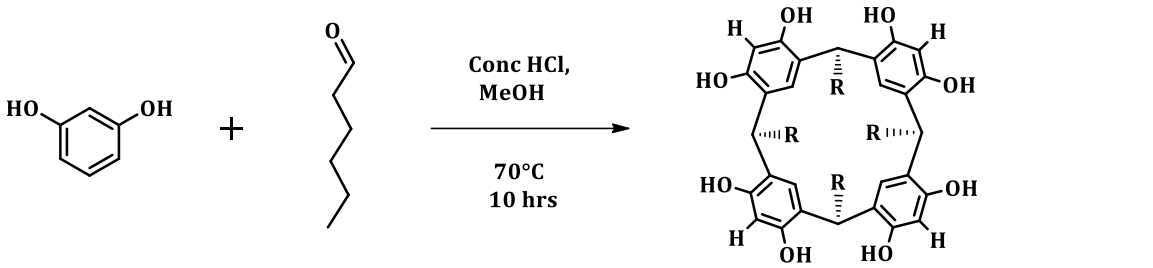

1 **R= $(CH_2)_4CH_3$**

Into a solution of resorcinol (50.0 g, 0.45 mol) dissolved in ethanol (500 mL), added hexanal (45.5 g, 0.45 mol). The mixture was cooled to 0 °C and conc. HCl (70 mL) was added dropwise under a dinitrogen atmosphere. The mixture was refluxed at 70 °C under nitrogen for 16 hours. Upon completion, reaction mixture was allowed to cool to room temperature and diluted with water (500 mL) to obtain a orange color precipitate with a fruity smell. It was filtered using a fritted Buchner funnel and washed with hot water until the filtrate is pH neutral. The product was air dried to yield **1** (77 g, 88 %). M.p. >280 ˚C; ^{1}H NMR (δH; 400 MHz, D_6-DMSO): 8.86 (s, 8H), 7.15 (s, 4H), 6.13 (s, 4H), 4.20 (t, J = 7.6Hz, 4H), 2.00 (m, 8H), 1.23-1.25 (m, 24H), 0.83 (t, 12 H, J=6.4Hz)

6.2.1.2 Synthesis of C-pentyltetrabromocalix[4]resorcinarene, 2[35]

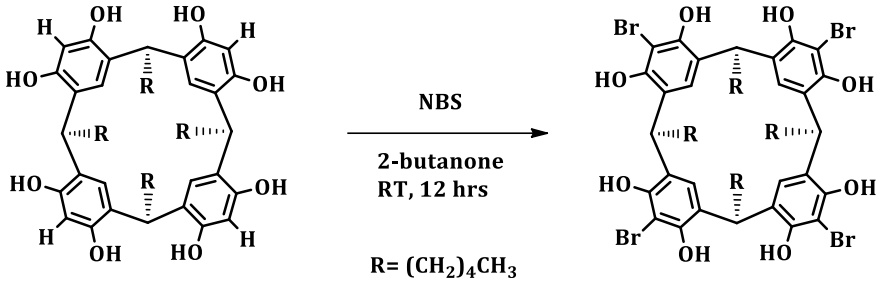

1 2

C-pentylcalix[4]resorcinarene, **1** (50.0 g, 0.065 mol) was added to the flask containing 2-butanone (375 mL) and stirred until all of **1** is dissolved. Reaction mixture was then cooled to 0 °C and was covered with aluminium foil. Under dark conditions, *N*-bromosuccinamide (69 g, 0.39 mol) was slowly added in small portions to the reaction mixture over a period of 1 hour. The reaction mixture was stirred at room temperature for 16 hours under dinitrogen atmosphere. After the addition of NBS, the reaction mixture was allowed to stir at room temperature for 12 hrs. The precipitate formed in the reaction was filtered and washed with cold 2- butanone (3 x 50 mL) then cold acetone (3 x 100 mL). Product **2** was air dried followed by drying in the oven overnight (at 100 °C) to produce off-white solid, (51.9 g, 74 %). M.p. >280 ˚C; ^{1}H NMR (δH; 400 MHz, D_6-DMSO) 9.1 (s, 8H), 7.34 (s, 4H), 4.34 (t, J = 6.4Hz, 4H), 2.17 (m, 8H), 1.28 (m, 24H), 0.84 (t, J = 7.2Hz, 12H)

6.2.1.3 Synthesis of C-pentyltetrabromocavitand, 3[36]

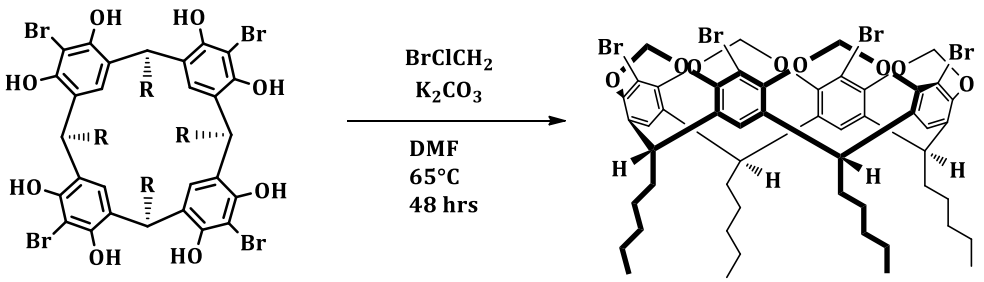

R= $(CH_2)_4CH_3$

2 3

To a stirred solution of C-pentyltetrabromoresorcin[4]arene, **2** (30.00 g, 27.80 mmol) dissolved in dry DMF (500 mL) was added K_2CO_3 (50.00 g, 510.0 mmol). The reaction mixture was purged with nitrogen for 20 minutes followed by the addition of CH_2BrCl (54.15 g, 418.51 mmol). A condenser was attached and solution was heated at 65 °C for 24 h under a dinitrogen

atmosphere. After 24 hours an additional amount of CH_2BrCl (7.50 g, 58.01 mmol) was then added, and the reaction mixture was stirred at 65 °C for a further 24 h. After completion, the reaction mixture was cooled to room temperature and poured into an aqueous HCl solution (2%, 600 mL). The solid, which contained mainly **3**, was filtered off and washed with water until pH is neutral. The solid was air dried and was then purified by column chromatography using Hexane : dichloromethane 1:1 mixture as the eluent. The product, **3** was isolated as a white solid, which upon recrystallization from dichloromethane gave colorless crystals. (23.6 g, 75 %). M.p. >280 ˚C; ^{1}H NMR (δH; 400 MHz, $CDCl_3$): 7.05 (s, 4H), 5.95 (d, J = 7.4Hz, 4H), 4.86 (t, J = 7.6Hz, 4H), 4.39 (d, J = 7.2Hz, 4H), 2.18 (m, 8H), 1.34 (m, 24H), 0.92 (t, 12H)

6.2.1.4 Synthesis of C-pentyltetracarboxyl cavitand, *4*[7a, 19b]

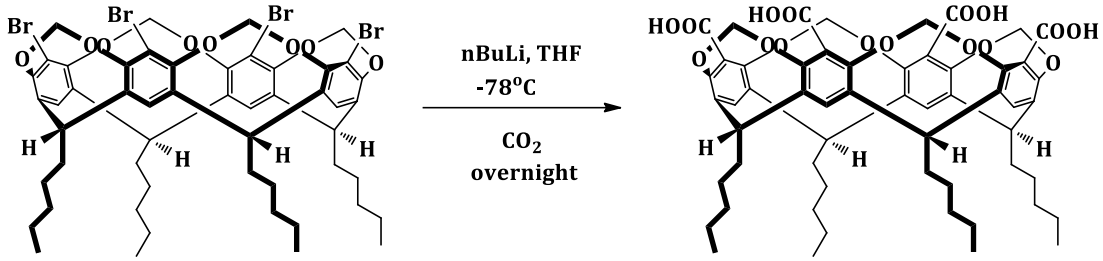

3 **4**

Dry freshly distilled tetrahydrofuran (20 mL) was added to C-pentyltetrabromocavitand **3** (2.16 g, 1.91 mmol), and then the solution was evaporated and dried at 80 °C (0.1 mmHg) for 2 h under an nitrogen atmosphere to get extremely dry solid of **3**. This procedure was repeated twice. At the end of the drying procedure, the solid, **3** was dissolved in dry tetrahydrofuran (200 mL) and cooled to -78 °C using dry ice/ acetone bath under dinitrogen atmosphere for 10 minutes. N-butyllithium (1.6 M in hexanes) (5.96 mL, 9.55 mmol) was slowly added dropwise to this solution upon which a milky solution begin to appear. After addition, the reaction mixture was stirred for 30 minutes under nitrogen. Then carbon dioxide gas was purged through the reaction mixture for 20 minutes at -78 °C. A balloon filled with carbon dioxide gas was then attached to the reaction flask and exchanged few times with fresh CO_2 balloons until the reaction mixture is saturated with CO_2 gas. The reaction was let warmed to room temperature and stirred over a CO_2 balloon overnight. Upon completion, a NaOH (1 M) aqueous solution (100 mL) was added to the reaction mixture at room temperature. THF was then removed under vacuum and the aqueous layer was washed with Et_2O (100 mL × 3), followed by acidifying with concentrated HCl at 0 °C. The resulted white solid of the product, **4** was then extracted with Et_2O (100 mL × 3). The

organic layer washed with water and brine, dried over anhydrous $MgSO_4$ and solvent removed under vacuum to yield **4** as colorless solid. The solid was then titurated with hexanes, filtered off and recrystallized from methanol to yield colorless crystals of **4** (1.5 g, 78%). M. p. > 280 ˚C; ^{1}H NMR (δH; 400 MHz, d_6-DMSO): 7.66 (s, 4H), 5.77 (d, J = 8.4Hz, 4H), 4.59 (t, J = 6.2Hz, 4H), 4.37 (d, J = 7.2Hz, 4H), 2.40 (m, 8H), 1.31 (m, 24H), 0.88 (t, 12H); 13C NMR (δC; 400 MHz, d6-DMSO) : 165.58, 149.86, 138.61, 125.54, 122.87, 99.27, 36.55, 31.62, 29.07, 27.42, 22.51, 14.19. IR : 3530, 3224, 2929, 2862, 1711, 1588, 1454, 1247, 1087, 954, 700 cm^{-1}.

6.2.1.5 Synthesis of C-pentyltetra(trimethylsilyl)ethynyl) cavitand, 5[37]

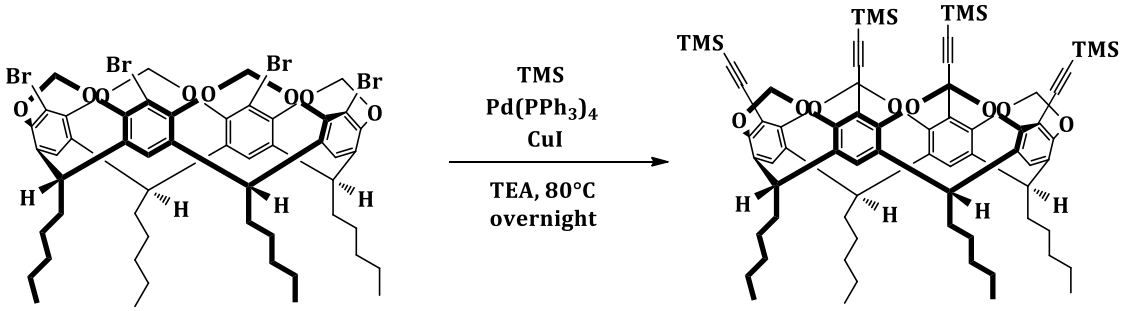

C-pentyltetrabromocavitand, **3** (4.02 g, 3.55 mmol) was dissolved in triethylamine (200 mL) and degassed by bubbling nitrogen through the reaction mixture for 20 minutes. TMS-acetylene (1.74 g, 17.75 mmol), $PdCl_2(PPh_3)_2$ (0.24 g, 0.35 mmol) and CuI (0.13 g, 0.71 mmol) were added and the mixture was heated under reflux at 70 ºC overnight under dinitrogen atmosphere. The solvent was removed by evaporation and the residue dissolved in diethyl ether (500 mL), was washed with 1 M HCl (200 mL) and brine (200 mL). The organic layer was separated and dried over anhydrous magnesium sulfate. The solvent was removed on a rotary evaporator and the residue was chromatographed on silica with hexane: ethyl acetate mixture as eluant to obtain a light brown colored powder. The crude product was purified by flash column chromatography with hexanes as the eluent, to give pure **5** as colorless crystalline powder (3.23 g, 76 %). ^{1}H NMR M. p. > 280 ˚C; ^{1}H NMR (δH; 400 MHz, $CDCl_3$): 6.99 (s, 4H), 5.86 (d, J = 7.2Hz, 4H), 4.79 (t, J = 7.6Hz, 4H), 4.52 (d, J = 8.4Hz, 4H), 2.18 (m, 8H), 1.34 (m, 24H), 0.92 (t, 12H), 0.20 (s, 36H)

6.2.1.6 Synthesis of C-pentyltetra(ethynyl) cavitand, 6

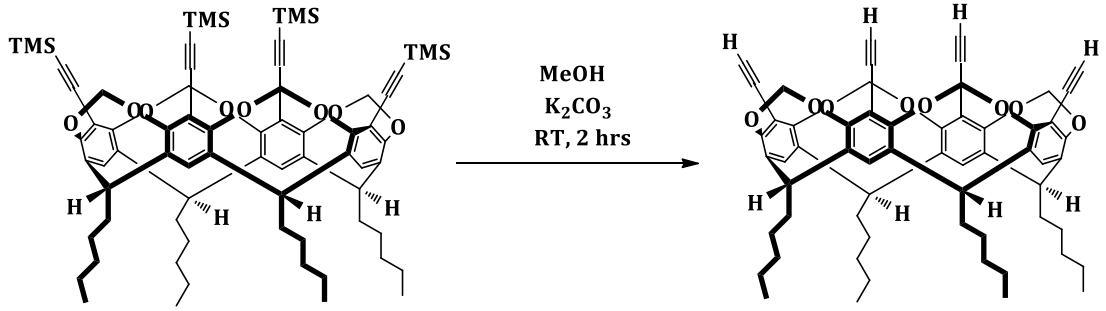

C-pentyltetra(trimethylsilyl)ethynyl) cavitand, **5** (5.3 g, 4.42 mmol) and potassium carbonate (2.44 g, 17.6 mmol) were stirred in methanol at room temperature for 2 hrs. Upon completion, the solvent was removed by rotary evaporation and the residue dissolved in diethyl ether and washed with water (2 x 50 mL). The combined organic layers were dried over anhydrous magnesium sulfate and concentrated via rotary evaporation to obtain the product, C-pentyltetra(ethynyl) cavitand, **6**, as a yellow crystalline solid. (3.14 g, 78%). M. p. > 280 ˚C; ^{1}H NMR (δH; 400 MHz, $CDCl_3$): 7.07 (s, 4H), 5.95 (d, J = 6.8Hz, 4H), 4.81 (t, J = 7.4Hz, 4H), 4.53 (d, J = 8.2Hz, 4H), 3.33 (s, 4H), 2.20 (m, 8H), 1.36 (m, 24H), 0.92 (t, 12H)

6.2.1.7 C-pentyltetra(iodoethynyl) cavitand, 7

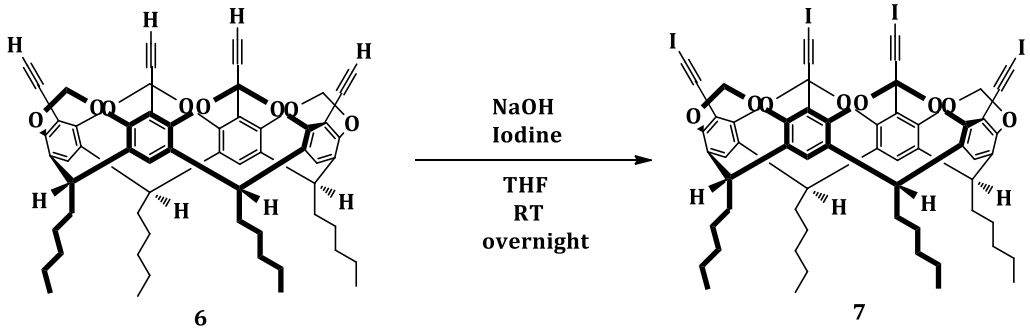

To a solution of C-pentyltetra(ethynyl) cavitand, **6** (1.05 g, 1.15 mmol) dissolved in methanol (100 mL), added dropwise simultaneously a concentrated solution of iodine in methanol (1.54 g, 6.072 mmol) and a 10% sodium hydroxide solution (10.49 mmol) over 30 min, vigorously stirring (Note : Initially the color of iodine disappears upon dropping into the reaction mixture and with time the color tend to persist. Therefore, NaOH should be added until the dropping iodine color no longer changes upon addition of NaOH in the reaction mixture). The mixture was stirred overnight, and quenched with 100 mL water upon which a light yellow color

precipitate forms. The filtered solid washed with sodium bisulfite solution afforded white color powder of **7** , (1.18 g, 73%). Dec. ˚C >280 °C. ^{1}H NMR (δH; 400 MHz, $CDCl_3$): 6.99 (s, 4H), 5.92 (d, J = 7.2Hz, 4H), 4.75 (t, J = 7.4Hz, 4H), 4.45 (d, J = 7.2Hz, 4H), 2.15 (m, 8H), 1.33 (m, 24H), 0.90 (t, 12H); ^{13}C NMR (δC; 400 MHz, $CDCl_3$) 156.38, 138.30, 120.25, 98.44, 36.34, 31.78, 29.37, 27.32, 22.62, 14.06.

6.2.1.8 C-pentyltetra(bromoethynyl) cavitand, 8

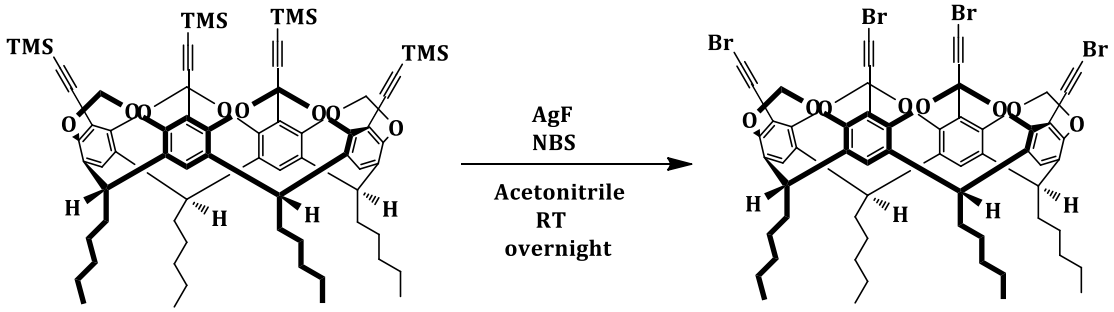

5 **8**

C-pentyltetra(trimethylsilyl)ethynyl) cavitand, **5** (1.2 g, 1.00 mmol) and AgF (0.51 g, 4.00 mmol) was placed in round-bottomed flask and CH_3CN (200 mL) was added. The mixture was stirred under purging nitrogen for 20 minutes. The flask was wrapped in aluminum foil and under dark conditions, NCS (0.71 g, 4.00 mmol) was added. The mixture was stirred for overnight at room temperature after which time it was passed through a 2 cm plug of silica gel. The solvent was removed by rotary evaporation. The resulting residue was dissolved in Et_2O and washed with H_2O (1000 mL x 2). The organic part was separated, dried over anhydrous magnesium sulfate and solvent was removed under vacuum to yield colorless crystals of **8** in 86 % yield (1.07 g, 0.86 mmol). Dec. ˚C >280 °. ^{1}H NMR (δH; 200 MHz, $CDCl_3$): 7.03 (s, 4H), 5.94 (d, J = 6.4Hz, 4H), 4.77 (t, J = 7.2Hz, 4H), 4.46 (d, J = 7.2Hz, 4H), 2.17 (m, 8H), 1.35 (m, 24H), 0.92 (t, 12H); ^{13}C NMR (δC; 400 MHz, $CDCl_3$) : 156.36, 138.65, 120.63, 112.88, 98.82, 72.29, 57.68, 36.68, 32.13, 29.72, 27.66, 22.95, 14.39

6.2.1.9 C-pentyltetra(4-pyridyl) cavitand, 9

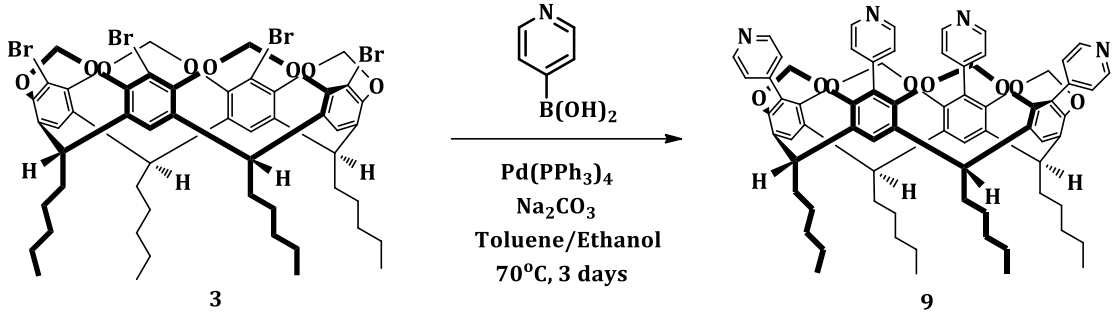

A mixture of *C*-pentyltetrabromocavitand, **3** (2.0 g, 1.77 mmol) and t*etrakis*triphenylphosphine palladium (II) (420 mg, 0.362 mmol) were placed in a round bottom flask under a stream of dinitrogen. To this added a mixture of toluene (30 mL), ethanol (20 mL) and aqueous sodium bicarbonate (100 mg, 5 mL) purged with dinitrogen. Then 4-pyridylboronic acid (2.8 g, 22.76 mmol) was added to the reaction mixture and was refluxed for 72 hours under a dinitrogen atmosphere. Upon completion the reaction was cooled to room temperature and diluted with water (100 mL). The aqueous phase was washed with dichloromethane (3 x 100 mL) and dried with anhydrous magnesium sulfate. The solvent was removed on a rotary evaporator and the residue purified by column chromatography using an ethanol/ethyl acetate (1:2) mixture as the eluant. The product **9** was isolated as a white crystalline solid, (1.44 g, 72%). Dec. ˚C >280 °C. ^{1}H NMR (δH; 400 MHz, $CDCl_3$): 8.53 (d, J = 4Hz, 8H), 7.37 (s, 4H), 7.03 (d, J = 6.2 Hz, 8H), 5.19 (d, J = 7.2Hz, 4H), 4.87 (t, J = 7.6 Hz, 4H), 4.26 (d, J = 7.0Hz, 4H), 2.36 (m, 8H), 1.48 (m, 24H), 0.97 (t, 12H); ^{13}C NMR (δC; 400 MHz, $CDCl_3$) : 152.48, 149.66, 142.44, 138.88, 127.21, 125.25, 121.16, 100.65, 37.30, 32.28, 30.53, 27.87, 22.97, 14.42

6.2.1.10 C-pentyltetra(3-pyridyl) cavitand, 10

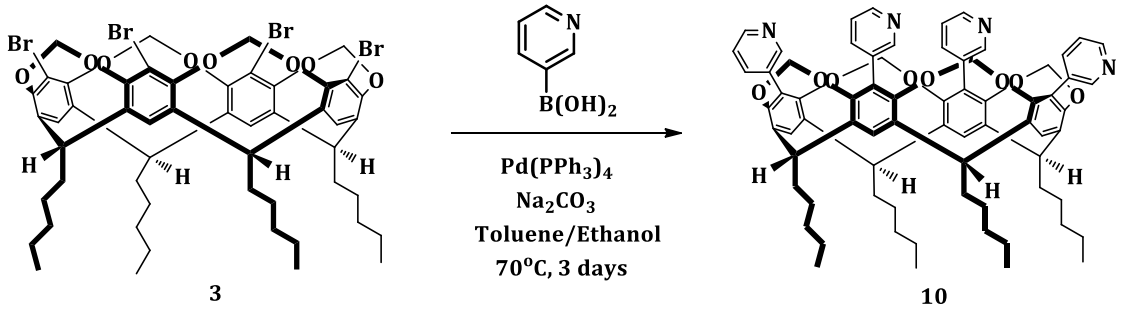

A mixture of C-pentyltetrabromocavitand, **3** (2.0 g, 1.77 mmol) and tetrakistriphenylphosphine palladium (II) (420 mg, 0.362 mmol) were placed in a round bottom

flask under a stream of dinitrogen. To this added a mixture of toluene (30 mL), ethanol (20 mL) and aqueous sodium bicarbonate (100 mg, 5 mL) purged with dinitrogen. Then 3-pyridylboronic acid (2.8 g, 22.76 mmol) was added to the reaction mixture and was refluxed for 72 hours under a dinitrogen atmosphere. Upon completion the reaction was cooled to room temperature and diluted with water (100 mL). The aqueous phase was washed with dichloromethane (3 x 100 mL) and dried with anhydrous magnesium sulfate. The solvent was removed on a rotary evaporator and the residue purified by column chromatography using an ethanol/ethyl acetate (1:2) mixture as the eluant. The product **10** was isolated as a white crystalline solid, (1.63 g, 92%). Dec. ˚C >280 °C. ^{1}H NMR (δH; 400 MHz, $CDCl_3$): 8.44 (d, J = 6.4Hz, 4H), 8.29 (s, 4H), 7.47 (d, J = 7.2Hz, 4H), 7.37 (s, 4H), 7.23 (d, J = 8Hz, 4H), 5.27 (d, J = 7.2Hz, 4H), 4.87 (t, J = 7.4Hz, 4H), 4.31 (d, J = 8Hz, 4H), 2.37 (m, 8H), 1.49 (m, 24H), 0.97 (t, 12H); ^{13}C NMR (δC; 400 MHz, $CDCl_3$): 153.84, 149.52, 147.98, 138.67, 130.46, 126.88, 123.40, 120.95, 100.49, 37.38, 32.35, 30.49, 27.92, 23.00, 14.46.

6.2.1.11 C-pentyltetra(4-pyridyl-N-oxide) cavitand, *11*[38]

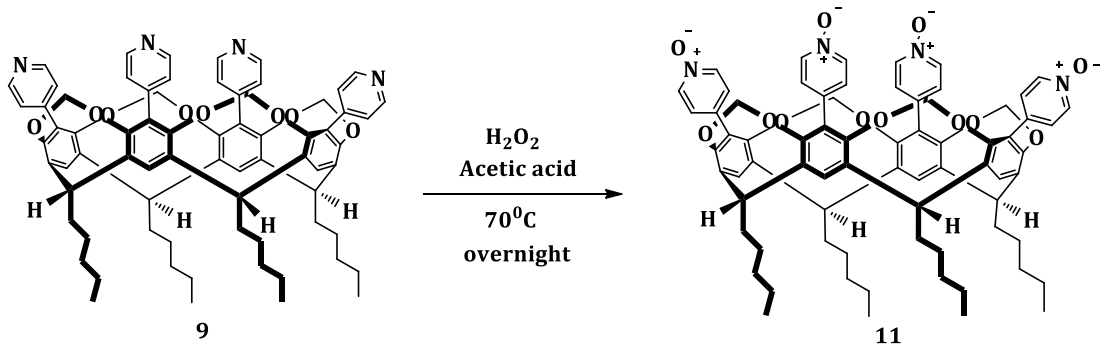

9 11

A mixture of *C*-pentyltetra(4-pyridyl)cavitand, **9** (1.05 g, 0.93 mmol), 30% hydrogen peroxide (1.3 mL, 0.44 g, 13.02 mmol) and glacial acetic acid (10 mL) was placed in a round bottom flask and refluxed overnight at 70 °C. Upon completion, reaction mixture was cooled to room temperature and diluted with water (20 mL) to precipitate C-pentyltetra(4-pyridyl-N-oxide) cavitand **11** as colorless solid. Recrystallization of the solid in ethylacetate:ethanol mixture gave colorless crystals of pure **11** (1.01 g, 92%). Dec. ˚C >280 °C. ^{1}H NMR (δH; 400 MHz, $CDCl_3$): 8.07 (d, J = 6Hz, 8H), 7.36 (s, 4H), 7.01 (d, J = 7.2Hz, 8H), 5.46 (d, J = 7.0Hz, 4H), 4.84 (t, J = 7.2Hz, 4H), 4.28 (d, J = 8Hz, 4H), 2.33 (m, 8H), 1.43 (m, 24H), 0.97 (t, 12H)

6.2.1.12 C-pentyltetra(3-pyridyl-N-oxide) cavitand, 12

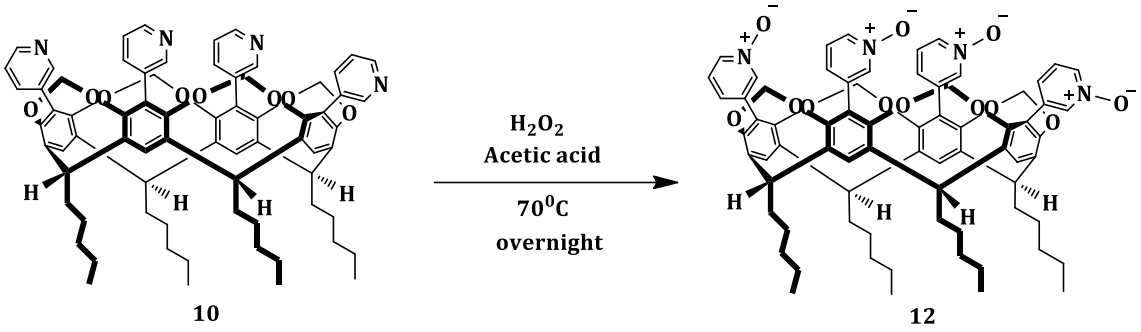

10 12

A mixture of *C*-pentyltetra(3-pyridyl)cavitand, **10** (0.95 g, 0.84 mmol), 30% hydrogen peroxide (1.2 mL, 0.39 g, 11.76 mmol) and glacial acetic acid (10 mL) was placed in a round bottom flask and refluxed overnight at 70 °C. Upon completion, reaction mixture was cooled to room temperature and diluted with water (20 mL) to crash out C-pentyltetra(3-pyridyl-N-oxide) cavitand **12** as orange color solid. Recrystallization of the solid in ethylacetate:ethanol mixture gave yellow color crystals of pure **12** (0.94 g, 95%). Dec. ˚C >280 °C. ^{1}H NMR (δH; 400 MHz, $CDCl_3$): 8.14 (d, J = 7.2Hz, 4H), 8.06 (s, 4H), 7.37 (d, J = 7.6Hz, 4H), 7.37 (s, 4H), 7.24 (d, J = 8Hz, 4H), 5.32 (d, J = 7.2Hz, 4H), 4.81 (t, J = 7.4Hz, 4H), 4.27 (d, J = 8Hz, 4H), 2.34 (m, 8H), 1.47 (m, 24H), 0.97 (t, 12H); ^{13}C NMR (δC; 400 MHz, $CDCl_3$) : 152.43, 139.35, 138.37, 137.76, 133.18, 129.00, 125.36, 123.98, 121.37, 100.32, 36.88, 31.89, 30.03, 27.48, 22.60, 14.06.

6.2.1.13 Extraction of ibuprofen from Advil tablets[39]

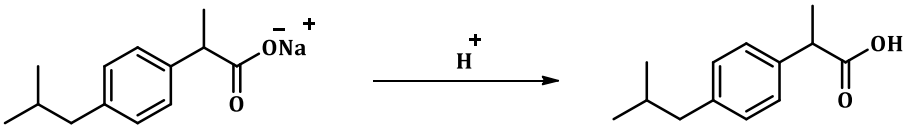

Advil tablets (800 mg x 5) were crushed using a mortar and pestle and to the resulting powder added 10 mL of 3M HCl. The contents were agitated gently and the aqueous solution was extracted with dichloromethane (3 x 5 mL). The organic layer was dried over anhydrous magnesium sulfate and the solvent removed under reduced pressure to yield crude ibuprofen as a white solid. For recrystallization, the solid was dissolved in minimum amount of hot isopropylalcohol and cooled back to room temperature after which water was added dropwise with swirling until the solution become cloudy. It was cooled on ice until the precipitation is complete to give pure ibuprofen as white crystalline solid (3.03 g). M.p. 76-78 ˚C. ^{1}H NMR (δH;

400 MHz, $CDCl_3$): 7.22 (d, 2H), 7.10 (d, 2H), 3.70-3.75 (m, 1H), 2.45 (d, 2H), 1.82-1.89 (m, 1H), 1.50 (d, 3H), 0.91 (d, 6H).

6.2.1.14 Extraction of naproxen from Aleve tablets[39]

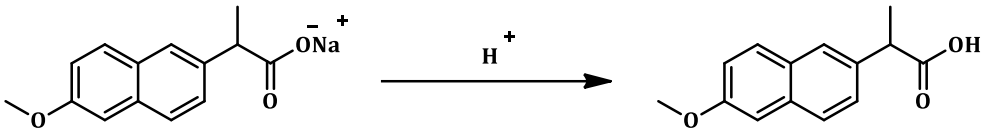

Aleve tablets (550 mg x 5) were soaked in 30 mL of methanol in a small beaker until outer layer of the tablets will begin to peel away from the inner tablet. As soon as this happens, the inner tablets were removed carefully with forceps leaving all of the outer coating in the methanol solution, which will be discarded. The 5 inner tablets were placed in 25 mL of fresh methanol and swirled to dissolve the naproxen sodium salt (dissolution is rather slow and require about 20 minutes at room temperature). When the naproxen is completely dissolved, the solution was filtered off to get rid of the flaky material that is still left undissolved. Methanol was removed by rotary evaporation to yield the solid naproxen sodium salt, which was then dissolved in water, and added 3 M HCl to precipitate the free acid of naproxen. The white precipitate of naproxen was filtered and dissolved in chloroform. It was washed with water, dried over $MgSO_4$ and solvent removed by rotary evaporation to yield naproxen as white solid (2.20 g). M.p. 154-156 ˚C. ^{1}H NMR (δH; 400 MHz, $CDCl_3$): 7.69-7.72 (m, 2H), 7.40 (d, 1H), 7.11-7.15 (m, 2H), 3.91 (s, 3H), 3.87-3.91 (q, 1H), 1.58 (d, 3H).

6.2.2 NMR titration experiments

6.2.2.1 Preparation of the solutions

The host (cavitand) concentration [H] was kept constant throughout the titration while the guest (active ingredients) concentration [G] was varied gradually. A stock solution of the host cavitand is prepared from which a constant amount is added to each NMR sample thus the concentration of each final sample is 1.6 mM. A stock solution of the guest is prepared from which successive volumes are added into the host during the titration. In our experiments, the concentrations of the guest [G] in the final solution would range from 0.25-12 mM.

6.2.2.2 Binding constant determination

A solution of known concentration of the guest is successively added to the host until an equilibrium is reached in the host-guest binding event which is indicated by a constant value of the chemical shift in the NMR spectrum. All the spectra were run at 298 K in $CDCl_3$ unless otherwise noted. A series of 9-10 data points were recorded for each titration experiment. The changes in the chemical shifts acquired from the titrations were graphed against the guest concentration with non-linear mathematical approach based on Benesi-Hildebrand analysis[40] using Origin 8.1 software. The equation used for curve fitting is given below,

$$\mathbf{H + G \leftrightarrow HG}$$

$$K_a = \frac{[HG]}{[H][G]}$$

$$\Delta\delta = \frac{\Delta\delta_{sat}}{2}\left[\left(\frac{[G]_0}{[H]_0} + 1 + \frac{1}{K_a[H]_0}\right) - \sqrt{\left(\frac{[G]_0}{[H]_0} + 1 + \frac{1}{K_a[H]_0}\right)^2 - 4\frac{[G]_0}{[H]_0}}\right] \quad \text{——— (1)}$$

where $[H]_o$ is the host concentration, $[G]_o$ is total concentration of the guest (bound and unbound), K_a is the association constant and $\Delta\delta$ is the change in the chemical shift.

6.3 Results and discussion

6.3.1 Guest binding in solid state

Solvent assisted grinding was performed by mixing the cavitand host and the guests in 1:4 stoichiometric ratio and grind them together in the presence of a drop of methanol until a solid paste is resulted, which was then analyzed by IR spectroscopy for presence of hydrogen bonding and halogen bonding between the host and the guest. The two broad stretches that appear at approximately 2500 and 1900 cm^{-1}, is an indicative of intermolecular O-H···N (heterocyclic) hydrogen bond. The shifts of the carbonyl stretch around 1700 cm^{-1} also suggests the presence of hydrogen bonds. The major characteristic band to observe the occurrence of a halogen bond is the C≡C stretch which appear in the range 2100 – 2260 cm^{-1} as mentioned in Chapter 4 and 5.

6.3.1.1 HB/XB donor cavitands

The HB/XB donor cavitands, **4**, **7** and **8** were reacted with a series of active ingredients (AI) with HB/XB acceptor moieties in order to evaluate their binding ability in solid state (Figure 6.7). The expected interactions that are intended to occur between the donor and the acceptor are shown in Figure 6.8.

The solid paste from the grinding experiments between **4** and active ingredient were analyzed using IR spectroscopy for detection of effective co-crystal formation with the assistance of characteristic OH···N stretch and the shift of the carbonyl peak of the cavitand donor. Two examples to illustrate a positive co-crystal formation by **4** reacting with $\mathbf{A_6}$ (Figure 6.9) and tridimefon (Figure 6.10) displaying the two stretches around 2200 cm^{-1} and 1800 cm^{-1} and by the shift of the carbonyl stretch. The salt formation was evident by the presence of COO^- anion which is formed upon proton transfer, display a strong asymmetric stretch around 1650-1550 cm^{-1}.[41] The outcome of all the grinding experiments are summarized in Table 6.1. All the active pharmaceutical ingredients exhibit interaction with **4** forming 20% salts and 80% co-crystals. The ground solid mixtures of **4**, containing pyraclostrobium, clomazone and cyprodinil did not show a carbonyl stretch around 1706 cm^{-1}, instead a new peak appear at 1654, 1677 and 1662 cm^{-1} respectively indicating salt formation. Overall, successful co-crystal formation was 50% with the agrochemicals (2/4) and 100 % with the fungicides (4/4).

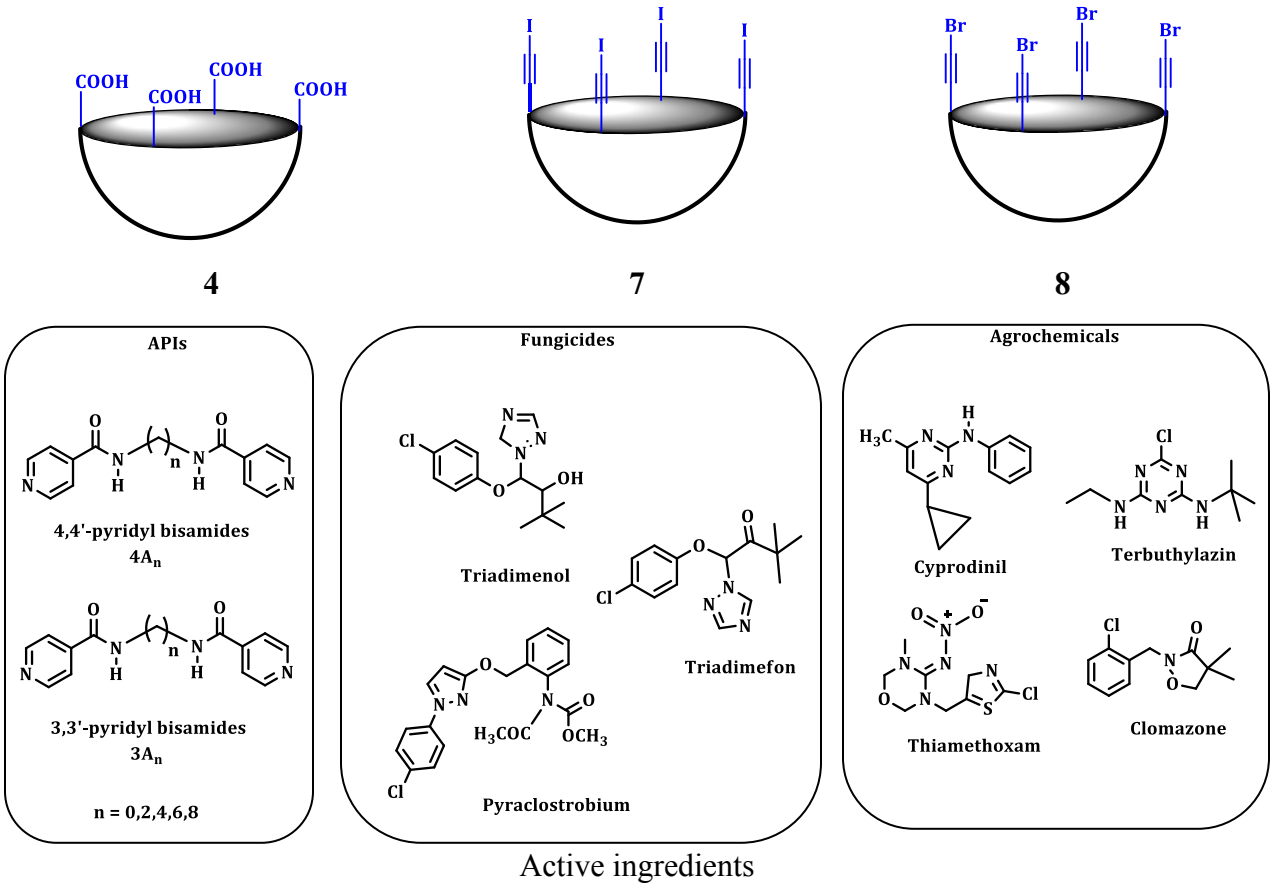

Figure 6.7 The HB/XB donor cavitands, (**4**, **7** and **8**) and the active ingredients used in the study

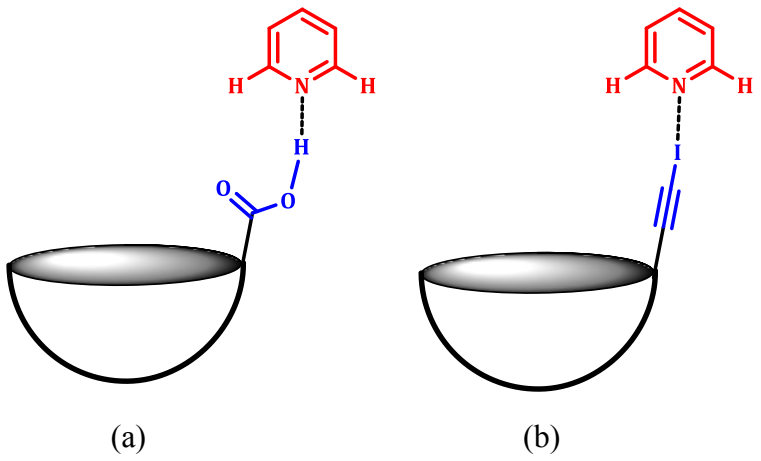

Figure 6.8 (a) OH···N hydrogen bonding between cavitand **4** and AI (b) C-I···N halogen bonding between cavitand **7** and active ingredient

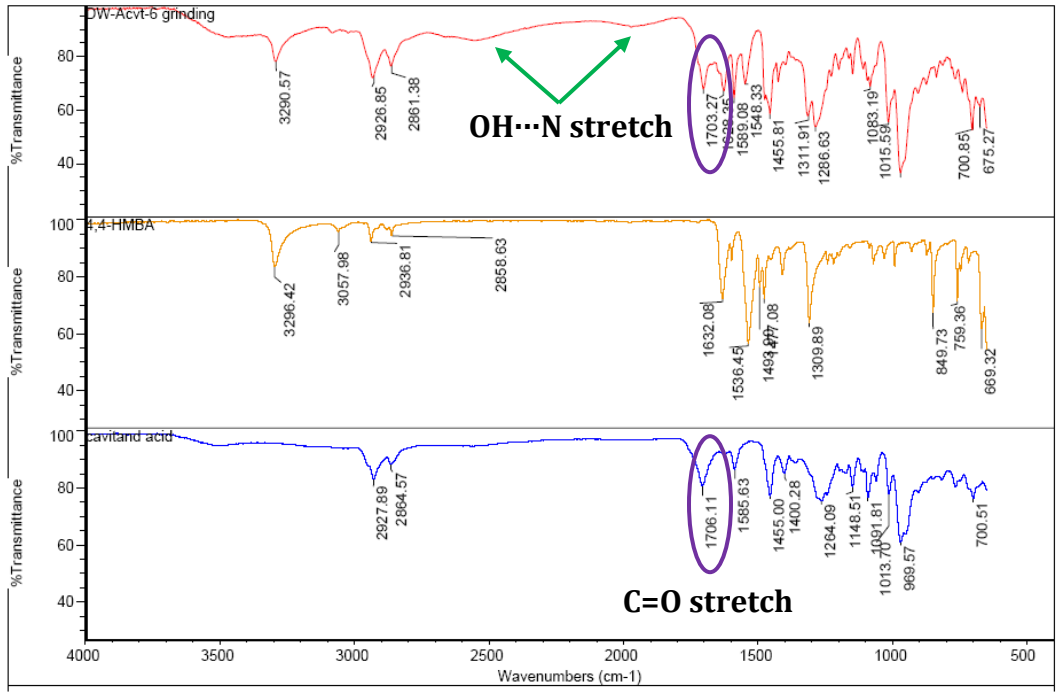

Figure 6.9 IR spectra of the ground mixture of cavitand **4** with API ($4A_6$) (top), in comparison with API ($\mathbf{A_6}$) (middle), cavitand **4** (bottom)

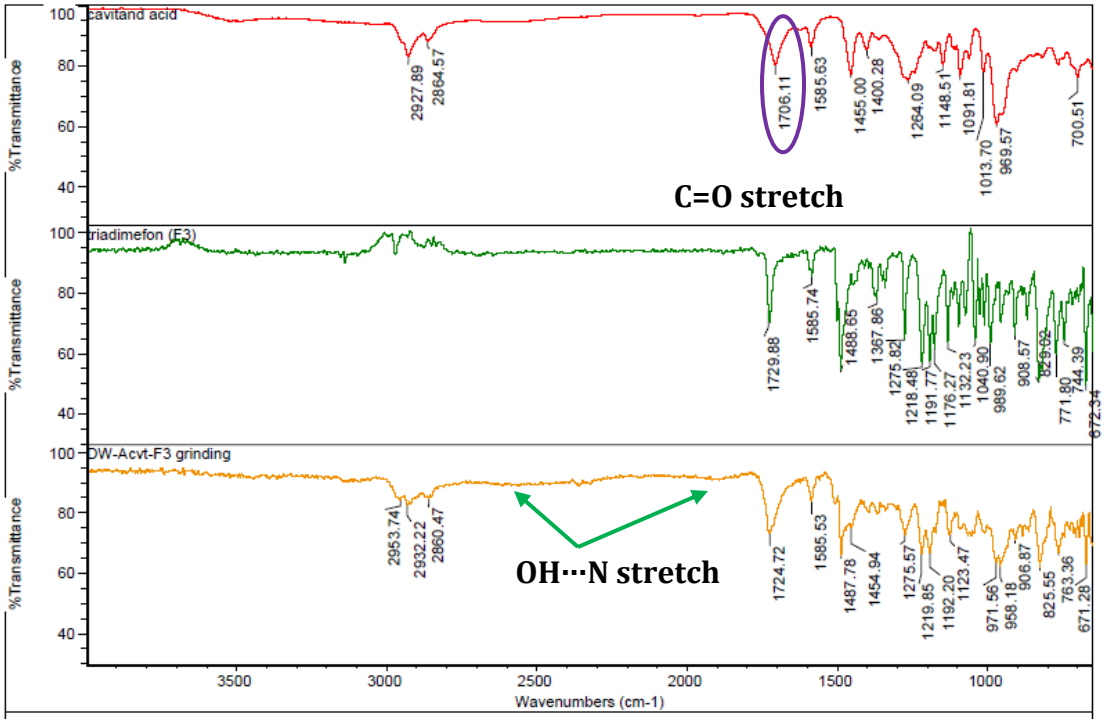

Figure 6.10 IR spectra of the ground mixture of cavitand **4** with tridimefon (bottom), in comparison with **tridimefon** (middle), cavitand **4** (top)

Table 6.1 Characteristic IR stretches evidenced for hydrogen bonding

Active ingredient (AI)	OH···N stretch (cm^{-1})	C=O stretch (cm^{-1}) (1706 cm^{-1})	Product
$4A_8$	2545, 1979	1705	Co-crystal
$4A_6$	2496, 1967	1710	Co-crystal
$4A_4$	2557, 1854	1707	Co-crystal
$4A_2$	2475, 1951	1678	Salt
$4A_0$	-	1675	Salt
$3A_8$	2534, 2033	1725	Co-crystal
$3A_6$	2545, 1928	1703	Co-crystal
$3A_4$	2557, 1975	1708	Co-crystal
$3A_2$	2545, 1986	1729	Co-crystal
$3A_0$	-	1709	Co-crystal
Triadimenol	2523, 1812	1712	Co-crystal
Triadimefon	2490, 1784	1724	Co-crystal
Pyraclostrobium	-	1654	Salt
Terbuthylazin	-	1704	No reaction
Thiamethoxam	-	1708	No reaction
Clomazone	-	1677	Salt
Cyprodinil	-	1662	Salt

However, attempts to proceed with cavitand **7** and **8** as XB donor cavitand using solvent assisted grinding was not successful, as we were unable to identify the C≡C stretch of **7** and **8** that was already weak and indistinct and became more weaker and disappeared when combined with a coformer, and thus characterization of whether or not complexation, based on IR data had occurred, was not possible (Figure 6.11).

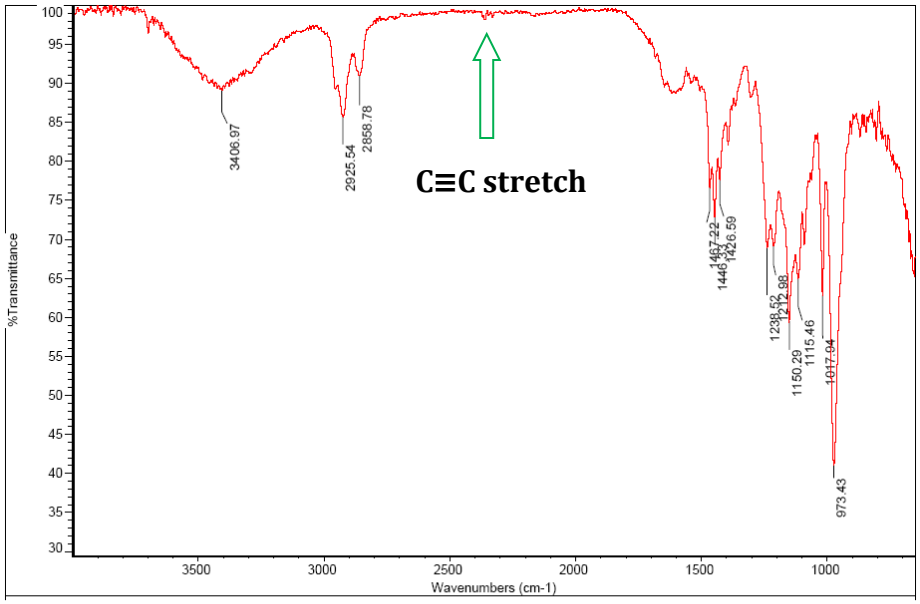

Figure 6.11 IR spectra of iodoethynyl cavitand with vague C≡C stretch

6.3.1.2 HB/XB acceptor cavitands

Cavitands **9** and **10** were combined with six active pharmaceutical ingredients (API) with hydrogen donor functionalities (Figure 6.12) paying particular attention to the OH···N stretch and the shift of the carbonyl peak of the API.

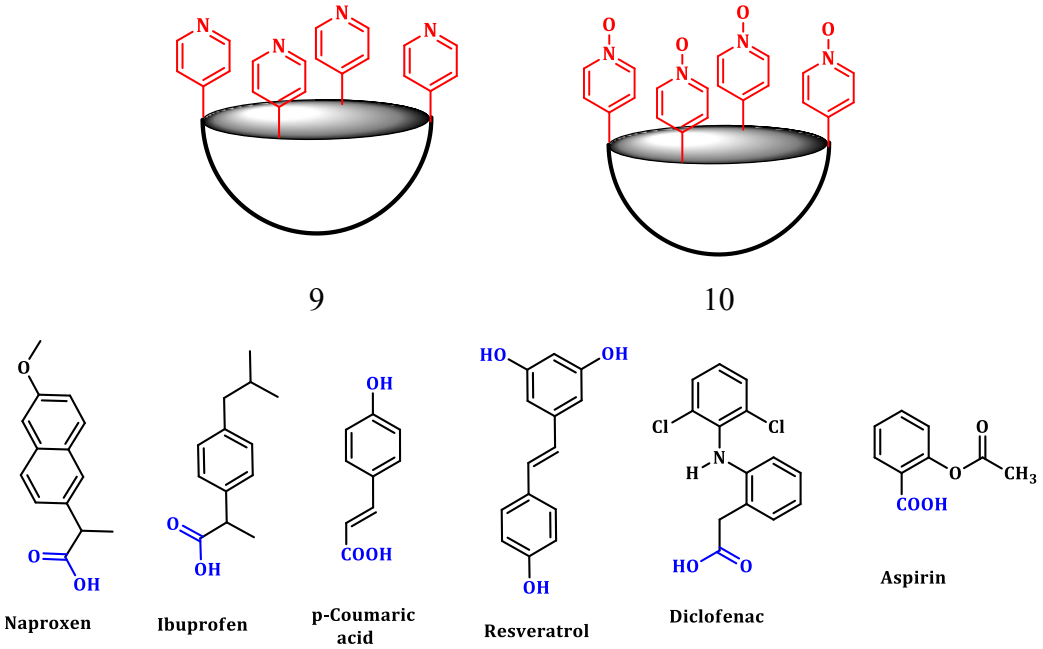

Figure 6.12 Cavitands **9** and **10** and APIs used in the study

An example of a successful co-crystal formation between cavitand **9** and ibuprofen is displayed by Figure 6.13, where the two characteristic broad stretches appear at 1984, 2579 cm^{-1} and the carbonyl peak is red shifted 10 cm^{-1} wave numbers compared to free ibuprofen. The physical mixture of ibuprofen either ground together with **9** or **10** turned out to be a sticky solid indicative of the interaction between the two components. Table 6.2 summarizes the vibrational stretches observed for each ground mixture. For the HB donor, resveratrol, the OH···N stretches were not prominent thus the shifts of the peaks of both the donor and acceptor was taken into consideration. Based on IR spectroscopy, cavitand **9** forms co-crystals with all the active ingredients except resveratrol and coumaric acid providing 67% supramolecular yield. Except resveratrol, cavitand **10** seemed to hydrogen bond with all the other active ingredients with an 83% supramolecular yield.

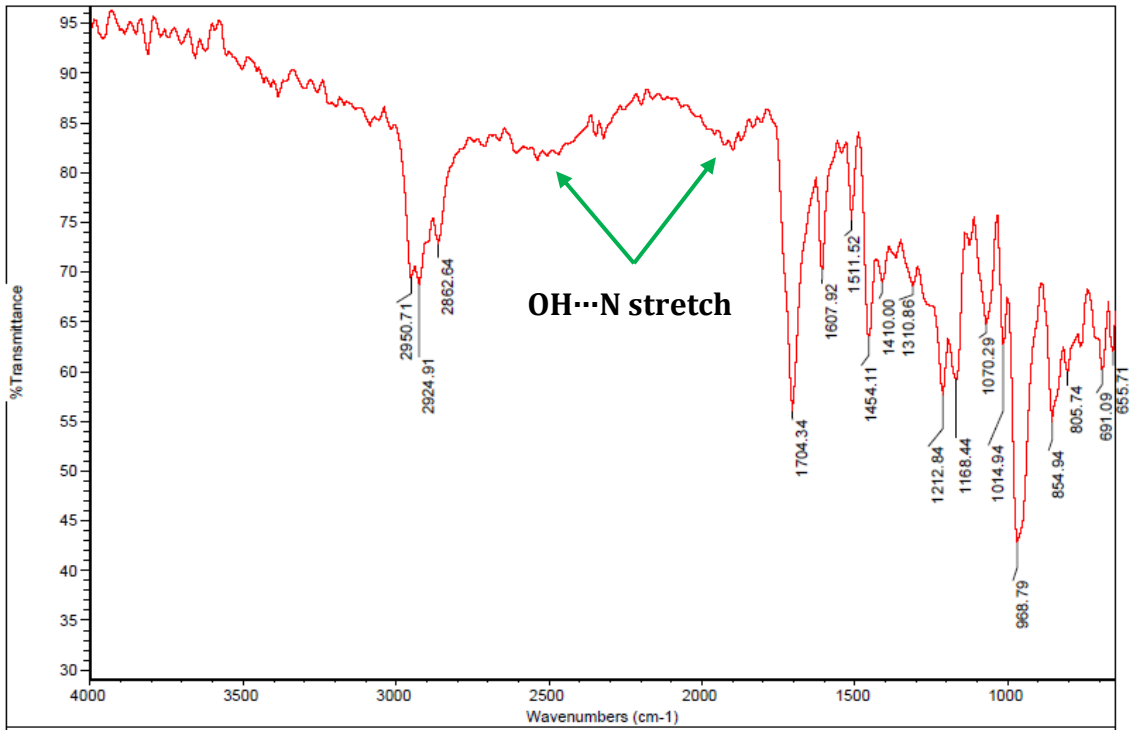

Figure 6.13 IR spectra of the grinding experiment between cavitand **9** and ibuprofen

Table 6.2 Summary of IR data (cm^{-1}) for cavitands **9** and **10**

	Cavitand 9 **OH···N stretch** **C=O stretch**	**Cavitand 10** **OH···N stretch** **C=O stretch**
Ibuprofen	1984, 2579 1704	1796, 2525 1708
Naproxen	1964, 2493 1721	1864, 2502 1724
Diclofenac	1835, 2613 1690	- 1689
Resveratrol	-	-
p-Coumaric acid	- 1750	1876, 2524 1670
Aspirin	1910, 2615 1751	- 1752
Supramolecular yield	***67%***	***83%***

6.3.2 Guest binding in solution via hydrogen bonding

The binding affinity and selectivity of the hosts, **9** and **10** towards the APIs (Figure 6.12) were evaluated in solution using ^{1}H NMR spectroscopy. We expected a multi component pentameric supramolecular assembly to form in solution since one cavitand bears four HB acceptor functionalities on the upper rim accessible for four HB donors (Figure 6.14a). We focused our work on ^{1}H NMR titration as a way of quantifying this binding event, where the binding of the HB donors to the cavitands **9** and **10** is monitored by changes in the chemical shifts of the hydrogen atoms, H_2 and H_6, *ortho* to the pyridyl N and N-oxide groups (Figure 6.14b).

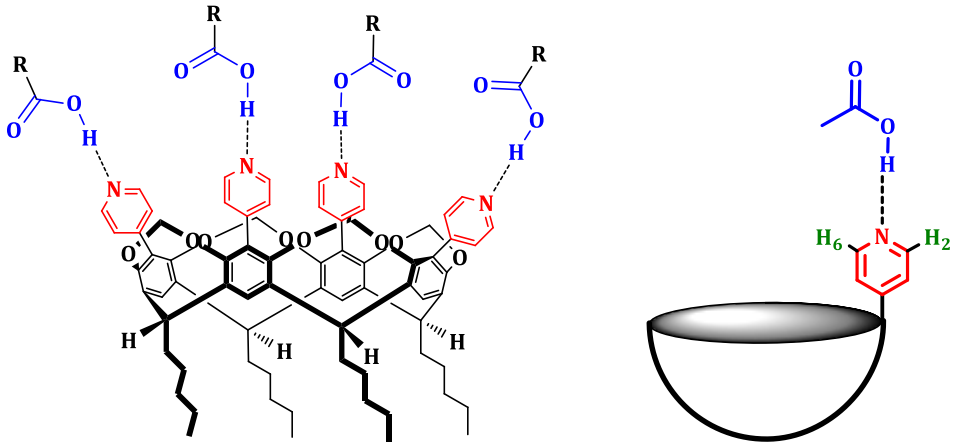

(a) (b)

Figure 6.14 (a) An example of proposed multicomponent supramolecular assembly created via hydrogen bonding (b) Schematic representation of the guest binding via hydrogen bonding; the *ortho* protons, H_2 and H_6 are indicated in green

Cavitands **9** and **10** are reacted with all the HB donors by adding excess amounts (10 equivalents) of the guest into a host solution. Particular attention is paid to the deshielding of the H_2 and H_6 protons upon addition of HB donors and the changes in δ ppm values ($\delta_{\text{bound host}} - \delta_{\text{free host}}$) were used for in determining the association constants, K_a and the stoichiometry. Figure 6.15 shows some examples of the changes in the chemical shifts of H_2 and H_6 protons of **9**, with the addition of Naproxen, Diclofenac, Ibuprofen and aspirin. Naproxen doesn't seem to hydrogen bond to **9** with no shift of H_2 and H_6, while the others did show interaction.

Table 6.3 summarizes the chemical shifts observed with the addition of excess guest into the hosts, **9** and **10**. All the guest molecules except naproxen and resveratrol seems to bind to **9**, where the peaks corresponding to *ortho* protons of the host (8.51-8.53) is shifted downfield by 0.10 ppm, 0.09 ppm, 0.1 ppm for ibuprofen, diclofenac and *p*-coumaric acid respectively. The average signal appears as a well-resolved sharp doublet. The *ortho* protons of cavitand **10**, which appear at 8.04-8.05, shifted downfield to ~8.22 ppm with the addition of all the guests except resveratrol, with an intact doublet.

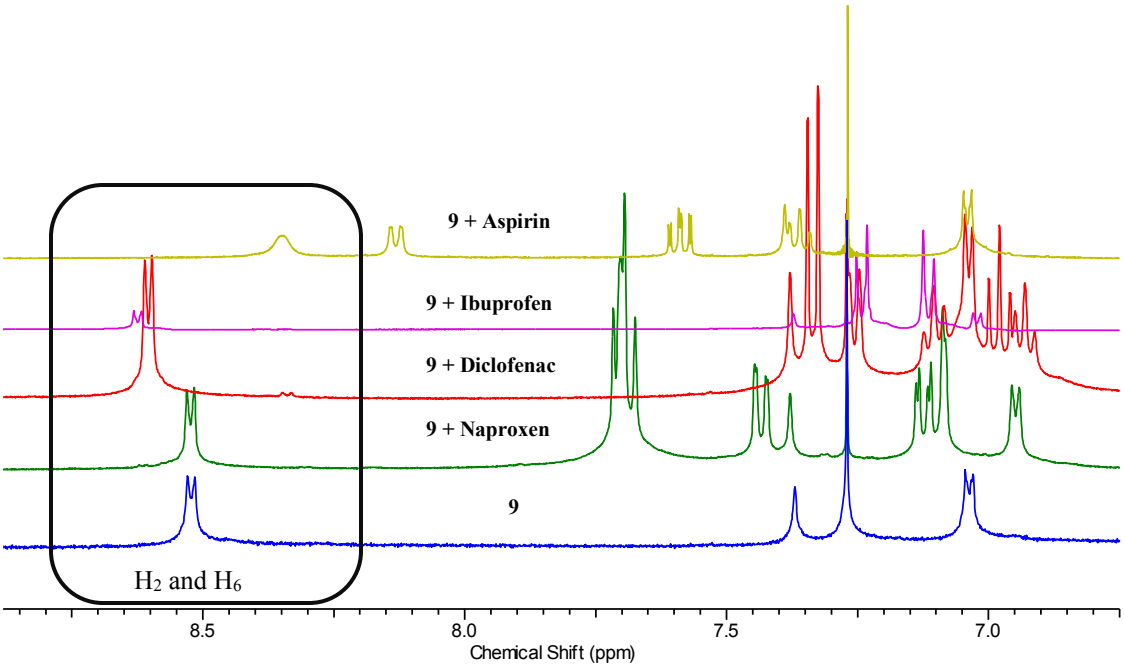

Figure 6.15 Chemical shift changes of H_2 and H_6 of **9** upon addition of 10 equivalents of naproxen, diclofenac, ibuprofen and aspirin

Table 6.3 Chemical shift changes of the *ortho* protons of cavitands **9** and **10** in ^{1}H NMR spectra by the addition of 10 equivalents of the guests in $CDCl_3$ at 25 °C. d - doublet, br, s- broad singlet

	Chemical shift (δ in ppm) of *ortho* protons after complexation	
	Cavitand **9**	Cavitand **10**
Active ingredient	Free (8.51-8.53)	Free (8.04-8.05)
Ibuprofen	8.62-8.63 (d)	8.18-8.20 (d)
Naproxen	8.52-8.53 (d)	8.20-8.22 (d)
Diclofenac	8.60-8.61 (d)	8.26-8.28 (d)
Resveratrol	-	-
p-Coumaric acid	8.61-8.63 (d)	8.20-8.21 (d)
Aspirin	8.36 (br, s)	8.21-8.22 (d)

The deshielding of the ortho protons is attributed to the reduced electron density on the N(py) and O-N(py) atoms due to hydrogen bonding. The complexes evaluated here are in host-

guest complexation equilibrium which show a fast exchange rate compared to the ^{1}H NMR chemical shift time scale. Therefore, the peaks assigned to the free and complexed host protons appear at a weighted average chemical shift of the free host and complexed host. Besides, no significant changes of the peaks corresponding to the guests are observed and they remained unchanged in all the cases presumably due to the fast exchange on the NMR time scale.

Nevertheless, the H_2 and H_6 protons were shielded and shifted upfield to 8.36 ppm as a broad singlet, with the addition of aspirin to cavitand **9** and they are deshielded as an intact doublet with the addition of aspirin into **10**. This unique binding event will be further explored in section 6.3.2.2.

6.3.2.1 [10-Naproxen] system for quantifying the binding event

From the results that we observed, we chose [**10**-Naproxen] system as an example to quantify the strength of binding and to determine the stoichiometry of the binding event. Successive addition of 0.25-12.5 equivalents naproxen into a solution containing **10**, induced progressive downfield shifts of the *ortho* protons of the O-N(py) moiety (Figure 6.16).

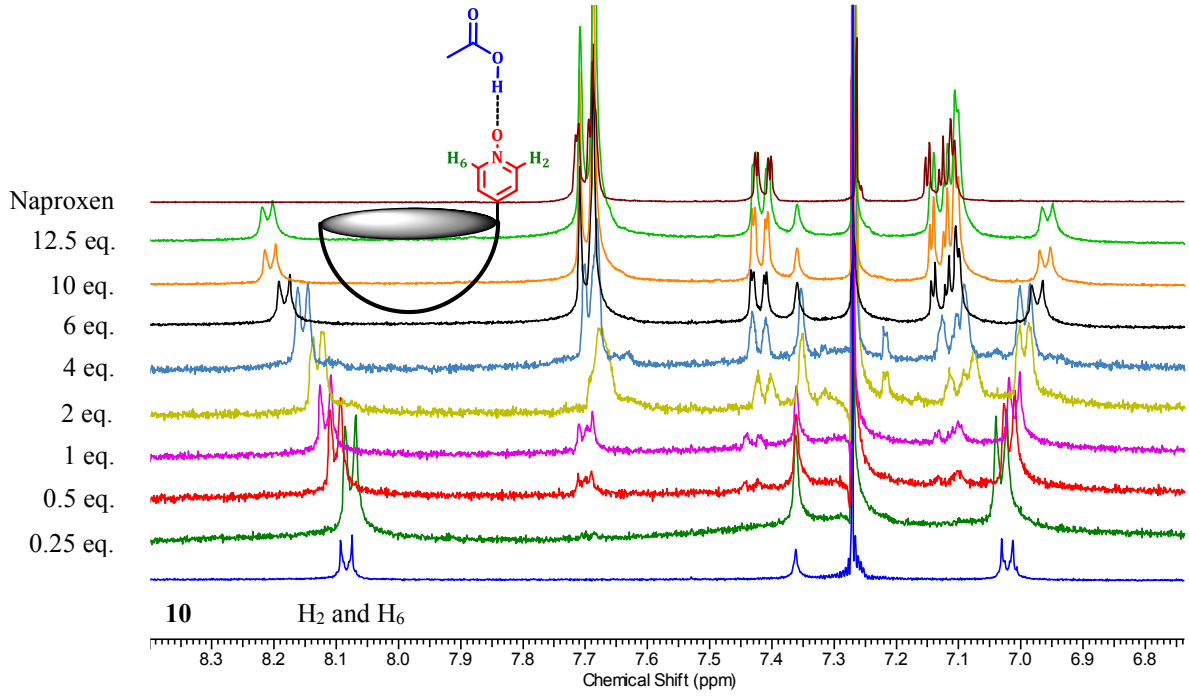

Figure 6.16 ^{1}H NMR spectral changes observed in H_2 and H_6 protons of **10** in $CDCl_3$ at 25 °C during the addition of up to 12 equivalents of naproxen

The changes in δ ppm values ($\delta_{bound\ host} - \delta_{free\ host}$) obtained by titrating naproxen into **10**, were plotted against naproxen concentration and by non-linear curve fitting into equation 1

afforded K_a = 1888 M^{-1} (Figure 6.17). Jobs plot analysis of the results revealed 1:4 complexation (Figure 6.18). These results are in agreement with the study performed by Aakeroy *et al*, where a pentameric hydrogen-bonded architecture formed between *C*-pentyltetra(3-pyridyl) cavitand and 4-nitrobenzoic acid in solution.[42] This hydrogen bonded assembly formed in solution was analyzed using isothermal titration calorimetry, gave binding constant of 4130 M^{-1}, which is higher compared to what we observed, and can be explained by the fact that, 4-nitrobenzoic acid is a comparatively strong acid.

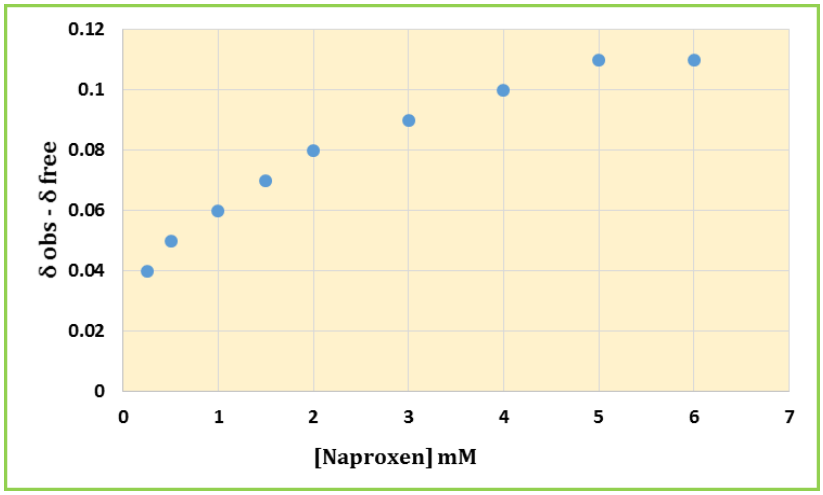

Figure 6.17 (a) Titration curve of naproxen into **10** in $CDCl_3$ at 25 °C where the chemical shift is plotted against the naproxen concentration (b) Job's plot of [naproxen-**10**] pair at 25 °C

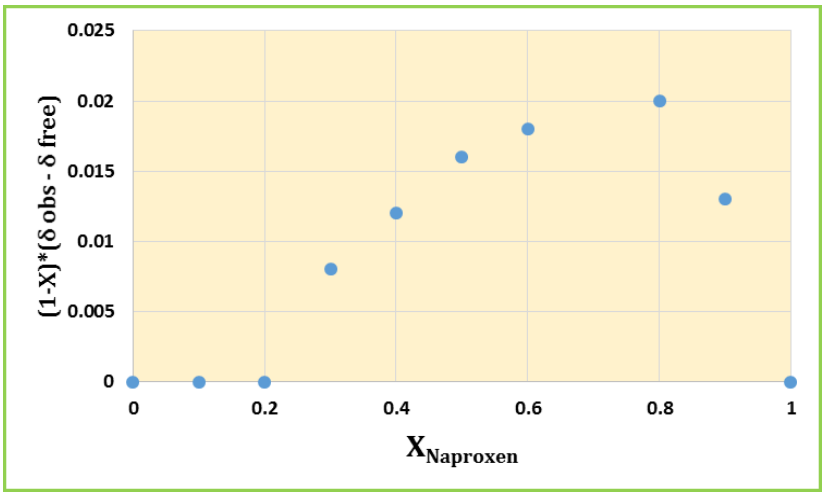

Figure 6.18 Job's plot of [naproxen-**10**] pair at 25 °C

Based on the results from the ^{1}H NMR titrations and Job's plot, guest binding takes place on the upper rim of the cavitand via OH···N hydrogen bonds and one cavitand is capable of binding to four guest molecules (Figure 6.19).

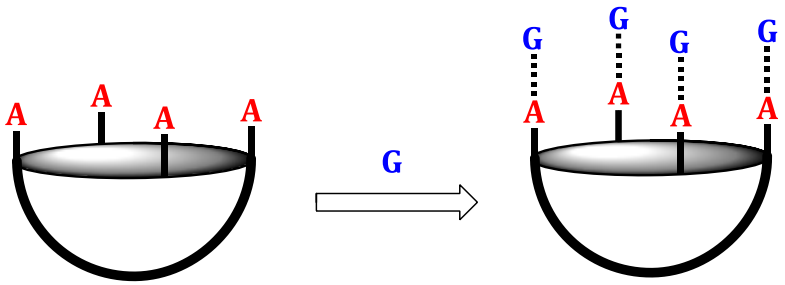

Figure 6.19 Cartoon representation of guest binding on the upper rim

6.3.3 The unique case of aspirin

Since aspirin was behaving differently, further studies were carried out by using four different cavitands, **9**, **10**, **11** and **12** with different orientations of the hydrogen bond acceptor functionalities (Figure 6.20).

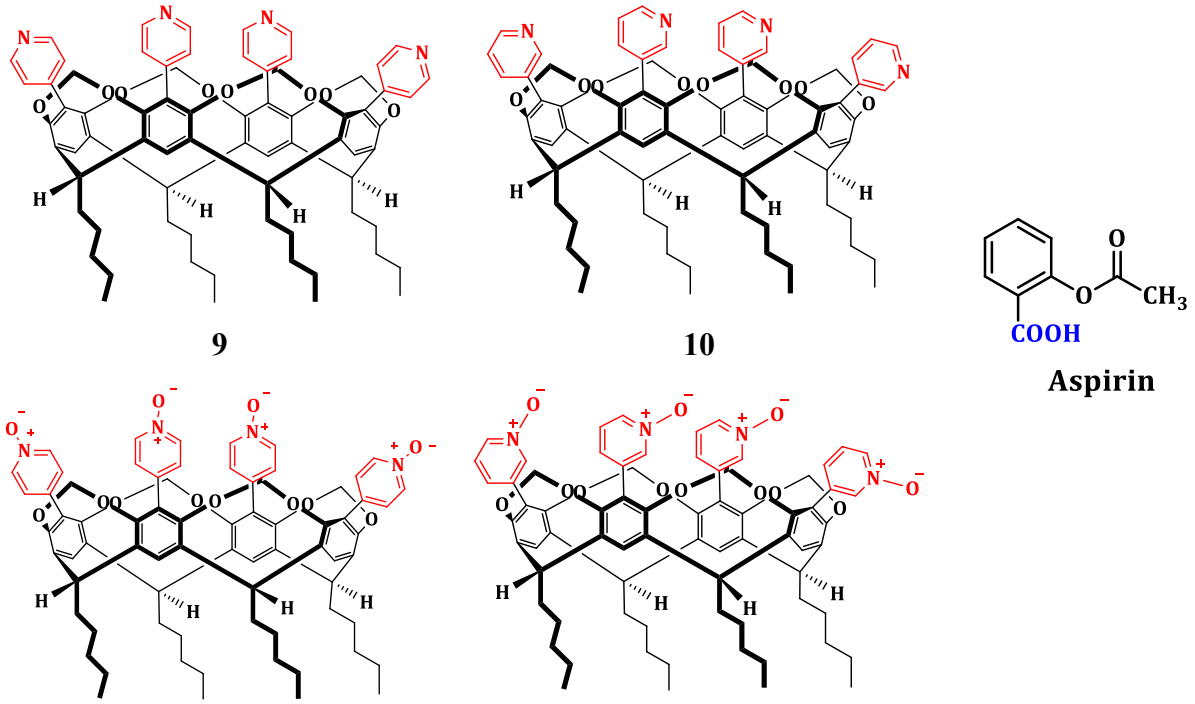

Figure 6.20 Tetrapyridyl and tetrapyridyl N-oxide functionalized cavitands and aspirin used in the study

6.3.3.1 Asprin binding with 9

Successive additions of 0.25-10 equivalents of aspirin into **9**, revealed some significant spectral changes of **9**. The protons affected by aspirin are H_2, H_6 and H_3, H_5 on the pyridyl ring and the H_{in} and H_{out} of the bridge (–O-$CH_{in}CH_{out}$-O-) (Figure 6.21a).

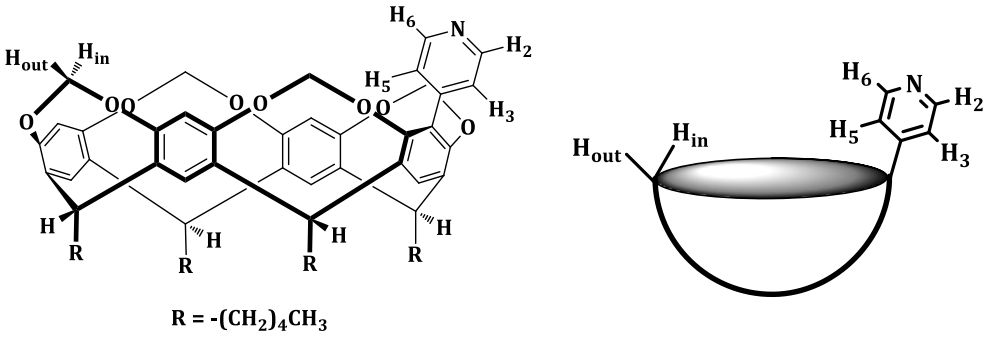

(a)

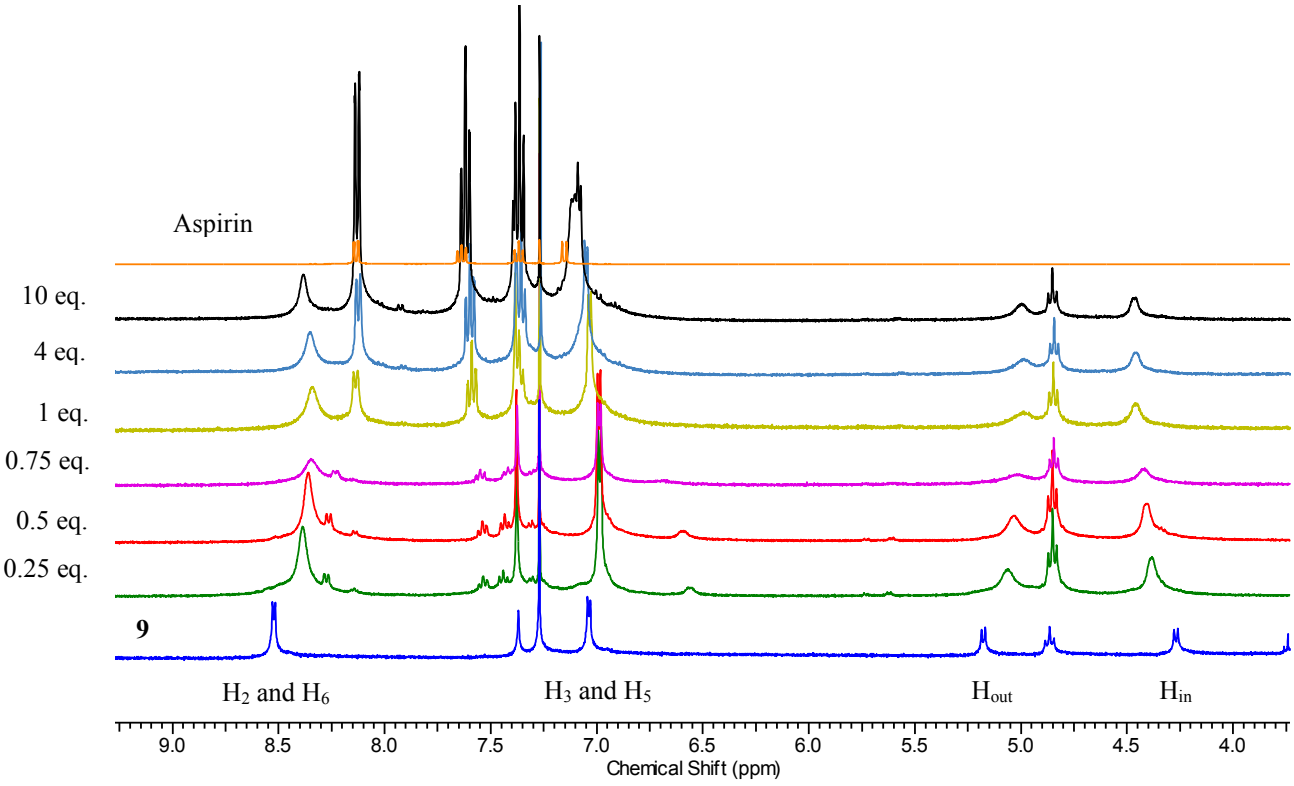

(b)

Figure 6.21 (a) Protons of the host that are affected by aspirin (b) ^{1}H NMR spectra of cavitand **9** in the presence of aspirin

The observations based on the spectral changes are as follows (Figure 6.21b).

- H_2 and H_6 protons lost their resolution and upfield shift as a broad singlet upto one equivalent of aspirin, however, after 4 equivalents, the peak gets relatively deshielded
- Protons H_3 and H_5 behaves the same manner
- H_{in} and H_{out} protons get deshielded and shielded respectively, however, remains constant after addition of 4 equivalents

The conclusions based on the observations;

- The pyridyl protons are shielded probably due to the presence of the guest at the vicinity of the upper rim. The deshielding effect after one equivalent of aspirin, might be attributed to the hydrogen bonding between the host and the guest.
- The deshielded H_{in} protons reveal hydrogen bonding of the guest to the bridge of the cavitand.
- The guest (aspirin) can reside inside the cavitand as well as it can hydrogen bond with the pyrine ring.
- The Job's plot analysis revealed 1:1 stoichiometry based on the H_2 and H_6 protons (Figure 6.22)

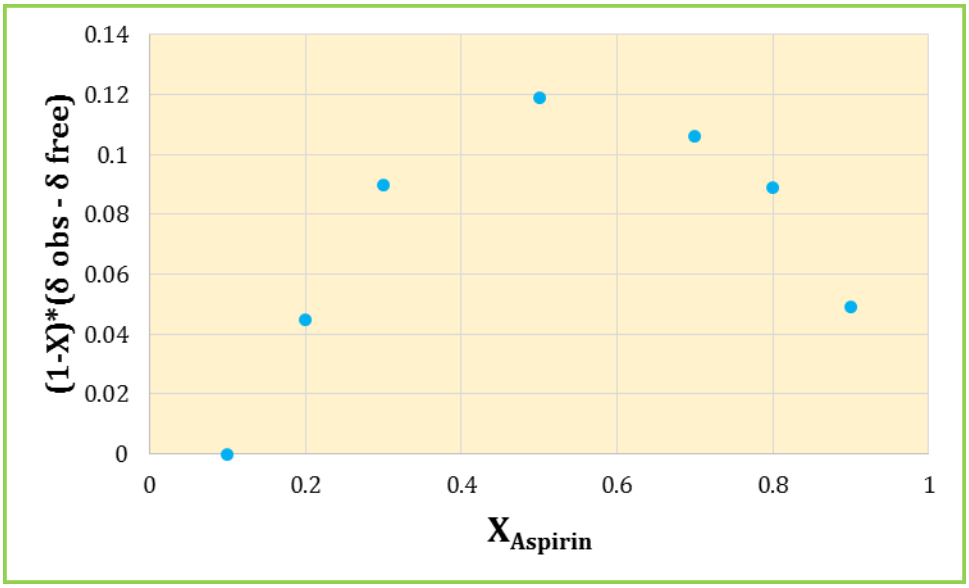

Figure 6.22 Job's plot based on the chemical shift of H_2 and H_6 protons

Variable temperature ^{1}H NMR experiments were carried out in order to gather more evidence of aspirin binding to **9**. (Figure 6.23). It is noticeable that a new peak begin to arise when the mixture is cooled to -20 °C and the intensity of this new peak increases with further cooling down to -50 °C. This reveals that the exchange of aspirin with **9** becomes slow on the NMR time scale and display two signals corresponding to free aspirin (2.37 ppm) and bound aspirin (-1.23 ppm at -20 °C and -1.31 ppm at -50 °C). This observation is consistent with aspirin residing in the cavity of **9**, in such a way that the O-CH_3 group is pointing into the cavity experiencing the shielding effect of the aromatic π electron cloud.

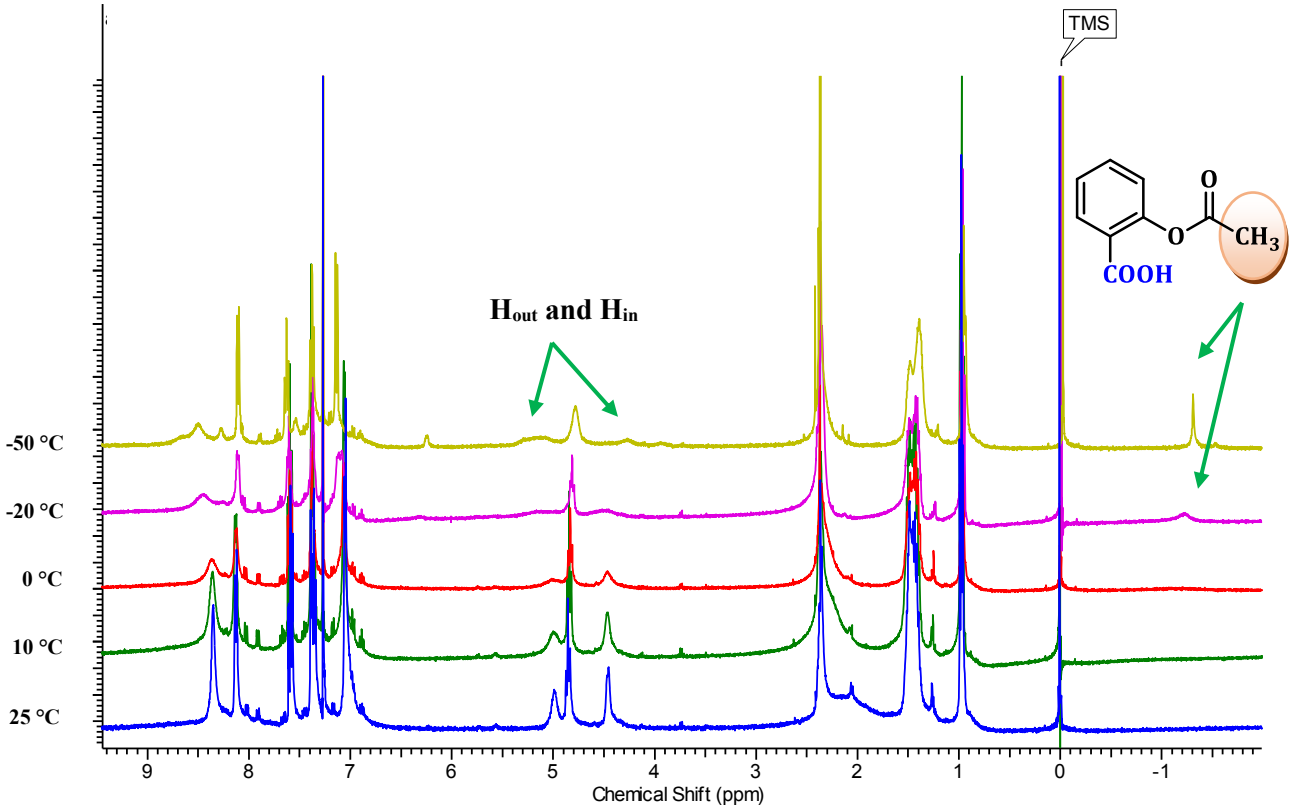

Figure 6.23 ^{1}H NMR spectra of [**9**-Aspirin] complex in $CDCl_3$ at 25 °C to 10 °C, 0 °C, -20 °C and -50 °C

6.3.3.2 Aspirin binding to 11

The pyridyl protons H_2 and H_6 and the bridging protons H_{in} are affected by the addition of aspirin (Figure 6.24). Based on these observations, the predicted sequential steps of aspirin binding to **11** is given in Figure 6.25 which will be further confirmed by hosts **10** and **12**.

- The bridging protons are downfield shifted with one equivalent of aspirin and does not change beyond that point. Aspirin binding to the bridging protons takes place first (Figure 6.25b).
- The pyridyl protons H_2 and H_6 are not affected by one equivalent of aspirin, however, they get deshielded with 4 equivalents of aspirin. Hydrogen bonding of aspirin to the upper rim of the cavitand takes place as the second step, Figure 6.25c.

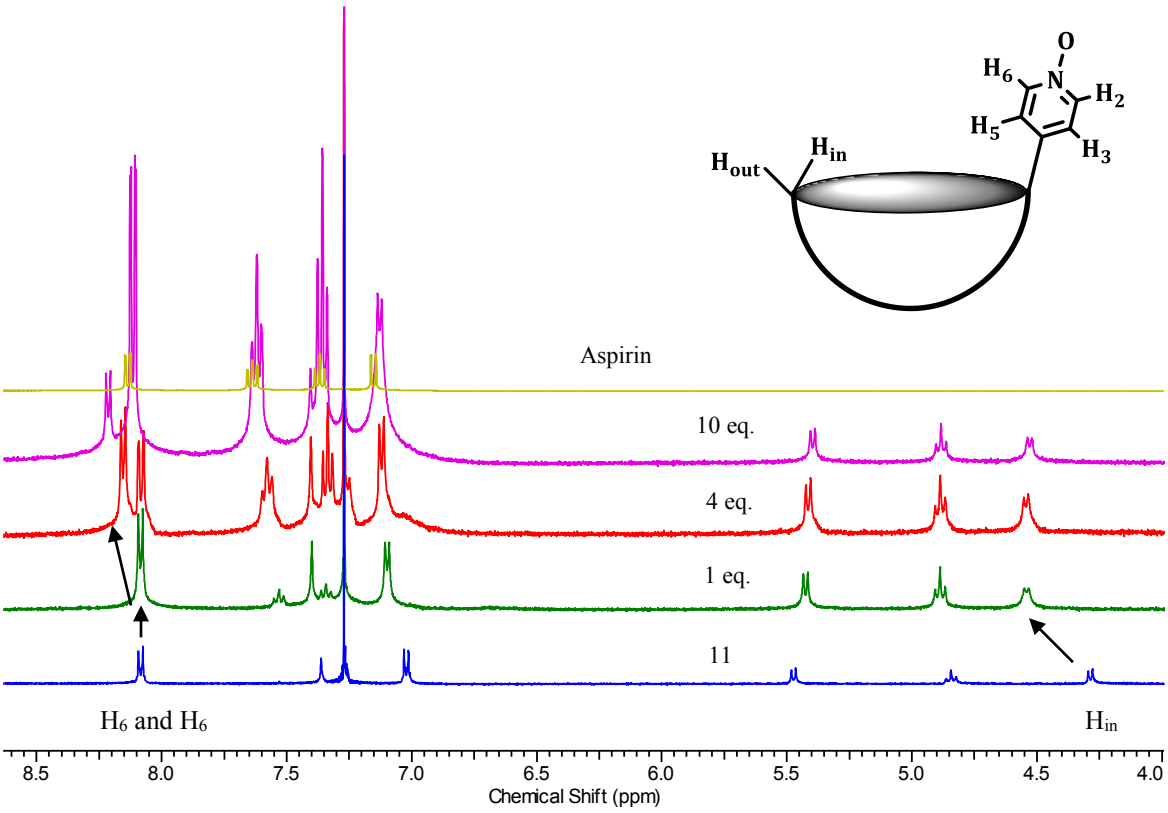

Figure 6.24 ^{1}H NMR spectra of the cavitand **11** upon successive addition of aspirin

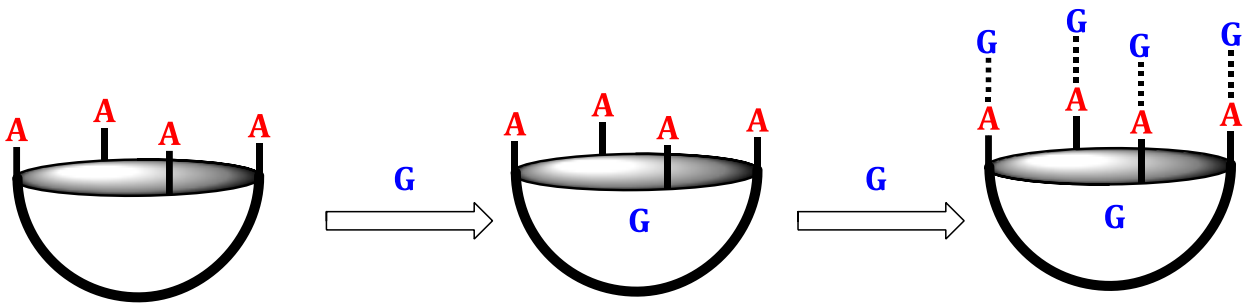

Without aspirin | [**11**-aspirin] 1:1 mixture | [**11**-aspirin] at high aspirin concentration

(a) (b) (c)

Figure 6.25 Sequential steps of aspirin binding

6.3.3.3 Aspirin binding to 10 and 12

A significant chemical shift of the protons of the host as well as guest, shown in Figure 6.26, was observed upon successive addition of 0.5-40 equivalents of aspirin into cavitands **10** and **12**. The host protons, H_2 and H_6 were significantly deshielded. The aromatic protons and the methyl protons of aspirin are shielded in the presence of the host.

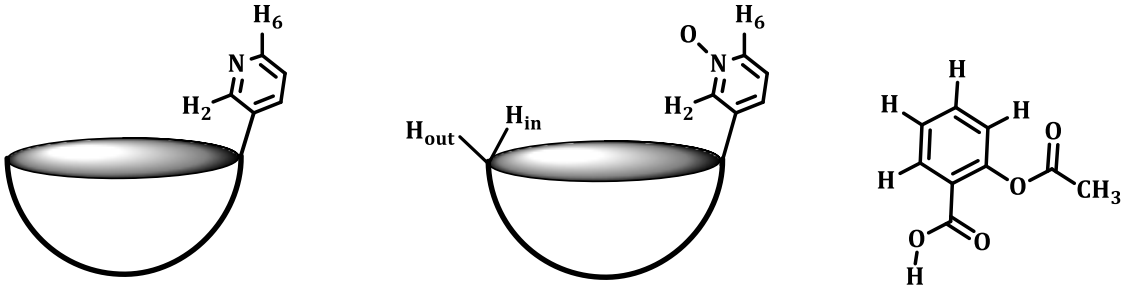

10 **12** Aspirin

(a) (b)

Figure 6.26 The protons that are affected by the host-guest interaction, (a) H_2, H_6 and H_{in} protons of **10** and **12** (b) aromatic protons and methyl protons of aspirin

6.3.3.3.1 [10-aspirin] system

The observations based on the chemical shifts are;

- H_2 protons are deshielded drastically at lower concentrations of aspirin and deshielding effect is relatively low at high concentrations (Figure 6.27a)
- The deshielding effect of the H_6 protons is less compared to the H_2 protons (Figure 6.27a)
- All the aromatic protons of aspirin are shielded (Figure 6.27a)
- Most importantly, the peak corresponding to the methyl protons of aspirin gets broadened, shielded and nearly coalesced at 0.5-1 equivalents of aspirin (Figure 6.27b)
- Job's plot analysis revealed 1:1 stoichiometry based on the chemical shift of H_{in} protons (Figure 6.28)

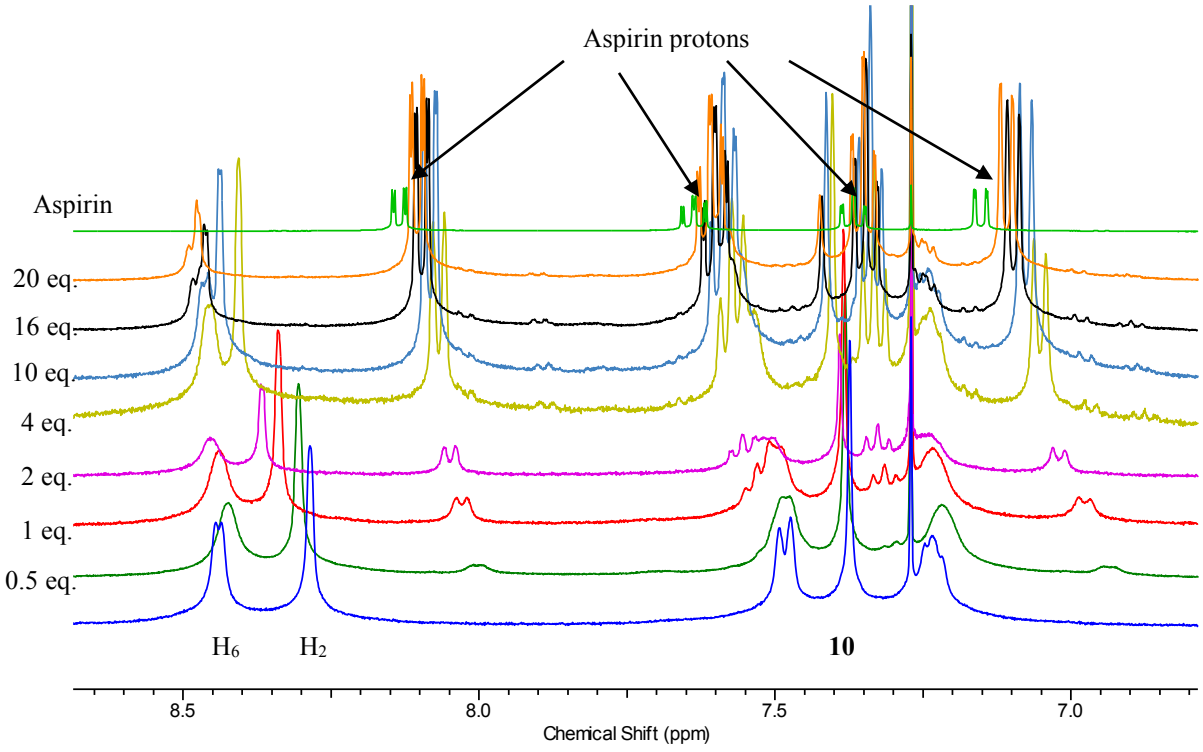

(a)

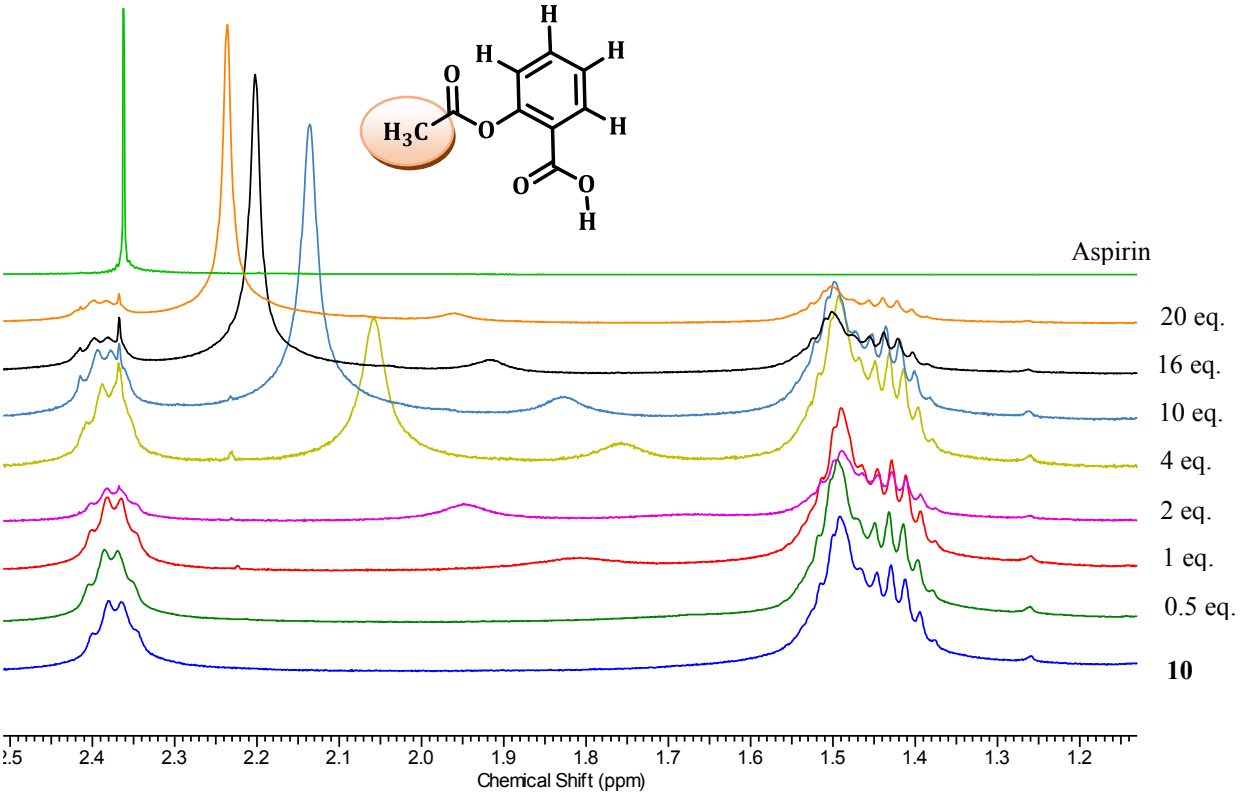

(b)

Figure 6.27 ^{1}H NMR showing (a) deshielding of host protons H_2, H_6 of **10** and shielding of aspirin aromatic protons (b) shielding of aspirin methyl protons

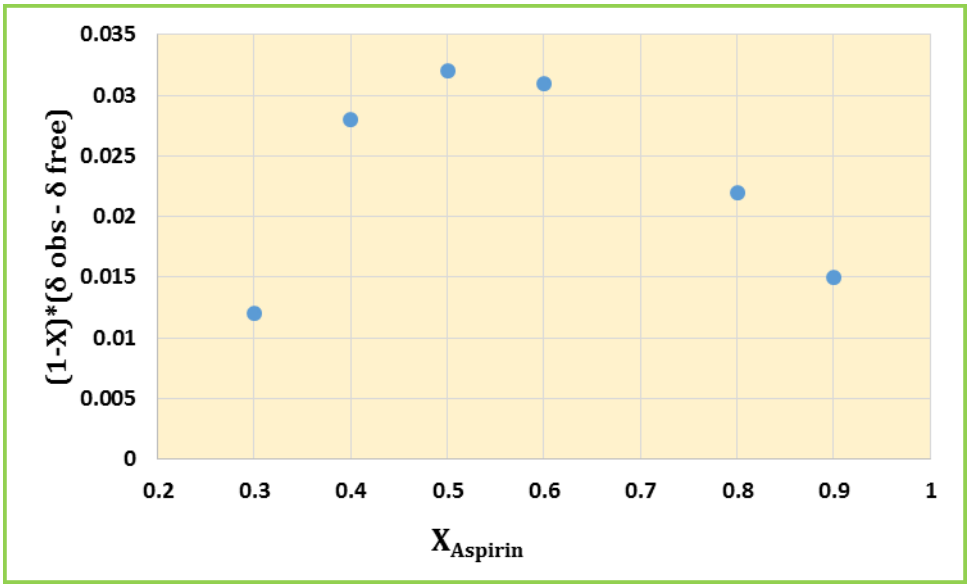

Figure 6.28 Job's plot based on H_{in}

6.3.3.3.2 [12-aspirin] system

The observations based on the chemical shifts are;

- H_2 protons experience a drastic deshielding effect, such that H_2 and H_6 protons start to switch with 0.5 equivalents of aspirin. This effect continues until 4 equivalents of aspirin is added and beyond this point they get relatively less deshielded
- The deshielding effect of the H_6 protons starts with 1 equivalent of aspirin
- All the aromatic protons of aspirin get shielded and nearly coalesced at low concentrations of aspirin
- The bridging proton, H_{in} gets deshielded up until 1 equivalent of aspirin is added and remains constant at higher concentrations
- The methyl protons of aspirin gets broadened at high concentrations of aspirin and get broadened and nearly coalesced at lower concentrations of aspirin
- Job's plot analysis revealed 1:1 stoichiometry based on the chemical shifts of H_{in} (Figure 6.30) and H_2 (Figure 6.31)

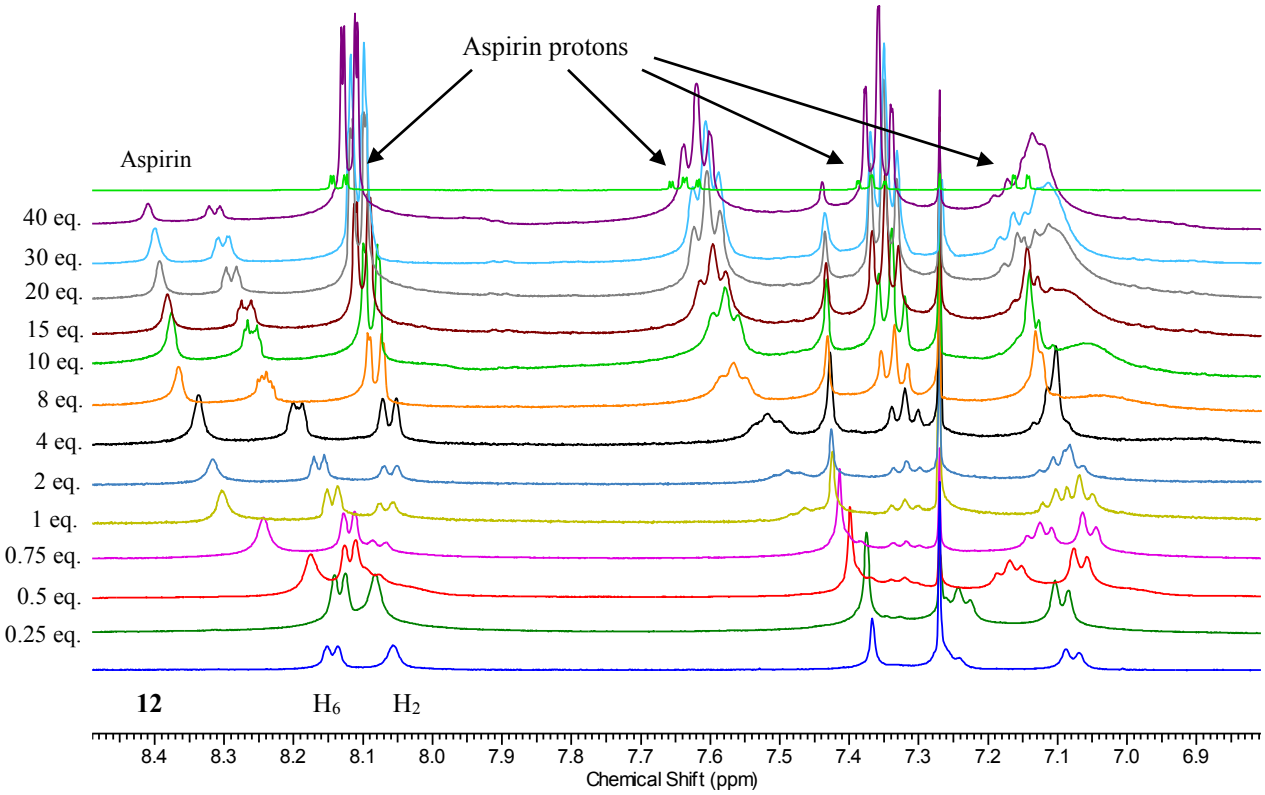

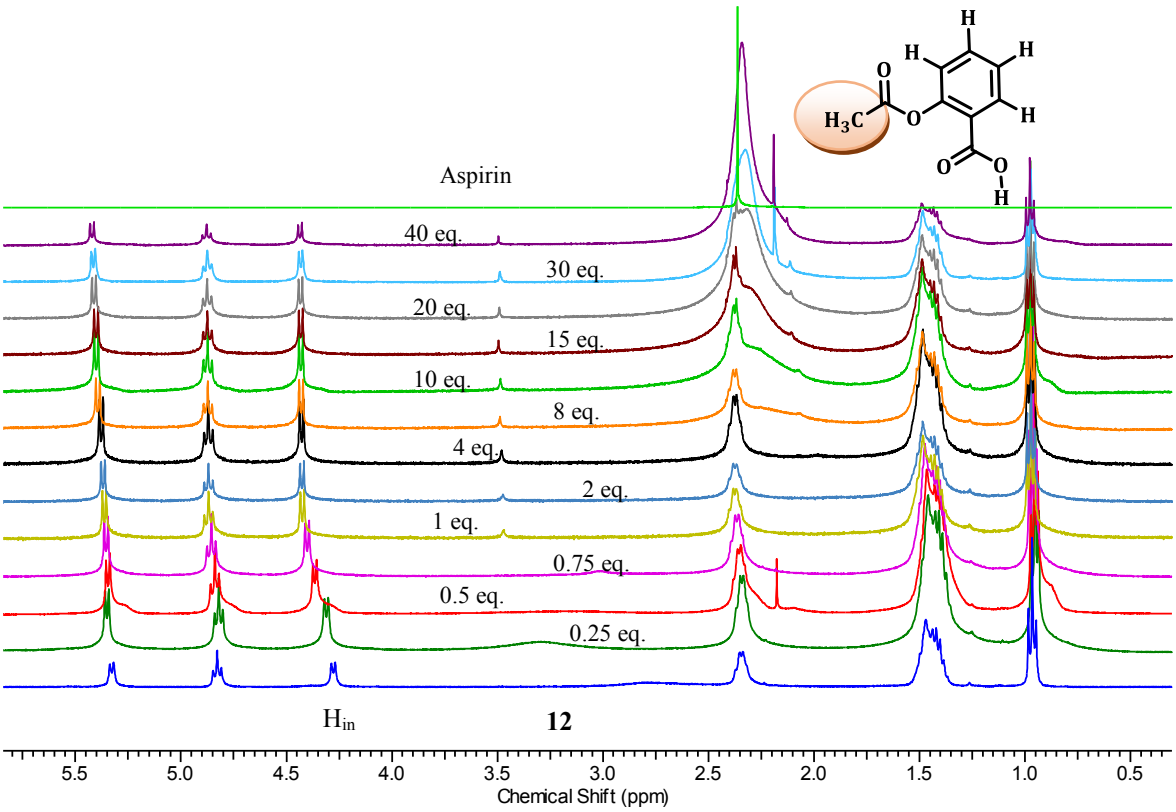

Figure 6.29 ^{1}H NMR showing (top) deshielding of host protons H_2, H_6 and shielding of aspirin aromatic protons (bottom) shielding of aspirin methyl protons and deshielding of the H_{in} bridging protons

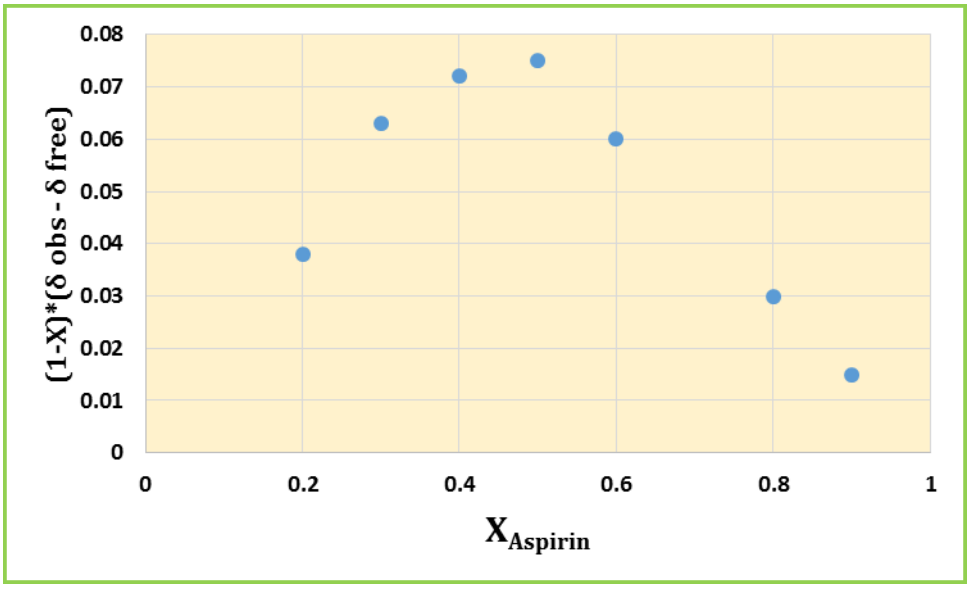

Figure 6.30 Job's plot based on the chemical shifts of H_{in}

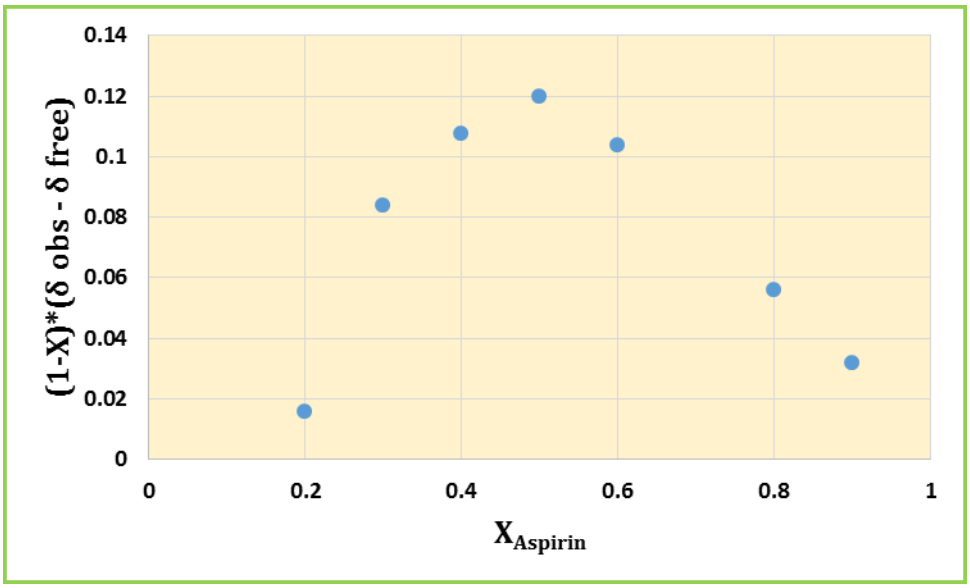

Figure 6.31 Job's plot based on the chemical shifts of H_2

*Conclusions based on the observations of aspirin binding to cavitands **10** and **12**;*

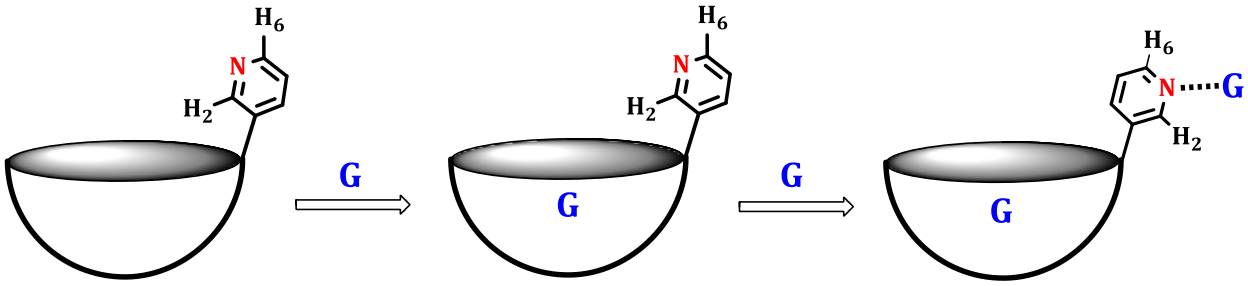

Without aspirin — [cavitand-aspirin] 1:1 mixture — [cavitand-aspirin] at high aspirin concentration

(a) (b) (c)

(a) Before addition of aspirin - the pyridyl rings are pointing into the cavity, because the H_2 protons are more shielded than the H_6 protons. Solid state structure of **12** also supports this evidence (Figure 6.32).

(b) With successive addition of aspirin, it binds into the cavity indicated by the huge upfiled shift of the methyl protons and the shielding of the aspirin aromatic protons

(c) With the addition of more than one equivalents of aspirin, a conformational change of the pyridine rings take place, in which pyridine N turn out of the cavity, causing a huge downfield shift of the H_2 protons. This conformational change now make the pyridine N

accessible for hydrogen bonding, indicated by the relatively small downfield shift of the H_2 and H_6 protons observed with high concentrations of aspirin. The solid state structure of **12** also supports the conformational change upon aspirin binding into the cavity, unless otherwise would be sterically hindered (Figure 6.32).

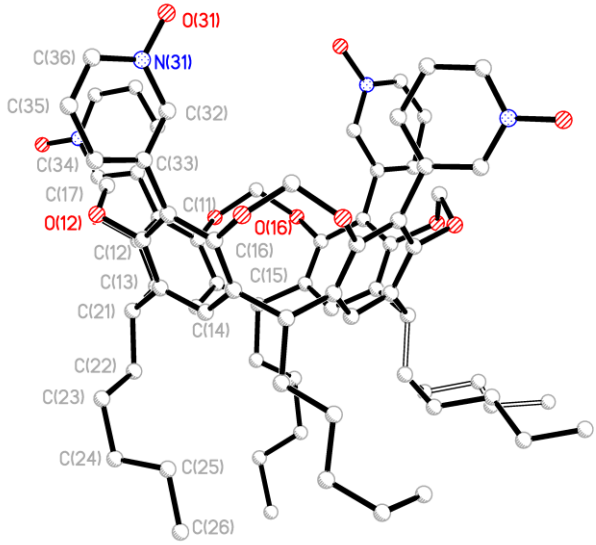

Figure 6.32 Ball and stick model of preliminary structure of **12**

6.3.4 Binding mode of aspirin inclusion

Based on our evidence gathered from aspirin binding to hosts **9**, **10**, **11** and **12**, it seems that at lower concentrations, aspirin binds inside the cavity via CH···π interactions and C=O···H_{in} hydrogen bonds, a two-point binding mode for aspirin binding into the cavity (Figure 6.33a). A different binding mode was proposed by Nguyen *et al*, where a superbowl receptor composed of five cavitands uptake aspirin via CH···π interactions and OH···O (–CH_2O–bridge) hydrogen bonds (Figure 6.33b).[43] Recently, the same binding mode was proposed in simple cavitand receptors where several structural features are required for aspirin binding (Figure 6.34).[44] However, our experiments show that aspirin does bind to hosts **9**, **10**, **11** and **12** in a sequential manner, when R = 4py, 4pyNO, 3py and 3pyNO respectively. It is clear that aspirin binding is stronger and favorable (slow on NMR time scale) when R = 3py and 3pyNO, which changes the conformation providing space for aspirin inclusion in the cavity.

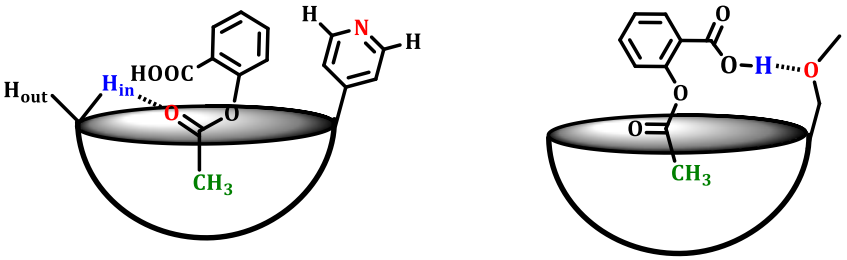

(a) (b)

Figure 6.33 (a) Proposed two-point binding mode (b) binding mode reported in literature[43]

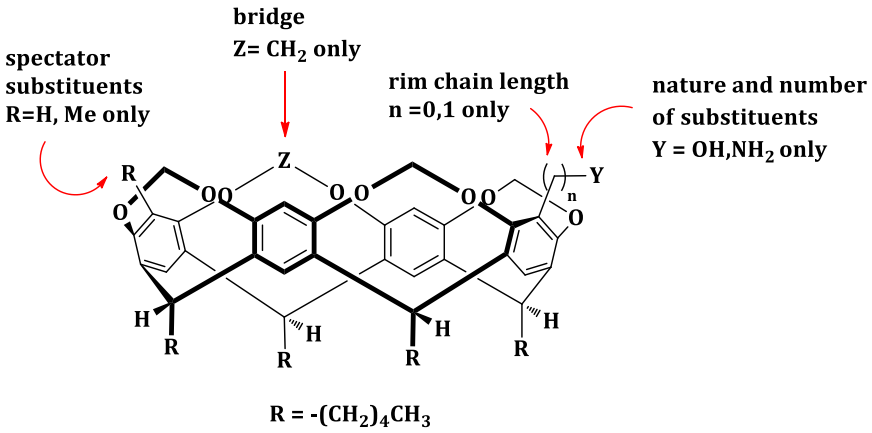

Figure 6.34 Structural features required for aspirin binding, reported by Nguyen *et al* [44]

Association constants (K_a) for aspirin inclusion in the cavity were obtained from the chemical shifts of H_{in} and H_2 protons (Figure 6.4). Results indicate that binding of aspirin to cavitands **10** and **12** is stronger compared to **9** and **10**. Initial orientation of the 3py and 3pyNO substituents towards the interior of the cavity, changes their conformation and switch out of the cavity, upon aspirin binding into the cavity, making aspirin inclusion more favorable with high affinity confirmed by the binding constant values.

Table 6.4 Binding constants of aspirin to **9**, **10**, **11** and **12**

Host	**9**	**11**	**10**	**12**
K_a (M^{-1})	4520	3975	6346	8734

6.3.5 Control experiment

A control experiment was performed with cavitand **11** and Naproxen, a similar candidate to aspirin which bears a O-CH_3 group.

- None of the protons corresponding to cavitand or naproxen did shift except a slight deshielding of H_2 and H_6 protons presumably due to the hydrogen bonding on to the upper rim of the cavitand.
- No cavity inclusion is taking place.

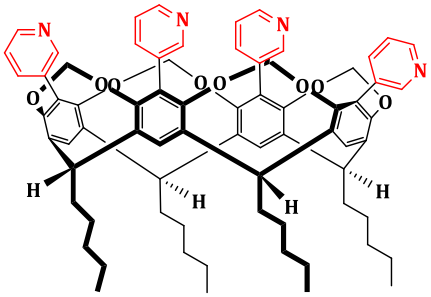

11

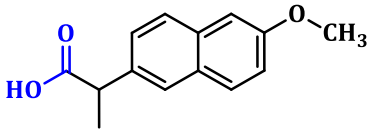

Naproxen

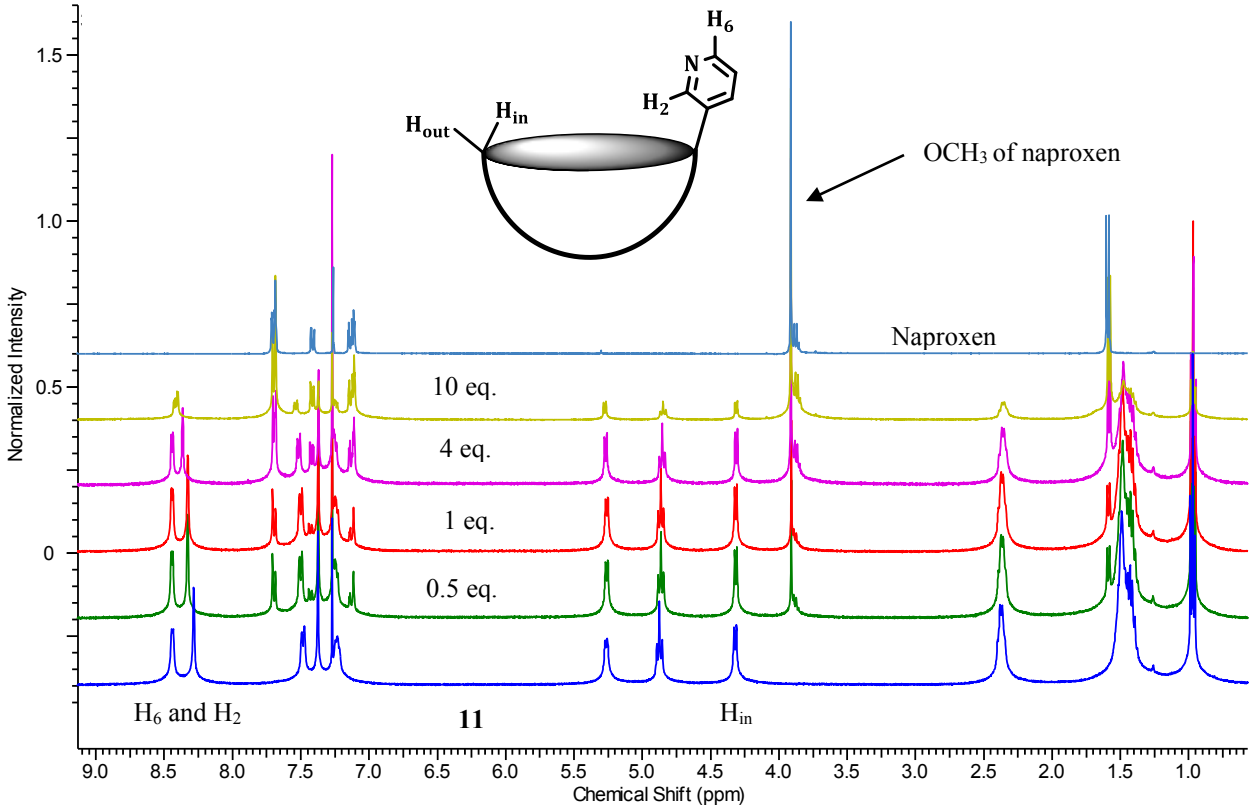

Figure 6.35 ^{1}H NMR spectra of the cavitand **11** upon successive addition of Naproxen

Aspirin inclusion was facilitated by two binding modes, CH···π interactions and C=O···H_{in} hydrogen bonds. Naproxen on the other hand show no CH···π interactions indicating that C=O···H_{in} hydrogen bonds are crucial and thus both binding modes are necessary for the host-guest complexation. Functional group discrimination of guests by a similar host was studied by Nishimura *et al*,[45] where they observed selectivity for –O-(C=O)CH_3 over –C(=O)OCH_3 and –OCH_3 groups which arises due to the combination of CH···π interactions and C=O···H_{in} hydrogen bonds taking place between the host and the –O-(C=O)CH_3 functionality of the guest.

6.4 Conclusions

We were able to successfully synthesize HB/XB donor and acceptor cavitands which were used as hosts in studying their binding preferences towards a series of active ingredients. Host-guest binding in solid state was confirmed by IR spectroscopy.

^{1}H NMR spectroscopy was used to analyze guest binding in solution and we observed two preferential ways of guest binding (Figure 6.36). Upper rim binding via OH···N hydrogen bonds was observed with almost all the active ingredients except aspirin. The stoichiometry determined in these cases were 1:4.

Aspirin binding to both upper rim as well as inside the cavity was observed with suitably functionalized cavitands, which occurred in a sequential manner (Figure 6.37).

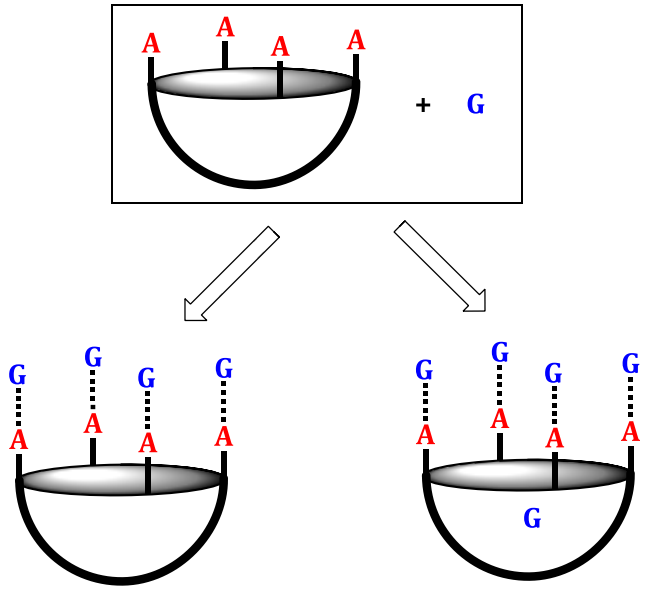

Figure 6.36 Two ways of host-guest binding observed in solution

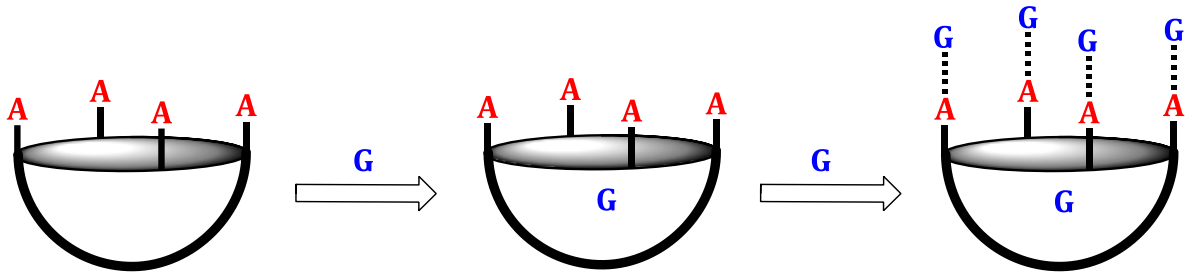

Figure 6.37 Sequential binding event of aspirin

We demonstrated selective and unique binding of aspirin inside the cavity via a two-point binding mode and ^{1}H NMR data show that one cavitand is capable of hosting five aspirin molecules. These findings establish a markedly distinct receptor-drug chemistry that widens the scope of drug delivery systems.

6.5 References

1. Whitesides, G.; Mathias, J.; Seto, C. *Science* **1991,** *254* (5036), 1312-1319.

2. (a) Sanders, J. K. *Angew. Chem.* **1995,** *107* (21), 2617-2617; (b) Parkin, I. P. *Appl. Organomet. Chem.* **2001,** *15* (3), 236-236.

3. (a) Ghang, Y.-J.; Perez, L.; Morgan, M. A.; Si, F.; Hamdy, O. M.; Beecher, C. N.; Larive, C. K.; Julian, R. R.; Zhong, W.; Cheng, Q.; Hooley, R. J. *Soft Matter* **2014,** *10* (48), 9651-9656; (b) Ruebner, A.; Kirsch, D.; Andrees, S.; Decker, W.; Roeder, B.; Spengler, B.; Kaufmann, R.; Moser, J. G. *J. Inclusion Phenom. Mol. Recognit. Chem.* **1997,** *27* (1), 69-84; (c) Ghang, Y.-J.; Lloyd, J. J.; Moehlig, M. P.; Arguelles, J. K.; Mettry, M.; Zhang, X.; Julian, R. R.; Cheng, Q.; Hooley, R. J. *Langmuir* **2014,** *30* (34), 10161-10166.

4. (a) Biavardi, E.; Ugozzoli, F.; Massera, C. *Chem. Commun.* **2015**; (b) Breslow, R.; Zhang, B. *J. Am. Chem. Soc.* **1996,** *118* (35), 8495-8496; (c) Rodriguez-Tenreiro, C.; Alvarez-Lorenzo, C.; Rodriguez-Perez, A.; Concheiro, A.; Torres-Labandeira, J. J. *Eur. J. Pharm. Biopharm.* **2007,** *66* (1), 55-62; (d) Szejtli, J. *Supramol. Chem.* **1995,** *6* (1-2), 217-223.

5. (a) Shin, J.-A.; Lim, Y.-G.; Lee, K.-H. *J. Org. Chem.* **2012,** *77* (8), 4117-4122; (b) Klöck, C.; Dsouza, R. N.; Nau, W. M. *Org. Lett.* **2009,** *11* (12), 2595-2598; (c) Assaf, K. I.; Nau, W. M. *Chem. Soc. Rev.* **2015,** *44* (2), 394-418; (d) Hooley, R. J.; Rebek Jr, J. *Org. Biomol. Chem.* **2007,** *5* (22), 3631-3636.

6. (a) Florea, M.; Nau, W. M. *Angew. Chem. Int. Ed.* **2011,** *50* (40), 9338-9342; (b) Ueno, A. *Supramol. Sci.* **1996,** *3* (1–3), 31-36; (c) Topkaya, D.; Dumoulin, F.; Ahsen, V.; Isci, U. *Dalton Trans.* **2014,** *43* (5), 2032-2037.

7. (a) Moran, J. R.; Karbach, S.; Cram, D. J. *J. Am. Chem. Soc.* **1982,** *104* (21), 5826-5828; (b) Wiseman, A. *J. Chem. Technol. Biotechnol.* **1995,** *63* (2), 195-195.

8. (a) Djernes, K. E.; Padilla, M.; Mettry, M.; Young, M. C.; Hooley, R. J. *Chem. Commun.* **2012,** *48* (94), 11576-11578; (b) Djernes, K. E.; Moshe, O.; Mettry, M.; Richards, D. D.; Hooley, R. J. *Org. Lett.* **2012,** *14* (3), 788-791; (c) Sambrook, M. R.; Notman, S. *Chem. Soc. Rev.* **2013,** *42* (24), 9251-9267.

9. (a) Tudisco, C.; Betti, P.; Motta, A.; Pinalli, R.; Bombaci, L.; Dalcanale, E.; Condorelli, G. G. *Langmuir* **2011,** *28* (3), 1782-1789; (b) Biavardi, E.; Federici, S.; Tudisco, C.; Menozzi, D.; Massera, C.; Sottini, A.; Condorelli, G.

G.; Bergese, P.; Dalcanale, E. *Angew. Chem. Int. Ed.* **2014,** *53* (35), 9183-9188; (c) Biavardi, E.; Tudisco, C.; Maffei, F.; Motta, A.; Massera, C.; Condorelli, G. G.; Dalcanale, E. *Proc. Natl. Acad. Sci. U. S. A.* **2012,** *109* (7), 2263-2268; (d) Paolesse, R.; Di Natale, C.; Nardis, S.; Macagnano, A.; D'Amico, A.; Pinalli, R.; Dalcanale, E. *Chem. Eur. J.* **2003,** *9* (21), 5388-5395; (e) Pirondini, L.; Dalcanale, E. *Chem. Soc. Rev.* **2007,** *36* (5), 695-706; (f) Pinalli, R.; Dalcanale, E. *Acc. Chem. Res.* **2012,** *46* (2), 399-411.

10. (a) Hooley, R. J.; Restorp, P.; Iwasawa, T.; Rebek, J. *J. Am. Chem. Soc.* **2007,** *129* (50), 15639-15643; (b) Körner, S. K.; Tucci, F. C.; Rudkevich, D. M.; Heinz, T.; Rebek, J. J. *Chem. Eur. J.* **2000,** *6* (1), 187-195; (c) Iwasawa, T.; Hooley, R. J.; Rebek, J. *Science* **2007,** *317* (5837), 493-496.

11. (a) Kaanumalle, L. S.; Gibb, C. L. D.; Gibb, B. C.; Ramamurthy, V. *Org. Biomol. Chem.* **2007,** *5* (2), 236-238; (b) Restorp, P.; Rebek, J. *J. Am. Chem. Soc.* **2008,** *130* (36), 11850-11851.

12. Ajami, D.; Rebek, J. *Angew. Chem. Int. Ed.* **2008,** *47* (32), 6059-6061.

13. (a) Nishimura, N.; Kobayashi, K. *J. Org. Chem.* **2010,** *75* (18), 6079-6085; (b) Samanta, S. R.; Parthasarathy, A.; Ramamurthy, V. *Photochem. Photobiol. Sci.* **2012,** *11* (11), 1652-1660.

14. (a) Middel, O.; Verboom, W.; Reinhoudt, D. N. *J. Org. Chem.* **2001,** *66* (11), 3998-4005; (b) Gavette, J. V.; Zhang, K.-D.; Ajami, D.; Rebek, J. *Org. Biomol. Chem.* **2014,** *12* (34), 6561-6563; (c) Lledó, A.; Kamioka, S.; Sather, A. C.; Rebek, J. *Angew. Chem. Int. Ed.* **2011,** *50* (6), 1299-1301.

15. (a) Barrett, E. S.; Sherburn, M. S. *Chem. Commun.* **2005,** (27), 3418-3420; (b) Barrett, E. S.; Irwin, J. L.; Edwards, A. J.; Sherburn, M. S. *J. Am. Chem. Soc.* **2004,** *126* (51), 16747-16749.

16. (a) Tunstad, L. M.; Tucker, J. A.; Dalcanale, E.; Weiser, J.; Bryant, J. A.; Sherman, J. C.; Helgeson, R. C.; Knobler, C. B.; Cram, D. J. *J. Org. Chem.* **1989,** *54* (6), 1305-1312; (b) Mezo, A. R.; Sherman, J. C. *J. Org. Chem.* **1998,** *63* (20), 6824-6829.

17. (a) Purse, B. W.; Rebek, J. *Proc. Nat. Acad. Sci. U.S.A.* **2005,** *102* (31), 10777-10782; (b) Purse, B. W.; Rebek, J. *Proc. Nat. Acad. Sci. U.S.A.* **2006,** *103* (8), 2530-2534.

18. (a) Hooley, R. J.; Van Anda, H. J.; Rebek, J. *J. Am. Chem. Soc.* **2006,** *128* (12), 3894-3895; (b) Hooley, R. J.; Biros, S. M.; Rebek, J. *Angew. Chem. Int. Ed.* **2006,** *45* (21), 3517-3519; (c) Cram, D. J.; Choi, H. J.; Bryant, J. A.; Knobler, C. B. *J. Am. Chem. Soc.* **1992,** *114* (20), 7748-7765.

19. (a) Kobayashi, K.; Shirasaka, T.; Yamaguchi, K.; Sakamoto, S.; Horn, E.; Furukawa, N. *Chem. Commun.* **2000,** (1), 41-42; (b) Yamanaka, M.; Ishii, K.; Yamada, Y.; Kobayashi, K. *J. Org. Chem.* **2006,** *71* (23), 8800-8806.

20. (a) Barrett, E. S.; Irwin, J. L.; Turner, P.; Sherburn, M. S. *J. Org. Chem.* **2001,** *66* (24), 8227-8229; (b) Kitagawa, H.; Kobori, Y.; Yamanaka, M.; Yoza, K.; Kobayashi, K. *Proc. Natl. Acad. Sci. U. S. A.* **2009,** *106* (26), 10444-10448.

21. Aakeröy, C. B.; Chopade, P. D. *Org. Lett.* **2010,** *13* (1), 1-3.

22. Aakeroy, C.; Schultheiss, N.; Desper, J. *CrystEngComm* **2007,** *9* (3), 211-214.

23. Gissot, A.; Rebek, J. *J. Am. Chem. Soc.* **2004,** *126* (24), 7424-7425.

24. Aakeröy, C. B.; Schultheiss, N.; Desper, J. *Org. Lett.* **2006,** *8* (12), 2607-2610.

25. Jiang, X.-F.; Cui, Y.-X.; Yu, S.-Y. *Synlett* **2014,** *25* (08), 1181-1185.

26. Jacopozzi, P.; Dalcanale, E. *Angew. Chem. Int. Ed. Engl.* **1997,** *36* (6), 613-615.

27. Aakeroy, C. B.; Rajbanshi, A.; Metrangolo, P.; Resnati, G.; Parisi, M. F.; Desper, J.; Pilati, T. *CrystEngComm* **2012,** *14* (20), 6366-6368.

28. Turunen, L.; Beyeh, N. K.; Pan, F.; Valkonen, A.; Rissanen, K. *Chem. Commun.* **2014,** *50* (100), 15920-15923.

29. (a) Kodiah Beyeh, N.; Cetina, M.; Rissanen, K. *Chem. Commun.* **2014,** *50* (16), 1959-1961; (b) Beyeh, N. K.; Valkonen, A.; Bhowmik, S.; Pan, F.; Rissanen, K. *Org. Chem. Front.* **2015**.

30. (a) Petti, M. A.; Shepodd, T. J.; Barrans, R. E.; Dougherty, D. A. *J. Am. Chem. Soc.* **1988,** *110* (20), 6825-6840; (b) Kearney, P. C.; Mizoue, L. S.; Kumpf, R. A.; Forman, J. E.; McCurdy, A.; Dougherty, D. A. *J. Am. Chem. Soc.* **1993,** *115* (22), 9907-9919.

31. (a) Melegari, M.; Massera, C.; Pinalli, R.; Yebeutchou, R. M.; Dalcanale, E. *Sens. Actuators B Chem.* **2013,** *179* (0), 74-80; (b) Rat, S.; Gout, J.; Bistri, O.; Reinaud, O. *Org. Biomol. Chem.* **2015,** *13* (11), 3194-3197.

32. (a) Trembleau, L.; Rebek Jr, J. *Science* **2003,** *301* (5637), 1219-1220; (b) Trembleau, L.; Rebek Jr, J. *Chem. Commun.* **2004,** (1), 58-59.

33. (a) Hooley, R. J.; Van Anda, H. J.; Rebek, J. *J. Am. Chem. Soc.* **2007,** *129* (44), 13464-13473; (b) Hooley, R. J.; Biros, S. M.; Rebek, J. J. *Chem. Commun.* **2006,** (5), 509-510.

34. Aoyama, Y.; Tanaka, Y.; Sugahara, S. *J. Am. Chem. Soc.* **1989,** *111* (14), 5397-5404.

35. Bryant, J. A.; Blanda, M. T.; Vincenti, M.; Cram, D. J. *J. Am. Chem. Soc.* **1991,** *113* (6), 2167-2172.

36. Moll, H. E.; Semeril, D.; Matt, D.; Youinou, M.-T.; Toupet, L. *Org. Biomol. Chem.* **2009,** *7* (3), 495-501.

37. Jude, H.; Sinclair, D. J.; Das, N.; Sherburn, M. S.; Stang, P. J. *J. Org. Chem.* **2006,** *71* (11), 4155-4163.

38. Forbes, S. Hydrogen-bond driven supramolecular chemistry for modulating physical properties of pharmaceutical compounds. Kansas State University, May 2010.

39. Walsh, T. D.; Koontz, C. S. *J. Chem. Educ.* **1997,** *74* (5), 585.

40. Kuntz, I. D.; Gasparro, F. P.; Johnston, M. D.; Taylor, R. P. *J. Am. Chem. Soc.* **1968,** *90* (18), 4778-4781.

41. Jennings, K. R. *Org. Mass Spectrom.* **1991,** *26* (9), 813-813.

42. Aakeroy, C. B.; Chopade, P. D.; Quinn, C. F.; Desper, J. *CrystEngComm* **2014,** *16* (18), 3796-3801.

43. Nguyen, T. V.; Yoshida, H.; Sherburn, M. S. *Chem. Commun.* **2010,** *46* (32), 5921-5923.

44. Nguyen, T. V.; Sherburn, M. S. *Chem. Eur. J.* **2014,** *20* (46), 14991-14995.

45. Nishimura, N.; Yoza, K.; Kobayashi, K. *J. Am. Chem. Soc.* **2009,** *132* (2), 777-790.

Chapter 7 - Future work

The knowledge and understanding of intermolecular forces in molecular recognition events as outlined in the thesis not only lead us to design new solid forms with high predictability and selectivity but also achieve preferential binding of guests with a series of hosts in solution. However, there is still much to be done to extend some of the systems to the next level.

First, a restricted coordination profile of halide ions was observed by using ditopic *bis*-haloethynyl compounds. Therefore, we can use multitopic and different geometrically oriented halogen bond donors as new tectons that will afford anion coordinated assemblies in a predictable manner (Figure 7.1). Understanding of the anion coordination under the control of halogen bonding can be utilized in rational design of new functional materials with predictable characteristics and properties, especially halogen bond based semiconducting materials.

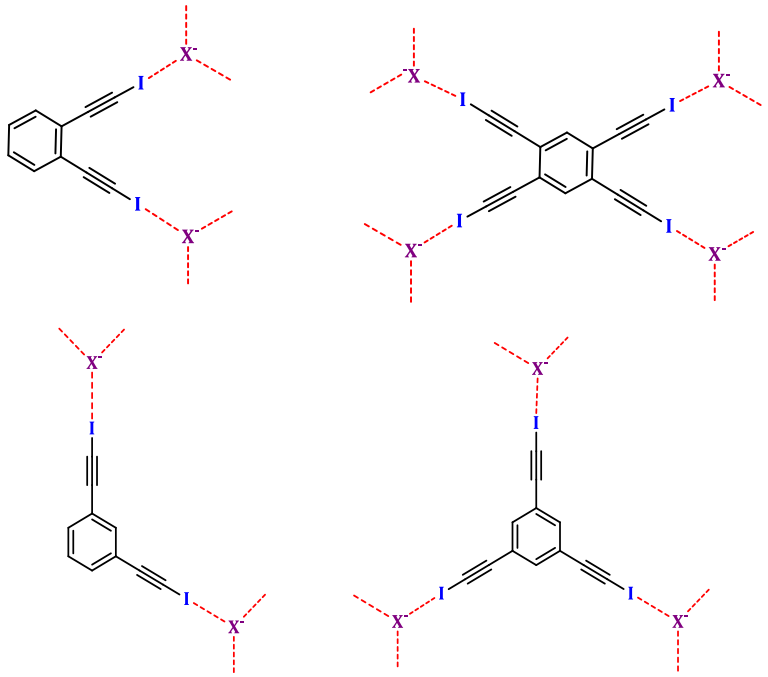

Figure 7.1 Some of the expected architectures of multitopic halogen bond donors, X^- = halide

As the C(*sp*)-H can act as a synthon mimic of C(*sp*)-I, C(*sp*)-H can be exploited in anion coordination as hydrogen bonding tectons. This will allow us gain a broader view on the hydrogen bond based anion coordination profile and will open alternative approaches in designing novel receptors for anion recognition.

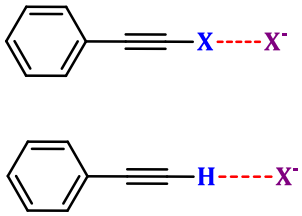

Figure 7.2 Synthon mimicry can be applied in anion coordination

Designing ternary co-crystals is of high importance and a challenging task in the context of crystal engineering[1] and the right balance between the intermolecular interactions is crucial in this regard.[2] Even though amino pyrimidines are known to form self-complementary ribbons via NH···N synthons, carboxylic acids and amides do form heteromeric interactions with 2-aminopyrimidines via OH···N and C=O···H interactions, disrupting the homomeric interactions (Figure 7.3). Therefore, **Hpym** and **Ipym** would be a good source of designing ternary co-crystals via hydrogen bonding and halogen bonding (Figure 7.4) and it will allow us create more complex supermolecules with three building blocks controlled in a predictable manner.

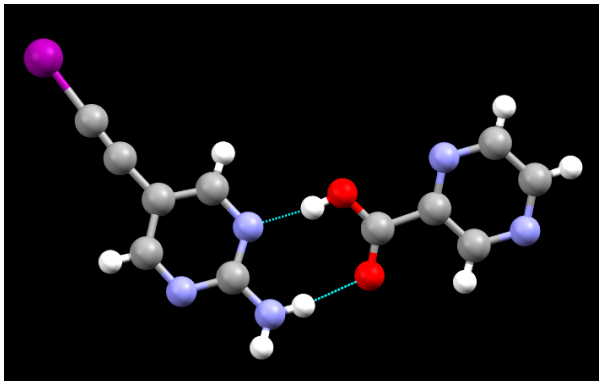

(a)

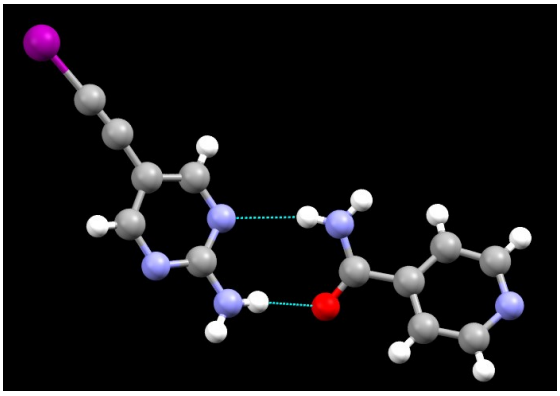

(b)

Figure 7.3 Supermolecules showing heteromeric interactions between **Ipym** and (a) carboxylic acid (b) amide

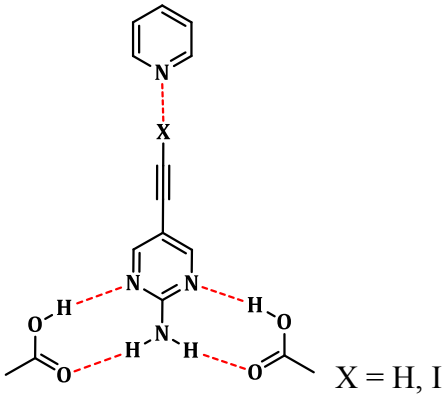

Figure 7.4 Proposed interactions that build up ternary co-crystals

Finally we can study the binding preferences of tetraethynyliodo/bromo cavitands towards a series of guest molecules in solution using UV spectroscopy. Tetraethynylhalo cavitands were not UV active, thus a series of UV active guest molecules can be selected in which the absorbance would be changed upon binding with the host.

7.1 References

1. (a) Desiraju, G. R.; Vittal, J. J.; Ramanan, A. *Crystal Engineering: A textbook*. World Scientific: Singapore, 2011; (b) Mukherjee, A.; Desiraju, G. R. *Chem. Commun.* **2011,** *47* (14), 4090-4092.

2. (a) Aakeröy, C. B.; Beatty, A. M.; Helfrich, B. A. *Angew. Chem. Int. Ed.* **2001,** *40* (17), 3240-3242; (b) Aakeroy, C. B.; Desper, J.; Urbina, J. F. *Chem. Commun.* **2005,** (22), 2820-2822; (c) Bhogala, B. R.; Basavoju, S.; Nangia, A. *Cryst. Growth Des.* **2005,** *5* (5), 1683-1686.

Appendix A - ^{1}H NMR, ^{13}C NMR, ^{19}F NMR and DSC data

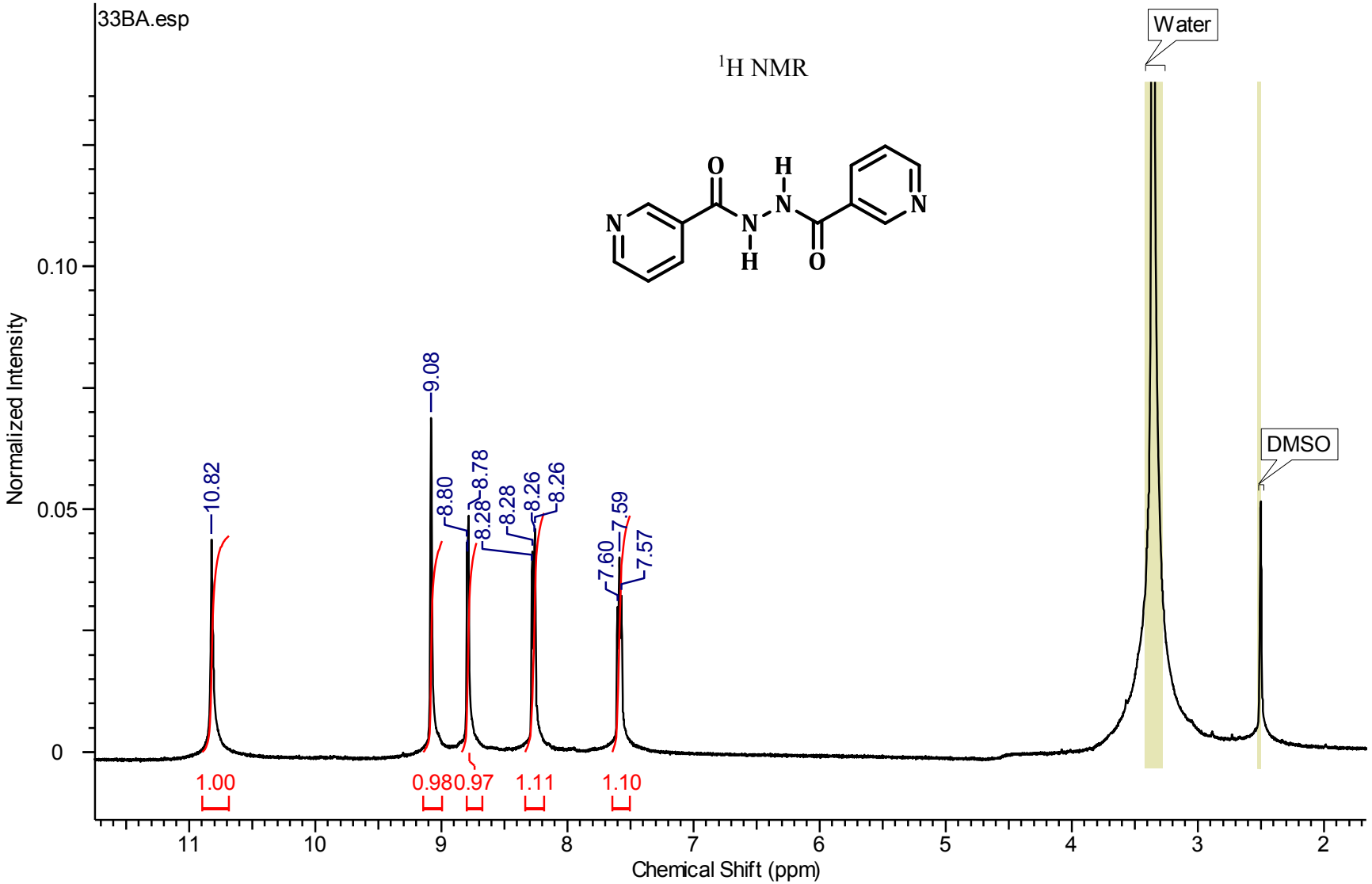
33BA.esp
^{1}H NMR
Water
DMSO
Normalized Intensity
0.10
0.05
0
10.82
9.08
8.80
8.78
8.28
8.28
8.26
8.26
7.60
7.59
7.57
1.00
0.98
0.97
1.11
1.10
11
10
9
8
7
6
5
4
3
2
Chemical Shift (ppm)

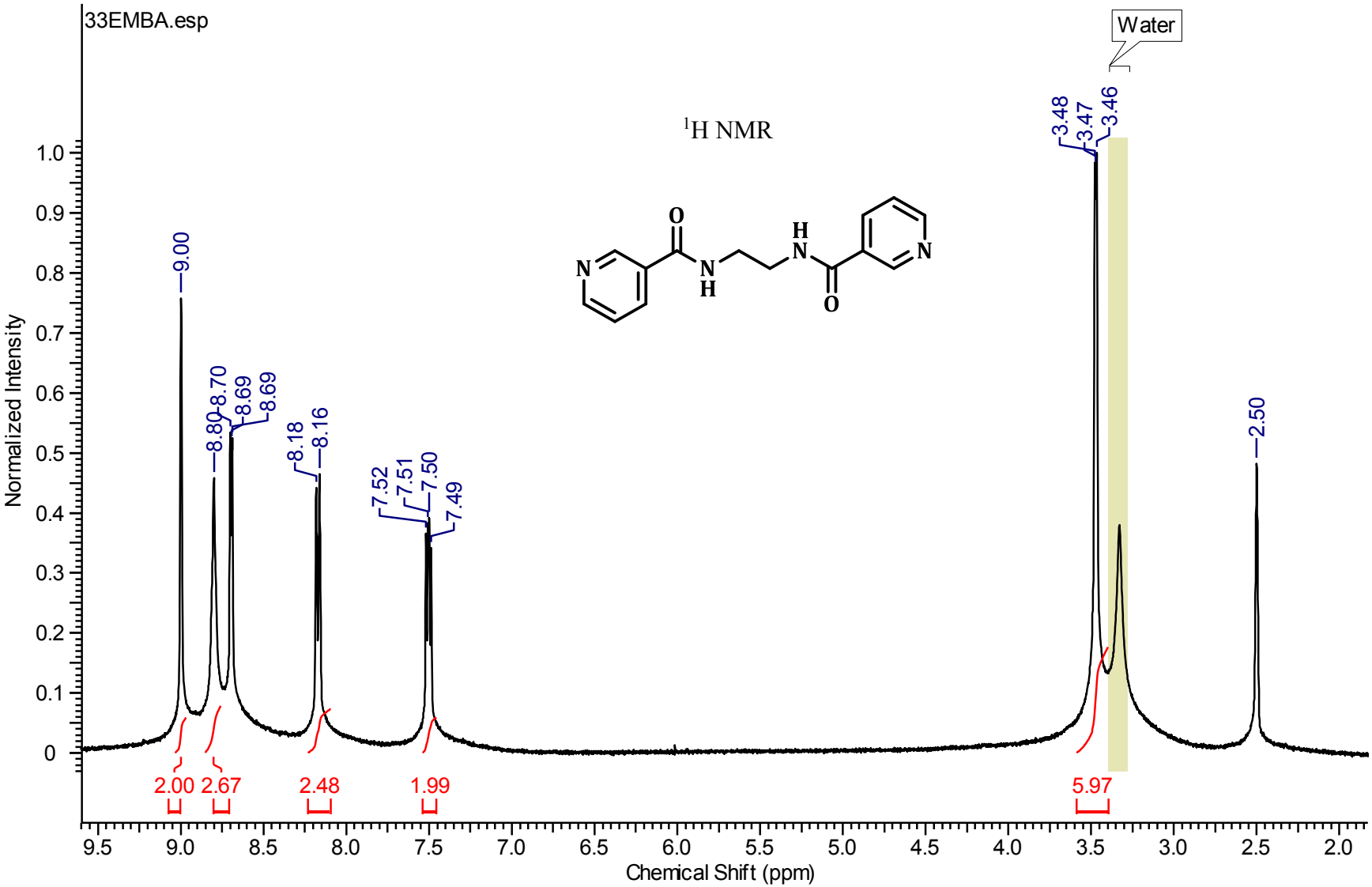
33EMBA.esp
Water
^{1}H NMR
9.00
8.80
8.70
8.69
8.69
8.18
8.16
7.52
7.51
7.50
7.49
3.48
3.47
3.46
2.50
2.00
2.67
2.48
1.99
5.97
Normalized Intensity
Chemical Shift (ppm)

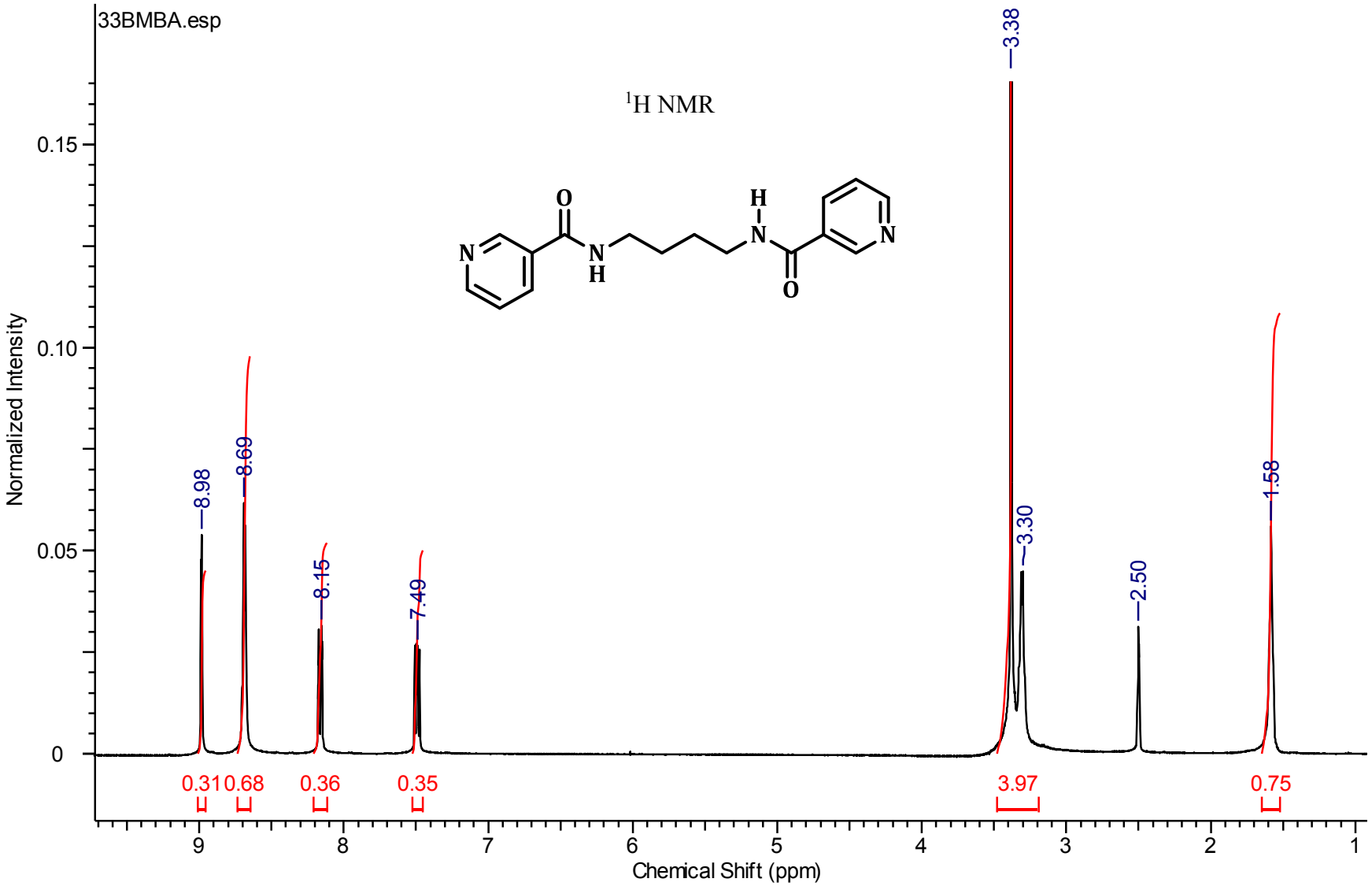
33BMBA.esp
^{1}H NMR
Normalized Intensity
0.15
0.10
0.05
0
8.98
8.69
8.15
7.49
3.38
3.30
2.50
1.58
0.31
0.68
0.36
0.35
3.97
0.75
9
8
7
6
5
4
3
2
1
Chemical Shift (ppm)

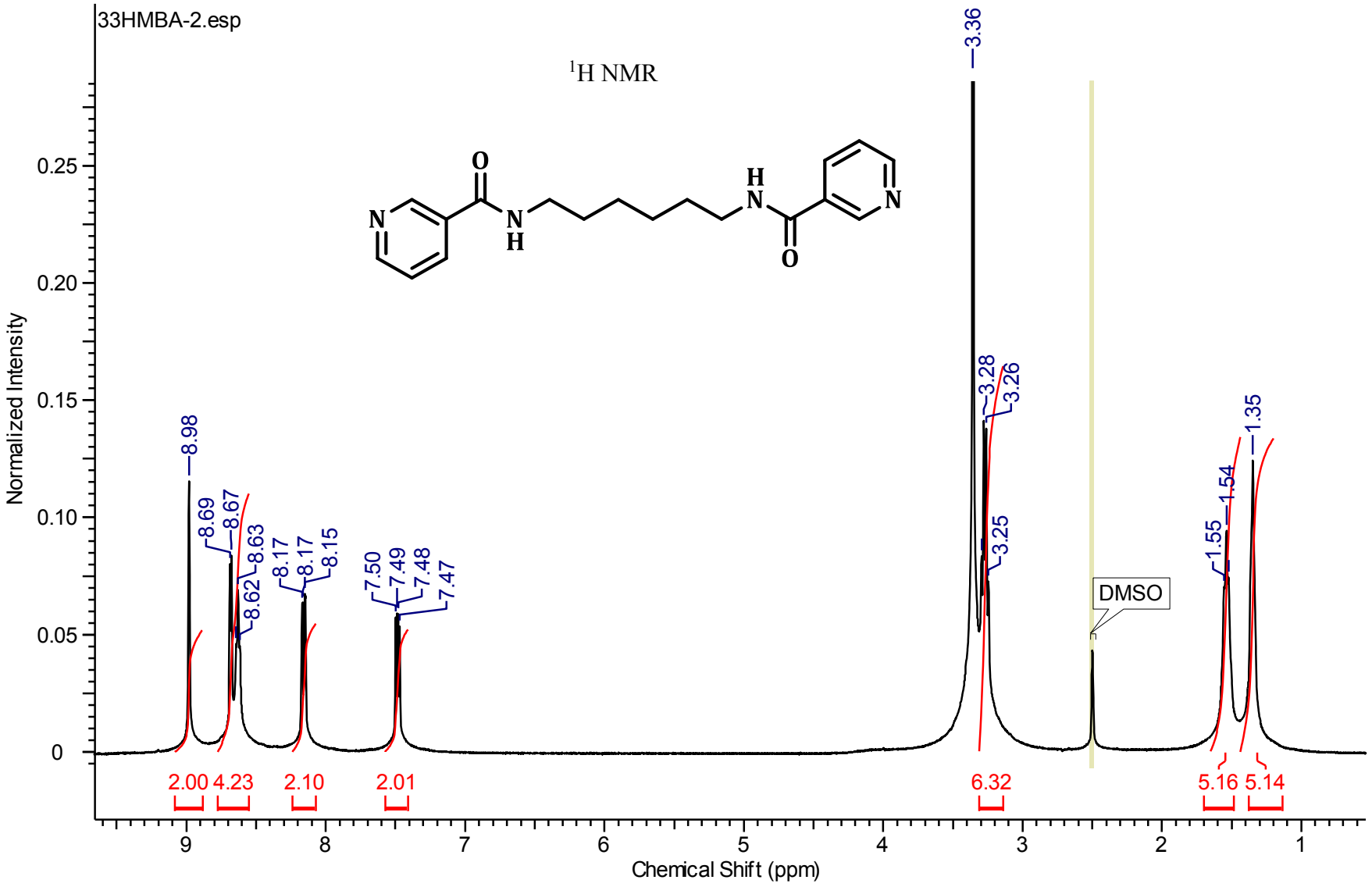
33HMBA-2.esp
^{1}H NMR
Normalized Intensity
Chemical Shift (ppm)
8.98
8.69
8.67
8.63
8.62
8.17
8.17
8.15
7.50
7.49
7.48
7.47
3.36
3.28
3.26
3.25
DMSO
1.55
1.54
1.35
2.00
4.23
2.10
2.01
6.32
5.16
5.14

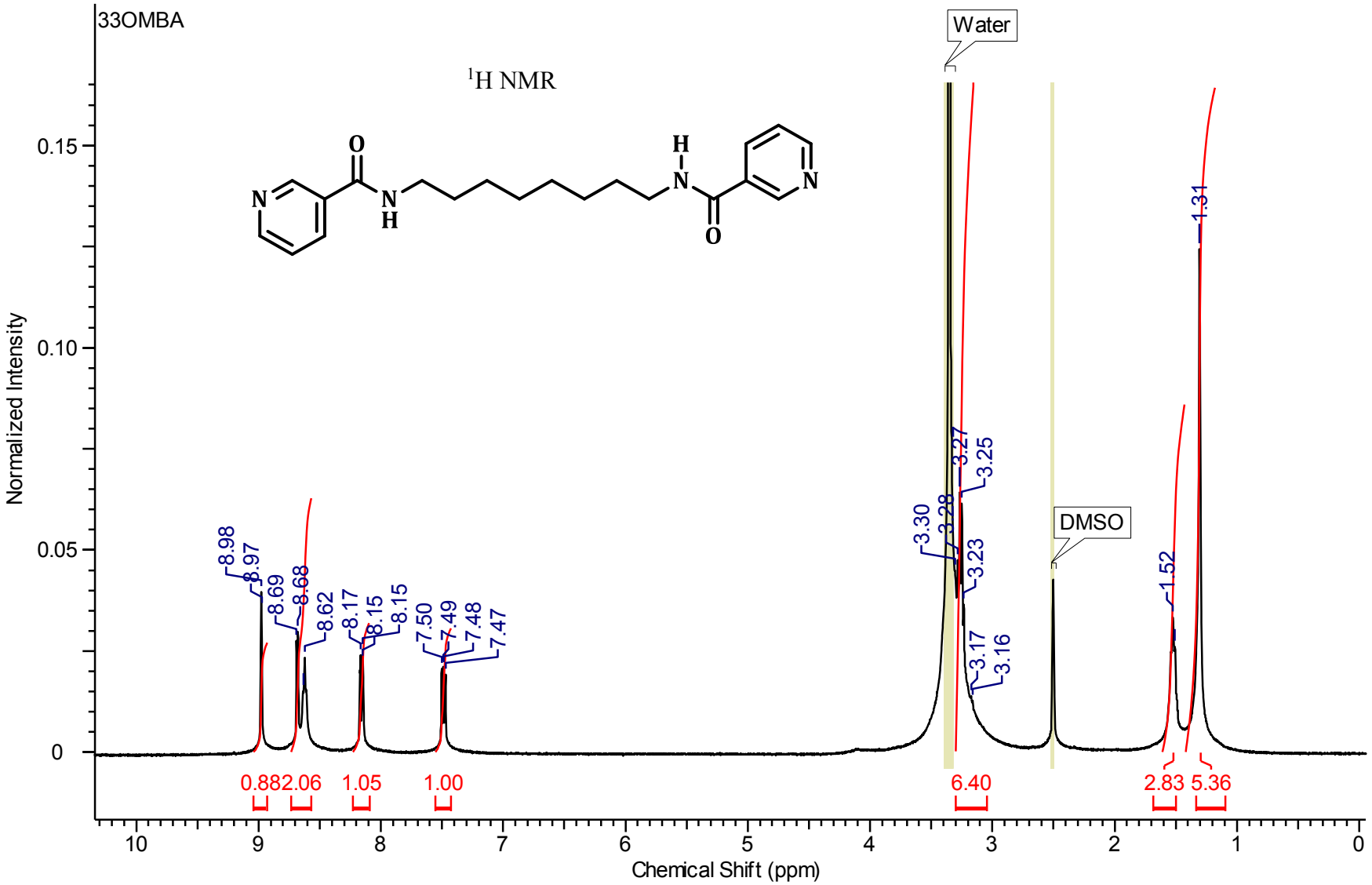
33OMBA
^{1}H NMR
Water
DMSO
Normalized Intensity
Chemical Shift (ppm)
8.98
8.97
8.69
8.68
8.62
8.17
8.15
8.15
7.50
7.49
7.48
7.47
3.30
3.28
3.27
3.25
3.23
3.17
3.16
1.52
1.31
0.88
2.06
1.05
1.00
6.40
2.83
5.36

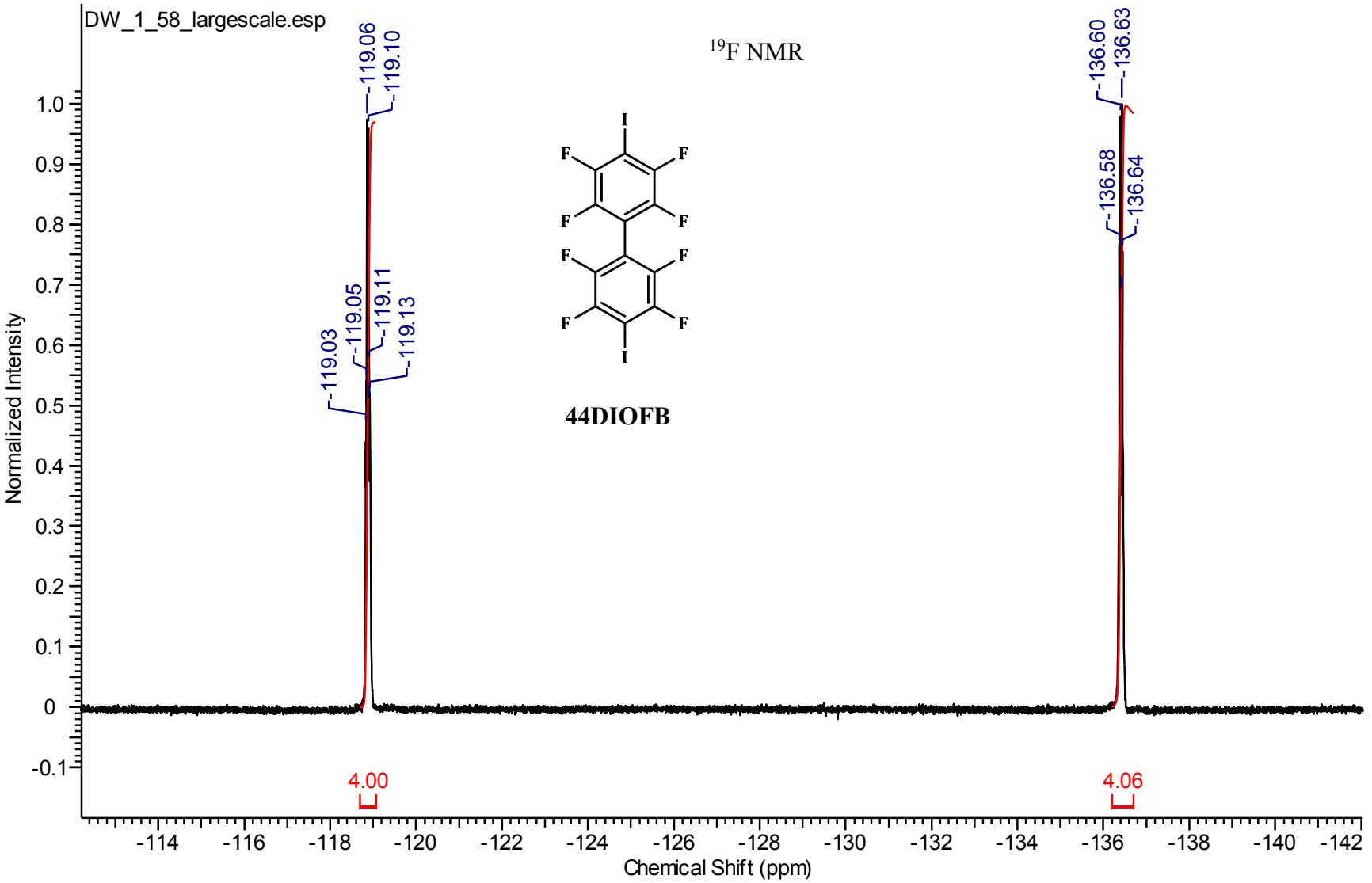
DW_1_58_largescale.esp
^{19}F NMR
-119.06
-119.10
-119.03
-119.05
-119.11
-119.13
-136.60
-136.63
-136.58
-136.64
44DIOFB
Normalized Intensity
Chemical Shift (ppm)
4.00
4.06

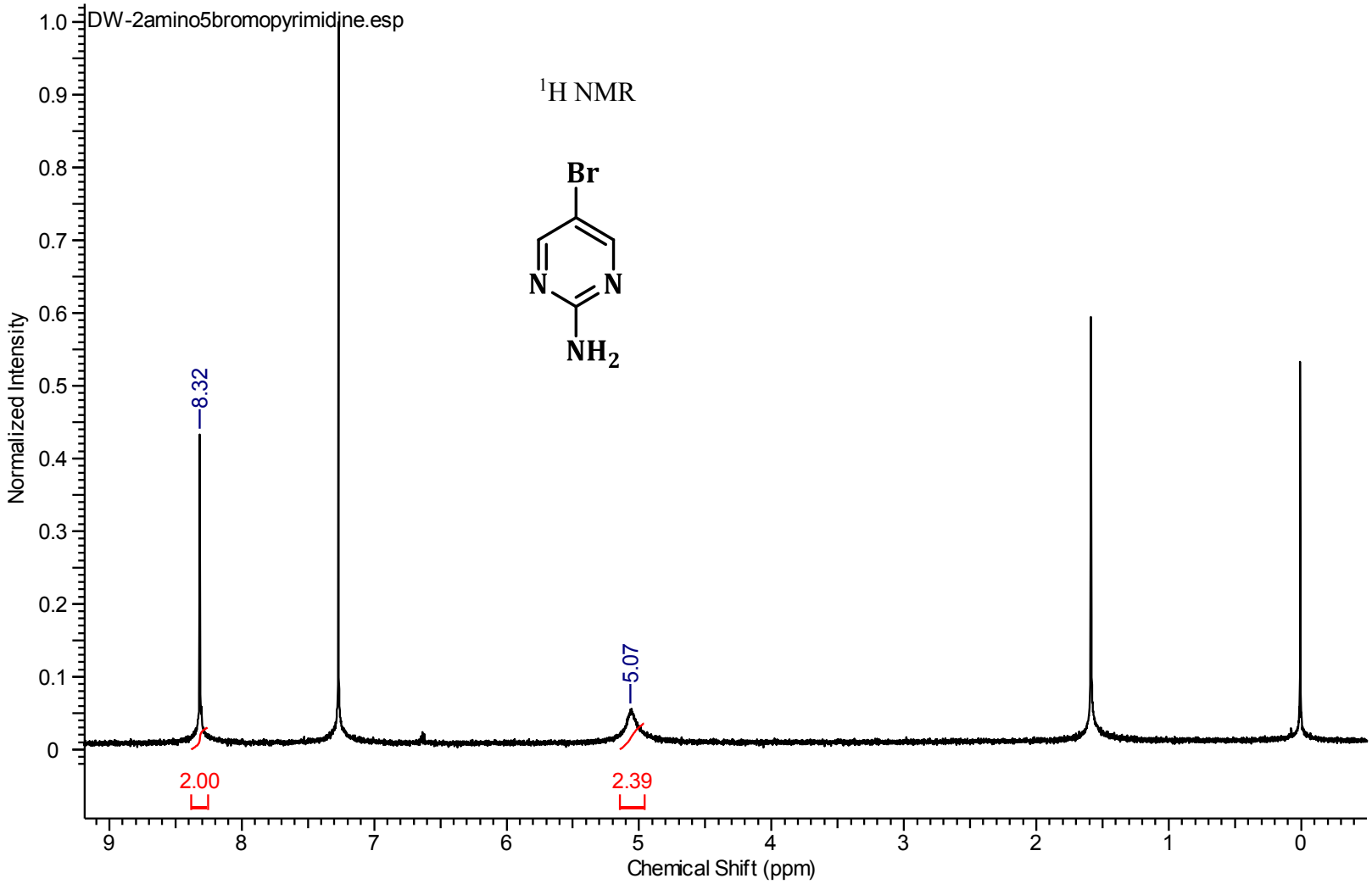
DW-2amino5bromopyrimidine.esp
^{1}H NMR
Br
N
N
NH$_2$
8.32
5.07
2.00
2.39
Normalized Intensity
Chemical Shift (ppm)
1.0
0.9
0.8
0.7
0.6
0.5
0.4
0.3
0.2
0.1
0
9
8
7
6
5
4
3
2
1
0

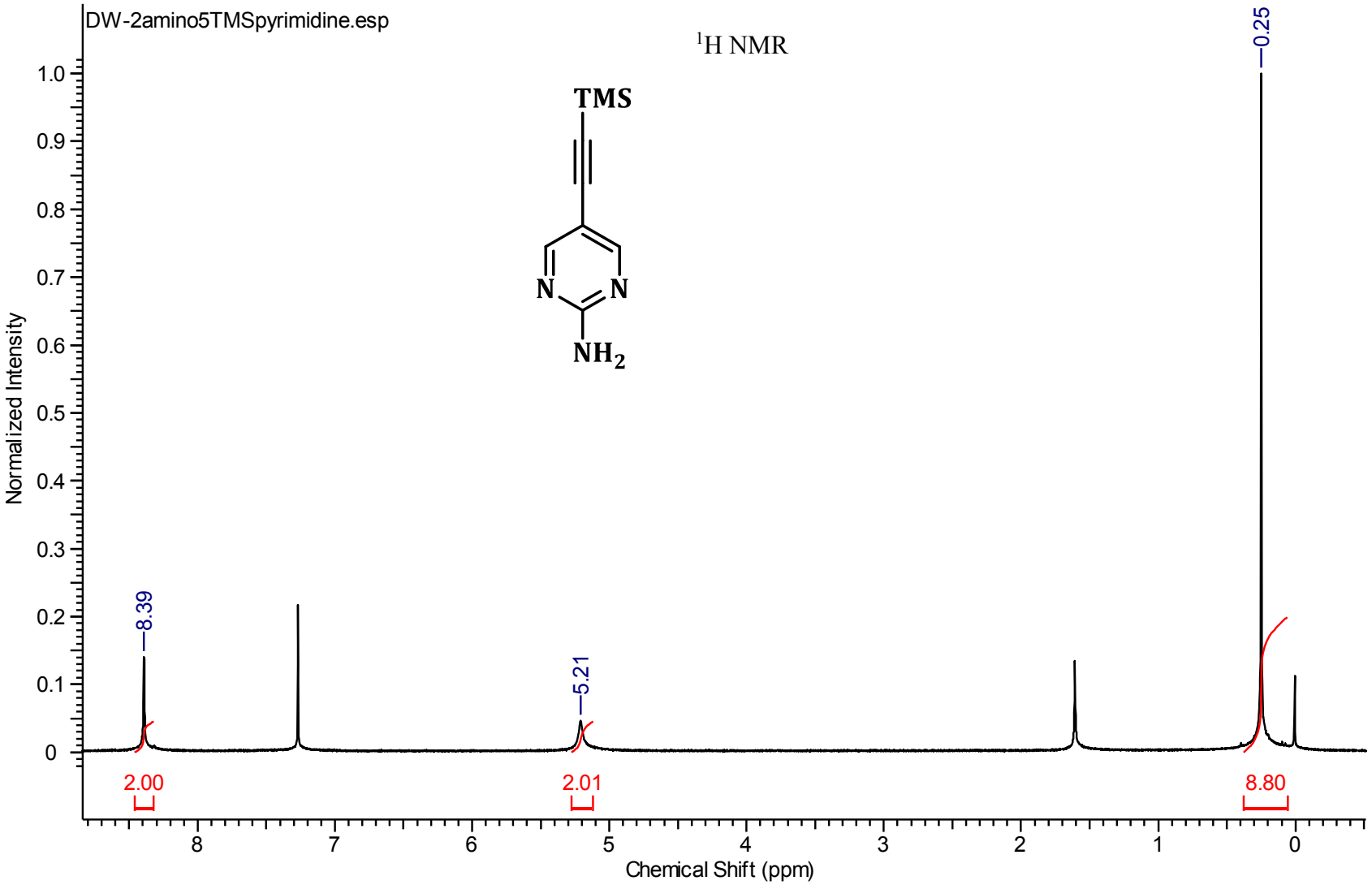
DW-2amino5TMSpyrimidine.esp
^{1}H NMR
TMS
N
N
NH$_2$
Normalized Intensity
Chemical Shift (ppm)
8.39
5.21
0.25
2.00
2.01
8.80

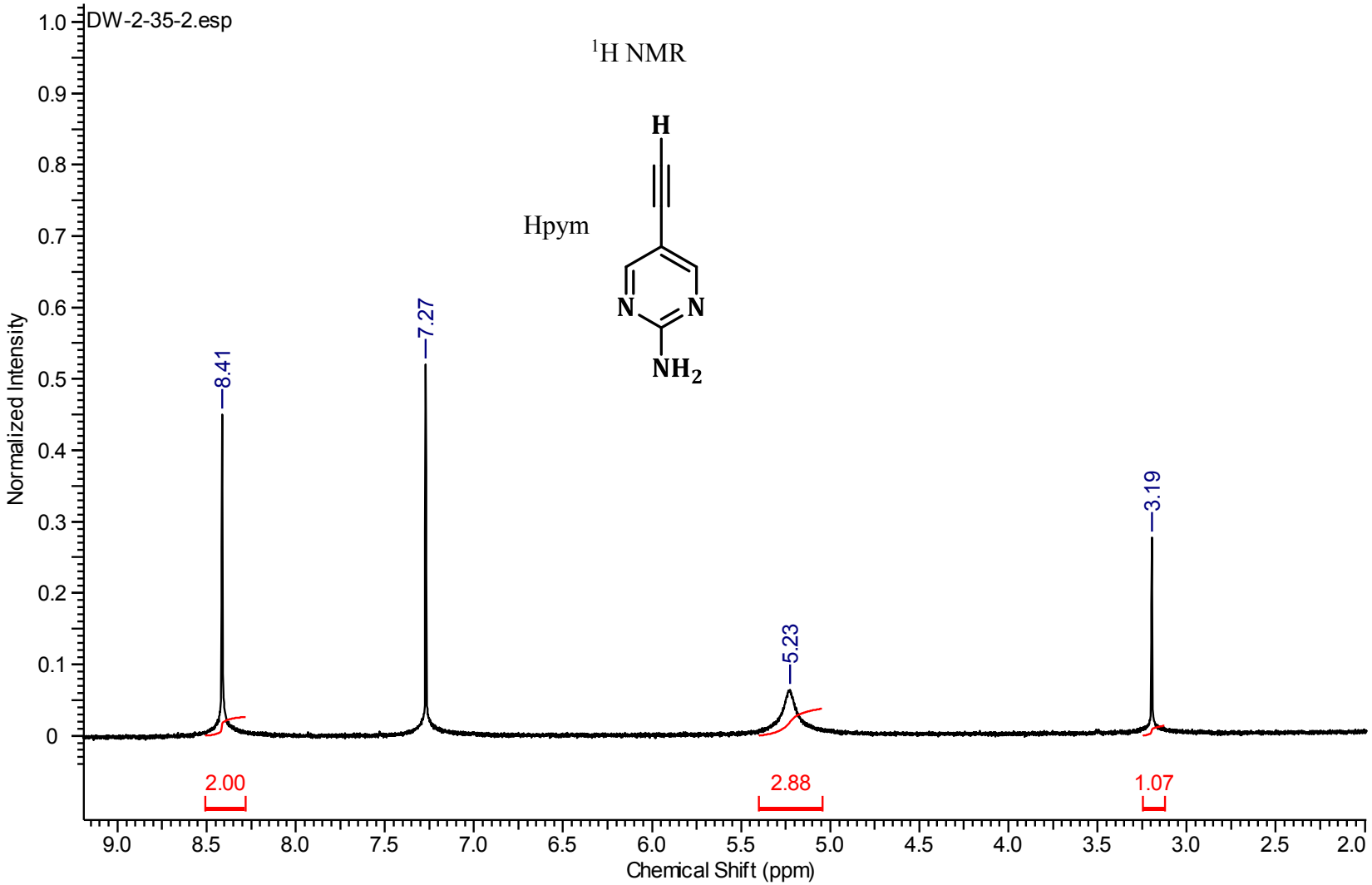
DW-2-35-2.esp
^{1}H NMR
Hpym
H
N
N
NH$_2$
Normalized Intensity
1.0
0.9
0.8
0.7
0.6
0.5
0.4
0.3
0.2
0.1
0
8.41
7.27
5.23
3.19
2.00
2.88
1.07
9.0
8.5
8.0
7.5
7.0
6.5
6.0
5.5
5.0
4.5
4.0
3.5
3.0
2.5
2.0
Chemical Shift (ppm)

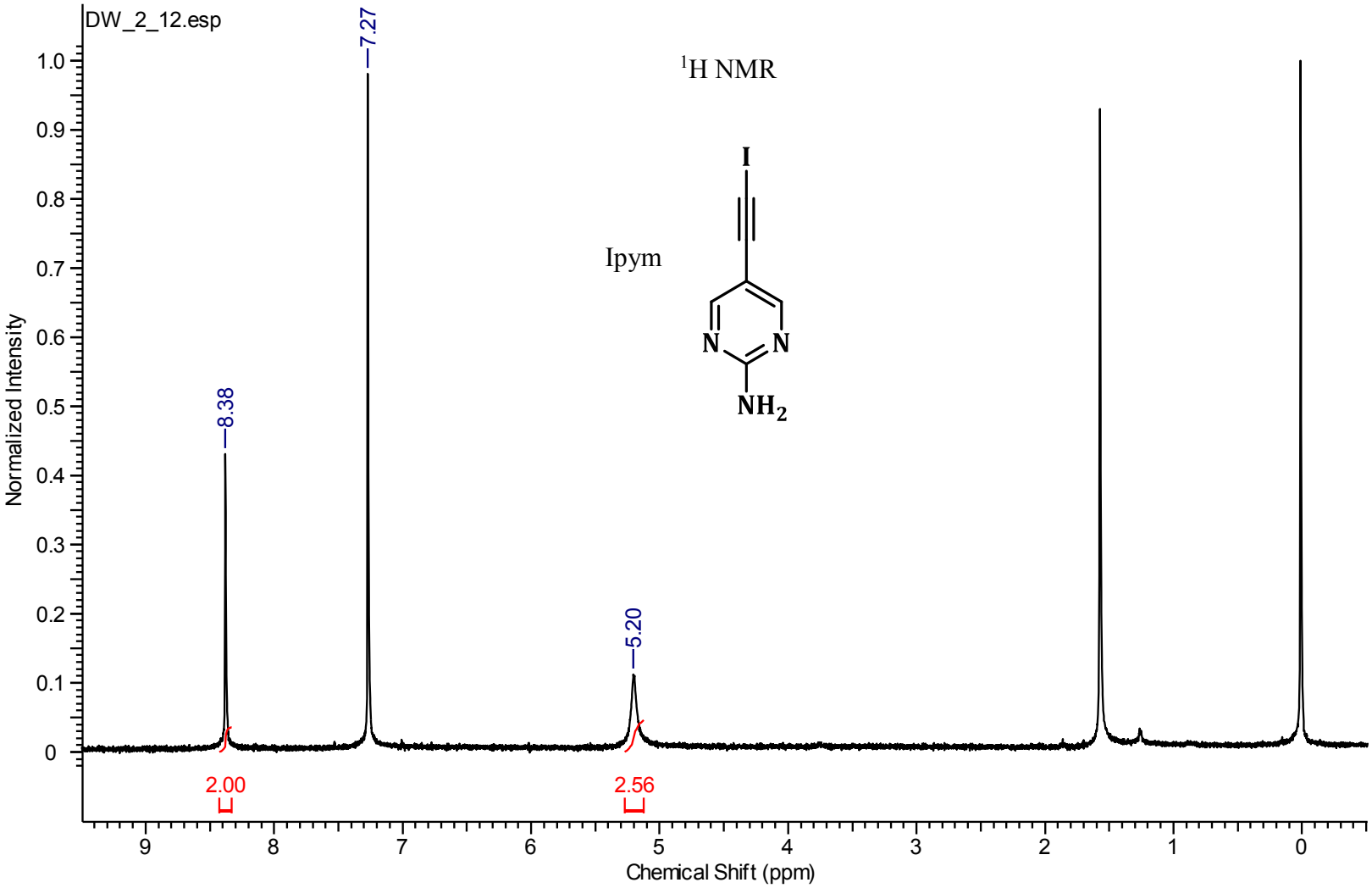
DW_2_12.esp
^{1}H NMR
Ipym
I
N
N
NH$_2$
7.27
8.38
5.20
2.00
2.56
Normalized Intensity
Chemical Shift (ppm)
1.0
0.9
0.8
0.7
0.6
0.5
0.4
0.3
0.2
0.1
0
9
8
7
6
5
4
3
2
1
0

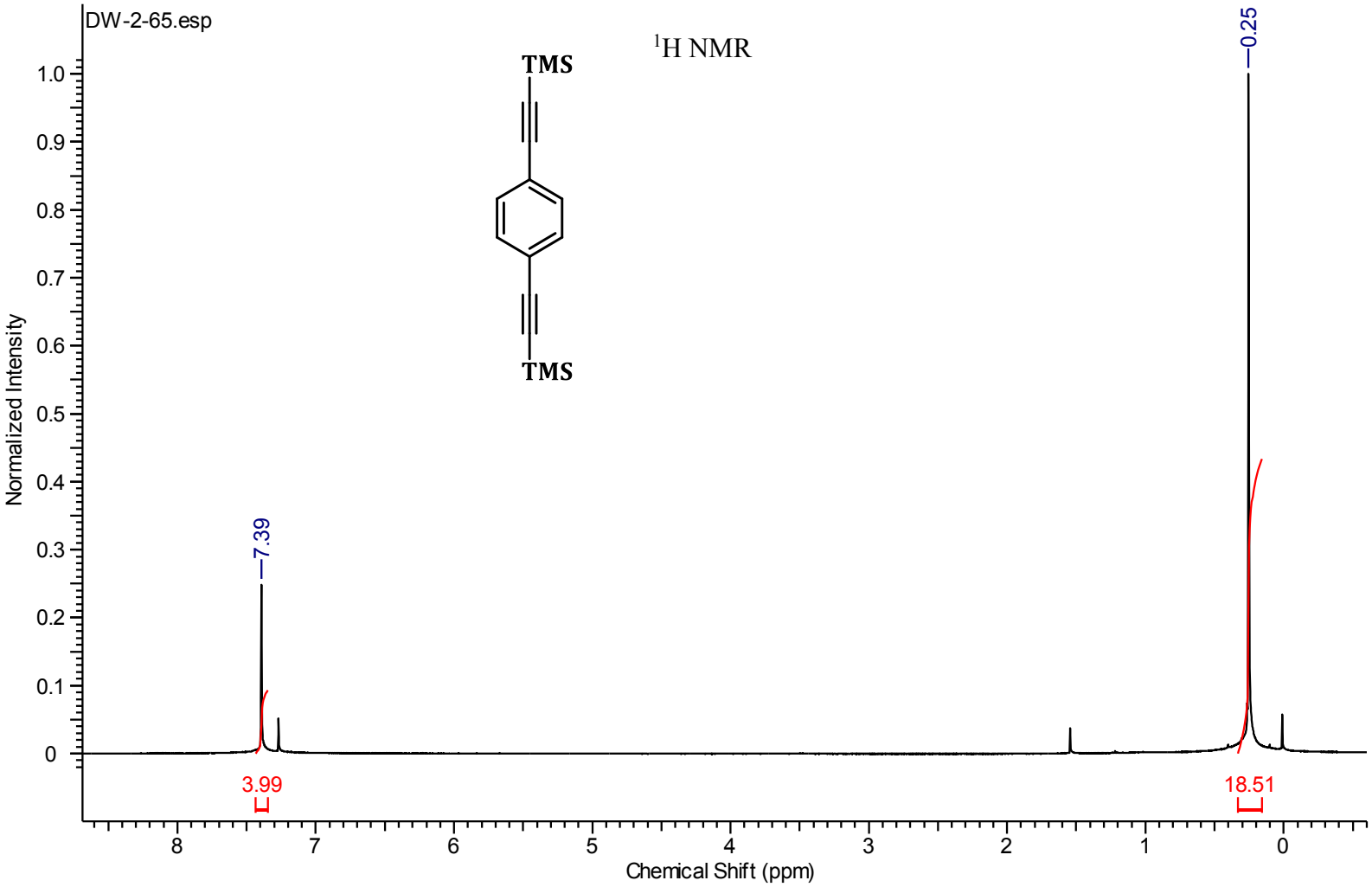
DW-2-65.esp
^{1}H NMR
TMS
TMS
7.39
0.25
3.99
18.51
Normalized Intensity
Chemical Shift (ppm)

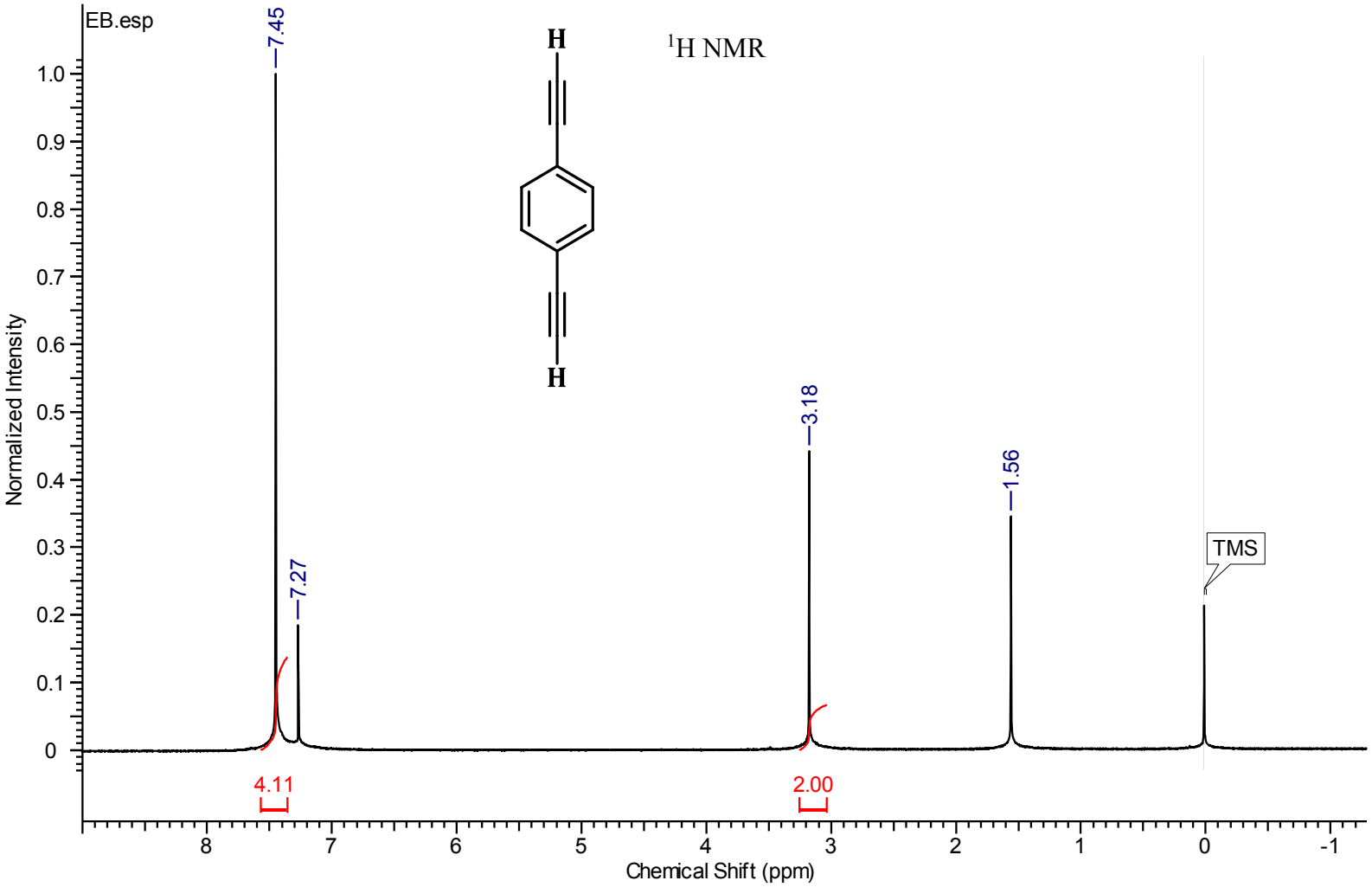
EB.esp
^{1}H NMR
H
H
7.45
7.27
3.18
1.56
TMS
4.11
2.00
Normalized Intensity
Chemical Shift (ppm)

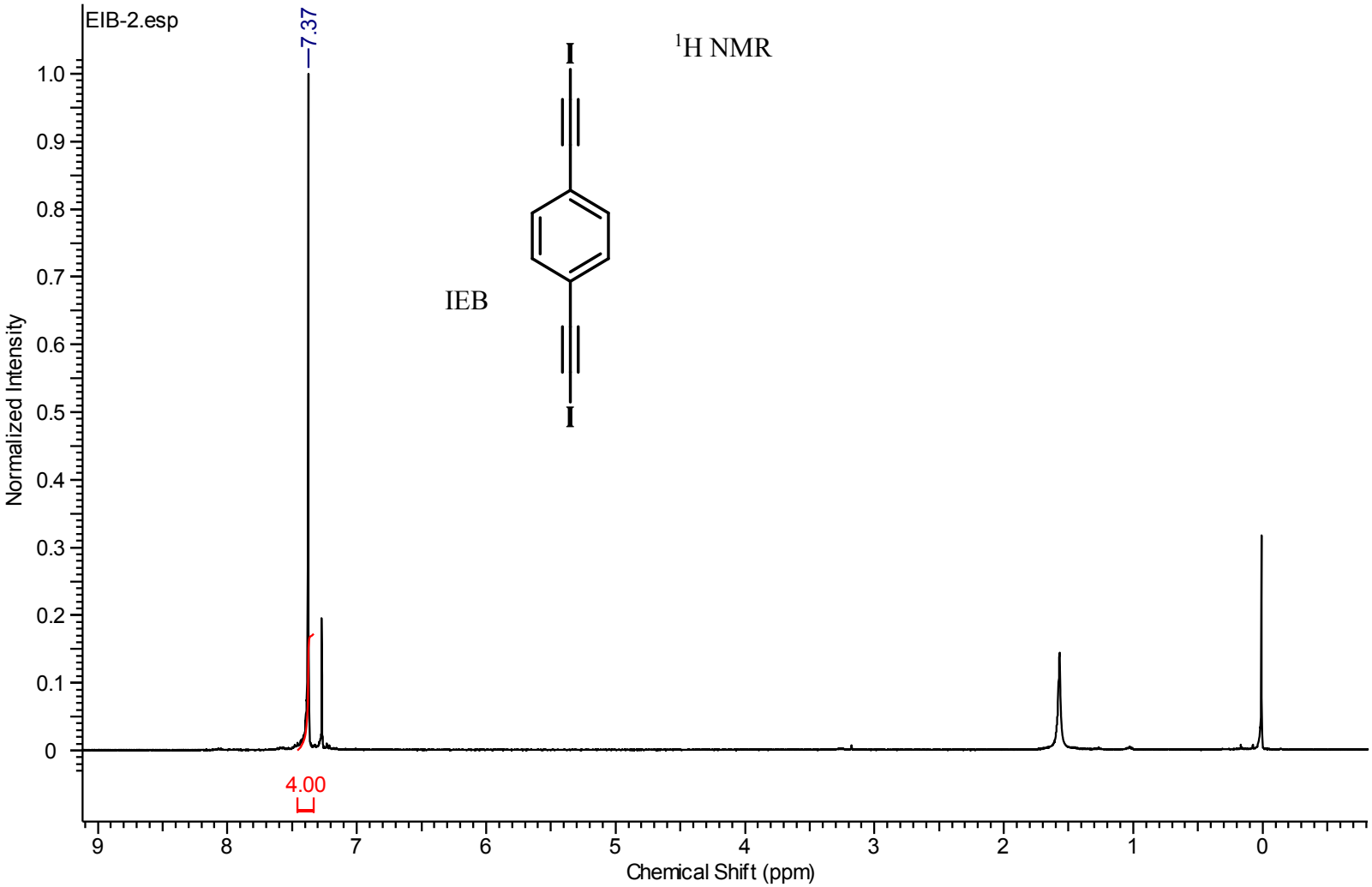
EIB-2.esp
7.37
^{1}H NMR
IEB
Normalized Intensity
1.0
0.9
0.8
0.7
0.6
0.5
0.4
0.3
0.2
0.1
0
4.00
9
8
7
6
5
4
3
2
1
0
Chemical Shift (ppm)

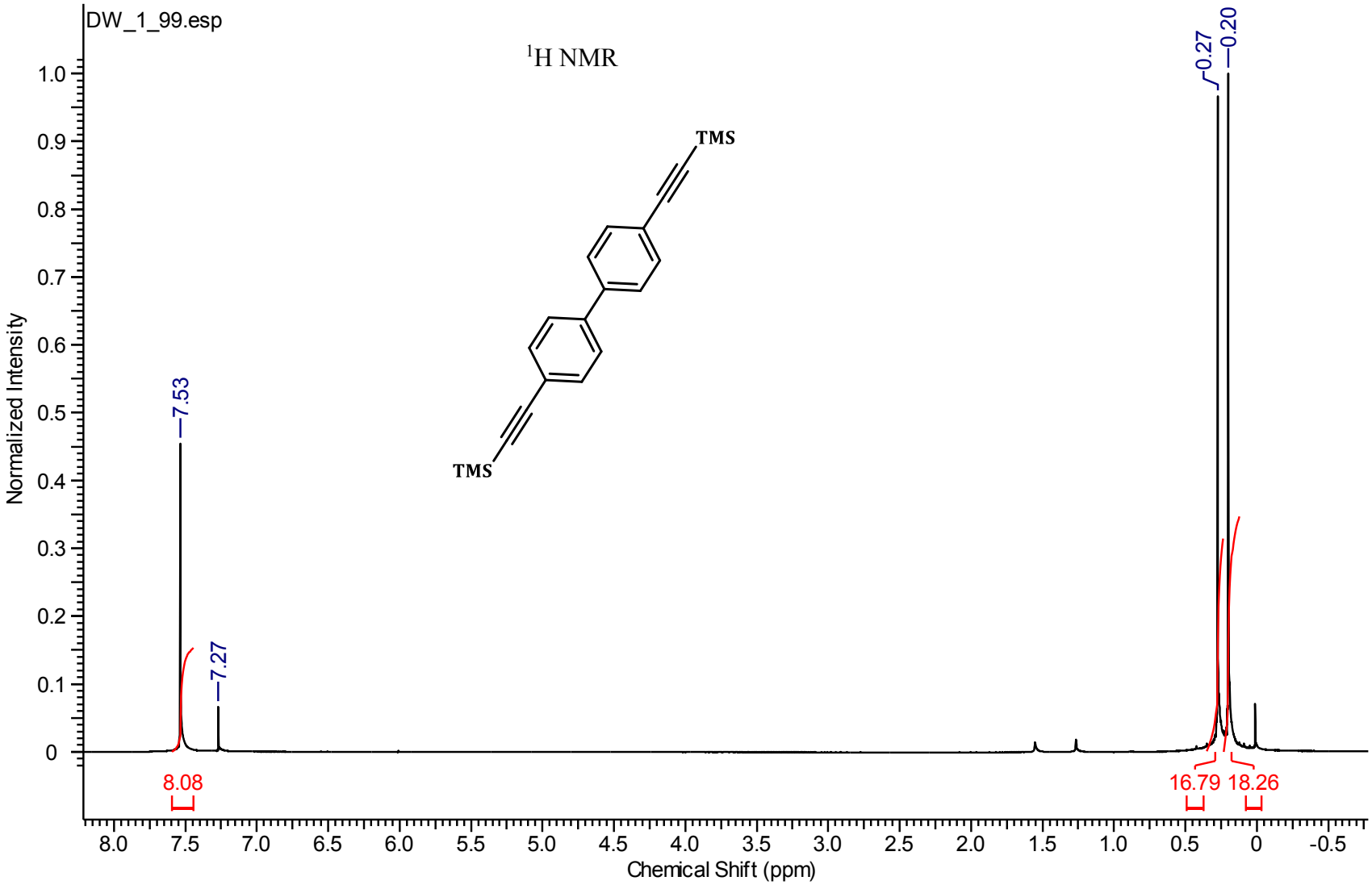
DW_1_99.esp
^{1}H NMR
TMS
TMS
Normalized Intensity
Chemical Shift (ppm)
7.53
7.27
0.27
0.20
8.08
16.79
18.26

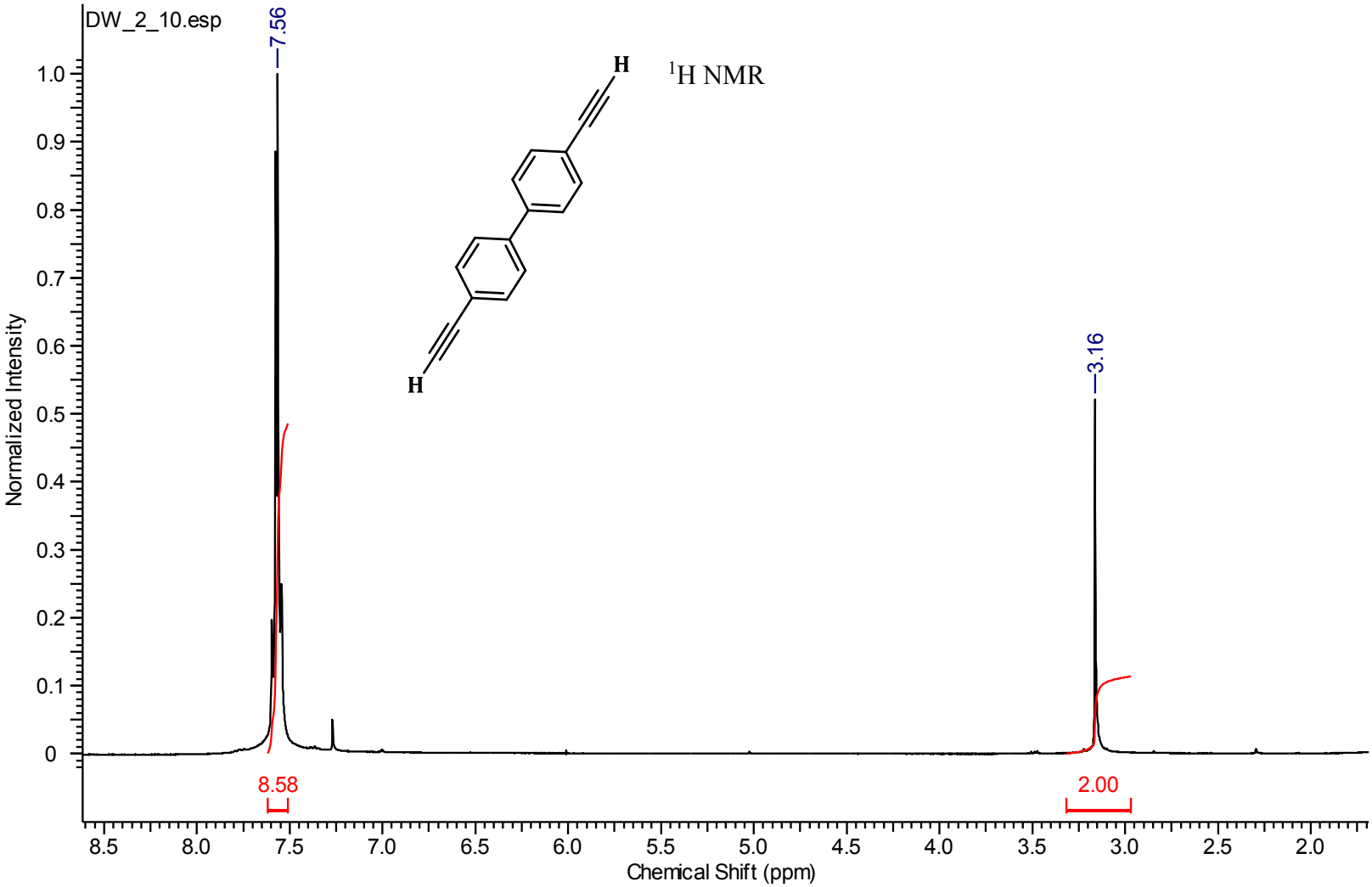
DW_2_10.esp
7.56
3.16
^{1}H NMR
H
H
Normalized Intensity
1.0
0.9
0.8
0.7
0.6
0.5
0.4
0.3
0.2
0.1
0
8.58
2.00
8.5
8.0
7.5
7.0
6.5
6.0
5.5
5.0
4.5
4.0
3.5
3.0
2.5
2.0
Chemical Shift (ppm)

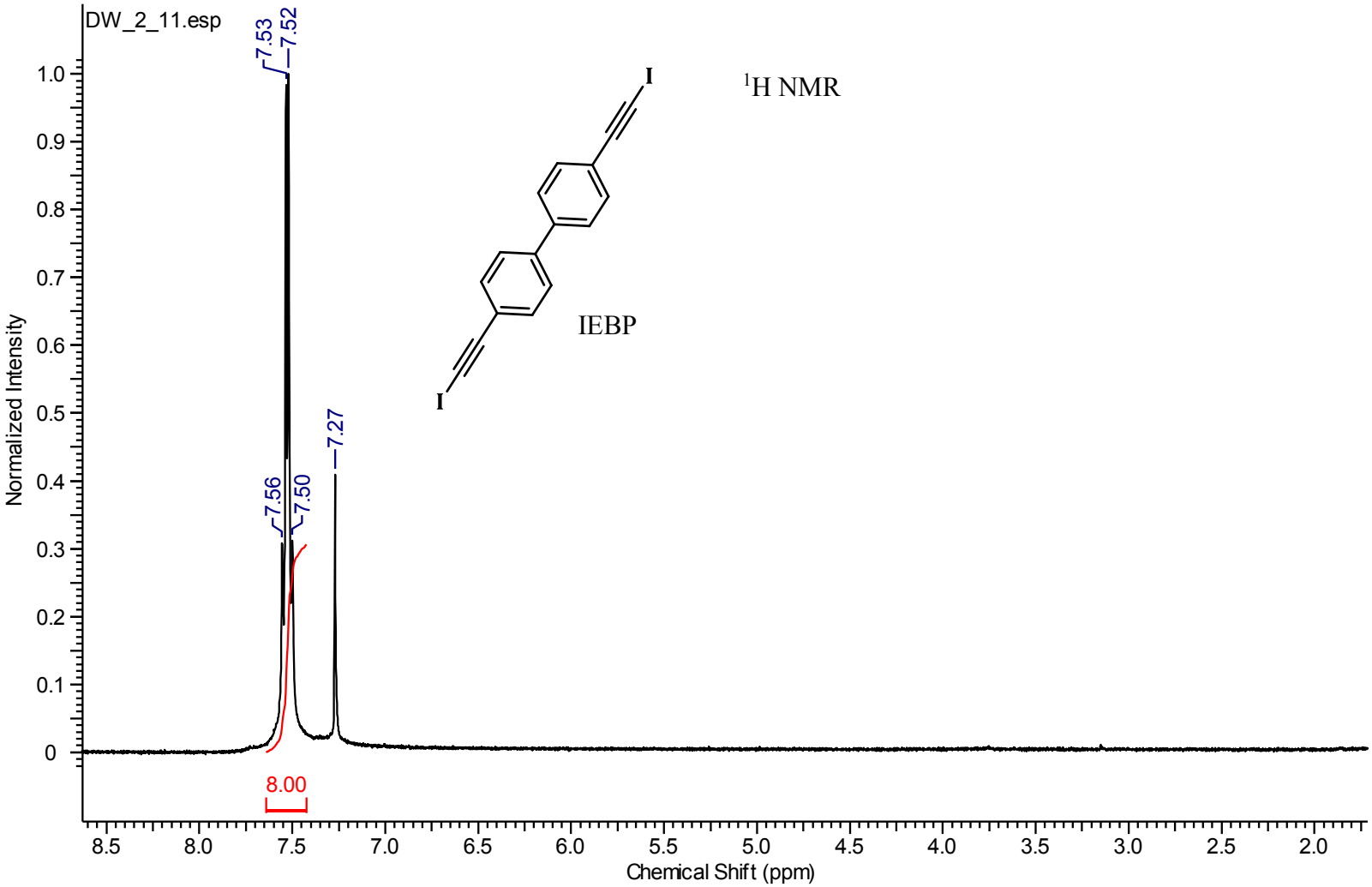
DW_2_11.esp
7.53
7.52
7.56
7.50
7.27
8.00
Normalized Intensity
Chemical Shift (ppm)
I
I
IEBP
^{1}H NMR

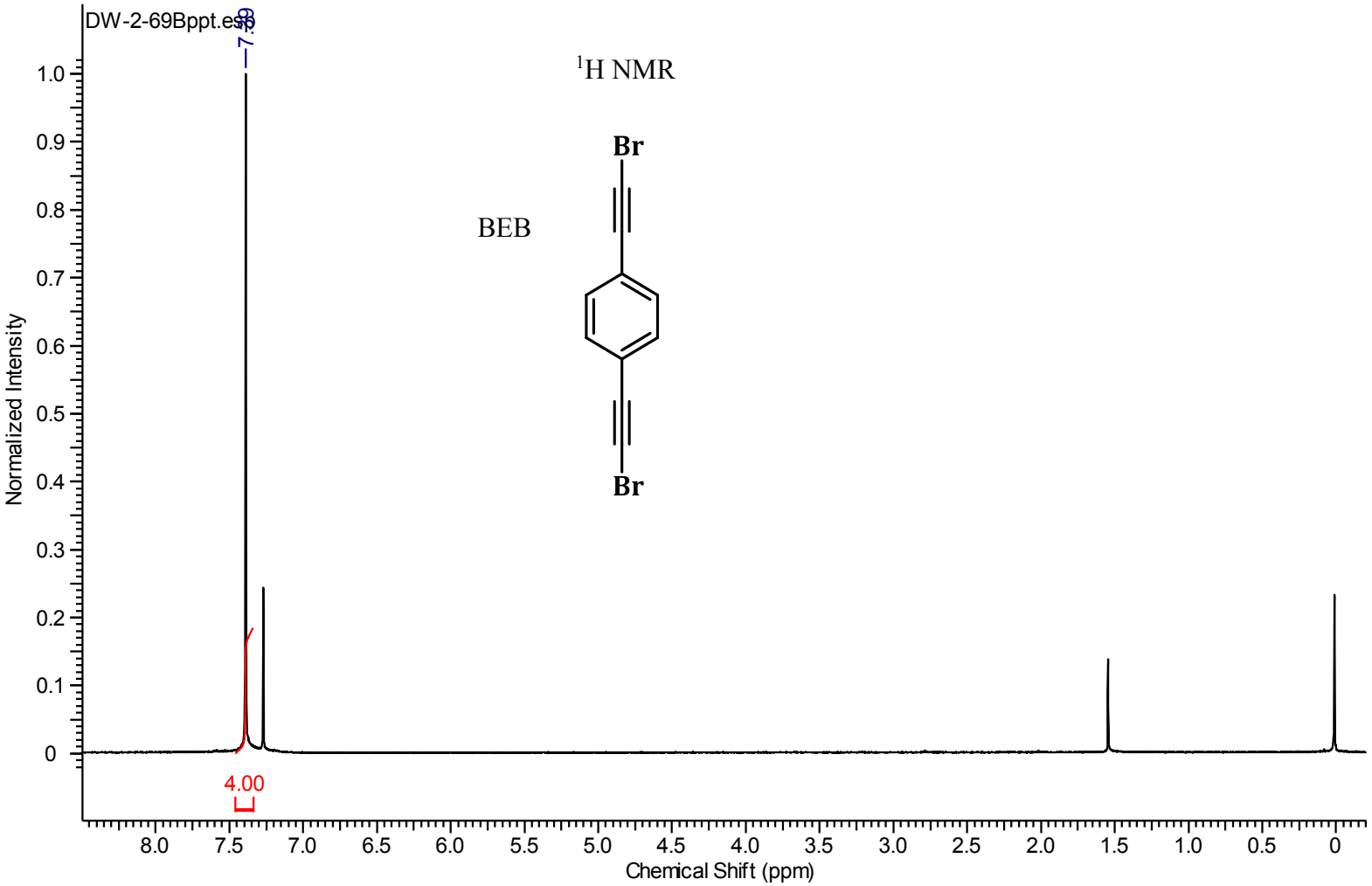
DW-2-69Bppt.esp
7.49
^{1}H NMR
BEB
Br
Br
Normalized Intensity
1.0
0.9
0.8
0.7
0.6
0.5
0.4
0.3
0.2
0.1
0
4.00
8.0
7.5
7.0
6.5
6.0
5.5
5.0
4.5
4.0
3.5
3.0
2.5
2.0
1.5
1.0
0.5
0
Chemical Shift (ppm)

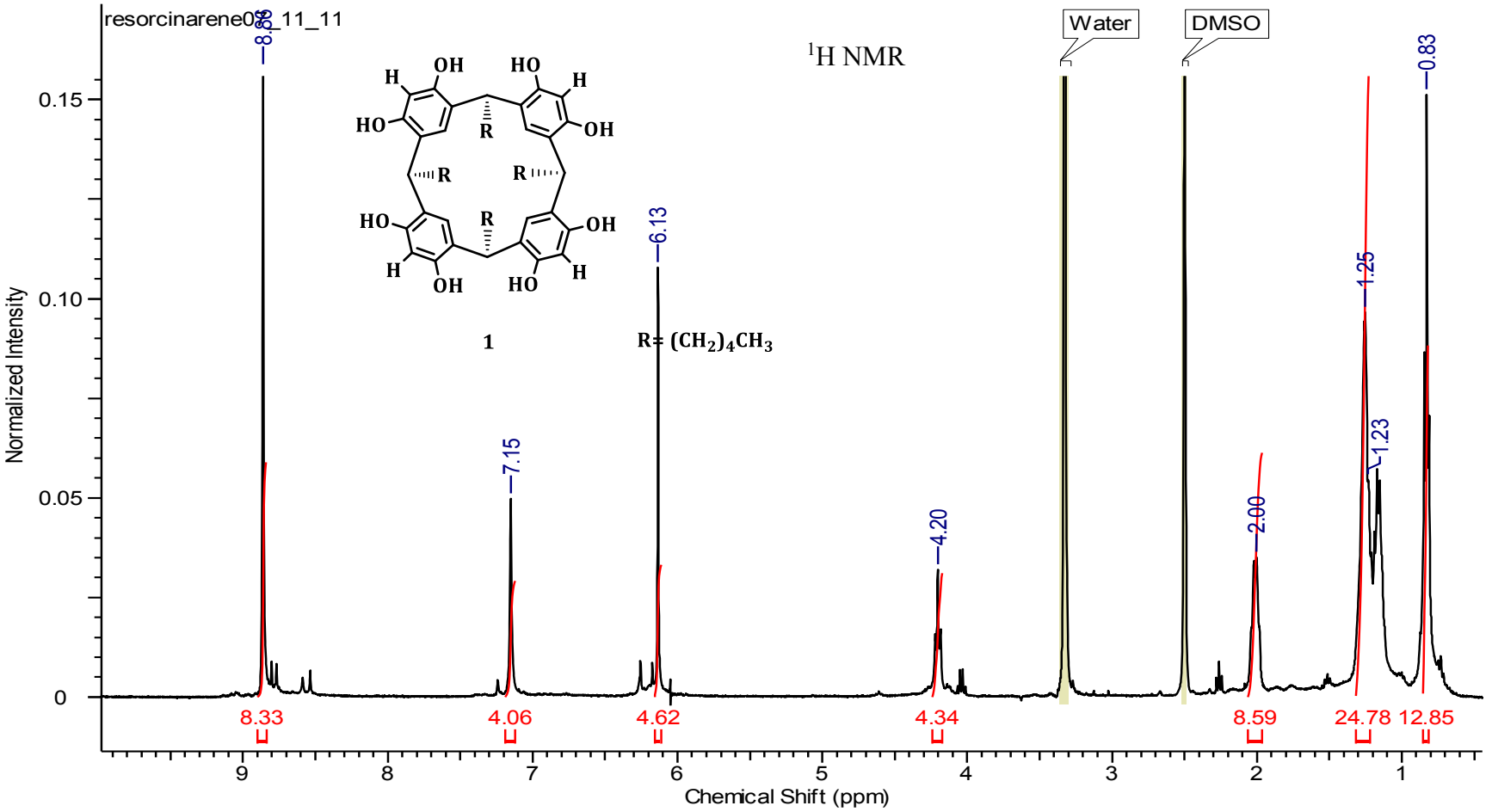
resorcinarene08_11_11
^{1}H NMR
Water
DMSO
8.33
7.15
6.13
4.20
2.00
1.25
1.23
0.83
1
R= $(CH_2)_4CH_3$
Normalized Intensity
0.15
0.10
0.05
0
8.33
4.06
4.62
4.34
8.59
24.78
12.85
9
8
7
6
5
4
3
2
1
Chemical Shift (ppm)

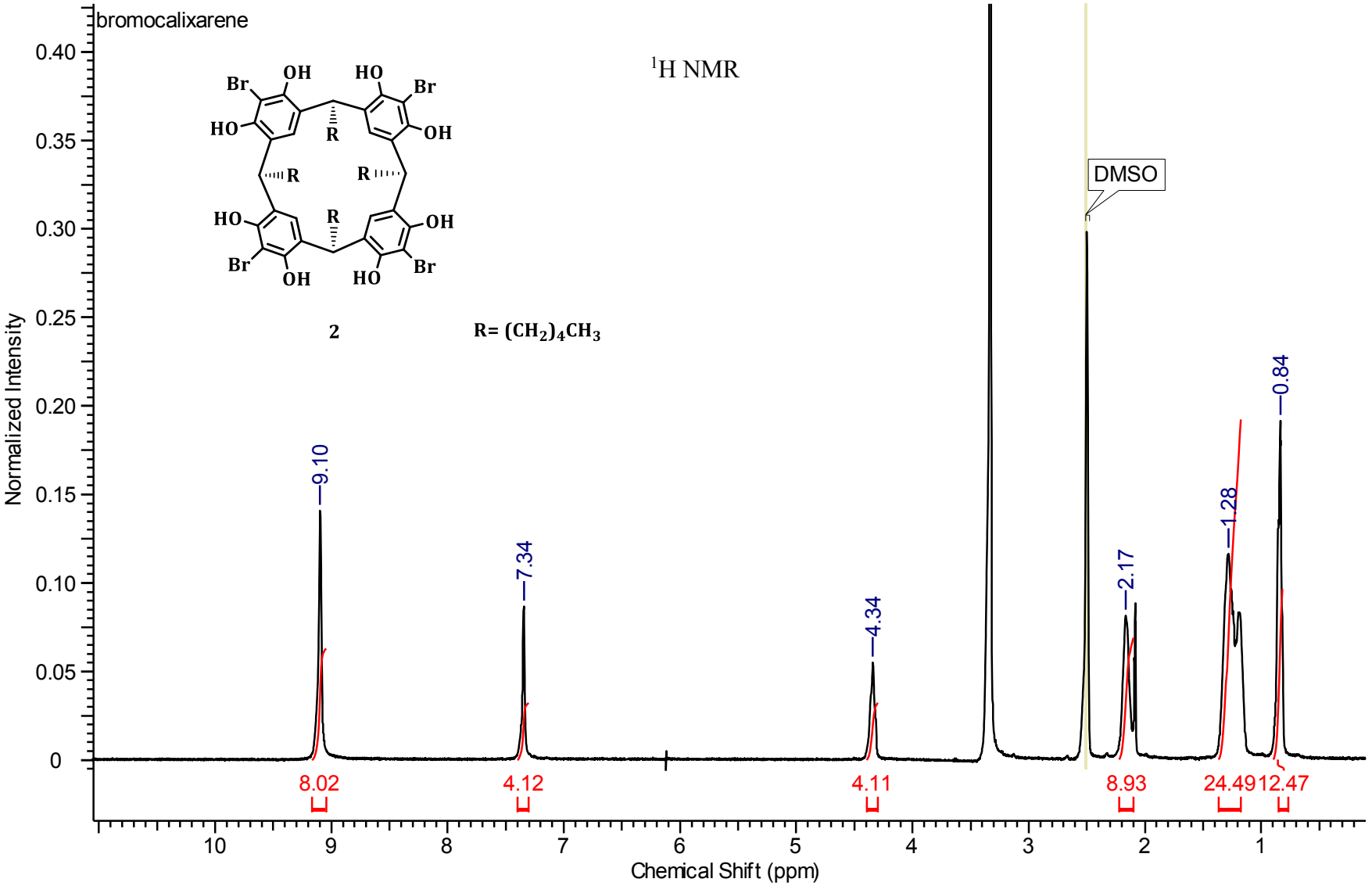
bromocalixarene
^{1}H NMR
2
R= $(CH_2)_4CH_3$
DMSO
9.10
7.34
4.34
2.17
1.28
0.84
8.02
4.12
4.11
8.93
24.49
12.47
Normalized Intensity
Chemical Shift (ppm)

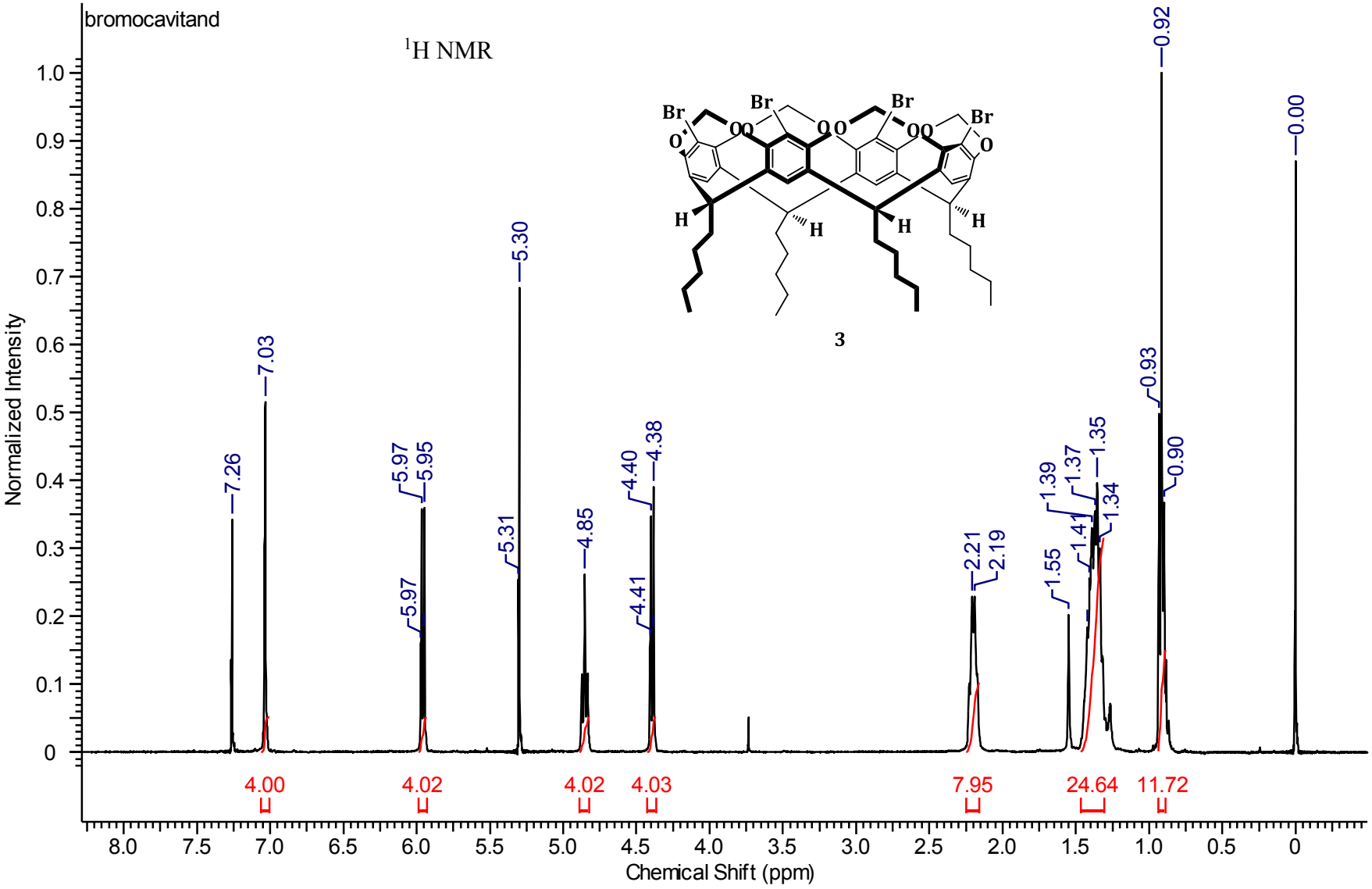
bromocavitand
^{1}H NMR
Br
O
H
3
Normalized Intensity
Chemical Shift (ppm)
7.26
7.03
5.97
5.95
5.97
5.31
5.30
4.85
4.40
4.38
4.41
2.21
2.19
1.55
1.39
1.37
1.41
1.35
1.34
0.93
0.92
0.90
0.00
4.00
4.02
4.02
4.03
7.95
24.64
11.72

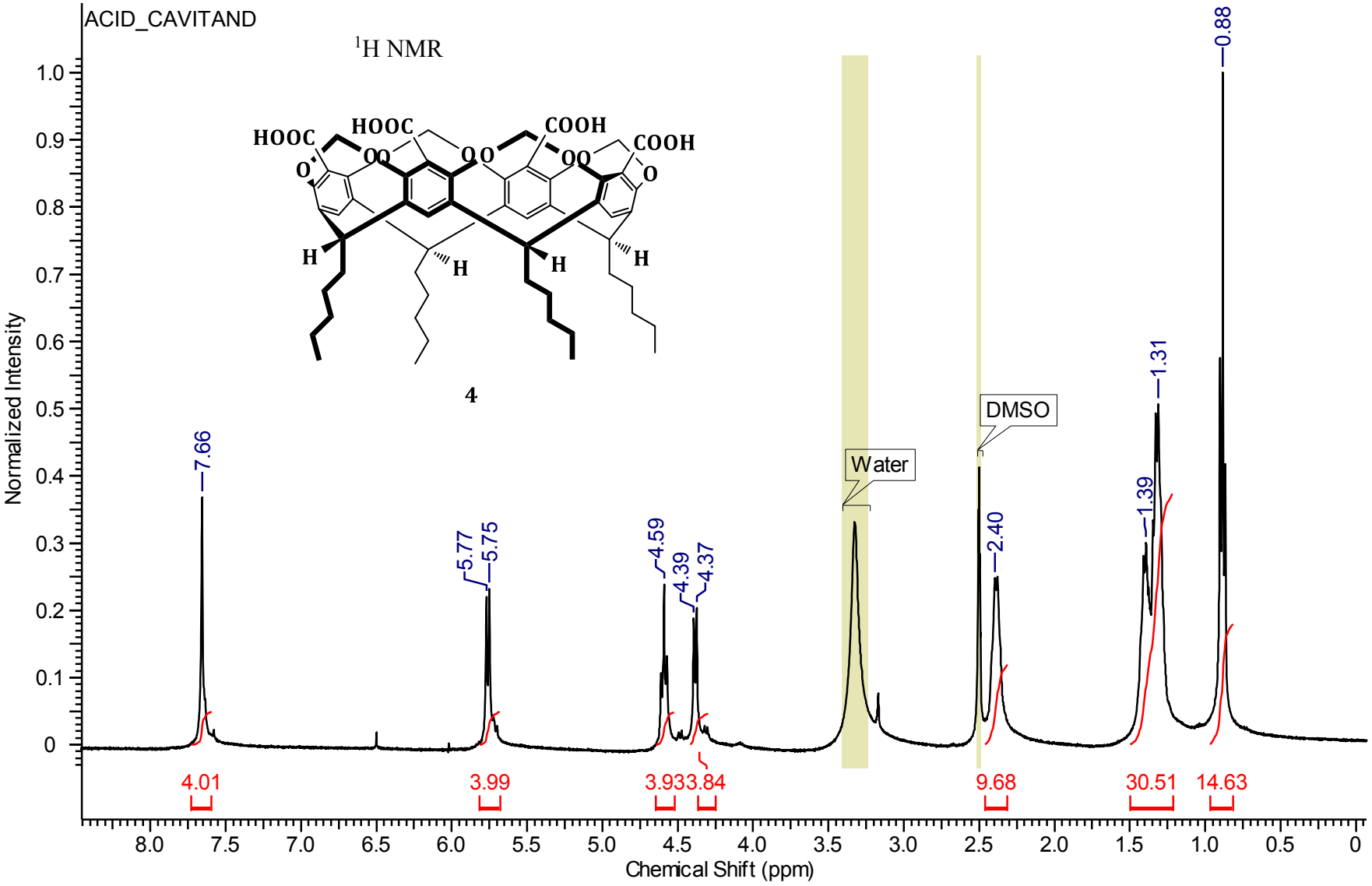
ACID_CAVITAND
^{1}H NMR
HOOC
HOOC
COOH
COOH
O
O
O
O
O
O
O
O
H
H
H
H
4
Normalized Intensity
1.0
0.9
0.8
0.7
0.6
0.5
0.4
0.3
0.2
0.1
0
7.66
5.77
5.75
4.59
4.39
4.37
Water
DMSO
2.40
1.39
1.31
0.88
4.01
3.99
3.93
3.84
9.68
30.51
14.63
8.0
7.5
7.0
6.5
6.0
5.5
5.0
4.5
4.0
3.5
3.0
2.5
2.0
1.5
1.0
0.5
0
Chemical Shift (ppm)

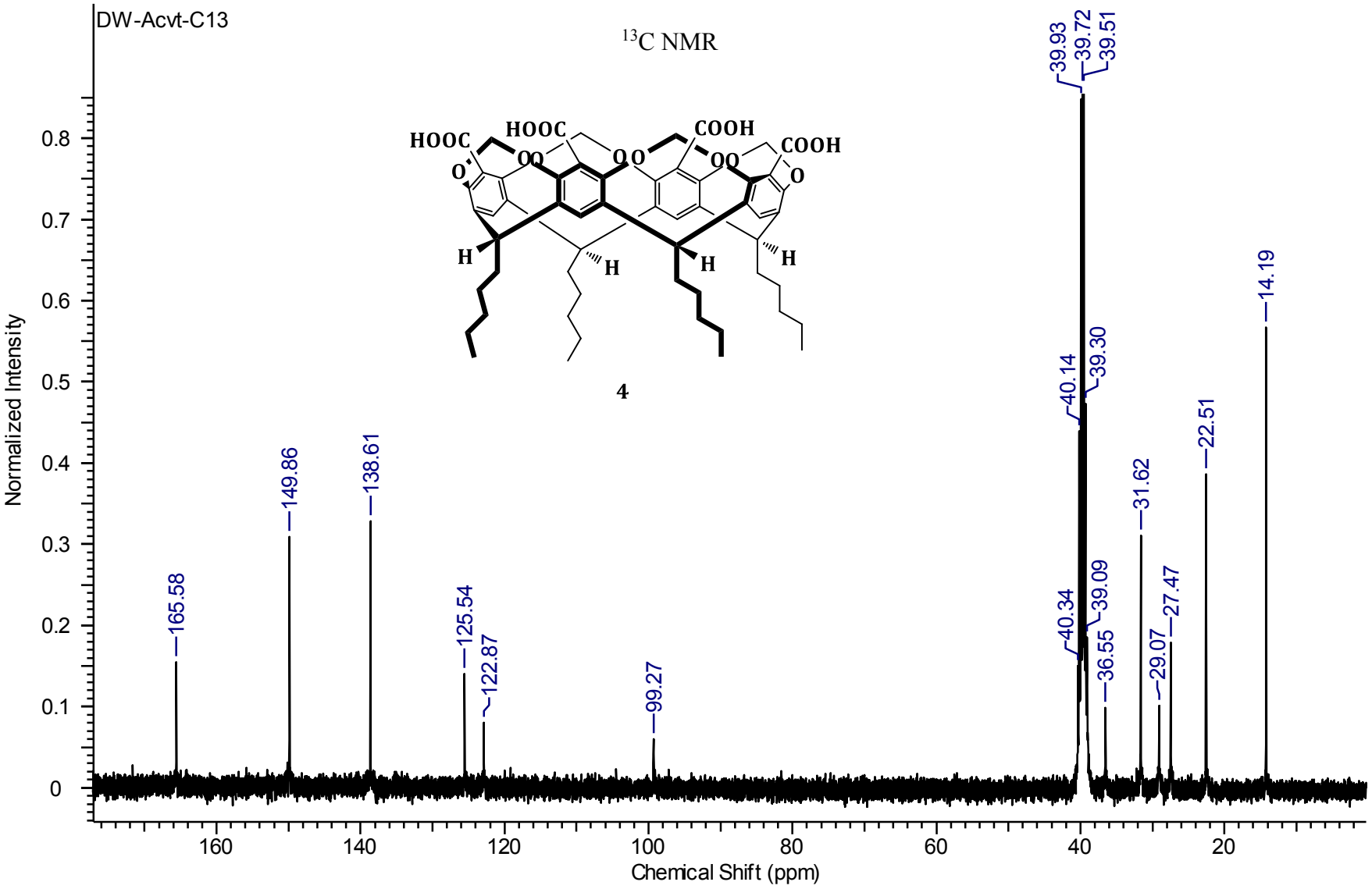
DW-Acvt-C13
^{13}C NMR
HOOC
HOOC
COOH
COOH
O
O
O
O
O
O
O
O
H
H
H
H
4
Normalized Intensity
0
0.1
0.2
0.3
0.4
0.5
0.6
0.7
0.8
165.58
149.86
138.61
125.54
122.87
99.27
40.34
40.14
39.93
39.72
39.51
39.30
39.09
36.55
31.62
29.07
27.47
22.51
14.19
160
140
120
100
80
60
40
20
Chemical Shift (ppm)

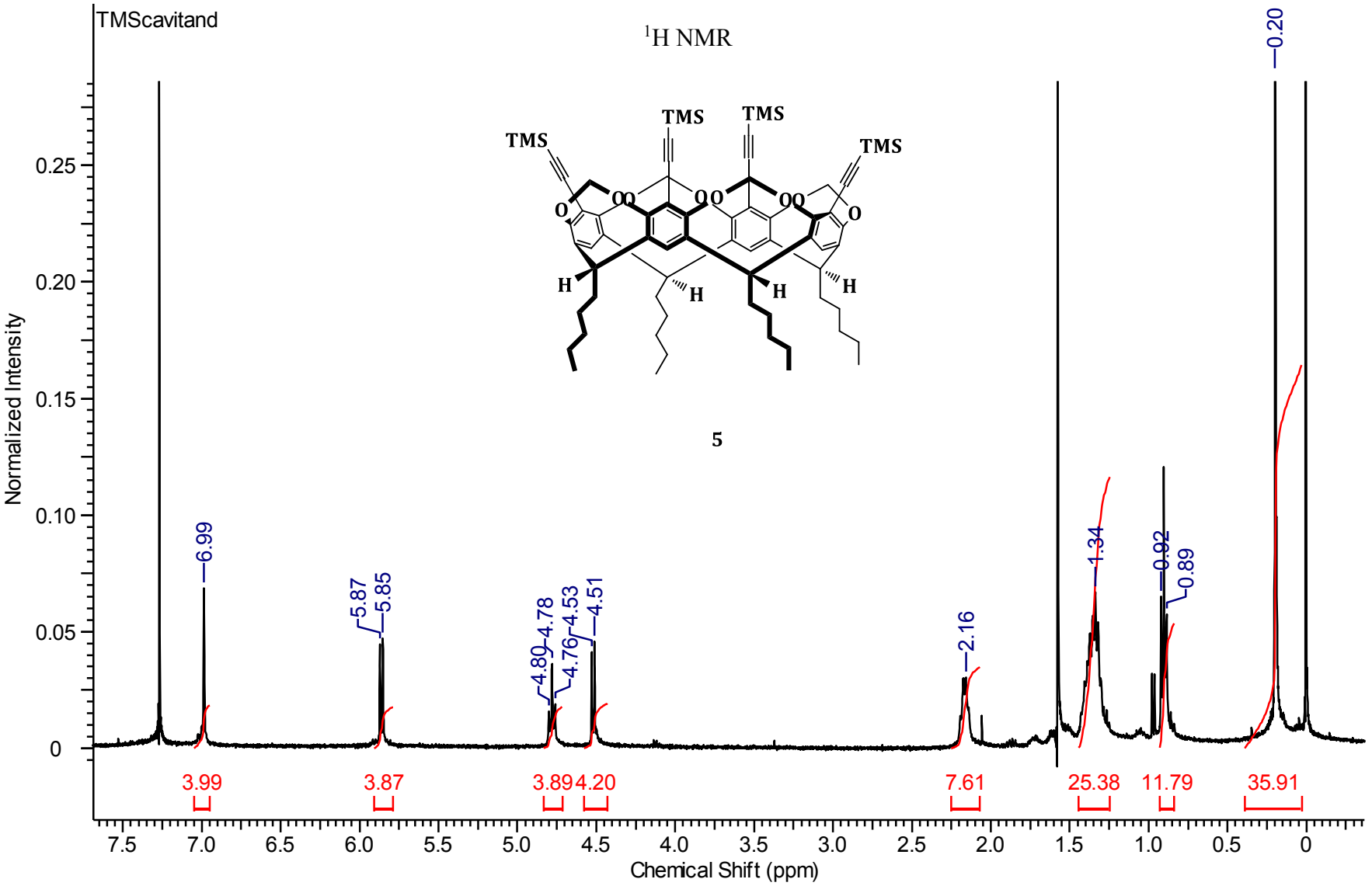
TMScavitand
^{1}H NMR
TMS
TMS
TMS
TMS
O
O
O
O
O
O
H
H
H
H
5
Normalized Intensity
0.25
0.20
0.15
0.10
0.05
0
6.99
5.87
5.85
4.89
4.78
4.76
4.53
4.51
2.16
1.34
0.92
0.89
0.20
3.99
3.87
3.89
4.20
7.61
25.38
11.79
35.91
7.5
7.0
6.5
6.0
5.5
5.0
4.5
4.0
3.5
3.0
2.5
2.0
1.5
1.0
0.5
0
Chemical Shift (ppm)

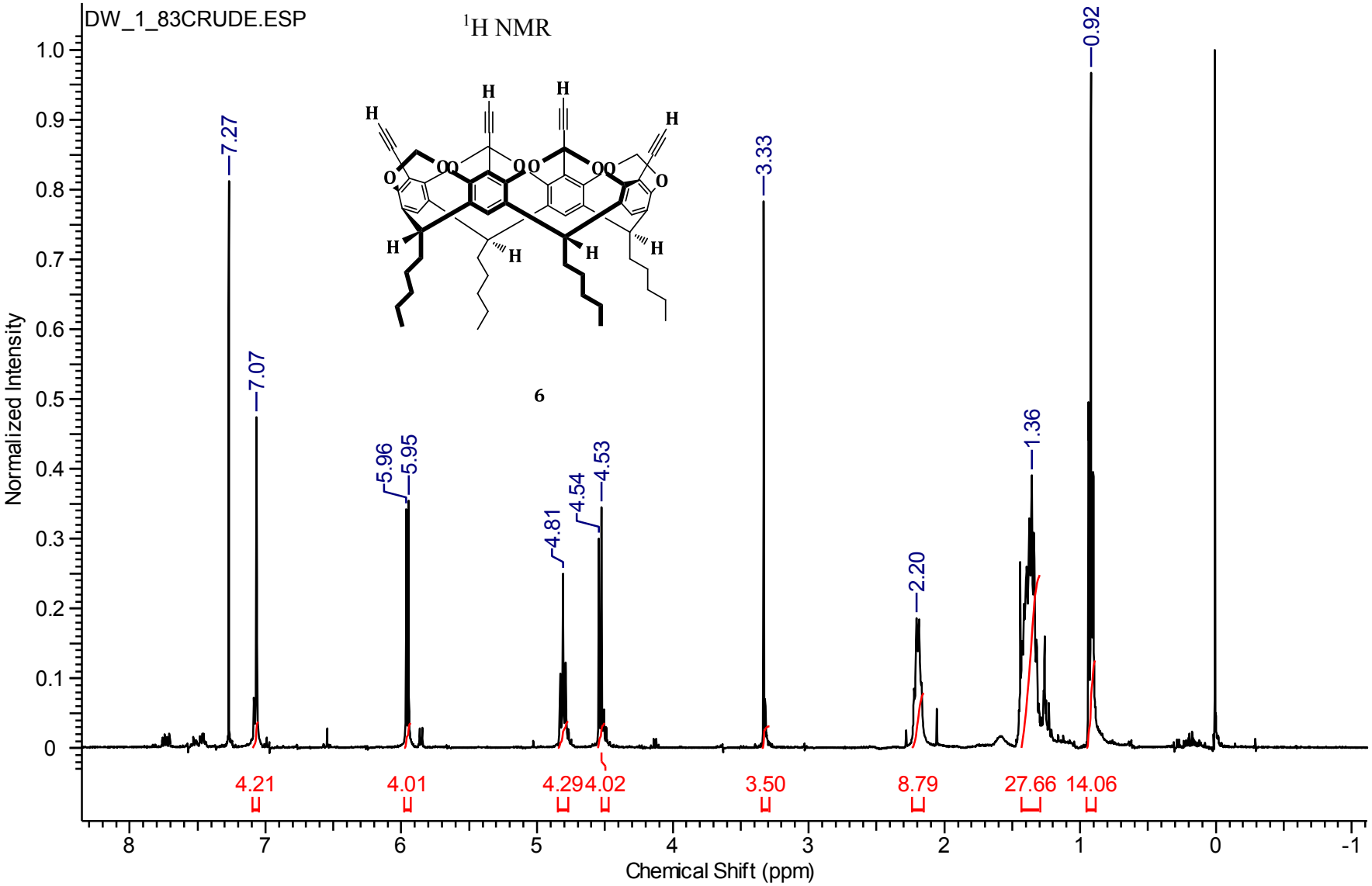
DW_1_83CRUDE.ESP
^{1}H NMR
6
Normalized Intensity
Chemical Shift (ppm)
7.27
7.07
5.96
5.95
4.81
4.54
4.53
3.33
2.20
1.36
0.92
4.21
4.01
4.29
4.02
3.50
8.79
27.66
14.06

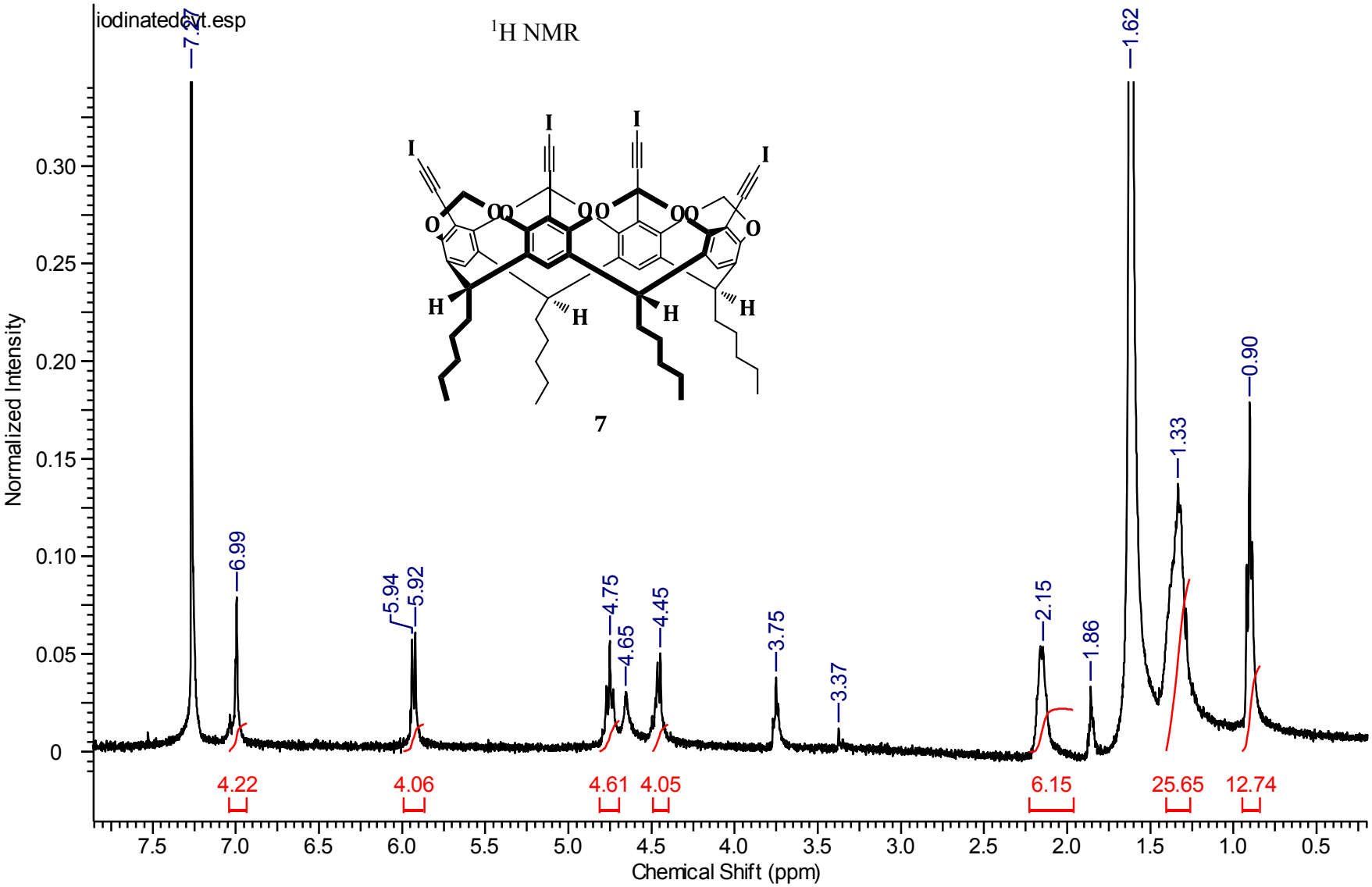
iodinated.vt.esp
^{1}H NMR
7
Normalized Intensity
Chemical Shift (ppm)
7.27
6.99
5.94
5.92
4.75
4.65
4.45
3.75
3.37
2.15
1.86
1.62
1.33
0.90
4.22
4.06
4.61
4.05
6.15
25.65
12.74

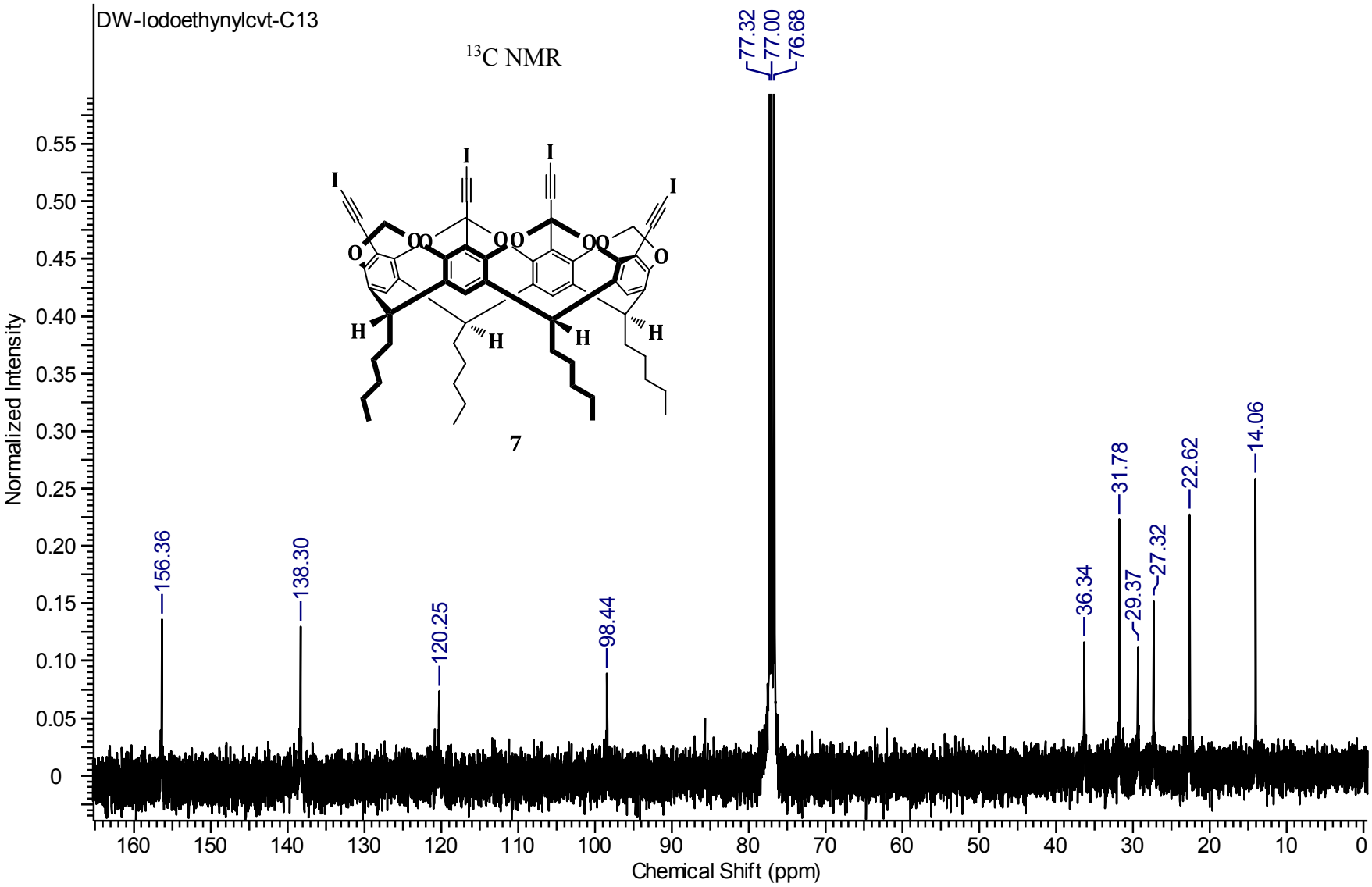
DW-Iodoethynylcvt-C13
^{13}C NMR
77.32
77.00
76.68
156.36
138.30
120.25
98.44
36.34
31.78
29.37
27.32
22.62
14.06
Normalized Intensity
Chemical Shift (ppm)
7

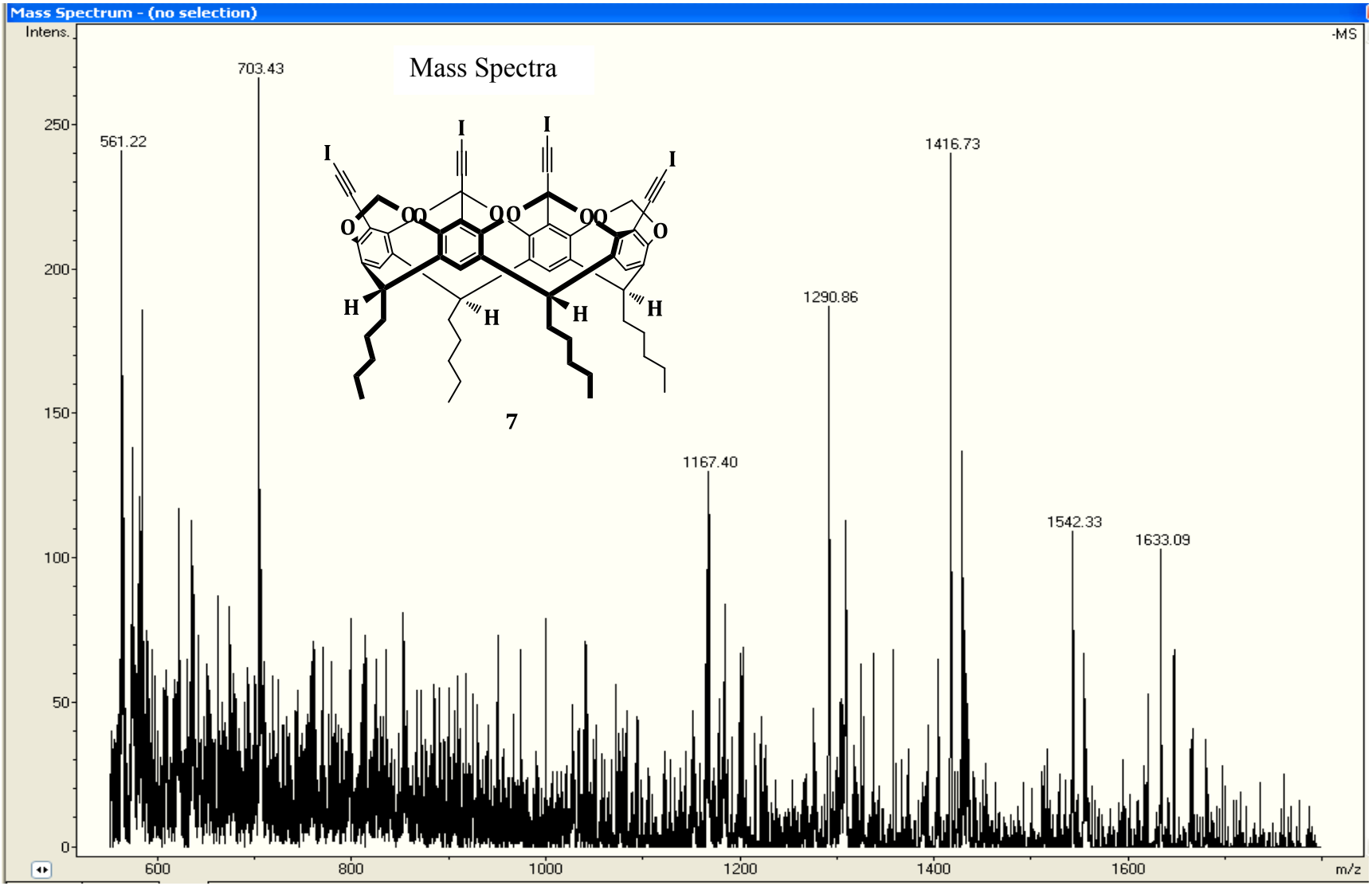
Mass Spectrum - (no selection)
Intens.
-MS
Mass Spectra
703.43
561.22
1416.73
1290.86
1167.40
1542.33
1633.09
250
200
150
100
50
0
600
800
1000
1200
1400
1600
m/z
I
O
H
7

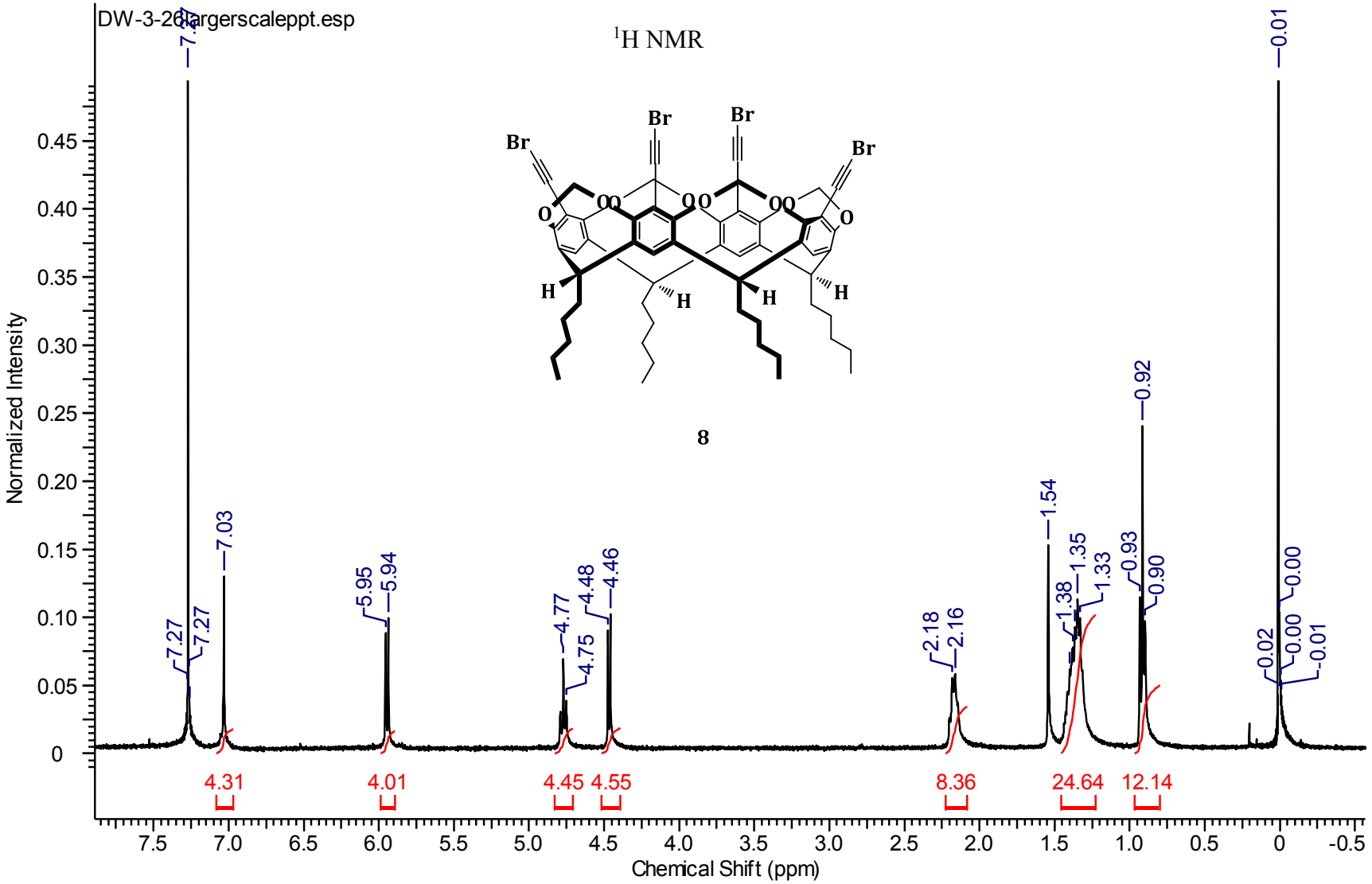
DW-3-26largerscaleppt.esp
^{1}H NMR
Br
Br
Br
Br
O
O
O
O
O
O
H
H
H
H
8
Normalized Intensity
0.45
0.40
0.35
0.30
0.25
0.20
0.15
0.10
0.05
0
7.27
7.27
7.03
5.95
5.94
4.77
4.75
4.48
4.46
2.18
2.16
1.54
1.38
1.35
1.33
0.93
0.92
0.90
0.02
0.00
0.00
-0.01
-0.01
4.31
4.01
4.45
4.55
8.36
24.64
12.14
7.5
7.0
6.5
6.0
5.5
5.0
4.5
4.0
3.5
3.0
2.5
2.0
1.5
1.0
0.5
0
-0.5
Chemical Shift (ppm)

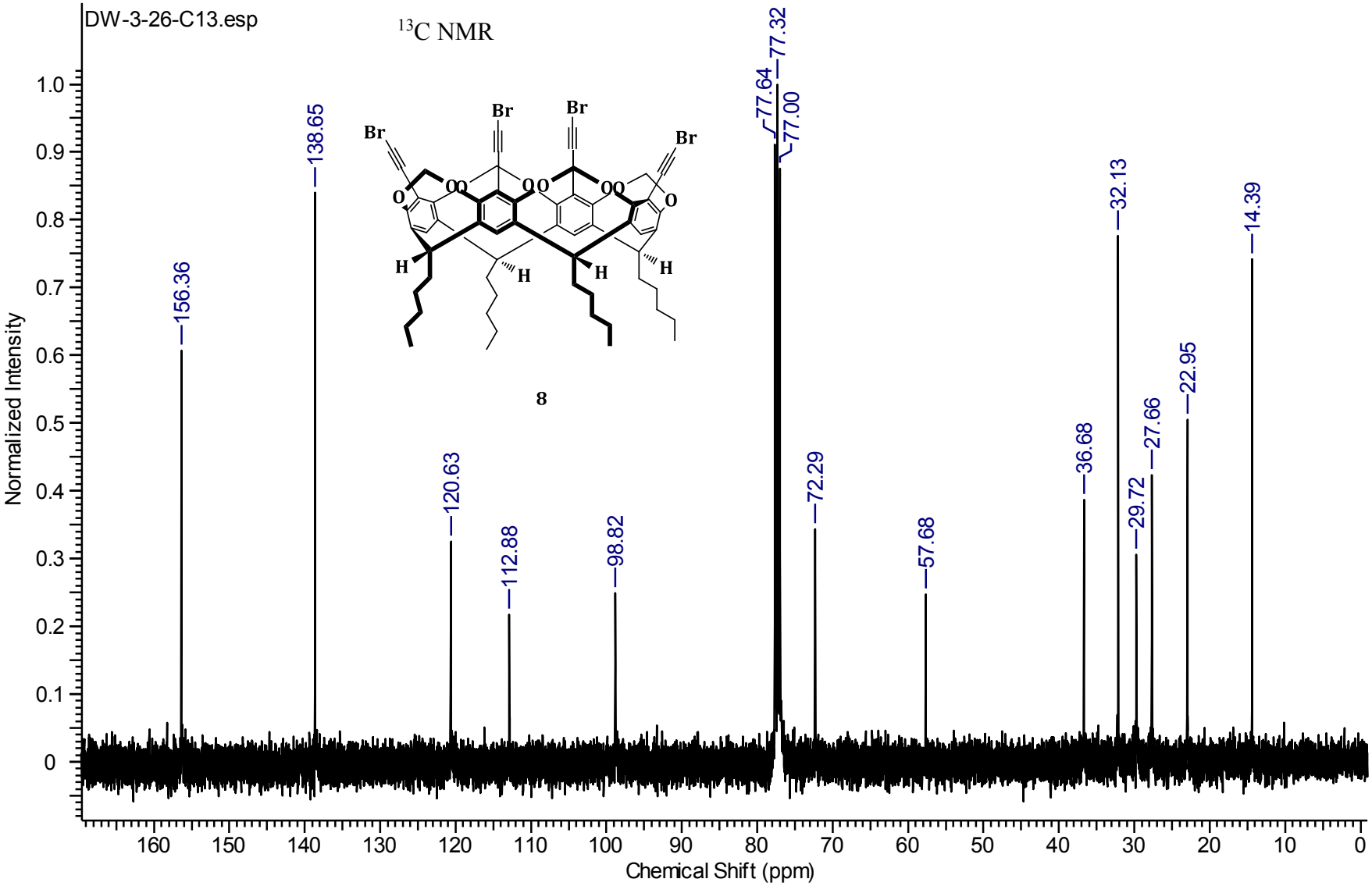
DW-3-26-C13.esp
^{13}C NMR
Normalized Intensity
Chemical Shift (ppm)
156.36
138.65
120.63
112.88
98.82
77.64
77.32
77.00
72.29
57.68
36.68
32.13
29.72
27.66
22.95
14.39
Br
O
H

8

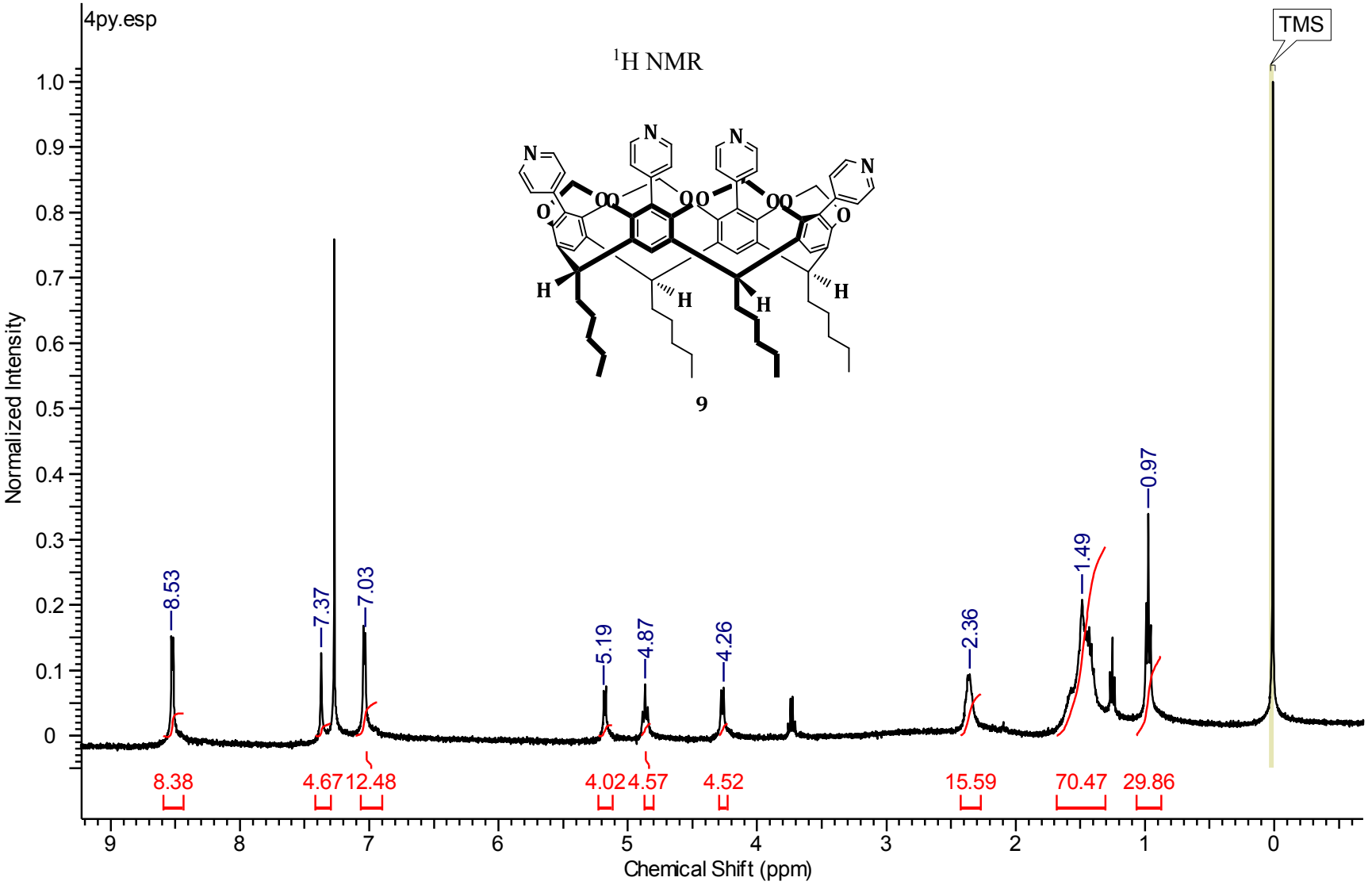
4py.esp
^{1}H NMR
TMS
Normalized Intensity
Chemical Shift (ppm)
8.53
7.37
7.03
5.19
4.87
4.26
2.36
1.49
0.97
8.38
4.67
12.48
4.02
4.57
4.52
15.59
70.47
29.86

9

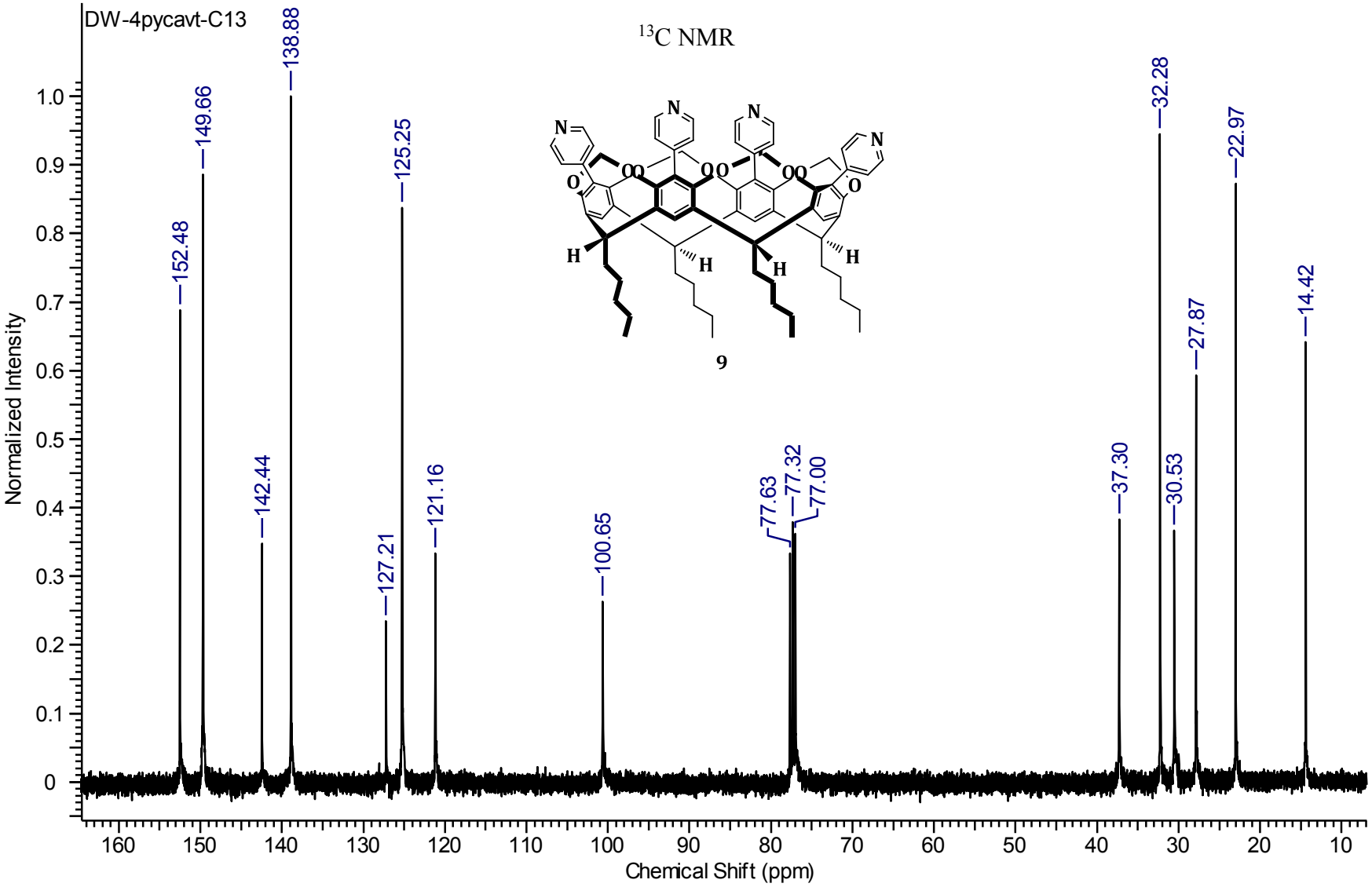
DW-4pycavt-C13
^{13}C NMR
152.48
149.66
142.44
138.88
127.21
125.25
121.16
100.65
77.63
77.32
77.00
37.30
32.28
30.53
27.87
22.97
14.42
Normalized Intensity
Chemical Shift (ppm)
9

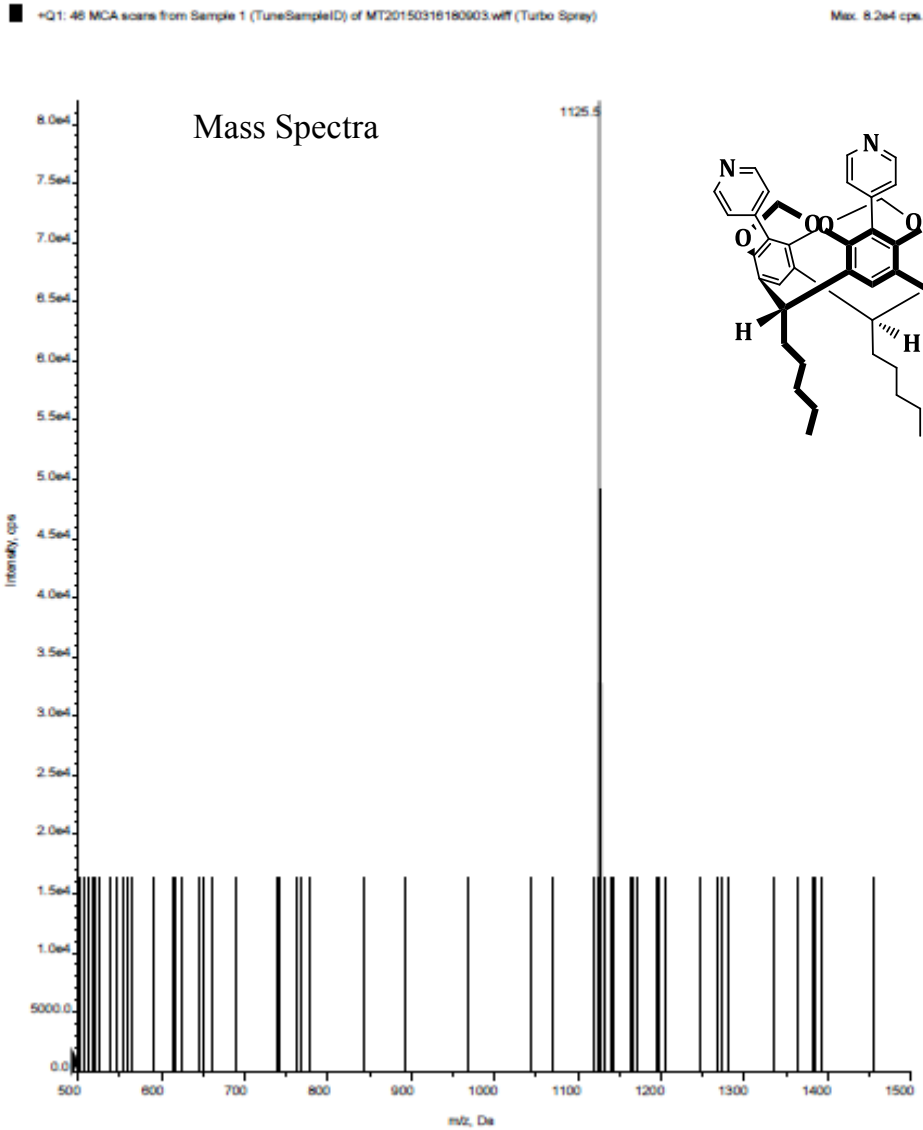
+Q1: 46 MCA scans from Sample 1 (TuneSampleID) of MT20150316180903.wiff (Turbo Spray)
Max. 8.2e4 cps.
Mass Spectra
1125.5
Intensity, cps
m/z, Da

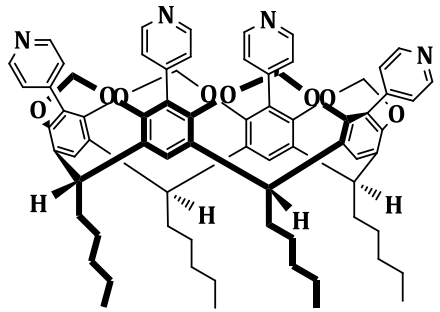

9

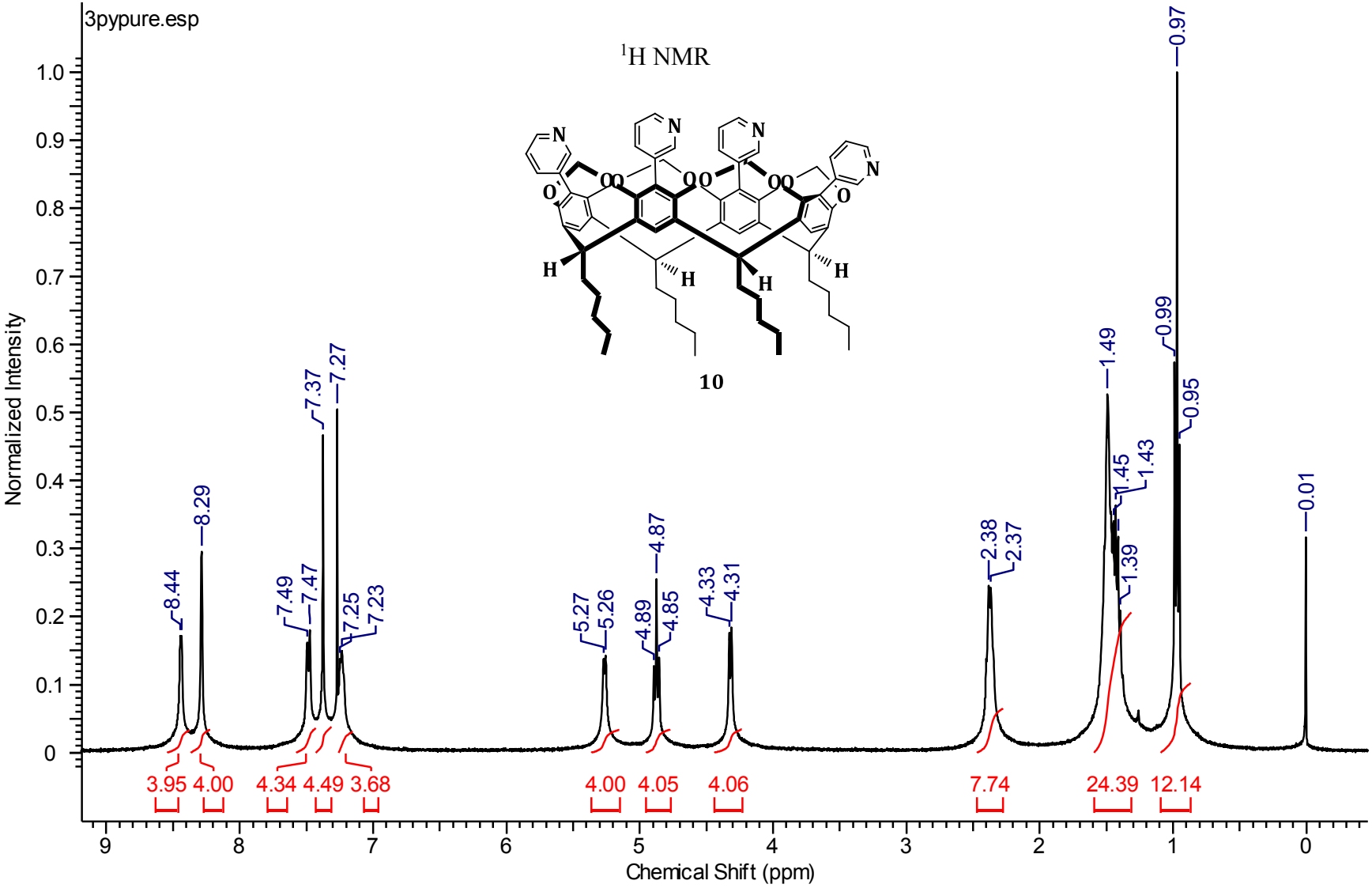
3pypure.esp
^{1}H NMR
10
Normalized Intensity
Chemical Shift (ppm)
8.44
8.29
7.49
7.47
7.37
7.27
7.25
7.23
5.27
5.26
4.89
4.85
4.87
4.33
4.31
2.38
2.37
1.49
1.45
1.43
1.39
0.99
0.97
0.95
0.01
3.95
4.00
4.34
4.49
3.68
4.00
4.05
4.06
7.74
24.39
12.14

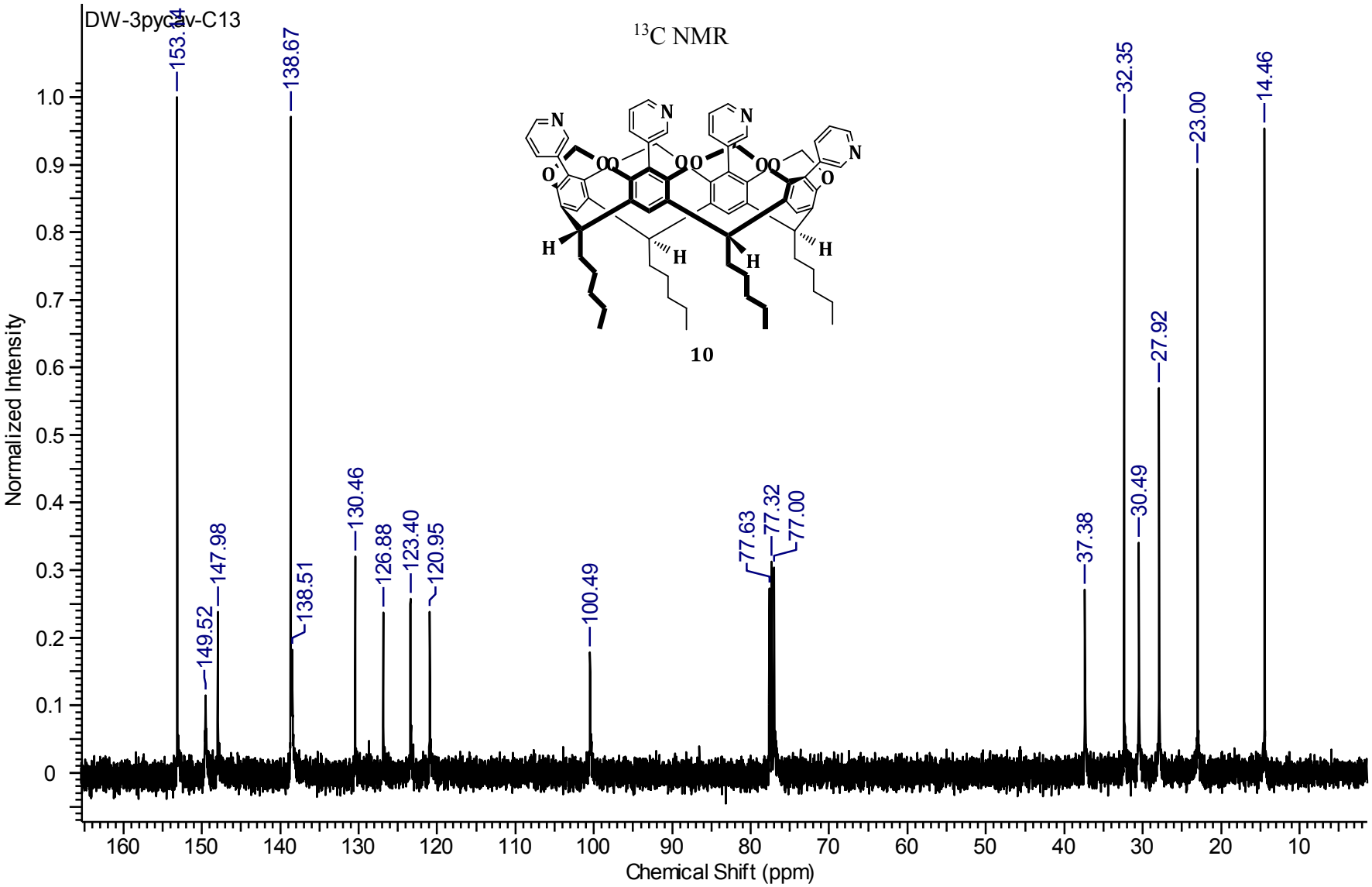
DW-3pycav-C13
153.84
138.67
32.35
23.00
14.46
149.52
147.98
138.51
130.46
126.88
123.40
120.95
100.49
77.63
77.32
77.00
37.38
30.49
27.92
Normalized Intensity
Chemical Shift (ppm)

^{13}C NMR

10

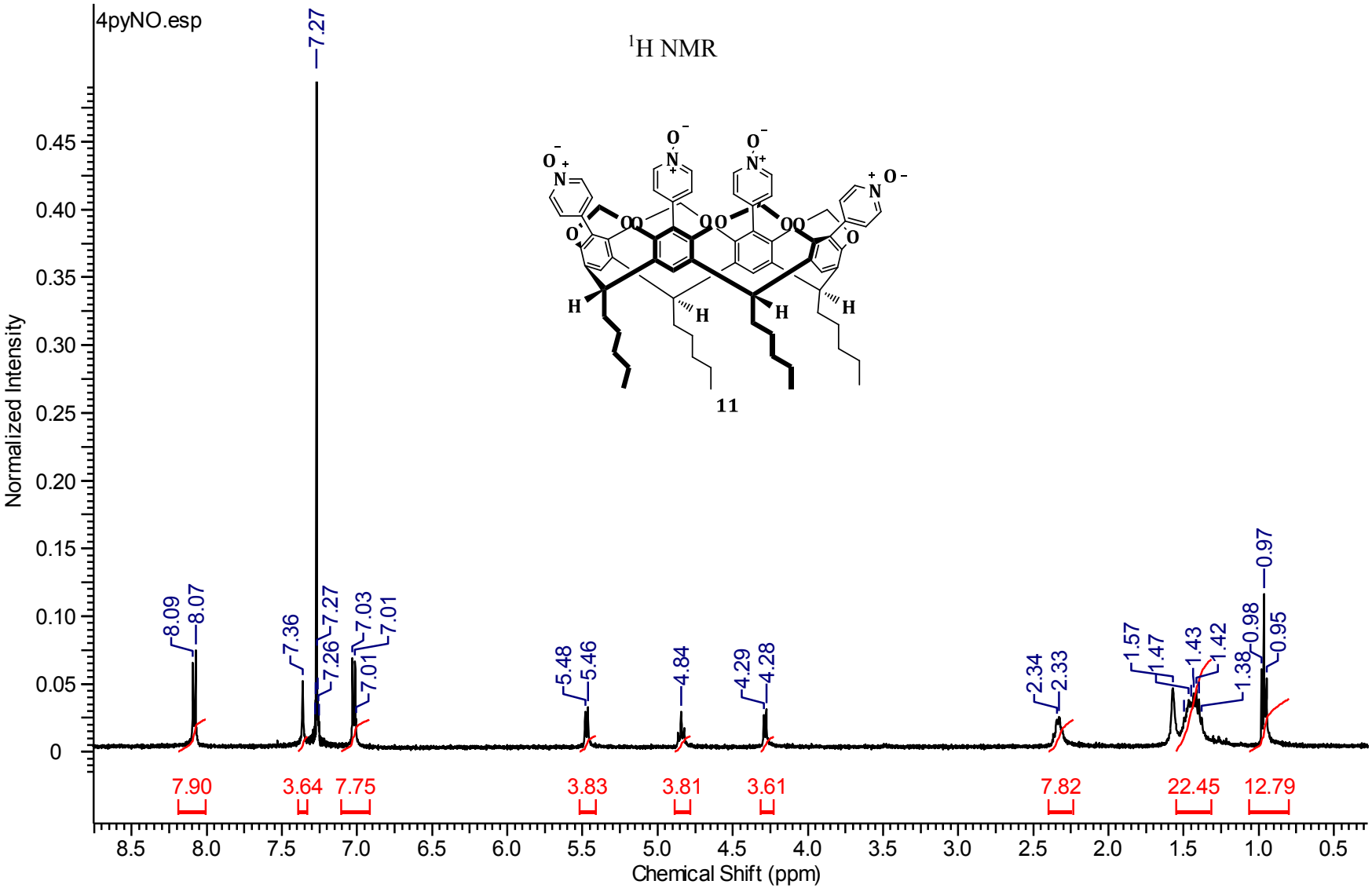
4pyNO.esp
^{1}H NMR
11
Normalized Intensity
Chemical Shift (ppm)
8.09
8.07
7.36
7.27
7.26
7.03
7.01
5.48
5.46
4.84
4.29
4.28
2.34
2.33
1.57
1.47
1.43
1.42
1.38
0.98
0.97
0.95
7.90
3.64
7.75
3.83
3.81
3.61
7.82
22.45
12.79

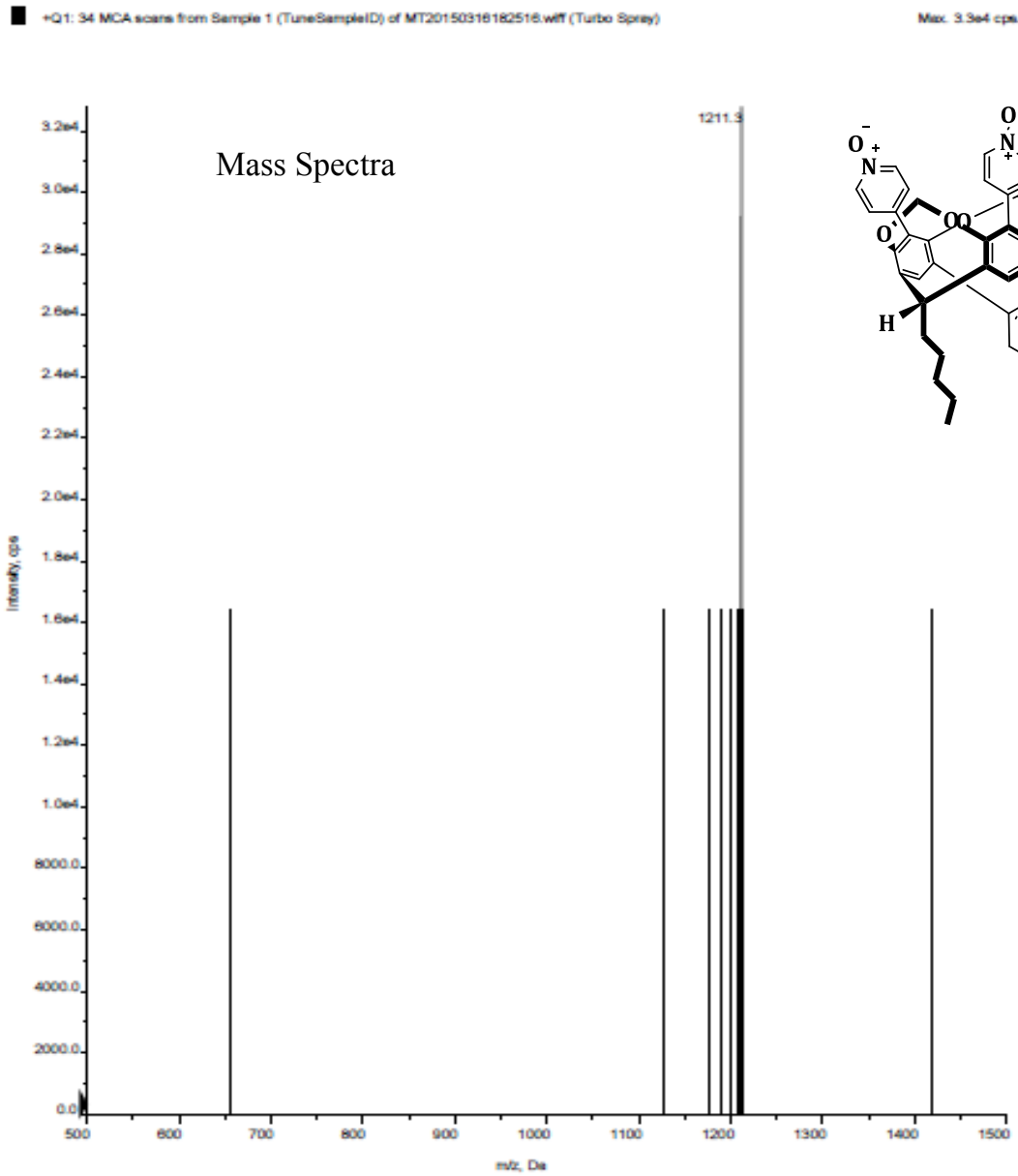
+Q1: 34 MCA scans from Sample 1 (TuneSampleID) of MT20150316182516.wiff (Turbo Spray)
Max. 3.3e4 cps.
Mass Spectra
1211.3
Intensity, cps
m/z, Da

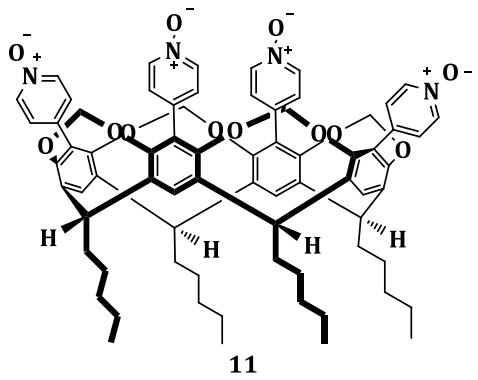

11

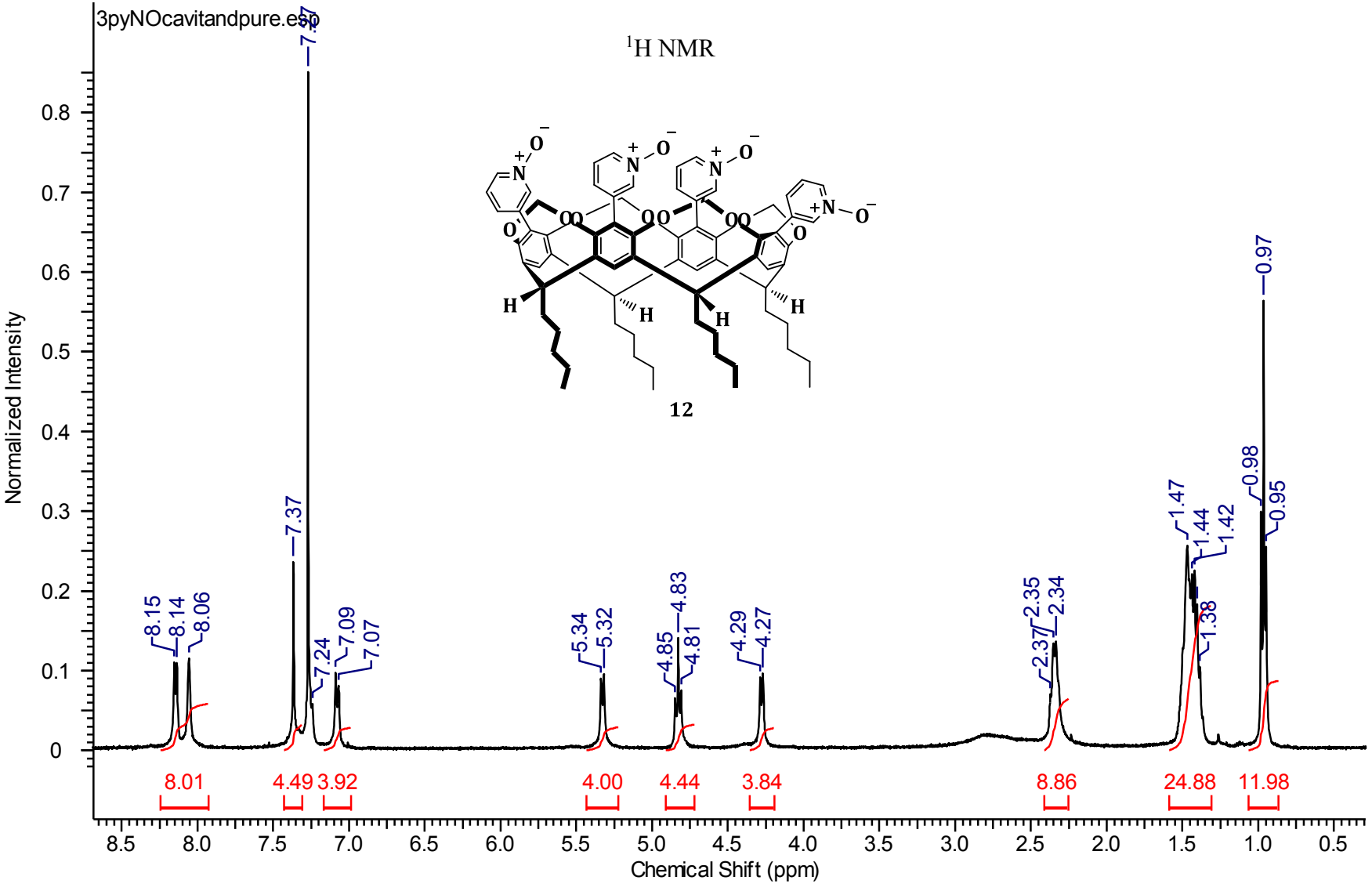
3pyNOcavitandpure.esp
^{1}H NMR
12
Normalized Intensity
Chemical Shift (ppm)
8.15
8.14
8.06
7.37
7.24
7.09
7.07
5.34
5.32
4.85
4.83
4.81
4.29
4.27
2.37
2.35
2.34
1.47
1.44
1.42
1.38
0.98
0.97
0.95
8.01
4.49
3.92
4.00
4.44
3.84
8.86
24.88
11.98

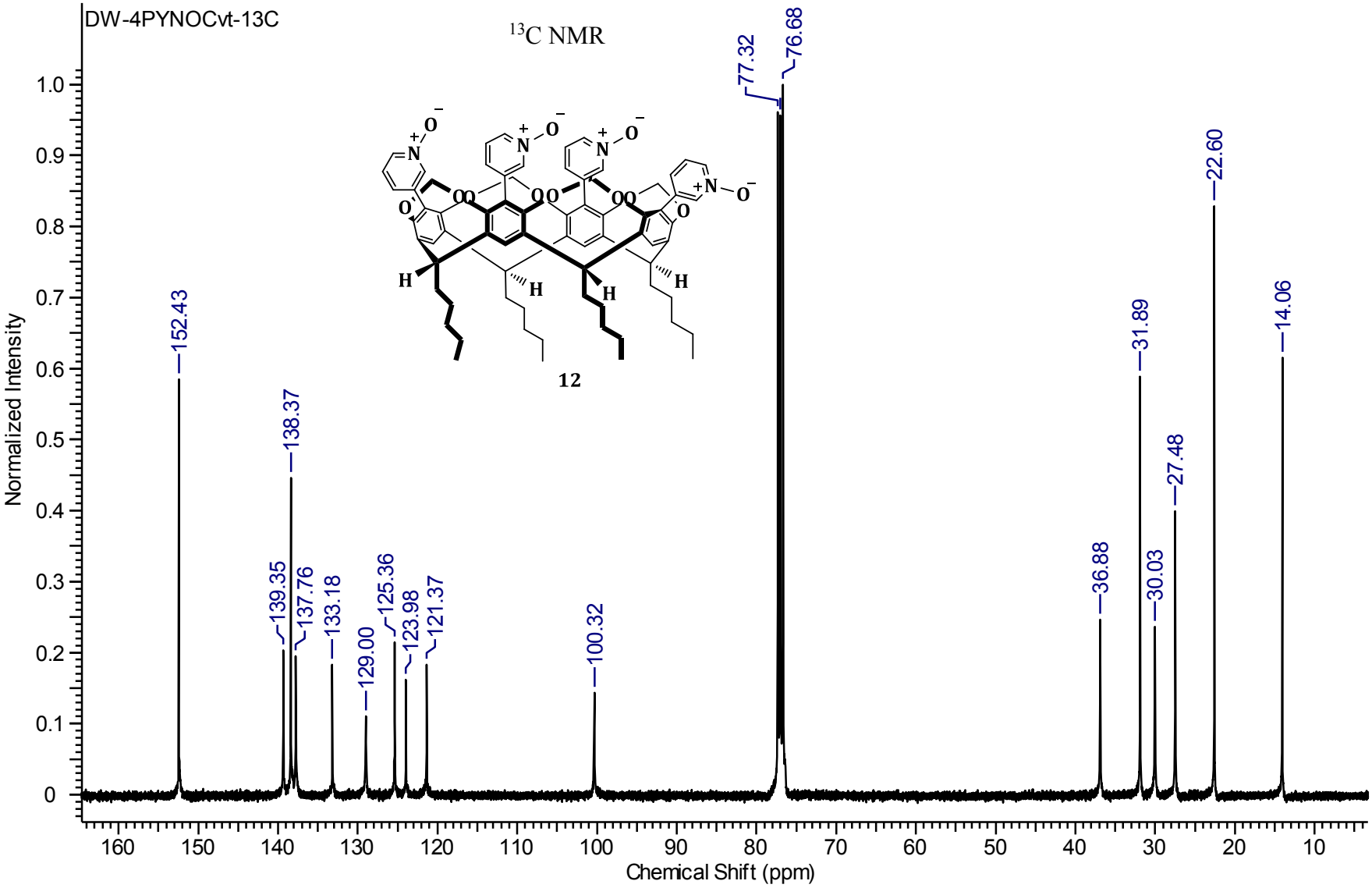
DW-4PYNOCvt-13C
^{13}C NMR
12
Normalized Intensity
Chemical Shift (ppm)
152.43
139.35
138.37
137.76
133.18
129.00
125.36
123.98
121.37
100.32
77.32
76.68
36.88
31.89
30.03
27.48
22.60
14.06

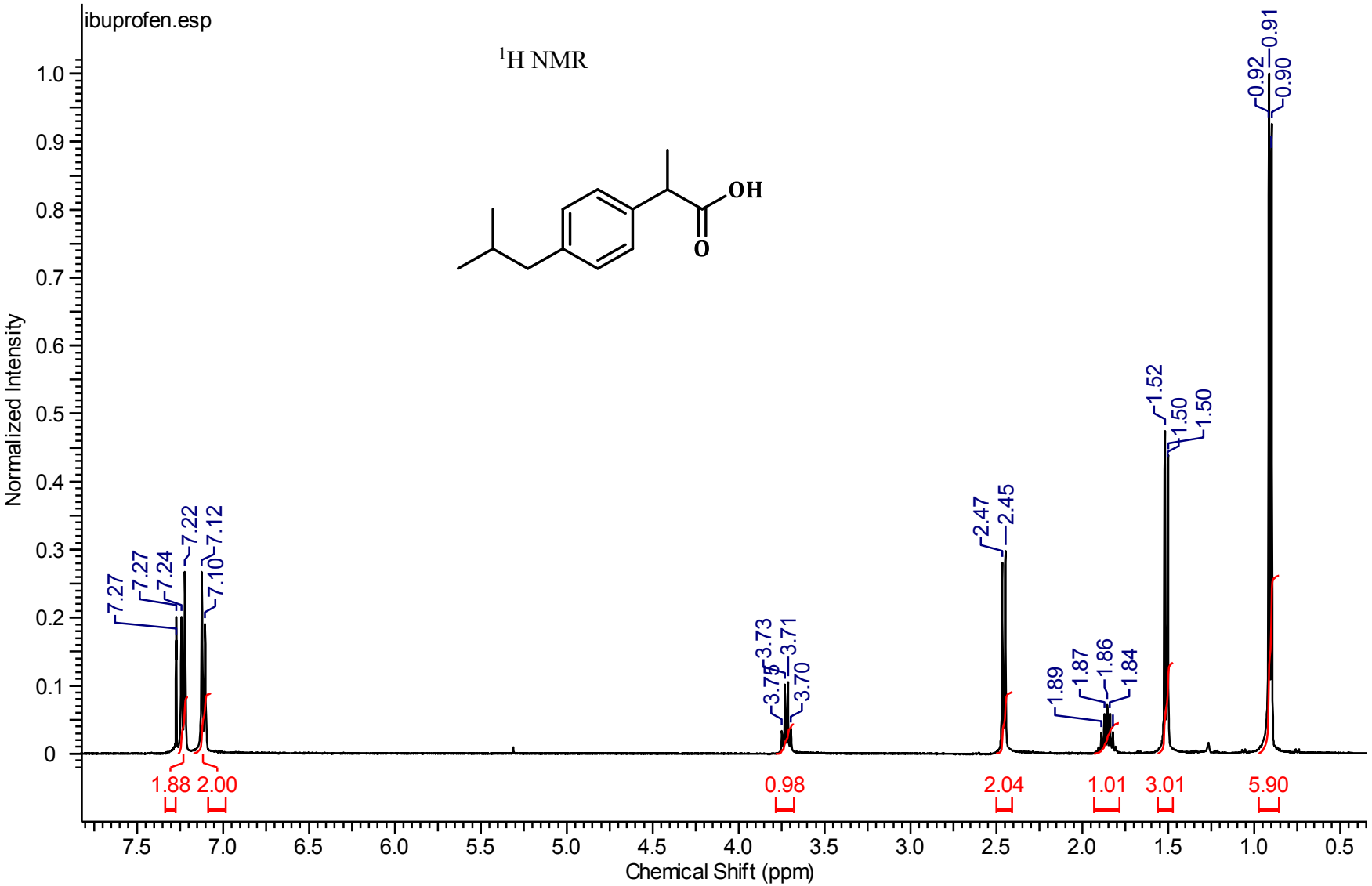
ibuprofen.esp
^{1}H NMR
OH
O
Normalized Intensity
Chemical Shift (ppm)
7.27
7.27
7.24
7.22
7.12
7.10
3.73
3.71
3.70
2.47
2.45
1.89
1.87
1.86
1.84
1.52
1.50
1.50
0.92
0.91
0.90
1.88
2.00
0.98
2.04
1.01
3.01
5.90

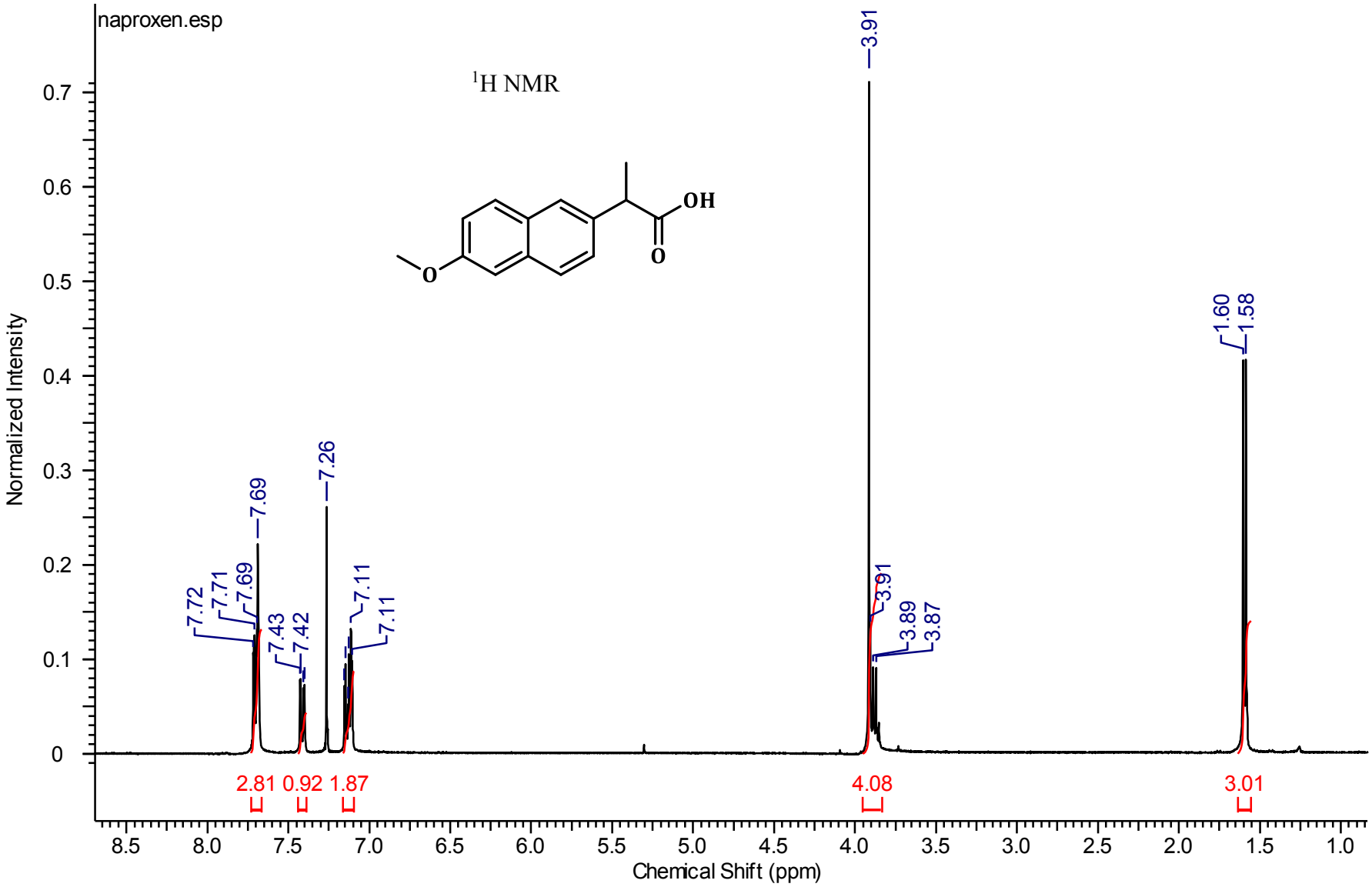
naproxen.esp
^{1}H NMR
OH
O
O
Normalized Intensity
Chemical Shift (ppm)
7.72
7.71
7.69
7.69
7.43
7.42
7.26
7.11
7.11
3.91
3.91
3.89
3.87
1.60
1.58
2.81
0.92
1.87
4.08
3.01

DSC profile of A_4·Succinic acid

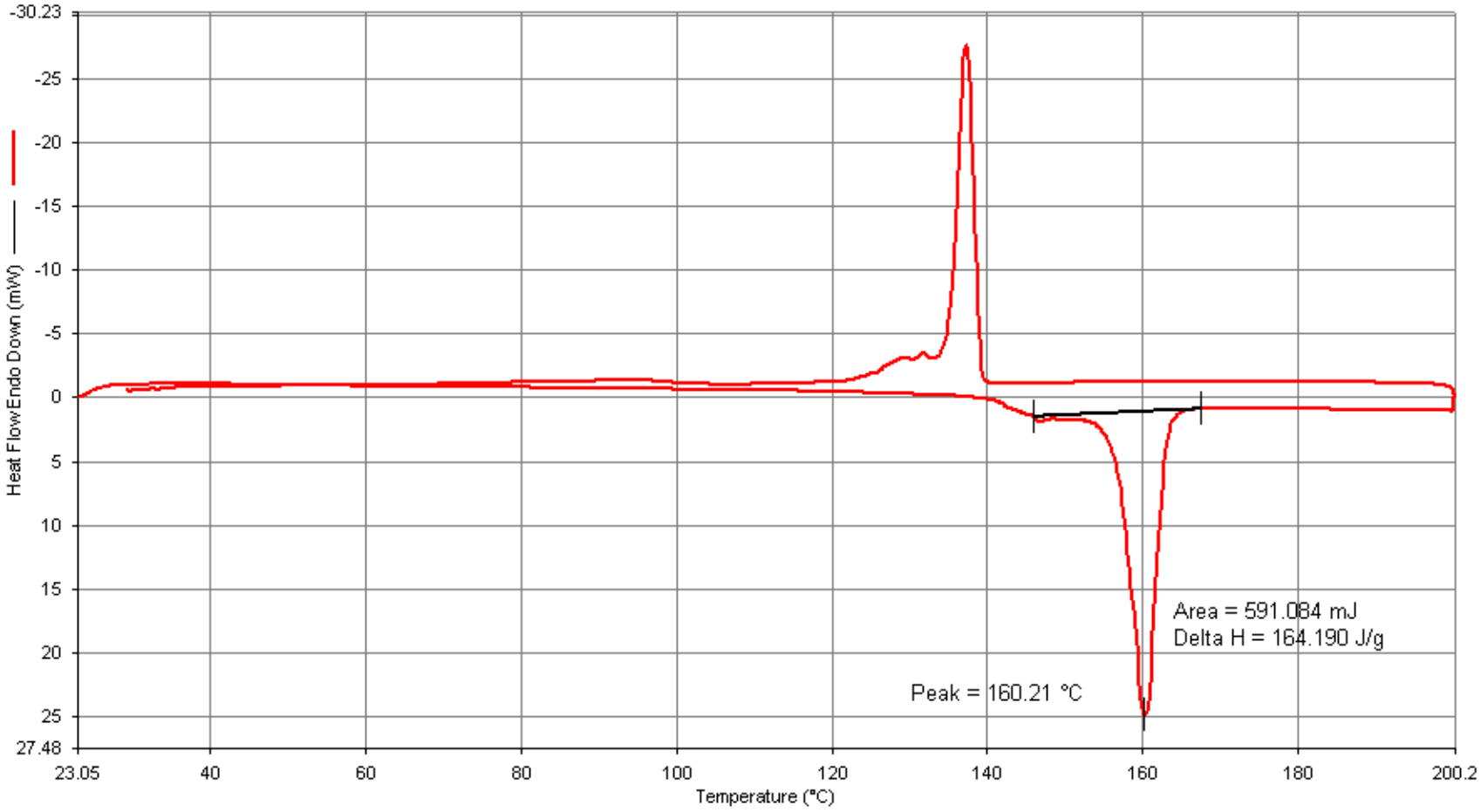

DSC profile of $A_4 \cdot D_2$